

Construction of a chemical vapour deposition reactor and the deposition of ZrC layers

By
Saphina Biira



**Submitted in partial fulfilment of the requirement for the degree of
Doctor of Philosophy (PhD) in Physics**

In the Faculty of Natural and Agricultural Sciences at the University of Pretoria

November, 2017

Supervisor: Prof. JB Malherbe

Co-supervisors: Prof. PL Crouse

Dr. H Bissett

Dr. TT Thulani

Summary

Construction of a chemical vapour deposition reactor and the deposition of ZrC layers

by

Saphina Biira

Submitted in partial fulfilment of the requirements for the degree of (PhD) in Physics in the Faculty of Natural and Agricultural Science, University of Pretoria

Supervisor/Promoter: Prof. JB Malherbe

Co-supervisors: Prof. PL Crouse

Dr. H Bissett

Dr. TT Thulani

Generation IV high temperature nuclear reactors use TRISO (tristructural isotropic) particles for containment of radioactive fission products. In these particles silicon carbide (SiC) is the main barrier for containing solid fission products. ZrC has been proposed either as an additional layer or replacement of SiC layer of the TRISO fuel particle. This is because ZrC would be a better barrier than SiC against the diffusion of Ag and will be more resistant against palladium attack. This suggestion is based on ZrC's excellent physical properties like: low neutron capture cross section, good thermal shock resistance, excellent thermal stability, etc. However these properties depend on a number of factors such as chemical composition, microstructure, morphology, the presence of impurities, etc. Many attempts have been made to grow ZrC layers. However, the growth of high quality polycrystalline ZrC layers with good stoichiometry has remained a challenge. This study focuses on designing a chemical vapour deposition (CVD) reactor for growing ZrC layers and studying the properties of ZrC layers grown under different conditions.

CVD was chosen as the most effective process to grow ZrC layers. CVD enables the production of relatively pure uniform layers with good adhesion and reproducibility at fairly good deposition rates. A thermal CVD reactor system operating at atmospheric pressure was designed to grow ZrC layers. Radio frequency (RF) induction heating was used as the energy source, with a vertical-flow design, using thermally stable materials. The ZrC layers were grown while varying the substrate temperature, gas flow ratios, substrate-gas inlet gaps, deposition time and partial pressures. The precursors utilised to grow ZrC were zirconium tetrachloride (ZrCl_4) and methane (CH_4) in an excess of argon and hydrogen. The deposited ZrC layers were then characterised by X-ray diffraction (XRD), energy dispersive X-ray spectroscopy (EDS), Raman spectroscopy and field emission scanning electron microscopy (FE-SEM).

To optimise the process parameters, response surface methodology was applied. A central composite design was used to investigate the effect of temperature (1200 °C–1600 °C) and molar ratio of $\text{CH}_4/\text{ZrCl}_4$ (6.04–24.44) on the growth rate, atomic ratio of C/Zr and crystallite size of ZrC layers. The temperature of 1353.3 °C and the $\text{CH}_4/\text{ZrCl}_4$ molar ratio of 10.41 were determined as the optimal conditions for growing near-stoichiometric ZrC layers. The optimum values for C/Zr atomic percentage ratio, growth rate and average crystallite size were 1.03, 6.05 $\mu\text{m}/\text{h}$ and 29.8 nm respectively.

The influence of the gap between the gas inlet and the substrate (70–170 mm) on the growth rate, surface morphology, phase composition and microstructure of ZrC layers deposited at different temperatures was investigated. The growth rate of ZrC layers prepared at 1400 °C was higher than at 1200 °C, and decreased with increase in the gap at both temperatures. The boundary layer thickness increased with an increase in substrate-inlet gap. The diffusion coefficients of the reactants increased with temperature. A model was used to illustrate the diffusion of source materials through the boundary layer to the reacting surface. An increase

in the gap from 70 mm to 170 mm at a temperature of 1400 °C, caused the layers to become more uniform. An increase in particle agglomeration was also observed. By contrast, at 1200 °C the surface crystallites had complex facets that decreased in size as the gap increased from 70 mm to 170 mm.

The effect of $ZrCl_4$ partial pressure on the growth rate, microstructure and surface morphology of the layers deposited at 1400 °C for 2 h was studied. The boundary layer thickness decreased as the $ZrCl_4$ partial pressure increased. The transport process of the source materials was laminar and forced convection flow. The flow process of the source materials through the boundary layer to the reacting surface was illustrated using a model. The growth rate and average crystallite size increased with $ZrCl_4$ partial pressure, while the lattice parameter, lattice strain and dislocation density decreased. The size of crystals increased and the cavities surrounding them decreased in number as the $ZrCl_4$ partial pressure increased.

The microstructure evolution and the growth characteristics of ZrC layers with deposition time (0.5 to 2.5 hours at 1400 °C) were investigated. The average crystallite size of the ZrC layers increased from 27.8 nm to 32.3 nm with deposition time from 0.5 h to 2.5 h. At short deposition times the Raman spectra showed the acoustic and optic branches indicating that the ZrC contained carbon vacancies. The D and G peaks were observed and their intensities increased with deposition time. This was an indication that carbon inclusions in the layers increased with deposition time. The surface morphology of the ZrC layers depended strongly on the deposition time. That is, for a short deposition time the surface of the layers was relatively flat and smooth but as the deposition time increased the size of the clusters increased.

DECLARATION

I, Saphina Biira, declare that the thesis, which I hereby submit for the degree of PhD in Physics at the University of Pretoria, is my own work and has not previously been submitted by me for a degree at this or any other tertiary institution.

Signature.....

Date.....

ACKNOWLEDGEMENTS

- First of all I would like to express my endless heartfelt gratitude to my promoter, Prof. JB. Malherbe for his unconditional patience, support and encouragement. I appreciate his determined supervision, invaluable suggestions, critical comments and cautions. Also my gratefulness goes to my co-supervisors Prof PL. Crouse, Dr. H. Bissett and Dr. TT. Hlatswayo for their endless support and scientific guidance which made this work to be this shape.
- This PhD study program was generously supported by funds from the African Union Commission (AU), the Department of Science and Technology (DST) of South Africa through nuclear materials development network (NMDN) of advance metals initiative (AMI), Busitema University, University of Pretoria and the South Africa Nuclear Energy Corporation (Necsa) to whom I am exceedingly grateful.
- I would also like to acknowledge the assistance from colleagues and staff at Necsa (Applied Chemistry Division) and University of Pretoria (Department of Physics and Department of Chemical Engineering).
- I am particularly indebted to my only sister and my children for their endless love. Please pardon me for cheating on your time. My apologies for any shortcomings this PhD study and my absence from you might have caused.
- For always and forever, is my husband George, my best friend, my cheer leader and the best thing that ever happened to me! He is the reason I have made this far. He has held me when I cried and cheered with me when I won, and I will love him forever.
- Life is worth a living because I have it. I acknowledge the contribution of my Mum (RIP) for everything she went through to have me alive. Mum, I miss you. I wish you

were there to witness this. My father, I appreciate his endless prayers and contributions towards my success.

- I thank all those whose names I have not mentioned here, but have been and are still part of my life journey. May you all be rewarded abundantly with good health, happiness and wealth?
- Finally I glorify the Almighty God for each and every aspect of my life and the people around me.

Table of Contents

Summary.....	i
CHAPTER 1	1
INTRODUCTION.....	1
1.1 Background	1
1.2 Motivation.....	3
1.3 Aims.....	4
1.4 Approach	4
1.5 Contributions.....	5
1.6 Thesis layout.....	5
1.7 References.....	6
CHAPTER 2	9
COATED FUEL PARTICLES FOR HIGH TEMPERATURE GAS COOLED NUCLEAR REACTORS	9
2.1 The TRISO fuel particle.....	9
2.2 SiC-TRISO coated fuel particle failure.....	10
2.3 Diffusion mechanism of fission products	13
2.4 References.....	17
CHAPTER 3	19
ZIRCONIUM CARBIDE.....	19
3.1 Properties of zirconium carbide	19
3.2 Cladding materials for nuclear reactor requirements.....	22
3.3 Zirconium carbide phases	23
3.4 Zirconium carbide synthesis	24
3.4.1 Preparation of ZrC by solid phase reactions.....	25
3.4.2 Preparation of zirconium carbide from solution-based precursors	28
3.4.3 Preparation of ZrC from vapour phase based reactions.....	29
3.5 Effect of oxygen and carbon content on ZrC lattice parameter	29
3.6 Effect of irradiation and oxidation on ZrC layers	30
3.7 Applications of ZrC	31

3.8	References	32
CHAPTER 4		36
FILM DEPOSITION		36
4.1	Overview of film growth.....	36
4.2	Film growth modes	37
4.3	Film deposition techniques.....	39
4.4	Chemical vapour deposition (CVD)	40
4.4.1	Thermal CVD	42
4.4.2	Closed and open CVD systems.....	43
4.4.3	Hot and cold wall CVD reactors.....	44
4.4.4	High and Low pressure CVD	45
4.5	The CVD process.....	46
4.5.1	Precursor requirements for CVD process	47
4.5.2	Vaporisation of precursors for the CVD process	48
4.5.3	The CVD process: Kinetics and thermodynamics	51
4.5.4	Effect of deposition temperature and concentration on the film growth.....	53
4.5.5	The boundary layer.....	55
4.6	Induction heating process in CVD.....	56
4.6.1	Electromagnetic formulation	57
4.7	References	60
CHAPTER 5		64
ANALYTICAL AND CHARACTERISATION TECHNIQUES.....		64
5.1	X-Ray Diffraction Technique.....	64
5.1.1	Background	64
5.1.2	Phase and composition identification	65
5.1.3	Crystal lattice structure and Bragg diffraction.....	66
5.1.4	Peak broadening of XRD patterns.....	67
5.1.5	Microstrain and residual stress in films.....	69
5.1.6	Texture analysis and preferred orientation.....	72
5.2	Energy dispersive X-Ray spectroscopy	75
5.2.1	Principle of analysis	75
5.3	What happens inside the EDS detector.....	77
5.4	Raman Spectroscopy	78

5.4.1	Introduction to Raman	78
5.4.2	Raman spectroscopy and Raman spectra	80
5.4.3	Raman scattering	82
5.5	Scanning electron microscopy.....	83
5.5.1	Description of the technique.....	83
5.5.2	Electron beam sample interaction and detection	85
5.5.3	Sample requirements	88
5.6	References	90
CHAPTER 6.....		95
EQUIPMENT FABRICATION AND CONSTRUCTION		95
6.1	Design and fabrication of the CVD system	95
6.1.1	Power supply system.....	97
6.1.2	Power supply calibration.....	98
6.1.3	The CVD reactor system	100
6.1.4	The gas delivery system	104
6.1.5	The ZrCl ₄ vaporisation system	105
6.1.6	ZrCl ₄ mass transfer rate calibration	108
6.1.7	The exhaust system	110
6.1.8	Low Flammable limits of Hydrogen and Methane	111
6.1.9	Leak detection	112
6.2	Substrate Preparation.....	112
6.3	References	113
CHAPTER 7		114
INVESTIGATING THE GROWTH OF ZrC LAYERS BY CHEMICAL VAPOUR DEPOSITION		114
7.1	Optimisation of the synthesis of ZrC layers in an RF induction-heating CVD system using response surface methodology	114
7.1.1	Introduction.....	114
7.1.2	Thermodynamic feasibility of ZrC growth.....	115
7.1.3	Design of experiments and response surface methodology	118
7.1.4	Growth rate of zirconium carbide.....	121
7.1.5	Crystallographic structure and phase composition	125
7.1.6	Average crystallite size	129

7.1.7	Optimisation of the experimental and model results	131
7.1.8	Surface morphology	132
7.2	Influence of the substrate gas-inlet gap on the growth rate, morphology and microstructure of ZrC layers	134
7.2.1	Introduction	134
7.2.2	Gas flow parameters in the reaction chamber	135
7.2.3	Growth rate	138
7.2.4	Crystallographic structure and phase composition	141
7.2.5	Crystallite size	144
7.2.6	Peak broadening and lattice strain	145
7.2.7	Preferred orientation	147
7.2.8	Surface morphology and microstructure	149
7.3	The role of ZrCl₄ on the growth characteristics of ZrC layers	151
7.3.1	Introduction	151
7.3.2	Gas flow behaviour and analytical description model of the gas flow process	154
7.3.3	Effect of ZrCl ₄ partial pressure on ZrC growth rate	157
7.3.4	Microstructural analysis	159
7.3.5	Lattice parameter, lattice strain and residual stress	161
7.3.6	Average crystallite size and dislocation density	164
7.3.7	Surface morphology analysis	166
7.4	Time dependence of microstructural and morphological evolution of ZrC layers	167
7.4.1	Introduction	167
7.4.2	Layer thickness and growth rate	168
7.4.3	XRD structural and phase analysis	170
7.4.4	Microstructure evolution	172
7.4.5	Raman analysis	174
7.4.6	Morphological evolution	177
7.5	References	178
CHAPTER 8		183
CONCLUSIONS AND FUTURE WORK		183
8.1	Conclusion	183
8.2	Future work	187
CHAPTER 9		188
PUBLICATIONS AND CONFERENCES		188

9.1 Publications	188
9.2 Conferences	189
Appendix A: Standard operating procedure (SOP) for the CVD of ZrC (Doc no. AC-AMI-SOP-15001).....	190
Appendix B: Safety risk evaluation for the project (DOC NO: AC-AMI-HRA-15002).....	197
Appendix C: Hazard and operability study (HAZOP) report on the CVD of ZrC (Doc no. AC-AMI-HRA-15001)	203
Appendix D: Close out report for Hazop on CVD of ZrC layers (DOC No: AC-AMI-HRA-15003)	209
Appendix E: Fire and explosion risk evaluation of the experimental CVD of ZrC layers	211

CHAPTER 1

INTRODUCTION

1.1 Background

A key feature of the modern world is the high consumption of electrical energy. Two competing factors shaping the world energy economy are the rapid industrialization of the developing countries and the global drive to reduce the carbon footprint. The industrialization leads to a corresponding growth in electricity consumption. Currently about 85% of the world's energy consumption comes from fossil fuel [1,2]. However, the Kyoto Protocol with its demand to lower the carbon footprint necessitates a movement away from traditional fossil fuel based power plants to alternative power production methods. Nuclear power is one with a low carbon footprint. However, the perception of the general public is very negative towards it [3]. This negativity is based on the fear of possible leakage of high level radioactive nuclear waste into the environment during long term storage of the waste and during accident conditions such as those that occurred at Three Mile Island, Chernobyl and Fukushima [3,4].

For fission reactors, the heavy mass reaction products start with nuclei with atomic number 30, i.e. $^{72}_{30}\text{Zn}$, and end with $^{158}_{63}\text{Gd}$ [5]. The generally regarded radiologically important fission products are ^{110m}Ag , ^{134}I , ^{131}Cs and ^{137}Cs , ^{90}Sr , ^{88}Kr , ^{133}Xe and ^{155}Eu with the following somewhat less important fission products ^{132}Te , ^{140}La and the actinide ^{239}Pu [5–7].

These and other factors have prompted the U.S. Department of Energy's Office of Nuclear Energy, Science and Technology to engage governments, industries, and the research communities worldwide in a wide-range of discussions on the development of next generation nuclear energy systems, the so-called Generation IV power plants [8]. These

reactors represent advances in sustainability, economics, safety, reliability and proliferation-resistance. An international task force is developing six Generation IV nuclear reactor technologies targeted for deployment by 2030 [8]. All of these operate at higher temperatures than today's reactors.

Generation IV high temperature nuclear reactors use TRISO (tristructural isotropic) particles for containment of radioactive fission products (FPs) [9]. The TRISO particles consist of uranium oxide or uranium carbide kernel coated with low density pyrolytic carbon (the buffer layer), high density Inner Pyrolytic Carbon (IPyC), silicon carbide (SiC), and dense Outer Pyrolytic Carbon (OPyC) [10]. In the TRISO particles SiC is the main barrier for containing solid FPs. These particles retain most FPs with the exception of silver at temperatures below 1000 °C. In a recent review paper by Malherbe on SiC [5], the problems of the diffusion of silver and other fission products in SiC was extensively discussed. In the same review, it was suggested that it would be advantageous to add a thin ZrC layer (in addition to the normal SiC layer) to the TRISO layer system because it is a better barrier than SiC against Ag diffusion and is more resistant against Pd attack [11,12]. ZrC would also act as an oxygen getter, thereby reducing the possibility of failure due to the amoeba effect.

ZrC has a high melting temperature of 3540 °C, and relatively low vapour pressure compared to SiC, which begins to decompose at about 1500 °C [13]. ZrC also has a low neutron capture cross section, good thermal shock resistance, relatively low density, excellent thermal stability, and high hardness [14,15]. It is important to note that the properties of ZrC coatings depend on a number of factors such as chemical composition, crystallite size and morphology, orientations of crystal planes, structural defects, porosity, and the presence of impurities. These factors are a function of the methods and conditions used in growing ZrC coatings. Chemical vapour deposition (CVD) produces coatings with very low levels of impurities and low porosity [16], which is why it is the preferred method.

Compared to SiC, little research has been published on the use of ZrC in nuclear reactors. The main reason is probably that SiC has proven nuclear applications and other desirable physical properties (e.g. a wide band gap semiconductor, it is the second hardest natural material, etc.). Another reason for this might be that it is difficult to grow good quality ZrC.

1.2 Motivation

ZrC either as a powder mixed with the fuel or as a thin layer on the fuel kernel has been proposed for use as an oxygen getter in the UO₂ kernel TRISO fuel. The high oxidation potential of ZrC (above room temperature) is perceived to act as a reducing agent for the oxygen generated from the fission process of UO₂. This avoids unfavourable oxidation reactions and reduces the formation of CO which are very detrimental more especially at high fuel burn-up levels. Another proposed use is the replacement of the SiC layer with a ZrC layer as barrier for containing fission products in the TRISO fuel particle. This is because ZrC has a low neutron capture cross section, an enhanced corrosion resistance to fission product attack and diffusion, and is stable even at high temperatures [17]. However, the properties of ZrC layers vary greatly depending on synthesis technique used and how well the deposition parameters are managed during its production.

The detailed chemical vapour deposition reactor design for the deposition of ZrC layers will enable the production of ZrC layers that have properties which are desired for nuclear applications, especially as fission product barrier. Increased understanding of ZrC deposition parameters will assist in the production of ZrC layers with optimum quality. Although, the deposition process parameters may not entirely be transferable between different CVD designs, the understanding of the effects of these process parameters and CVD reactor geometry is crucial. This is because deposition parameters affect the properties of ZrC layers and hence make it hard to give specifications of ZrC layers to a particular application.

1.3 Aims

This work is aimed at detailing the development of a deposition process for the preparation and optimisation of ZrC layers from ZrCl₄-Ar-CH₄-H₂ precursors using induction thermal CVD at atmospheric pressure. With objectives:

1. To fabricate and develop a laboratory scale CVD system so as to produce ZrC layers of various stoichiometry.
2. To investigate the microstructure and composition of ZrC coatings deposited as a function of the input variables.
3. To investigate the effect of the CVD deposition parameters on the properties of the deposited ZrC layers.

1.4 Approach

The vertical-wall RF inductively heated CVD system was developed in-house at The South African Nuclear Energy Cooperation (Necsa) SOC Ltd. This study was carried out experimentally on a laboratory scale. The effect of substrate temperature, methane/zirconium tetra chloride molar ratio, precursor partial pressures (methane, zirconium tetra chloride and hydrogen), substrate-gas inlet gap and deposition time were studied.

The focus of this study was geared at fabricating the CVD reactor system and understanding the effect of deposition process on the properties of ZrC layers deposited at atmospheric pressure. The characterised properties were crystallite size, composition (stoichiometry), lattice strain, lattice parameter, dislocation density, surface morphology and preferred orientation. Layer thickness and growth rate were also investigated as a deposition process output at various deposition parameters.

1.5 Contributions

This study contributes significantly to the existing body of knowledge. As much as some of the techniques employed in this study are not new, many aspects of this study are unique.

These include but are not limited to:

1. Design and fabrication of a vertical-wall thermal CVD system with special reference to ZrC layers.
2. Optimisation of the ZrC growth process by response surface methodology.
3. Investigation of the effect of substrate-gas inlet gap on the properties of the deposited ZrC layers.
4. Investigation of the effect of ZrCl_4 partial pressure on the properties of the deposited ZrC layers.
5. The role of deposition time on the growth and evolution of microstructure and morphology of the ZrC layers.

1.6 Thesis layout

In this study ZrC layers were grown on a graphite substrate by CVD and characterised by scanning electron microscopy, X-ray diffraction, Raman spectroscopy and Energy dispersive X-ray spectroscopy. During the growth of ZrC layers, several growth parameters were varied in the CVD reactor. The most important of these are the temperature profile in the reactor, the gas flow parameters (gas speed, ratio of the different gases, partial pressures of the gases), deposition time and also the parameters of the reactor geometry. As each of these parameters is interdependent, experimentation, by changing these variables, is important for growing a stoichiometric ZrC layer with a polycrystalline microstructure.

The rest of the thesis is organised as follows: **Chapter 2** is an introduction to coated fuel particles for high temperature gas cooled reactors. The SiC-TRISO coated fuel particle

failures and the diffusion mechanism of fission products has been briefly highlighted. **Chapter 3** discusses the properties, characteristics and applications of ZrC. Different synthesis techniques that are used to produce ZrC are highlighted. **Chapter 4** outlines general aspects of film deposition, the chemical vapour deposition process and its variants are discussed. The use of induction heating in the CVD process has also been explained. **Chapter 5** provides details with respect to the analytical and characterisation techniques used. These techniques include scanning electron microscopy, X-ray diffraction, Raman spectroscopy and energy dispersive X-ray spectroscopy. **Chapter 6** details the CVD equipment design and fabrication. The deposition process of ZrC layers at different deposition parameters used in this work is explained. **Chapter 7** presents the results of the investigation of the growth of ZrC layers by the CVD process. The effect of various CVD process parameters on the growth characteristics and properties of ZrC layers have been extensively discussed. **Chapter 8** contains the conclusions and recommendations of the study. **Chapter 9** lists the publications originating from this thesis and conferences attended. This is followed by the **appendices** detailing the procedures followed to construct and use the CVD system. This includes the standard operating procedures, safety evaluation for the project and hazard and operability study of the CVD process.

1.7 References

- [1] M.I. Hoffert, K. Caldeira, G. Benford, D.R. Criswell, C. Green, H. Herzog, A.K. Jain, H.S. Khesghi, K.S. Lackner, J.S. Lewis, others, Advanced technology paths to global climate stability: energy for a greenhouse planet, *Sci. S Compass*. 298 (2002) 981–987.
- [2] J.B. Malherbe, E. Friedland, N.G. van der Berg, Ion beam analysis of materials in the PBMR reactor, *Nucl. Instruments Methods Phys. Res. Sect. B Beam Interact. with Mater. Atoms*. 266 (2008) 1373–1377.
- [3] N.F. Pidgeon, I. Lorenzoni, W. Poortinga, Climate change or nuclear power—No thanks! A quantitative study of public perceptions and risk framing in Britain, *Glob.*

- Environ. Chang. 18 (2008) 69–85.
- [4] A.A. Spence, W. Poortinga, N.N.F. Pidgeon, I. Lorenzoni, Public perceptions of energy choices: the influence of beliefs about climate change and the environment, *Energy Environ.* 21 (2010) 385–407.
- [5] J.B. Malherbe, Diffusion of fission products and radiation damage in SiC, *J. Phys. D. Appl. Phys.* 46 (2013) 27.
- [6] D. Hanson, A review of radionuclide release from HTGR cores during normal operation, *Electr. Power Res. Institute, Rep.* 1009382 (2004).
- [7] K. Minato, T. Ogawa, K. Fukuda, H. Sekino, H. Miyanishi, S. Kado, I. Takahashi, Release behavior of metallic fission products from HTGR fuel particles at 1600 to 1900 C, *J. Nucl. Mater.* 202 (1993) 47–53.
- [8] L. Herrera, S. Schuppner, U.S. Department of Energy international nuclear energy research initiative (IAEA-CN-108/79), in: IAEA (Ed.), *Innov. Technol. Nucl. Fuel Cycles Nucl. Power*, International Atomic Energy Agency, Vienna, 2004: pp. 165–168.
- [9] I.E. Porter, T.W. Knight, M.C. Dulude, E. Roberts, J. Hobbs, Design and fabrication of an advanced TRISO fuel with ZrC coating, *Nucl. Eng. Des.* 259 (2013) 180–186.
- [10] E. López-Honorato, J. Boshoven, P.J. Meadows, D. Manara, P. Guillermier, S. Jühe, P. Xiao, J. Somers, Characterisation of the anisotropy of pyrolytic carbon coatings and the graphite matrix in fuel compacts by two modulator generalised ellipsometry and selected area electron diffraction, *Carbon N. Y.* 50 (2012) 680–688.
- [11] T.M. Besmann, R.E. Stoller, G. Samolyuk, P.C. Schuck, S.I. Golubov, S.P. Rudin, J.M. Wills, J.D. Coe, B.D. Wirth, S. Kim, others, Modeling Deep Burn TRISO particle nuclear fuel, *J. Nucl. Mater.* 430 (2012) 181–189.
- [12] K. Sawa, S. Ueta, Research and development on HTGR fuel in the HTTR project, *Nucl. Eng. Des.* 233 (2004) 163–172.
- [13] N.G. van der Berg, J.B. Malherbe, A.J. Botha, E. Friedland, Thermal etching of SiC, *Appl. Surf. Sci.* 258 (2012) 5561–5566.
- [14] H.O. Pierson, *Handbook of Refractory Carbides & Nitrides: Properties, Characteristics, Processing and Apps.*, Noyes Publications, New Jersey, 1996.
- [15] Y.S. Won, V.G. Varanasi, O. Kryliouk, T.J. Anderson, L. McElwee-White, R.J. Perez,

- Equilibrium analysis of zirconium carbide CVD growth, *J. Cryst. Growth.* 307 (2007) 302–308.
- [16] Y. Katoh, G. Vasudevamurthy, T. Nozawa, L.L. Snead, Properties of zirconium carbide for nuclear fuel applications, *J. Nucl. Mater.* 441 (2013) 718–742.
- [17] L.L. Snead, Y. Katoh, S. Kondo, Effects of fast neutron irradiation on zirconium carbide, *J. Nucl. Mater.* 399 (2010) 200–207.

CHAPTER 2

COATED FUEL PARTICLES FOR HIGH TEMPERATURE GAS COOLED NUCLEAR REACTORS

2.1 The TRISO fuel particle

There are many new designs of nuclear reactors based on coated fuel particles. Among them are the high temperature gas-cooled reactors (HTGRs). HTGRs belong to the Gen-IV reactor category which has a bright future in the electricity and hydrogen production because of their superior characteristics. Much attention has been paid to the inherent safety characteristics of HTGRs, even more so after the Fukushima nuclear accident. The most important safety assurance is the HTGR nuclear fuel element based on the coated fuel particles. That is why the coating process of nuclear fuel particles is one of the most important subjects for research [1]. The current advanced designs are modifications of the German UO_2 and the US UCO coated particles. These are promising and feasible under the worldwide cooperation and efforts: (1) the spherical fuel element used in the pebble bed concept in Germany, Russia, China and South Africa (shelved); and (2) the block-type fuel element applied in the prismatic core in the United States, the United Kingdom and Japan. As much as HTGR fuel designs are being developed in various countries, they all use the same generic refractory coated fuel particles [2].

The fuel of the HTGR, known as TRISO (tristructural isotropic) coated fuel particles is made of a uranium kernel (about 0.5 mm in diameter) coated with a low density (buffer) pyrolytic carbon, a highly dense inner pyrolytic carbon layer (IPyC), a silicon carbide (SiC) coating and a final dense outer pyrolytic carbon coating (OPyC) [3] as shown in Figure 2-1.

The low density pyrocarbon buffer provides the void volume for gaseous fission products and also accommodates kernel swelling. It also reduces the effect of fission product fragment

recoil, thus protecting other layers from damage [4]. The IPyC is a gas-tight coating and acts as a substrate to the SiC layer and provides it with mechanical support. It shields the kernel from chlorine attack, which is produced during the CVD of the SiC layer. It is also a metallic fission products diffusion barrier and reduces tensile stresses on the SiC [3,4]. The high density SiC acts as a pressure retaining layer and a primary metallic fission product diffusion barrier. The OPyC is a further diffusion barrier for gaseous and metallic fission products and it also reduces tensile stress on the SiC. The OPyC protects the SiC during particle handling and sphere or compact formation, and provides a bonding surface for the over coating. The four coating layers are deposited on kernels in a heated furnace by CVD. Flowing gases in the furnace suspend the kernels so that they form a fluidized bed [5].

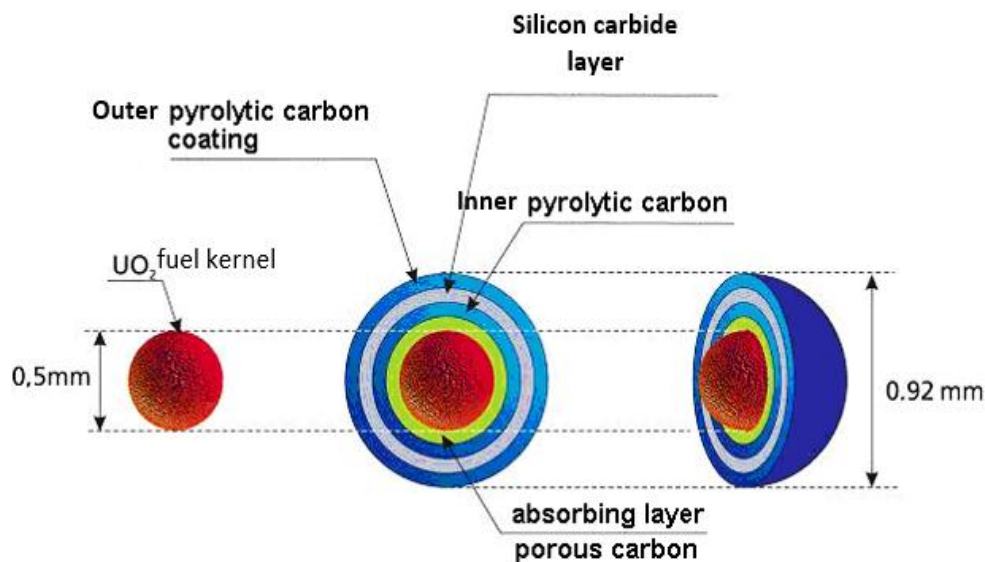


Figure 2-1: Illustrative cutaway drawing of the coated TRISO fuel particle. Taken from [6].

2.2 SiC-TRISO coated fuel particle failure

The performance of the fuel particle depends upon temperature, fast fluence and burn-up trajectory experienced in service, which varies spatially within the core. The Generation-IV concept, with its emphasis on safety features, relies upon the capability of the fuel to retain radionuclides to a very high degree during both normal operation and accident conditions [5].

A TRISO particle is considered to have failed when the structural layers surrounding the

kernel have been damaged or breached in a manner that allows the release of fission products. The SiC coating supported by other layers provides the barrier that prevents the escape of fission products. The main fuel failures for TRISO fuel are over pressurization, fission product attack and the amoeba effect [7]. Attack of the fuel particle by carbon monoxide (CO) and fission products can reduce the thickness and strength of its coating [5,7]. The fission products, carbon and uranium, all compete for oxygen in this closed system. The system oxygen potential determines which elements are oxidized and which are not. The oxygen potential, μ_{O_2} is defined as $\mu_{O_2} = RT \ln P_{O_2}$ [8]. In this case R is the gas constant, T is the absolute temperature, and P_{O_2} is partial pressure of oxygen. In pure UO_2 fuel, the oxygen potential increases as a function of burn-up and results in the production of CO. This CO increases the pressure in the particle. The gaseous fission products released from the fuel kernel also increases the internal pressure. Cracks will develop in the layers if the pressure exerted by CO and the gaseous fission products is greater than the tensile strength of the structural layers [7]. This will cause the SiC layer to fail. It is assumed that the SiC layer carries the entire internal pressure and the stress (σ) in the layer is approximated by $\sigma = \frac{rP}{2t}$, where r is the radius, P is the pressure, and t is the layer thickness. Therefore the total gas pressure (P_{Total}) in the particle is the sum of the CO gas pressure (P_{CO}) and the pressure by released fission gases (P_{FPS}) [8] given by $P_{Total} = P_{FPS} + P_{CO}$.

The CO gas also provides a mechanism for enhanced carbon transport inside the kernel. The carbon transport mechanism is elevated with increase in temperature gradient, which yields different equilibria of CO gas with solid carbon. The carbon transport to the colder side of the particle leads to a concomitant migration of the kernel along the temperature gradient, the so called amoeba effect (see Figure 2-2). This kernel migrates toward the SiC layer where it can chemically attack and also fracture the layer [7]. Kernel migration Δx is given by

$\Delta x = K \frac{1}{T^2} \frac{dT}{dx} t$, where t is time, T is the temperature and K is the migration factor. Particle

failure due to kernel migration is said to occur when the kernel touches the SiC layer [8].

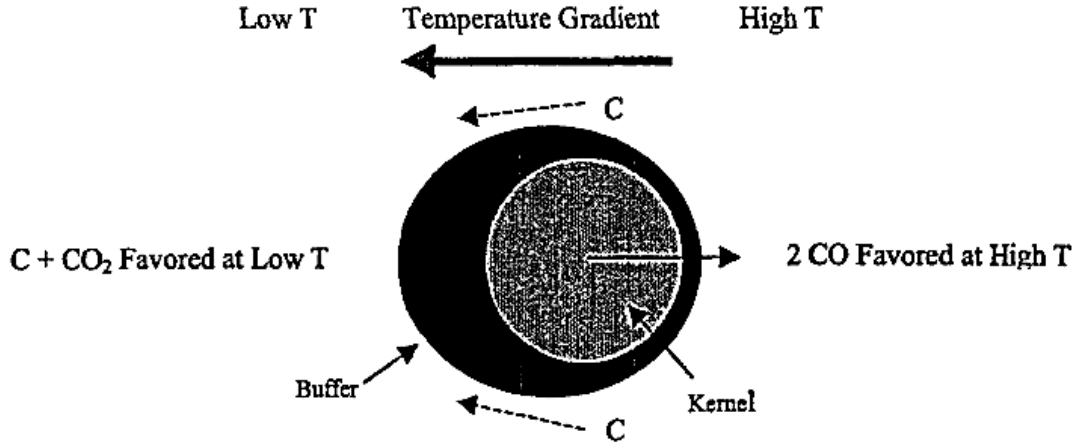


Figure 2-2: Illustration of the amoeba effect. Carbon is transported from the hot to the cool side. Taken from [8].

Therefore, the failure probability of the TRISO particle depends on burn-up and internal gas pressure. As already noted, crack extension and fracture are observed in case of tensile loading. The cumulative failure probability for each coating layer is expressed by a Weibull

distribution with the following equation; $f(t) = 1 - \exp \left\{ -\ln 2 \times \left(\frac{\sigma(t)}{\sigma_0} \right)^m \right\}$, where $f(t)$ is the

failure probability of the layer at irradiation time t , $\sigma(t)$ is the stress on the layer at irradiation time t , σ_0 is the median strength of the layer and m is the Weibull modulus of the layer. The σ_0 values for the pyrocarbon layers and SiC are 200 MPa and 873 MPa respectively. The Weibull moduli values for the pyrocarbon and SiC layers are 5.0 and 8.02 respectively [9].

As proposed in the Generation-IV International Forum, the Generation-IV nuclear energy system requires a gas outlet temperature beyond 1600 °C for supplying electricity and for hydrogen production. This temperature is close to the transition temperature of the current

commonly used materials in the nuclear industry. The Generation-IV fuel reactors are required to have excellent safety performance up to burn-ups of about 15–20% FIMA and fluence values of $6 \times 10^{25} \text{ n/m}^2$ ($E > 0.1 \text{ MeV}$). This is to allow economic operation of the reactor system and good fissile material utilization [10]. As much as SiC has excellent properties, it may not fulfil the Generation-IV nuclear energy system requirements since it gradually loses strength due to neutron irradiation and mechanical integrity at very high temperatures, especially at about 1500 °C, by thermal dissociation. Degradation of the SiC coating layer leads to extensive release of fission products from the TRISO-coated fuel particles [7,11]. Achieving these goals requires the use of a better material than SiC by either replacing it or by enhancing it. Studies have proposed that ZrC could replace SiC layer in the TRISO fuel particle [12]. Another suggestion is that a thin layer of ZrC could be applied inside the typical TRISO coatings [7,13]. Since the kernel migration is due to the presence of free oxygen, the addition of ZrC as gettering material to the kernel can suppress oxygen release and hence prolong the fuel particle's life span.

2.3 Diffusion mechanism of fission products

Ideally, diffusion takes place as a random walk process within the crystalline material [14]. The diffusion mechanism attempts to describe the details of atomic migration associated with mass transport through a medium [15]. The transport of atoms through a crystalline material, especially metals and alloys, at elevated temperature is associated with diffusion [16]. Thermally excited atoms may be transferred from a crystal lattice site to an interstitial site or an adjacent site [17]. As with fuel particle failure, a number of mechanisms have been identified which govern the transport of radionuclides in HTGR core materials [18]. The source and the pathway of the fission products from HTGRs are given in Figure 2-3.

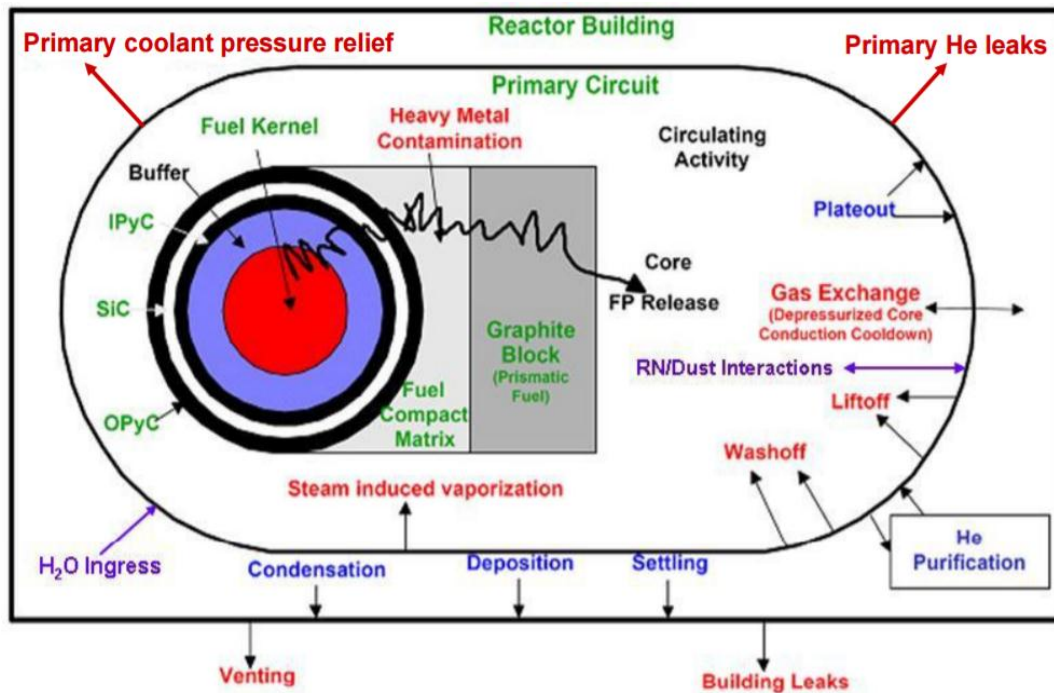


Figure 2-3: HTGR fission products sources and pathways. Taken from [18].

The principal steps and pathways of the transport of radionuclides from the location of their birth through the various material regions of the core to their release into the helium coolant are also shown schematically in Figure 2-4. The two main sources of fission product released from the core are: as-manufactured heavy metal contamination and particles whose coatings fail in service [18,19]. The latter source can be further categorized into (1) coating failure during normal operation and (2) incremental coating failure during core heat up accidents. In addition, certain volatile fission metals can, at sufficiently high temperatures and long operation time, diffuse through the SiC coatings of intact TRISO particles [19].

The fractional release of a radionuclide from the core can be expressed by the relationship:

$$f = \frac{Cf_C + Ff_F + [1 - C - F]f_D}{A_g},$$

where f is fractional release of radionuclides from the core, C

is the heavy metal contamination fraction, f_C is the fractional release from contamination, F is the failure fraction, f_F is the fractional release from failed particles, f_D is the fractional diffusive release from intact particles and A_g is the matrix/graphite attenuation factor [19].

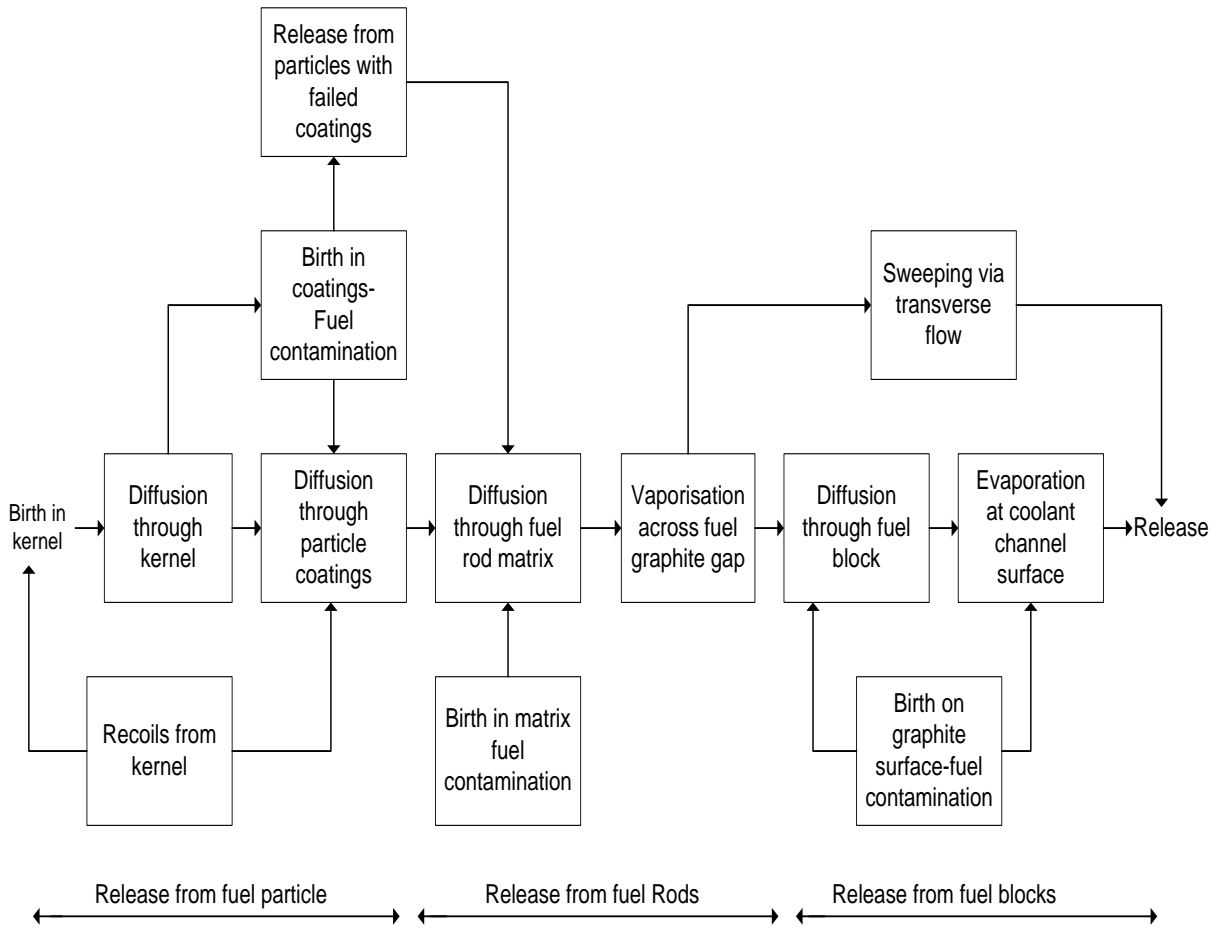


Figure 2-4: Principal steps in radionuclide release from an HTGR core. Taken from [19].

Radionuclide transport is essentially treated as a transient solid-state diffusion problem with various modifications to account for the effects of irradiation and heterogeneities in the core materials [18,19]. Fick's first law of diffusion (considered to be in slab geometry) suggests that the diffusive flux of atoms ϕ is proportional to the negative of the concentration gradient Δc , with the proportionality constant being the diffusion coefficient D , i.e. $\phi = -D \frac{\partial c}{\partial x}$, where x is the spatial coordinate. If the radioactive decay of the fission products is ignored, then net flux in or out of the given volume per unit length is equal to the concentration gradient of fission products per unit time (mass balance equation): $\frac{\partial c}{\partial t} = -\frac{\partial \phi}{\partial x}$.

Since concentration is assumed to vary with time and the diffusion coefficient is taken to be independent of concentration, then the diffusion process can be described by Fick's second law of diffusion (for unidirectional mass flow under non steady conditions), i.e.

$\frac{\partial c}{\partial t} = \frac{\partial}{\partial x} \left(D \frac{\partial c}{\partial x} \right)$ [16,19]. Considering constant source diffusion, the solution for this equation

may be given by $c(x,t) = \frac{A}{\sqrt{\pi Dt}} \exp\left(-\frac{x^2}{4Dt}\right)$, where A is a constant.

For fission metal transport in the fuel kernel, the diffusivity is given by $D' = \frac{D}{r^2}$. In this case

D' is the reduced diffusion coefficient and r is the radius of the kernel [19]. Therefore, the radioactive fission products will penetrate deeper into the protective layer with increase in time. As already mentioned the diffusion coefficient may actually be affected by several factors, including concentration. The solution to Fick's second law of diffusion then has to be modified to cater for other factors. Radionuclides are produced by various nuclear reactions in the core, and the radiologically significant ones decay so that the mass balance equation is modified to include a source term s (volumetric source rate) and a decay term λ (decay

constant): $\frac{\partial c}{\partial t} = \frac{\partial}{\partial x} \left(D \frac{\partial c}{\partial x} \right) - \lambda c + s$. Since the release of fission products from the fuel kernel

is treated as a transient diffusion process, for spherical geometry the generalized continuity

equation can be given by $\frac{\partial c}{\partial t} = \frac{1}{r^2} \frac{\partial}{\partial r} \left(D \frac{\partial c}{\partial r} \right) - \lambda c + s$. The diffusion mechanism of fission

products in the fuel particle is very complex and always modelled [19].

For solid-state diffusion processes, the diffusion coefficient depends on the temperature, composition and crystal structure of the material. The dependence of D on temperature is

described by Arrhenius exponential relationship: $D = D_0 \exp\left(-\frac{Q}{RT}\right)$, where D_0 is a pre-

exponential factor which depends on bonding forces between atoms of the crystalline lattice, Q is the activation energy of diffusion and R is the gas constant [16,19].

2.4 References

- [1] M. Liu, Coating Technology of Nuclear Fuel Kernels : A Multiscale View, in: A. Mahmood (Ed.), Mod. Surf. Eng. Treat., InTech, Rijeka, 2013: pp. 159–184.
- [2] X.W. Zhou, C.H. Tang, Current status and future development of coated fuel particles for high temperature gas-cooled reactors, Prog. Nucl. Energy. 53 (2011) 182–188.
- [3] E. López-Honorato, J. Boshoven, P.J. Meadows, D. Manara, P. Guillermier, S. Jühe, P. Xiao, J. Somers, Characterisation of the anisotropy of pyrolytic carbon coatings and the graphite matrix in fuel compacts by two modulator generalised ellipsometry and selected area electron diffraction, Carbon N. Y. 50 (2012) 680–688.
- [4] F. Charollais, S. Fonquernie, C. Perrais, M. Perez, O. Dugne, F. Cellier, G. Harbonnier, M.-P.P. Vitali, CEA and AREVA R&D on HTR fuel fabrication and presentation of the CAPRI experimental manufacturing line, Nucl. Eng. Des. 236 (2006) 534–542.
- [5] K. Verfondern, H. Nabielek, J.M. Kendall, Coated particle fuel for high temperature gas cooled reactors, Nucl. Eng. Technol. 39 (2007) 603–616.
- [6] J.J. Powers, B.D. Wirth, A review of TRISO fuel performance models, J. Nucl. Mater. 405 (2010) 74–82.
- [7] I.E. Porter, T.W. Knight, M.C. Dulude, E. Roberts, J. Hobbs, Design and fabrication of an advanced TRISO fuel with ZrC coating, Nucl. Eng. Des. 259 (2013) 180–186.
- [8] F. Eltawila, TRISO-Coated Particle Fuel Phenomenon Identification and Ranking Tables (PIRTs) for Fission Product Transport due to Manufacturing, Operations, and Accidents, Washington D.C, 2004.
- [9] O.Ö. Gülol, Ü. Çolak, B. Yildirim, Performance analysis of TRISO coated fuel particles with kernel migration, J. Nucl. Mater. 374 (2008) 168–177.
- [10] S. Ueta, J. Aihara, A. Yasuda, H. Ishibashi, T. Takayama, K. Sawa, Fabrication of uniform ZrC coating layer for the coated fuel particle of the very high temperature reactor, J. Nucl. Mater. 376 (2008) 146–151.
- [11] N.G. van der Berg, J.B. Malherbe, A.J. Botha, E. Friedland, Thermal etching of SiC,

- Appl. Surf. Sci. 258 (2012) 5561–5566.
- [12] K. Minato, T. Ogawa, K. Sawa, A. Ishikawa, T. Tomita, S. Iida, H. Sekino, Irradiation experiment on ZrC-coated fuel particles for high-temperature gas-cooled reactors, Nucl. Technol. 130 (2000) 272–281.
- [13] J.B. Malherbe, Diffusion of fission products and radiation damage in SiC, J. Phys. D. Appl. Phys. 46 (2013) 27.
- [14] J.L. Plawsky, Transport phenomena fundamentals, 3rd ed., CRC Press, Florida, 2014.
- [15] M. Ohring, Materials science of thin films, 3rd ed., Academic press, London, 2002.
- [16] S.L. Kakani, A. Kakani, Material science, New Age International, New Delhi, 2004.
- [17] C.O. Mosiori, W.K. Njoroge, High Speed Semiconductor Physics. Theoretical Approaches and Device Physics, Anchor Academic Publishing, Hamburg, 2015.
- [18] P. Sabharwall, E. Kim, H. Gougar, High temperature gas-cooled reactors, Int. J. Energy, Environ. Econ. 20 (2012) 75–105.
- [19] D. Hanson, A review of radionuclide release from HTGR cores during normal operation, Electr. Power Res. Institute, Rep. 1009382 (2004).

CHAPTER 3

ZIRCONIUM CARBIDE

3.1 Properties of zirconium carbide

ZrC is a Group IV transition metal carbide possessing a NaCl-structure i.e. a face centered cubic close packed structure (Fm-3m, space group 225) [1], as seen in Figure 3-1. It has the appearance of a dark-grey metallic substance with lattice parameter of about 4.698 Å [1,2]. The carbon atoms occupy the octahedral interstitial sites of the zirconium lattice. This imposes size limitations on both carbon and zirconium for the available carbon to fit in the existing sites. This in turn determines the ZrC stoichiometry [1].

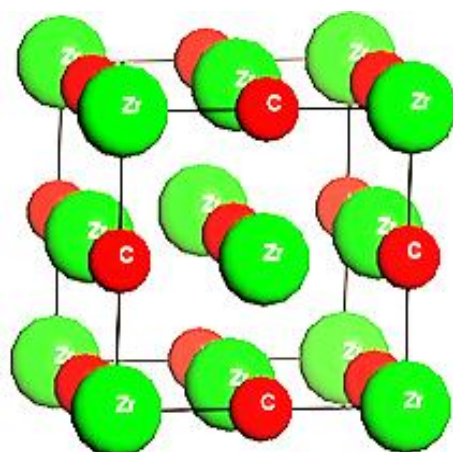


Figure 3-1: The NaCl (rock salt) structure of bulk ZrC. Taken from [3].

The electronic configurations of zirconium and carbon are $[\text{Kr}]5s^24d^2$ and $[\text{He}]2s^22p^2$ respectively [1,4]. The interstitial structure of ZrC leads to a combination of metallic, covalent and ionic bonds. The ionic bonding is due to the difference in electronegativity between zirconium and carbon. Carbon is more electronegative; the electronegativity values of carbon and zirconium are 2.55 and 1.33 respectively [4,5]. The interactions between the 2p states of carbon and 4d states of zirconium results in both covalent and metallic bonding [2,4]. Normally in ZrC, the Zr-C bond is much stronger compared to the Zr-Zr and the C-C

bonds [1,2,6]. This is demonstrated by their bond lengths and charge densities as shown in Table 3-1. The Zr-C bond has combined characteristics of both ionic and covalent bonding [1]. Therefore, ZrC is a polar covalent compound just like other transitional metal carbides [2,6]. However, there is considerably more contribution to the properties of ZrC by the covalent bond compared to the ionic bond, irrespective of the high charge transfer from zirconium to carbon (0.42 e/pair) [1,6]. The covalent character of an ionic bond depends on the polarising power of the positive ion and the polarisability of the negative ion, both of which increase with charge [7]. Since both Zr^{4+} and C^{4-} have high charges, this explains why the covalent character dominates.

Table 3-1: Bond lengths and charge densities of C-C, Zr-C and Zr-Zr bonds of ZrC [6][8].

Bonds	Bond type	Bond length (Å)	Charge density (e/au³)
C-C	Covalent	3.340	0.0226
C-Zr	ionic/covalent	2.209	0.0412
Zr-Zr	Metallic	3.340	0.0218

Metallic bonding results from the ionisation of the atoms; the electrostatic attraction between the positive metal ions located in the lattice, and the delocalised electrons moving freely throughout the lattice gives rise to the metallic bonds [1,4]. Due to metallic bonding, ZrC possesses good thermal and electrical conductivity, close to that of the zirconium metal itself [6]. ZrC has a high elastic modulus and hardness due to the strong covalent bond between zirconium and carbon [1,2]. ZrC is thermally stable with very low vapour pressure and decomposes at very high temperature, i.e. above 3500 °C. It is also chemically inert to various reagents and highly resistant to corrosion and wear [6]. Compared to other carbides like tungsten carbide (15.8 g/cm³), tantalum carbide (14.5 g/cm³) and hafnium carbide (12.67 g/cm³), ZrC has a relatively low density (6.59 g/cm³). It has a relatively low work function (3.4 eV) compared to other emitter materials such as SiC (4.52 eV) and molybdenum carbide (4.6 eV) [1]. At carbon contents higher than 0.98 (i.e. ZrC_{0.98}), the

material contains free carbon. ZrC is both thermally and chemically stable for a carbon-to-metal ratio ranging from 0.65 to 0.98 and has a large heat capacity of about 37.8 J/mol K compared to other refractory carbides [1,9].

Owing to its very good properties listed above, ZrC has been proposed in TRISO coated fuel microspheres. It has been reported that ZrC coated fuel particles only failed a post irradiation heating test after about 6000 seconds at 2400 °C, whereas nearly 100 % of SiC coated fuel particles failed instantaneously at about 1700 °C. ZrC layers retained most metallic fission products (e.g. Pd, Cs) and it remained chemically stable [10–12]. The CVD SiC used for TRISO particles is usually the cubic β -type. At temperatures above 1500 °C β -SiC starts transforming into the hexagonal α -type SiC, with the process going to completion at 2400 °C [10,13]. In this range of temperatures SiC also undergoes thermal dissociation. Additional physical properties of ZrC are listed in Table 3-2.

It is important to note that the properties of ZrC depend on a number of factors, e.g. chemical composition, crystallite size and morphology, crystal orientation, structural defects, porosity, stoichiometry, presence of impurities and presence of different phases. These factors are functions of the methods and conditions used in the growth of the ZrC films (layers or coatings).

In this study the deposition conditions were optimized so as to obtain ZrC layers with uniform structure and stoichiometric composition (or with a composition close to stoichiometry) by CVD. The growth parameters were varied and investigated. Parameters such as the temperature profile in the reactor, the gas flow parameters (gas speed, ratio of different gases and partial pressure of the gases), parameters of the substrate, reactor geometry, and deposition procedure were investigated. These results are presented in Chapter 7.

Table 3-2: Properties and characteristics of ZrC

Property and characteristic	Nature and Value
Atomic structure	Cubic close packed (Fcc B1, NaCl) [1,2]
Space Group	<i>Fm3m</i> [1]
Colour	Silver gray [1]
Lattice Parameter	4.689 Å [14] 4.698 Å [1], 4.7017 Å [2]
Pearson Symbol	cF8 [1,2]
Composition	ZrC _{0.55} to ZrC _{0.99} [6]
Molecular Weight	104.91 g/mole
X-ray Density	6.59 g/cm ³ [1,2]
Melting Point	3540 °C (melts without decomposition) [15]
Thermal Conductivity	20.5 W/m°C [1]
Thermal Expansion	6.7×10 ⁻⁶ /°C [1,14]
Electrical Resistivity	45–55 μΩcm [1], 63–75 μΩcm [16]
Magnetic Susceptibility	-23 × 10 ⁻⁶ emu/mol
Hall Constant	9.42×10 ⁻⁴ cmAs
Superconductive transition temperature	< 1.2 K
Vickers Hardness	25.5 GPa [1]
Modulus of Elasticity	350–440 GPa
Bulk Modulus	207 GPa [1]
Shear Modulus	172 GPa [1]
Poisson's Ratio	0.191 [1]

3.2 Cladding materials for nuclear reactor requirements

With the current Generation-IV nuclear reactor agenda, a material to qualify for use as a suitable cladding material for nuclear reactors should concurrently be able to withstand high temperature effects and intense gamma and neutron irradiation [17]. The material should also have a low neutron absorption cross section and be able to confine the radioactive fission products generated during nuclear processes [18]. Under these harsh conditions, the mechanical properties of the material should remain uncompromised [17]. Furthermore, it is essential that the material must be chemically inert or should have a low rate of corrosion with respect to the fuel, fission products, moderator and coolant [17,18]. The fabrication

process of the material in its pure form should be relatively easy and the cost should be reasonable [18].

Comparing these requirements with the properties of ZrC described in Section 3.1, it is clear that ZrC qualifies for use as a cladding material in nuclear reactors. However, compared to SiC, the fabrication process of ZrC is more complex [19]. CVD of stoichiometric and impurity free ZrC layers has remained a challenge. Whereas ZrC has a low neutron absorption cross section, the presence of impurities in the ZrC layers is likely to increase it. A nuclear reactor core material must have a low neutron absorption cross section so as to sustain the nuclear chain reactions and also to have a high retention capacity for fission products. There is, however, a lack of adequate information on some of the behavioral properties of ZrC as a nuclear cladding material. For instance, little is known of the basics of defect formation, clustering and evolution of ZrC under irradiation [20]. Data on high burn-up, long-duration irradiation exposure tests on ZrC are also very scanty [19].

3.3 Zirconium carbide phases

Stable ZrC exists in a wide composition range. Because of this reason, ZrC is usually regarded as a non-stoichiometric compound. The vacancies that exist in ZrC are commonly the missing carbon atoms, and therefore its empirical formula is always written as ZrC_x , where $x < 1$ [1,6]. From the phase diagram for ZrC given in Figure 3-2, the ZrC_x phase exists from around 37.5 to 49.5 atomic percent of carbon [4]. The highest melting point of the ZrC_x phase is observed at around 3732 K for $ZrC_{0.85}$. At atomic percentages of carbon less than approximately 37.5, the ZrC_x phase coexists with a hexagonal close packed Zr (α -Zr) phase until around 1200 K. Beyond this temperature up to about 2127 K, the α -Zr metal becomes body centred cubic (β -Zr). Above 2127 K, the β -Zr phase starts to melt, giving rise to a liquid Zr phase and a solid ZrC_x phase. It is also observed from the phase diagram in Figure 3-2 that ZrC_x does not exist when x is greater than 1. The phase diagram only indicates that at a

carbon content of more than 49.5 atomic percent, the phases present are $ZrC_x + C$ [4,6]. It is important to note that the $ZrC + C$ phases are more commonly formed during ZrC processing, compared to other phases; this is also revealed by its phase diagram.

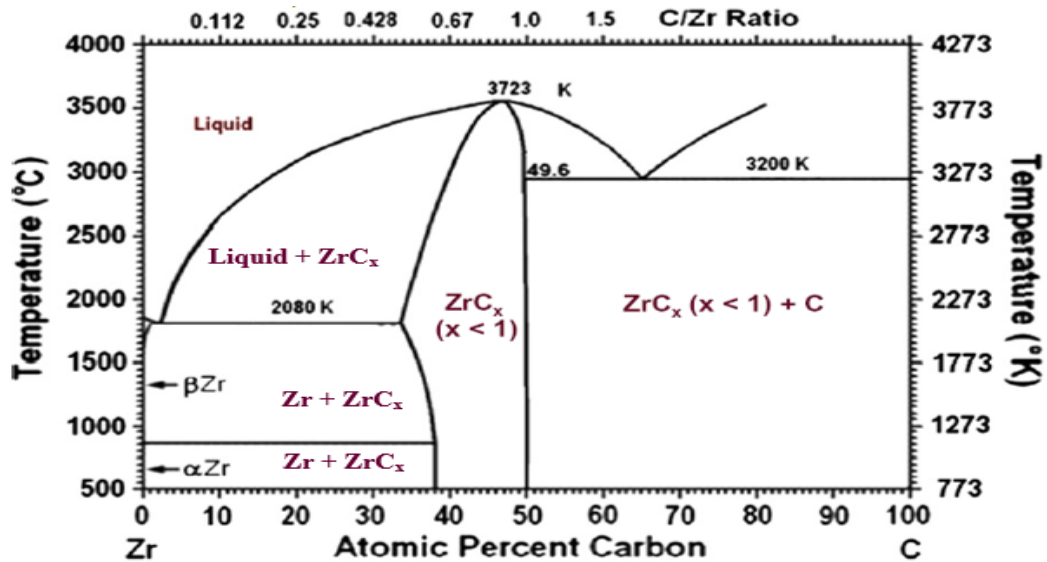


Figure 3-2: Zr-C system phase diagram. Taken from [6].

3.4 Zirconium carbide synthesis

Zirconium carbide has been synthesised predominantly by three reaction types: (1) solid state reactions; (ii) reactions using solution based precursors; and (iii) vapour based reactions. The characteristics of ZrC vary with the methods of preparation. These characteristics include chemical composition, microstructure and the amount/nature of impurities present. Therefore, when choosing a method of preparation and during the preparation of ZrC a number of factors need to be evaluated. These include: (1) chemical impurities (e.g. oxygen and other gaseous impurities), (2) the stoichiometry of the product (i.e. carbon to zirconium ratio), (3) grain size and texture orientation, (4) the existence of secondary phases and (5) pore size, porosity and morphology [6].

3.4.1 Preparation of ZrC by solid phase reactions

The preparation of ZrC from carbon and zirconia (ZrO_2) is one of the earliest techniques used to obtain ZrC [2]. Several groups like Maître et al. [21], Dong et al. [22], Sarkar et al. [23] and Jain [24] (among others) have prepared ZrC by this method. The solid phase reaction technique is generally one of the earliest and the most common methods of ZrC bulk preparation. The preparation of ZrC from ZrO_2 and carbon combines basically three processes: (1) hot pressing; (2) carbothermal reduction; and (3) sintering in a single process [2,6]. It relies on the reaction of heated graphite and ZrO_2 in an airtight furnace [2,6]. Equation (3-1) represents the general chemical equation for the reaction that takes place:



The temperatures used in this method of preparation are high, ranging from 1800 °C to 2600 °C. The preparation process requires a prolonged duration of heating of between 16 h to 24 h [6]. The ZrC produced by this method contains many impurities in its structure. The most common source of impurity is oxygen, which, if present, produces zirconium oxycarbide (ZrC_xO_y). Several attempts have been made to reduce the oxygen content by heating ZrC_xO_y under controlled conditions so as to attain a sample of the required shape, grain size, lattice parameter and density [2,6]. Equation (3-2) represents one of the reactions related to the heating of ZrC_xO_y in the presence of carbon to give ZrC:



It has been reported that the complete removal of oxygen impurities from ZrC is very difficult. The lowest levels of oxygen impurities were realized when the zirconium oxycarbide compound was close to its melting temperature. Even though it is possible to obtain pure ZrC at the melting point of zirconium oxycarbide, reproducibility and compositional homogeneity are hard to achieve [2].

In 1963 Norton and Lewis [2] prepared ZrC by reacting zirconium hydride (ZrH) and carbon powders in a heated evacuated furnace at 2200 °C for 3 h. This reaction is referred to as a combustion synthesis reaction or self-heating synthesis. Since then, several other groups have prepared ZrC using the same method in the temperature range of 2500 °C to 3200 °C [2,6]. This reaction can also be conducted by heating the sample using induction and letting the heat propagate through the entire sample material. This processing technique of ZrC suffers the same problem mentioned above, namely the presence of oxygen in the product [2]. It was reported that the lattice parameter of these as-prepared samples was lower than that expected of a pure ZrC sample. This was due to the increased oxygen content associated with this synthesis route. ZrH highly reacts with oxygen, resulting into ZrC combined with oxygen [2,6]. The increased oxygen content reduces the carbon content in the compound, as shown in Figure 3-3.

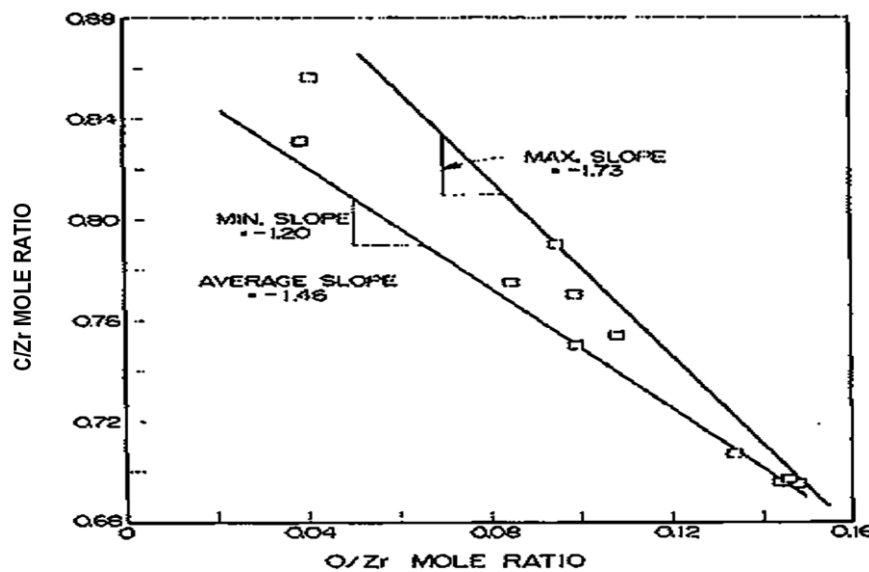


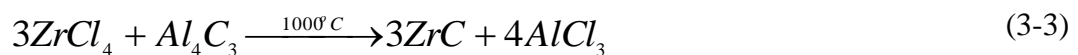
Figure 3-3: Carbon content as a function of oxygen content in zirconium oxycarbide. Taken from [23].

Using the same technique, some researchers resorted to using zirconium powder instead of ZrH. For example, Gokul et al. [25] processed ZrC cylindrical compacts by direct combustion

of zirconium and graphite powders. The powder mixture was cold pressed in argon and then inductively heated at a temperature up to 2400 °C for about 15 min.

ZrC has also been processed through a reactive melt infiltration method. In this case, graphite substrates are used as the carbon source. The zirconium powder is then placed around the graphite substrates in a crucible (preferably graphite) [26,27]. The crucible containing the sample is then heated beyond the melting point of zirconium (i.e. between 1900 and 2300 °C) for about one hour. The molten zirconium powder then reacts with graphite to form a ZrC coating. The sample is then cooled naturally before the heating furnace is opened [27]. It has been reported that this method produces ZrC coatings which are very brittle and the coating develops a number of cracks compared to layers produced by other methods like CVD [26,28].

Another method for producing ZrC is called solid state metathesis. In this case a zirconium halide (e.g. ZrCl₄) and zirconium metal are reacted with a metallic compound containing carbon (e.g. CaC₂ or Al₄C₃). The zirconium source and the carbon source are ground together and heated in a sealed evacuated container. The chemical reactions for the halide ZrCl₄ and the carbide Al₄C₃ are indicated by Equations (3-3) and (3-4):



The CaCl₂ by-product can be removed by dissolution in methanol and water, and the AlCl₃ by sublimation. This method produces a single crystalline phase of ZrC. This ZrC synthesis technique was carried out by researchers such as Nartowski et al. [29] and Zou et al. [30].

3.4.2 Preparation of zirconium carbide from solution-based precursors

ZrC has also been synthesised through the wet chemical route from solution based precursors. This process has the ability of mixing constituents at a much finer scale leading to a more efficient diffusion reaction than when using the powder processing methods [6,31]. The most commonly applied solution-based precursor method for preparing ZrC is the sol-gel process. In the sol-gel process, ZrC is prepared by reacting organic compound solutions containing carbon and zirconium [6]. Different liquid precursors have been used in this method: (1) Single source metalorganic precursors such as tetraneopentyl zirconium $Zr[CH_2C(CH_3)]_4$: ZrC has been grown from this metallo-organic compound at relatively low temperatures, ranging from 300 °C to 750 °C. However, the ZrC obtained is non-stoichiometric because of a high carbon content, with the ratio of C:Zr ranging from 2:1 to 5:1 [9]. (2) Metal alkoxides such as zirconium-n-propoxide ($[Zr(OC_3H_8)]_4$ or ZNP), zirconium 2,4,-pentanedionate (ZNT), and zirconium n-butoxide: The alkoxide is usually mixed with controlled amounts of other solvents, commonly water, to form a gel of required viscosity. After mixing, the alkoxide precursor is successively condensed and hydrolysed. This reaction of the metal alkoxides with water spontaneously produces a precipitate. To get a gel, the alkoxide is modified chemically so that the reactivity with water is reduced. The most commonly used stabilising and modifying agent is acetic acid. Acetic acid prevents the precipitation process by decreasing the rate of hydrolysis and condensation [32,33]. Lengthy comprehensive drying for about 24 h and heat treatment for about 6 h (carbothermic reduction reaction) are applied in order to separate the final product from the solution. This method also faces the challenge of residual oxygen affecting the material properties and stoichiometry. However, if the proportions of reactant precursors are carefully varied, ZrC with varying stoichiometry may be produced [6].

3.4.3 Preparation of ZrC from vapour phase based reactions

Vapour phase synthesis of ZrC has now become the most common technique of producing ZrC layers and coatings. This method produces films with very low levels of impurities and porosity. That is why vapour phase synthesis is the method predominantly used for nuclear fuel coatings, since TRISO-fuel particles require uniform, dense and isotropic coatings normally produced in a fluidized bed reactor [6,34]. Earlier studies on the production of ZrC films and coatings involved the reaction of heated zirconium metal sponge with the halogens (typically I_2 , Br_2 and Cl_2) to produce zirconium halide. The zirconium halide is then reacted with a carbon source, normally a hydrocarbon in gaseous form [35,36]. Also direct applications of zirconium halides ($ZrCl_4$, ZrI_4 and $ZrBr_4$) as a feed precursor (as a zirconium metal source) have been used extensively [6,36–40]. For this study $ZrCl_4$ was used as Zr metal source, because it is not as dangerous as $ZrBr_4$ and can more effectively produce ZrC of good stoichiometry than ZrI_4 [37]. CVD of ZrC from $ZrCl_4$ and CH_4 in the presence of H_2 was used for this study.

3.5 Effect of oxygen and carbon content on ZrC lattice parameter

ZrC has been prepared with several C/Zr molar ratios, varying from extremely low or high carbon content to near-stoichiometric ZrC. In a bid to produce pure and stoichiometric ZrC, the relationship between C/Zr and O/Zr and the lattice parameter has been studied extensively by various workers [2,23,41,42]. Studies have indicated that if the amount of oxygen in ZrC is increased, the lattice parameter is decreased. Figure 3-4 illustrates this behaviour. It was further noted that the lattice parameter increases when the molar ratio C/ZrC increases; this behaviour is illustrated in Figure 3-5 [23]. The lattice parameter of ZrC combined with oxygen is generally less than that of ZrC with no oxygen. When the oxygen content in ZrC is reduced, the lattice parameter increases. This means that the difference between the lattice

parameter values of ZrC with oxygen and ZrC without oxygen reduces with reduced oxygen content [41].

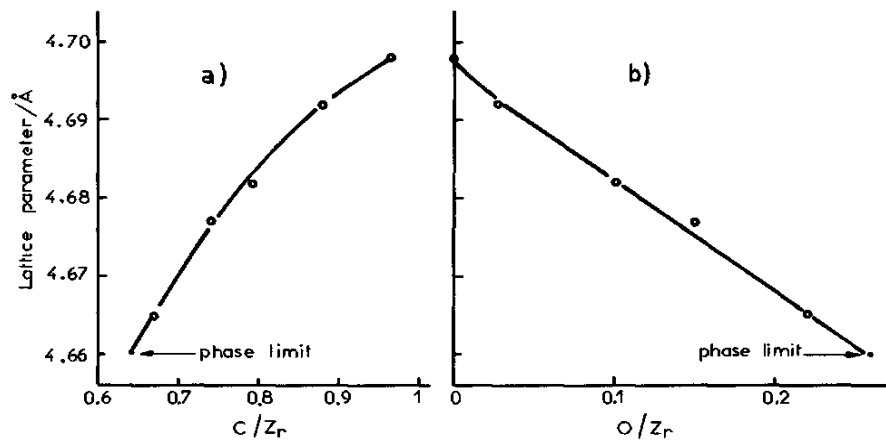


Figure 3-4: Variation of the lattice parameter of zirconium oxycarbide with (a) carbon and (b) oxygen concentration. Taken from [41].

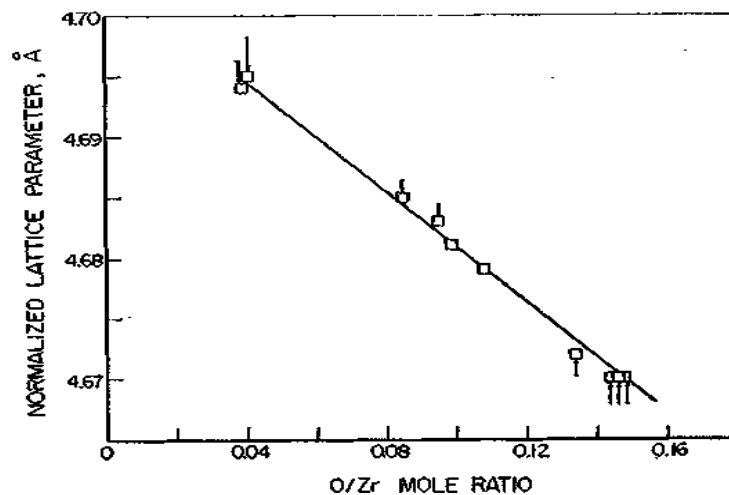


Figure 3-5: Effect of oxygen content on lattice parameter of zirconium oxycarbide (lattice parameter normalized to C/Zr ratio of 0.75; arrows indicate magnitude and direction of correction used). Taken from [23].

3.6 Effect of irradiation and oxidation on ZrC layers

Studies have indicated that the properties of ZrC vary with its stoichiometry (C/Zr atomic percentage ratio) [6]. For example, Yang et al. [43] indicated that the C/Zr ratio had a notable effect on the irradiation response of zone-refined ultra-high pure ZrC. They noted that the sub-stoichiometric ZrC samples (C/Zr < 1) had an improved irradiation resistant

microstructure compared to hyper-stoichiometric ZrC samples ($C/Zr > 1$). Huang et al. [44] reported that ZrC_x , after proton irradiation at 800 °C, was highly decorated with dislocation loops. The loop size and density depended both on dose and stoichiometry, with $ZrC_{1.2}$ showing quite different behaviour compared to the lower C-ratio stoichiometries.

Information about the oxidation behaviour for various ZrC stoichiometries is limited. However, in the review by Katoh et al. [6], it is speculated that the excess carbon in ZrC can change the oxidation behaviour of ZrC materials. The excess carbon can increase the production of CO_2 , which may increase the chances of inter-crystalline fracture and fracture below normal temperature.

3.7 Applications of ZrC

Zirconium carbide, either as a powder, bulk material, or as a layer, is a potential material in a number of applications. Some of these applications include:

- (1) Thermophotovoltaic radiators and field emitter tips and arrays. This is because ZrC exhibits high emissivity and high current density at elevated temperatures [45].
- (2) In addition to its other good properties, ZrC has a low neutron capture cross section and therefore can be used as a diffusion barrier for fission products for nuclear fuel TRISO particle.
- (3) Because of its hardness, ZrC can be used as a cutting and drilling tool, and as a wear resistant coating.
- (4) ZrC has found use in aircrafts because of its low density, hardness, corrosion resistance, and its capacity to withstand high temperatures.

3.8 References

- [1] H.O. Pierson, Handbook of Refractory Carbides & Nitrides: Properties, Characteristics, Processing and Apps., Noyes Publications, New Jersey, 1996.
- [2] E.K. Storms, The refractory carbides, Academic Press, New York, 1967.
- [3] A. Arya, E.A. Carter, Structure, bonding, and adhesion at the ZrC(100)/Fe(110) interface from first principles, Surf. Sci. 560 (2004) 103–120.
- [4] R.W. Harrison, W.E. Lee, Processing and properties of ZrC, ZrN and ZrCN ceramics: a review, Adv. Appl. Ceram. 115 (2016) 294–307.
- [5] J.A. Dean, Handbook of chemistry, 15th ed., McGraw-Hill, Inc., New York, 1972.
- [6] Y. Katoh, G. Vasudevamurthy, T. Nozawa, L.L. Snead, Properties of zirconium carbide for nuclear fuel applications, J. Nucl. Mater. 441 (2013) 718–742.
- [7] M. Clugston, R. Flemming, Advanced chemistry, Oxford University Press, New York, 2000.
- [8] Y. Xiao-Yong, L. Yong, Z. Fa-Wei, Z. Ping, Mechanical, electronic, and thermodynamic properties of zirconium carbide from first-principles calculations, Chinese Phys. B. 24 (2015) 116301.
- [9] Y.S. Won, V.G. Varanasi, O. Kryliouk, T.J. Anderson, L. McElwee-White, R.J. Perez, Equilibrium analysis of zirconium carbide CVD growth, J. Cryst. Growth. 307 (2007) 302–308.
- [10] T. Ogawa, K. Fukuda, S. Kashimura, T. Tobita, F. Kobayashi, S. Kado, H. Miyanishi, I. Takahashi, T. Kikuchi, Performance of Zrc-Coated Particle Fuel in Irradiation and Postirradiation Heating Tests, J. Am. Ceram. Soc. 75 (1992) 2985–2990.
- [11] K. Minato, T. Ogawa, Research and development of ZrC-coated particle fuel, Proc. Glob. Atoms Prosper. Updat. Eisenhower's Glob. Vis. Nucl. Energy. 1068 (2003).
- [12] K. Sawa, S. Ueta, Research and development on HTGR fuel in the HTTR project, Nucl. Eng. Des. 233 (2004) 163–172.
- [13] J. Fan, P.K.-H. Chu, Silicon carbide nanostructures: fabrication, structure, and properties, Springer, New York, 2014.
- [14] L. Toth, Transition metal carbides and nitrides, Academic press, New York, 1971.
- [15] F. Charollais, S. Fonquernie, C. Perrais, M. Perez, O. Dugne, F. Cellier, G.

- Harbonnier, M.-P.P. Vitali, CEA and AREVA R&D on HTR fuel fabrication and presentation of the CAPRI experimental manufacturing line, *Nucl. Eng. Des.* 236 (2006) 534–542.
- [16] P. Schwarzkopf, R. Kieffer, F. Benesousky, *Refractory hard metals: borides, carbides, nitrides and silicides*, Macmillan, New York, 1953.
- [17] C.R.F. Azevedo, Selection of fuel cladding material for nuclear fission reactors, *Eng. Fail. Anal.* 18 (2011) 1943–1962.
- [18] S.J. Zinkle, G.S. Was, Materials challenges in nuclear energy, *Acta Mater.* 61 (2013) 735–758.
- [19] D. Wongsawaeng, Performance modeling of Deep Burn TRISO fuel using ZrC as a load-bearing layer and an oxygen getter, *J. Nucl. Mater.* 396 (2010) 149–158.
- [20] A. Motta, K. Sridharan, D. Morgan, I. Szlufarska, *Understanding the Irradiation Behavior of Zirconium Carbide*, Washington D.C, 2013.
- [21] A. Maitre, P. Lefort, Solid state reaction of zirconia with carbon, *Solid State Ionics.* 104 (1997) 109–122.
- [22] D.-W. Lee, S.-M. Jin, J.-H. Yu, H.-M. Lee, Synthesis of Ultrafine ZrC Powders by Novel Reduction Process, *Mater. Trans.* 51 (2010) 2266–2268.
- [23] S.K. Sarkar, A.D. Miller, J.I. Mueller, Solubility of oxygen in ZrC, *J. Am. Ceram. Soc.* 55 (1972) 628–630.
- [24] A. Jain, *Synthesis and processing of nanocrystalline zirconium carbide formed by carbothermal reduction*, Georgia Institute of Technology, 2004.
- [25] G. Vasudevamurthy, T.W. Knight, E. Roberts, T.M. Adams, Laboratory production of zirconium carbide compacts for use in inert matrix fuels, *J. Nucl. Mater.* 374 (2008) 241–247.
- [26] X. Yang, Z. Su, Q. Huang, L. Chai, P. Zhong, L. Xue, Y. Xin, S.U. Zhe-an, H. Qi-zhong, A zirconium carbide coating on graphite prepared by reactive melt infiltration, *J. Cent. South Univ.* 21 (2014) 472–476.
- [27] L. Zou, N. Wali, J. Yang, N.P. Bansal, Microstructural development of a C_f/ZrC composite manufactured by reactive melt infiltration, *J. Eur. Ceram. Soc.* 30 (2010) 1527–1535.

- [28] Y. Wang, X. Zhu, L. Zhang, L. Cheng, C/C–SiC–ZrC composites fabricated by reactive melt infiltration, *Ceram. Int.* 38 (2012) 4337–4343.
- [29] A.M. Nartowski, I.P. Parkin, M. Mackenzie, J. Craven, I. Macleod, Solid state metathesis routes to transition metal carbides, *J. Mater. Chem.* 9 (1999) 1275–1281.
- [30] X. Zou, K. Zheng, X. Lu, Q. Xu, Z. Zhou, Solid oxide membrane-assisted controllable electrolytic fabrication of metal carbides in molten salt, *Faraday Discuss.* 190 (2016) 53–69.
- [31] C. Ang, T. Williams, A. Seeber, H. Wang, Y.-B. Cheng, Synthesis and evolution of zirconium carbide via sol-gel route: features of nanoparticle oxide-carbon reactions, *J. Am. Ceram. Soc.* 96 (2013) 1099–1106.
- [32] M. Aparicio, A. Jitianu, L.C. Klein, *Sol-gel processing for conventional and alternative energy*, Springer Science & Business Media, New York, 2012.
- [33] M. Dollé, D. Gosset, C. Bogicevic, F. Karolak, D. Simeone, G. Baldinozzi, Synthesis of nanosized zirconium carbide by a sol-gel route, *J. Eur. Ceram. Soc.* 27 (2007) 2061–2067.
- [34] B. Liu, C. Liu, Y. Shao, J. Zhu, B. Yang, C. Tang, Deposition of ZrC-coated particle for HTR with ZrCl₄ powder, *Nucl. Eng. Des.* 251 (2012) 349–353.
- [35] T. Ogawa, K. Ikawa, K. Iwamoto, Chemical vapor deposition of ZrC within a spouted bed by bromide process, *J. Nucl. Mater.* 97 (1981) 104–112.
- [36] K. Ikawa, K. Iwamoto, Coating microspheres with zirconium carbide-carbon alloy by iodide process, *J. Nucl. Sci. Technol.* 11 (1974) 263–267.
- [37] J.H. Park, C.H. Jung, D.J. Kim, J.Y. Park, Temperature dependency of the LPCVD growth of ZrC with the ZrCl₄-CH₄-H₂ system, *Surf. Coatings Technol.* 203 (2008) 324–328.
- [38] G.H. Reynolds, J.C. Janvier, J.L. Kaae, J.P. Morlevat, Irradiation behavior of experimental fuel particles containing chemically vapor deposited zirconium carbide coatings, *J. Nucl. Mater.* 62 (1976) 9–16.
- [39] K. Ikawa, Vapor deposition of zirconium carbide-carbon composites by the chloride process, *J. Less Common Met.* 29 (1972) 233–239.
- [40] S. Ueta, J. Aihara, A. Yasuda, H. Ishibashi, T. Takayama, K. Sawa, Fabrication of uniform ZrC coating layer for the coated fuel particle of the very high temperature

- reactor, *J. Nucl. Mater.* 376 (2008) 146–151.
- [41] P. Barnier, F. Thévenot, Synthesis and hot-pressing of single-phase ZrC_xO_y and two-phase ZrC_xO_y - ZrO_2 materials, *Int. J. High Technol. Ceram.* 2 (1986) 291–307.
- [42] M. Gendre, A. Maître, G. Trolliard, Synthesis of zirconium oxycarbide (ZrC_xO_y) powders: Influence of stoichiometry on densification kinetics during spark plasma sintering and on mechanical properties, *J. Eur. Ceram. Soc.* 31 (2011) 2377–2385.
- [43] Y. Yang, W.-Y. Lo, C. Dickerson, T.R. Allen, Stoichiometry effect on the irradiation response in the microstructure of zirconium carbides, *J. Nucl. Mater.* 454 (2014) 130–135.
- [44] Y. Huang, B.R. Maier, T.R. Allen, Irradiation-induced effects of proton irradiation on zirconium carbides with different stoichiometries, *Nucl. Eng. Des.* 277 (2014) 55–63.
- [45] F.M. Charbonnier, W.A. Mackie, R.L. Hartman, T. Xie, F.M. Charbonnier, W.A. Mackie, R.L. Hartman, T. Xie, Robust high current field emitter tips and arrays for vacuum microelectronics devices, *J. Vac. Sci. Technol. B.* 19 (2001) 1064–1072.

CHAPTER 4

FILM DEPOSITION

4.1 Overview of film growth

Films are layers or coatings produced by laying down particles which may or may not subsequently react with each other to form a truly continuous layer [1,2]. In this section we shall concentrate on backed films (film on a substrate) rather than unsupported films. Film technology deals mainly with fabrication, characterization and applications of the films. Films have a number of applications including optics, optical electronics, microelectronics, catalysis, communication, coating applications, and in the generation and conservation of energy [3]. In this study we are concerned with ZrC films for nuclear energy applications.

There are usually three general attributes that must be controlled when growing films. These are: (1) stoichiometry (the right stoichiometry or composition is an important aspect since materials show certain properties only within a given composition range), (2) surface morphology (the film surface is a very important factor that needs to be controlled during deposition, since some film properties depend on the surface morphology [4]) and (3) crystal structure (the films can be classified as crystalline (epitaxial), polycrystalline or amorphous). Crystallinity is important in controlling certain film properties [5]. Thus, the right crystal structure and orientation should be ensured in order to optimise the desired properties. The choice of the substrate is also very important in growing films so that the best alignment of the film is achieved. This is because the presence of grain boundaries affects the properties of the films [6].

In order to minimise the substrate influence on the grown films, the deposition of films is usually carried out relatively slowly (especially for thin films). The substrates are very

important in film growth because they play an important part in controlling the microstructure and other film properties [6,7]. The considerations for selecting a substrate for growing the films include: chemical compatibility, matching coefficients of thermal expansion, nature of the surface, cleanliness, substrate homogeneity and thermal stability [7]. Lattice mismatch and crystal structure of the substrate are also required in the growth of epitaxial films [6]. Graphite substrates were used for this study since it satisfied most of the requirements for a good substrate for the growth of polycrystalline ZrC films.

4.2 Film growth modes

There are generally three film growth modes for growing epitaxial films on a substrate. These are: (1) Frank-van der Merwe (FM) mode, (2) Volmer-Weber (VW) mode and (3) Stranski-Krastanov (SK) mode [8]. These three film growth modes are illustrated in Figure 4-1. Even though these growth modes were specified for epitaxial growth, they are also often used to describe the growth modes of polycrystalline films.

The FM mode is also called layer by layer mode or 2D mode. In this growth mode the adsorbed atoms have very good lattice match with the substrate they are being deposited onto. Due to the good lattice match, the adsorbed atoms attach themselves directly to the substrate, which limits the growth of clusters. The substrate and the adsorbed atoms are strongly attached, more than the atoms are attached to each other. Consequently, the coverage of the growing film onto the substrate is even (there is complete wetting of the substrate) [8,9]. Here, one layer has to be completely grown for the next one to start growing. The VW growth mode is also referred to as island or 3D growth mode. As the name suggests, here 3D islands are formed. In this growth mode the adsorbed atoms are more strongly bound to themselves than they are to the substrate. Therefore, the deposited material pile together

forming three dimensional islands [8]. The nucleation of new islands takes place even when the previous layer is not completely grown.

The SK mode is a combination of both FM and VW growth modes. At the start, the growth of the crystals is layer by layer (FM mode) until the film reaches a ‘critical’ thickness. When the ‘critical’ thickness is attained, islands are created, dominating the growth process (i.e VW mode) as depicted in Figure 4-1 [8,9].

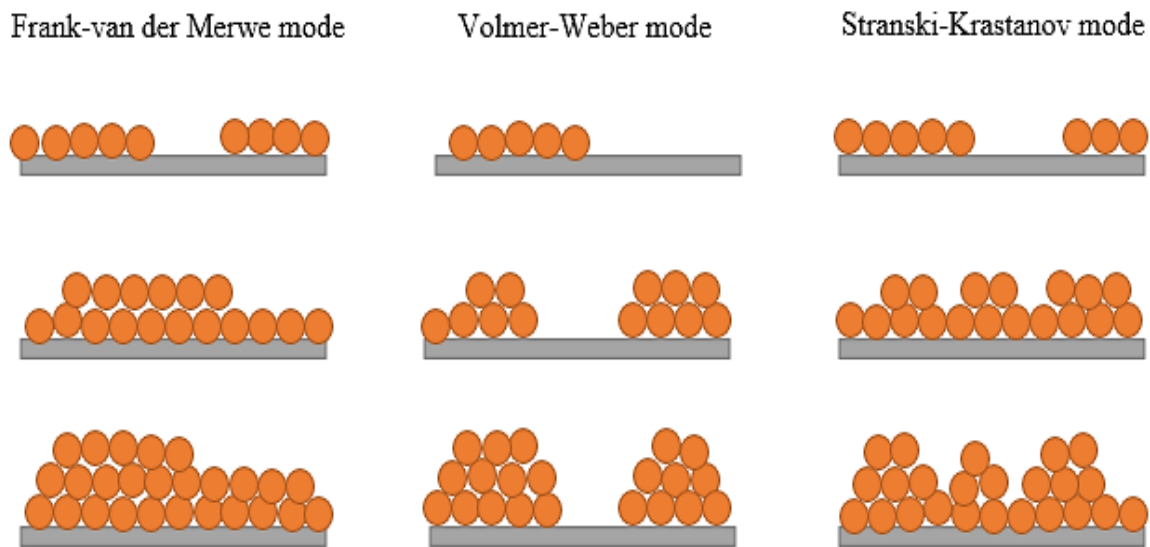


Figure 4-1: Schematic diagram of the film growth modes. Taken from [9].

These three growth modes occur as a result of varying interactions between the adatoms (the growing film or the deposit) and the substrate [8,10]. If we consider the point of contact between the growing film island and the substrate, then the surface tension can be taken as the force per unit length of the boundary [8]. In other words, surface tension exists due to the interface between two ‘phases’. The relationship of the interfacial tension between substrate-deposit (γ_{SF}), substrate-vapour (active gases) (γ_{SV}) and deposit-vapour (γ_{FV}) can be expressed by: $\gamma_{SV} = \gamma_{SF} + \gamma_{FV} \cos \theta$, where θ is the contact angle. The contact angle is an indication of the degree of wetting when a substrate and the growing film interact. The smaller the contact angle the higher is the wettability of the growing film on the substrate surface (Figure 4-2).

When $\theta=0$, we have layer by layer growth (i.e. $\gamma_{SV} = \gamma_{FS} + \gamma_{FV}$), hence it is energetically favourable for the film to cover the substrate surface completely. If $\theta > 0$, island growth (VW) mode is realised. In this case we have; $\gamma_{SV} < \gamma_{FS} + \gamma_{FV}$. For SK the growth mode the condition for FM is first fulfilled, but then growth of intermediate layers changes the amount of surface tension of the substrate and that of the film substrate-interface, leading to island growth [8,9,11]. For this case, the surface energy of the substrate surpasses the sum of the deposit surface energy and the substrate-deposit interfacial energy: (i.e. $\gamma_{SV} > \gamma_{FS} + \gamma_{FV}$) [11]. The SK mode normally occurs when there is a lattice mismatch between the substrate and the growing film which generates a build-up in strain. It has been reported that when films are under a state of strain, island formation is more energetically favourable so as to reduce the strain energy in the crystal [12]. Therefore the SK growth mode is as a result of the compromise involving the surface, strain relaxation and interface energy minimization.

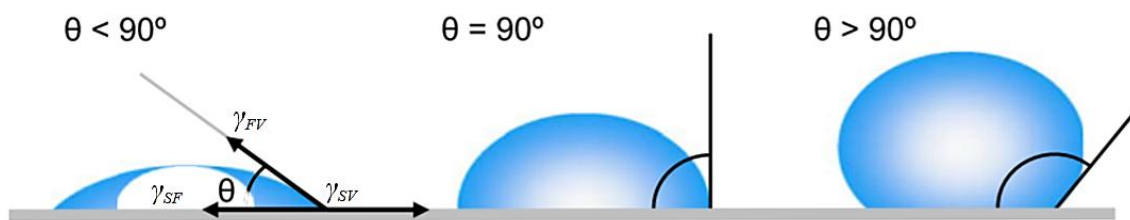


Figure 4-2: Diagrammatic illustration of the correlation between the contact angle and wettability of the substrate by a growing film. Taken from [13].

4.3 Film deposition techniques

The properties of films depend strongly on the deposition techniques and conditions under which they are being deposited [1]. In this work therefore, emphasis has been put on describing and understanding both the different methods of film deposition as well as the methods available for analysis and characterisation of films. The techniques used for the deposition of films are generally grouped into two classes, namely physical deposition and chemical deposition, as shown in Table 4-1 [14,15]. Among them, physical vapour deposition

(PVD) and chemical vapour deposition (CVD) are the two techniques that have been widely used to produce films from the vapour or the gaseous phase. However, CVD has been preferred since it produces films of superior quality as compared to PVD [15]. Therefore the emphasis in this chapter is on the CVD technique. The methods that were used in this study to analyse and characterise ZrC films are elaborated in Chapter 5.

Table 4-1: Thin film deposition techniques [15]

Film deposition techniques			
Physical deposition processes		Chemical deposition processes	
<i>Sputtering techniques</i>	<i>Vacuum evaporation techniques</i>	<i>Vapour phase techniques</i>	<i>Liquid phase techniques</i>
Glow discharge	Resistive heating	Thermal CVD	Electro deposition
Triode sputtering	Flash evaporation	Laser CVD	Spray pyrolysis
A.C. sputtering	Electron beam evaporation	PECVD	Sol-gel process
Magnetron sputtering	Laser ablation	MOCVD	Solution growth
Face target sputtering	Arc evaporation	APCVD	Anodization
Ion beam sputtering	RF heating	Photo CVD	Liquid phase epitaxy
RF sputtering	Ion plating	ALD	SILAR
			Electroless deposition

4.4 Chemical vapour deposition (CVD)

In CVD, activated gaseous reactants chemically react to form a stable solid film on a heated substrate [16]. The precursors' chemical reactions take place in the gaseous phase in the neighborhood of a hot substrate [7,16]. In other words, the CVD process involves the transportation of volatile precursor(s) in vapour form (often with the help of a carrier gas) to the reaction chamber, where they decompose and get deposited as a solid film on a heated substrate. After the deposition, volatile byproducts are eliminated [17]. A detailed description of the CVD process is given in Section 4.5.

The CVD process is normally classified in terms of the parameters used during the deposition process [14]. These parameters are the nature of the precursor used, the method of activation, the reactor pressure, the deposition temperature, the deposition time, cold/hot wall heating and the condition of gas flow [4] (see Figure 4-3). For example, if the process is enhanced by heat, plasma or high frequency radiation (e.g. ultra violet radiation) it is referred to as thermal CVD, plasma-enhanced CVD (PECVD) or photo-assisted CVD, respectively [7].

The CVD technique is complex. However, it has acquired a lot of preferences in the growing of layers and coatings due to its distinctive attributes compared to other methods like PVD. CVD enables the production of pure uniform films with good adhesion and reproducibility at relatively good deposition rates [16,18]. By controlling the CVD process parameters (pressure, temperature, flow rate, composition of the gas mixture, etc.), the desired crystal structure, stoichiometry, surface morphology and orientation can be obtained. Also, since CVD can use a broad variety of precursors like hydrides, halides, nitrides, organometallics and others, a variety of materials (e.g. sulphides, carbides, oxides, nitrides, III-V and II-VI materials) can be deposited [16]. In the CVD film growth process, the substrate is expected not to have influence on the properties of the film. However, the allowed limits vary from application to application [19]. For effective operation and deposition processes, the thermal CVD reactor should be composed of the following fundamental units: (1) an inlet gase delivery and supply system, (2) a reaction chamber, (3) a loading/unloading system, (4) a power system, (5) a process control system and (6) an exhaust gas treatment system [19].

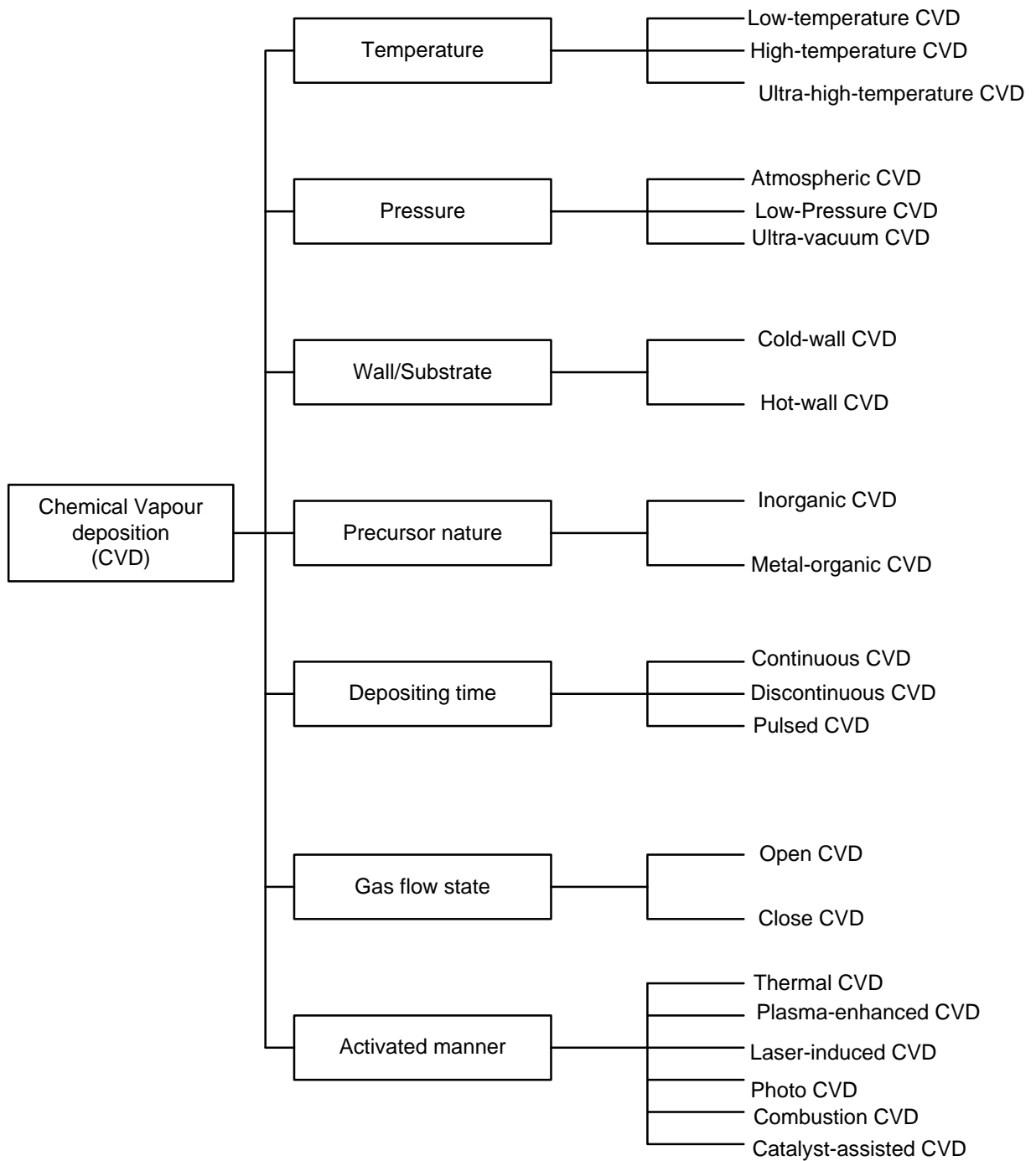


Figure 4-3: Break down of CVD methods. Taken from [4].

4.4.1 Thermal CVD

Thermal CVD is the conventional CVD technique which operates at high temperature. This technique uses heat energy to activate the gas and gas-solid phase reactions needed for the deposition process [5]. The heat is generated by resistive heating, or by high frequency

induction heating, radiant heating, or hot plate heating, or a combination of these sources [20]. Thermal CVD is usually used to deposit films for high temperature applications and for wear-resistant applications [4] like the ones used for the TRISO nuclear fuel particle [21]. The deposition temperatures usually range from 800 °C to 2000 °C [20]. This poses a limitation on certain substrates with low melting temperatures. When the substrate melting temperature is low, other methods like plasma enhanced CVD (PECVD), laser CVD (LCVD), photo-assisted CVD (PCVD) or catalytic assisted CVD are employed, which reduce the deposition temperature [20].

The wide range of materials deposited by thermal CVD methods has stimulated the design and construction of a large number of processes and systems [4,20]. In general, thermal processes have been distinguished by terms such as low or high temperature, atmospheric or low pressure, a cold or hot wall reactor, and a closed or open system. For a particular category of process, the variant distinctions in design and operation often make it hard to compare the performance of a particular systems or reactors, even when depositing the same material [5].

4.4.2 Closed and open CVD systems

A CVD system is said to be closed, or sometimes referred to as a chemical transport system, when the products are recycled for reuse within an enclosure. It is basically used for metal purification and protective coatings [4]. In a closed system the applied temperature differential produces the driving force for the reaction [20], whereas a CVD system is termed “open” or a flowing gas system if the reactants are introduced continuously and flow through the reactor. This is the most commonly used CVD system for the deposition of films [19]. In this study an open CVD system was used for the deposition of ZrC films.

4.4.3 Hot and cold wall CVD reactors

The deposition process can be carried out in a cold or a hot wall CVD system. The discussion about cold and hot wall reactors is very important to this study, mainly because of two reasons [22]:

1. The type of reactor and its operating conditions can impact greatly on the deposition process.
2. Quantitative information can be generated when the right mode of reactor operation is chosen.

In a hot wall reactor, the reactor wall is completely surrounded by an isothermal furnace [20]. The reaction gases are usually introduced into the reactor after the temperature has been raised to the required level. These reactors are usually large and many substrates can be accommodated, hence a large number of films can be produced in one operation [4,5,19]. The hot wall reactor is easy to operate and it can operate under a range of pressures and temperatures. Different orientations of the substrate in relation to the direction of gas flow can be achieved. Here the temperature is more uniformly distributed. However, the walls of the reactor may also be coated and this has a number of disadvantages. Some of the disadvantages are listed below [5,20]:

- (a) it limits the reactor to growing films from only one type of precursor mixture,
- (b) the deposits may end up falling off the wall and this can contaminate the substrate and the deposit,
- (c) the amount of active species arriving at the substrate surface may be reduced. This will decrease the deposition rate of the film on the substrate (i.e. feed rate limited deposition),
- (d) the deposition on the wall can change the conditions of the experiment leading to problems of reproducibility of the films,

(e) Furthermore, homogeneous gas-phase reactions in the heated gas may take place, causing reduced deposition rates.

Hence, hot-wall reactors are used essentially on the laboratory scale to examine the general feasibility of using a given precursor. Hot wall reactors are frequently used to find reaction product distributions, since the large heated surface area consumes the precursor completely and produces high yields of the reaction products [22].

In cold wall reactors, the heated part of the reactor is only around the substrate position. The rest of the reactor remains at lower temperatures. The heating process is usually by RF induction heating or by high radiant heating [4,22]. Unlike for the hot wall reactor where most reactions are exothermic, for cold wall reactors most reactions are endothermic (heat is absorbed). Because the substrates are at a higher temperature than the reaction chamber wall, the deposition will mainly take place on the substrate surfaces. Therefore, no depositions occur on the reaction chamber walls since it is at lower temperatures. In this case contaminations caused by the interaction between the reactor wall and the precursor vapour can be considerably minimised. Cold wall reactors are cheap, simple to manufacture and to control. The reaction and deposition rate is reduced, but the layer uniformity is improved [4,5,19].

4.4.4 High and Low pressure CVD

The deposition pressure during the CVD process has a considerable effect on the nature of the films deposited. A CVD process where the deposition is carried out at pressures close to or higher than atmospheric pressure is termed high pressure CVD (HPCVD). In this case the deposition reactions are diffusion limited (mass transport limited) [20]. The rate of deposition is much faster, but with poor step coverage. In simple terms, step coverage (sometimes referred as conformality) is determined from the ratio of the film thickness at its thinnest part to that at its thickest part. When this ratio is close to one, then there is good step coverage. To

avoid vapour phase precipitation, some precursors may require dilution with inert gases or sometimes hydrogen when operating at atmospheric pressure. CVD reactors operating at atmospheric pressure are usually cheaper and simpler to fabricate [5,7].

Compared to HPCVD, a low pressure CVD (LPCVD) process (typically 10 to 1000 Pa), the reactant mass transfer rate towards the substrate is improved relative to the surface reaction rate [15]. This implies that the growth rate controlling mechanism is due to surface reactions than to mass transport. Films with better uniformity, conformality and improved quality can be produced [5,15]. However, the film growth rate may be reduced. To compensate for low pressure, normally high concentrations of precursor gases are used. When the deposition pressures are very low, i.e. below 10^{-6} Pa, the CVD process is referred to as ultra-high vacuum CVD (UHVCVD) [4,5].

4.5 The CVD process

CVD systems are of various types, as already mentioned in the previous sections (low or high temperature, low or high pressure, cold or hot wall, closed or open reactor system). Regardless of the category of the CVD system, a CVD process must have a process controller to deliver and control precursors to the reaction chamber [14]. It must also have an energy source to drive the chemical reactions and an exhaust system to remove the byproducts and the depleted gases from the chamber [7,14]. However, the selection of the CVD technique is influenced by several aspects, such as the initial and running costs of the CVD system, reactant(s) used in the CVD process, purity of the deposit, maximum acceptable air leak rate into the system and size and shape of the substrate [18].

In the CVD film growth process, key sequential steps are involved as illustrated in Figure 4-4. Normally, active gaseous reactants are generated and then transported from the gas inlets to the reaction chamber. In the reaction chamber the gaseous reactants go through gas phase

reactions, producing film precursors and by-products [6,12]. This is followed by mass transport of the film precursors and the-by-products to the surface of a hot substrate. At this point the gaseous reactants get adsorbed (chemically or physically) onto the surface of the hot substrate, and the film deposit and other by-products are produced by chemical reactions at the gas-solid interface [5,16,19]. The film deposits then spreads out along the surface of a hot substrate, producing centres for crystallization and growth of the film. The gaseous by-products including the unreacted gaseous precursor(s) are then taken away from the boundary layer by means of diffusion or convection [5,16,19].

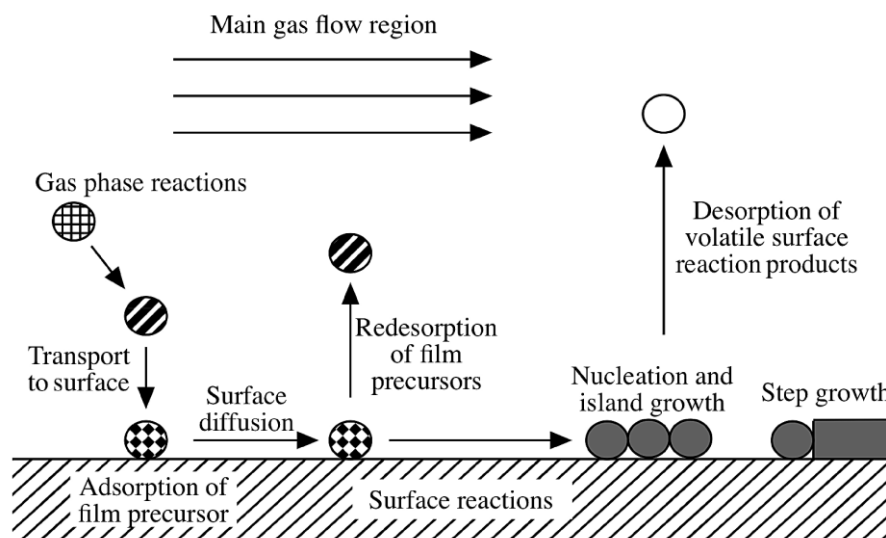


Figure 4-4: The major progressions of the process of CVD. Taken from [19].

4.5.1 Precursor requirements for CVD process

The chemical reactions with respect to the precursors used in the CVD process may generally be classified into 8 categories. These categories are: (1) hydrolysis, (2) reduction, (3) disproportionation, (4) oxidation, (5) thermal decomposition (also referred to as pyrolysis), (6) synthesis, (7) reversible transfer and (8) compound formation (carbide formation and nitridation) [5,16,20]. For example, the reaction type in which ZrC is produced from

zirconium tetrachloride and methane, or other higher hydrocarbons like cyclopropane, is called compound formation [5,20]; This chemical reaction is represented by Equation (4-1):



Therefore the nature of the CVD reaction type determines the category of the precursor to be used [20].

This section highlights the nature and general characteristics of a good precursor for film growth using CVD. A good precursor should have a high level of purity to prevent contamination of the deposit with unwanted products. Therefore the precursors should react without generating side or parasitic reactions [18,20]. The rate of deposition or reaction of the precursor should be neither too slow nor too fast. The reactions should occur on the substrate surface and the precursor should not be so reactive as to react in the vapour phase under the delivery conditions. It should be stable under normal storage conditions (room temperature) to avoid the need for special storage. A good precursor should have a low vaporisation temperature and a high vapour pressure [7,14,18]. This means that for a precursor to qualify to be used in a CVD process, it should possess a sufficient level of volatility at low temperatures, well below that of its decomposition. Moreover, it should have low levels of explosivity, toxicity and flammability. This allows for safe manipulation of the precursor and disposal of unreacted chemicals without using special procedures. It is also desirable that the precursors are readily available and cost effective for the production of the films [7,16,20].

4.5.2 Vaporisation of precursors for the CVD process

At ambient temperatures precursors exist in three forms; liquids, gases and solids. Of these, the gaseous precursors are easy to deliver and are sometimes diluted with inert gases to curb accidents [14,23]. Liquid precursors are the most commonly used precursors for CVD. Liquid and solid precursors are normally vaporized by heating to the required temperature so that they may be carried to the reaction chamber by the carrier gas [14,22,23]. A high vapour

pressure is necessary for easy precursor delivery into the reaction chamber and to realize high deposition rates. The solid precursors are the most difficult to deliver to the reaction zone, because they tend to block the delivery channels and most of them are not very volatile. The temperatures used to vaporise the precursor must be below their decomposition temperatures, since this may lead to precursor delivery rates which are irreproducible. Some unknown species may also be generated and transported to the reaction chamber [22].

As already mentioned, $ZrCl_4$ powder and CH_4 were used as precursors in the CVD process of ZrC films. $ZrCl_4$ is a white monoclinic hygroscopic powder which hydrolyses in water. It is soluble in alcohol and concentrated hydrochloric acid [24–26]. The physical properties of $ZrCl_4$ are shown in Table 4-2. It has been reported that metal halides such as $ZrCl_4$ normally do not produce pure films below 600 °C. They usually need a reducing agent such as H_2 gas to avoid impurities in the film [22]. Accurate control of the flow rate of $ZrCl_4$ plays a very important role. The flow rate of $ZrCl_4$ is controlled by the temperature of $ZrCl_4$ and the flow rate of the carrier gas. The temperature at which $ZrCl_4$ is maintained, determines its vapour pressure. This means the vapour pressure and thermal chemical changes of $ZrCl_4$ during vaporisation are very crucial for growing ZrC films with the desired properties [27].

Table 4-2: Physical properties of zirconium tetrachloride [25,26].

Property	Specification
Appearance	White powder at room temperature
Molecular weight	233.03 g/mol at 15 °C
Density	2.80 (g/cm ³)
Transition temperature	331 °C
Latent heat of sublimation	4.54×10 ⁵ J/kg at 331 °C
Specific gravity	2.805 g/cm ³ at 15 °C
Triple point temperature	473 (°C)
Triple point pressure	22.36 (bar)
Critical point temperature	504 (°C)
Critical point pressure	57.66 (bar)
Critical point volume	319 (ml/mol)

The relationship between temperature and vapour pressure P of a precursor may be expressed using the Clausius-Clapeyron Equation (4-2):

$$\frac{dP}{dT} = \frac{\Delta H_{sub}}{T\Delta V_m} \quad (4-2)$$

where ΔH_{sub} is the change enthalpy of sublimation (the enthalpy of a phase transition has little dependence on temperature), ΔV_m is the change in molar volume of two phases ($\Delta V_m = V_g - V_s$) and T is the transformation temperature [5]. However, the volume of a vapour V_g is much more than that of a solid (V_s). This means that the vapour volume V_g can represent the volume change (ΔV_m). If we assume the vapour to be a perfect gas, such that $V_g = nRT/P$, then the Clausius-Clapeyron equation can be written as in Equation (4-3):

$$\frac{d(\ln P)}{dT} = \frac{\Delta H_{sub}}{RT^2} \quad (4-3)$$

Equation (4-3), when integrated gives Equation (4-4), which can also be expressed as given in Equation (4-5).

$$\ln P = A - \frac{\Delta H_{sub}}{RT} \quad (4-4)$$

$$\log_{10} P = A - \frac{B}{T} \quad (4-5)$$

where A and B are constants [4,5]. For $ZrCl_4$ the values of A and B for $T \leq 583$ K have been reported to be 11.605 and 5317, respectively [28]. Thus, if the temperature is known the vapour pressure can be determined. However, the values A and B may be influenced by the experimental conditions at hand. Therefore, it is important to determine the precursor vapour pressure at the operating experimental conditions and set up at hand. In the literature, the vaporisation temperatures of $ZrCl_4$ that have been used in the CVD process for the deposition of ZrC range from 160 to 315 °C [24,28–32].

4.5.3 The CVD process: Kinetics and thermodynamics

Thermodynamic analysis of a CVD process provides information about the possible chemical reactions at equilibrium conditions. Therefore, thermodynamic studies determine the feasibility of a given CVD reaction. For the production of high quality films, determining the feasibility of the CVD process should always be the first step. This allows for proper selection of suitable precursors and the CVD reactor components. Deposition conditions such as reactant concentration, temperature and pressure can be predicted based on minimisation of the Gibbs free energy. The phase diagrams showing the possible equilibrium phases present as a result of the chemical reaction system can also be generated [4] [5]. The feasibility analysis of the current study is given in Chapter 6. It is important to note that CVD reactions and processes are complex and non-equilibrium [4].

The rate of the deposition process in a CVD system is determined by the process kinetics. There are several CVD kinetics steps involved during film growth. The slowest of the steps limits the general deposition rate of the films [4] [20]. The four main rate-limiting factors or controls in a CVD process commonly identified are: (1) thermodynamic control, (2) nucleation control, (3) mass transport control and (4) surface kinetics control [18]. In thermodynamic control, the rate of deposition of the films is the same as the rate of mass input into the reactor. This usually takes place at limiting conditions of deposition (for example at high temperatures, very low flow rates, etc.). The dependence of the deposition rate on temperature is determined from thermodynamic calculations. In addition to the CVD process being thermodynamically favourable, the barrier to nucleation has to be overcome. The rate of deposition is controlled by nucleation normally at very low reactant concentrations [14,18]. Nucleation is the kinetics of formation of the “nuclei” of a solid phase of the material being deposited from the gaseous phase. These nuclei create sites upon which additional particles are deposited as the crystal grows [18]. Nucleation can either be

homogeneous or heterogeneous. Heterogeneous nucleation occurs when the formation of the nuclei is influenced by a foreign material (e.g. a substrate). In homogeneous nucleation the nuclei formation occurs away from the substrate surface and thereafter falls on the substrate [5,14,20]. Coatings are more firmly bound to a substrate in reactions involving heterogeneous nucleation than those involving homogeneous nucleation [5,14]. In this study, the formation of ZrC occurred only when the active species were in contact with the substrate (i.e. heterogeneous nucleation).

Of all the CVD kinetics the most dominant deposition rate controls are the surface reaction and mass transport. The reaction is said to be mass transport controlled when the transport of the reactants transport and/or the reactant products across the boundary layer determines the deposition rate. It often takes place when the deposition temperatures and pressures are high. Mass transport is used to control the processes in the vapour phase in the reactor.

If the mass transport through the boundary layer is sufficiently large the system is controlled by surface kinetic reactions [14]. Therefore surface kinetic control occurs when the rate of deposition is lower than the rate of mass input into and/or from the reactor. Surface kinetic control is the favoured process control for producing films with uniform thickness and complex shapes. The surface reaction rate rises exponentially with an increase in temperature, which results into a mass transport limited growth mode at very high temperatures [14,18].

There are four distinct mass transport processes across a boundary layer in the CVD process. These are [18]:

- (1) Fickian diffusion which arises from a concentration gradient across the boundary layer.

- (2) Thermal diffusion, also called Soret diffusion, that is influenced by temperature differences in the reactor. This category of diffusion is very significant in systems with big deviations in molecular size and molecular weights between the vapour species.
- (3) A concentration gradient that results in a density gradient, leading to a buoyancy-driven advective flux.
- (4) In the general CVD reaction, the number of moles of gas can be altered. This may produce a flux towards or away from the surface of the substrate [18]. So the film growth rate depends on the precursor concentrations.

4.5.4 Effect of deposition temperature and concentration on the film growth

As already discussed in Section 4.5.3, the rate limiting mechanisms for film growth in a CVD system are influenced by many factors. However, the deposition temperature and concentration(s) of the reactants between the gas inlet C_g and the substrate surface C_s dominate [5,33]. Reaction resistances are normally applied to predict the rate limiting steps in a CVD process [18]. If the process is mass transport limited, then according to Fick's law, the reactant flux can be given by Equation (4-6);

$$J_i = -D \frac{dC_i}{dx} \quad (4-6)$$

where J_i is the diffusion flux of species i across the boundary layer, D is the diffusivity of the reactants, C_i is the concentration of species i and x is the direction perpendicular to the substrate surface [14].

Considering the gas diffusion through a fixed boundary layer having a thickness of δ in the neighbourhood of the substrate, the mass flux can be approximated by Equation (4-7) [5];

$$J_{gs} = D \frac{C_g - C_s}{\delta} \quad (4-7)$$

The flux of reactants utilised by the reaction occurring at the surface of the growing film is equal to the surface reaction flux and is given by Equation (4-8):

$$J_s = k_s C_s \quad (4-8)$$

where k_s is the surface reaction rate constant. In steady state: $J_{gs} = J_s$. This leads to Equation (4-9):

$$C_s = C_g \left(1 + \frac{k_s}{h_g} \right)^{-1} \quad (4-9)$$

where $h_g = \frac{D}{\delta}$ is the gas phase mass transfer coefficient. Equation (4-9) predicts that the surface concentration drops to zero if $k_s \gg h_g$, hence mass transfer control. In this case, slow gas transport through the boundary layer limits the otherwise rapid surface reaction. Surface reaction control dominates when $h_g \gg k_s$. In this case, $C_s \sim C_g$. Here the surface reaction is sluggish even though sufficient reactant gas is available. It is important to note that k_s and h_g depend on temperature. Figure 4-5 shows a model illustrating the thin film growth process. The growth rate \dot{G} of the film is expressed as the ratio of reactant flux J to the number of atoms per unit volume in the film (atomic density) N [5] (i.e. $\dot{G} = J/N$). Then the film growth rates for surface reaction and mass transport controlled processes are $\dot{G} \approx \frac{C_g}{N} k_s$

for $k_s \gg h_g$ and $\dot{G} \approx \frac{C_g}{N} h_g$ for $h_g \gg k_s$, respectively.

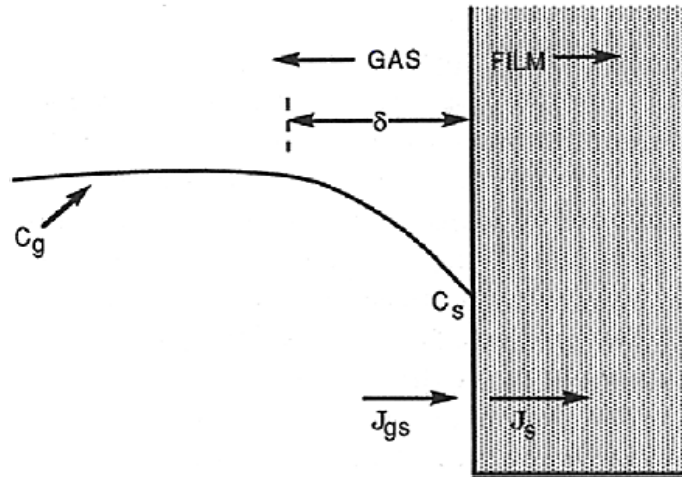


Figure 4-5: Schematic diagram of the CVD film growth process model. Taken from [5].

4.5.5 The boundary layer

The boundary layer is the region near the substrate surface where the gas stream velocity, the concentrations of the vapour species and the temperature are not equal to those in the main gas stream [20]. The variations of these parameters along the deposition chamber have an effect on the film properties (e.g. film growth rate and uniformity). The boundary layer is thus one of the significant factors considered so as to produce high quality films. When the thickness of the boundary layer is increased, the flux of the reactants towards the substrate is reduced, hence reducing the film growth rate. The boundary layer is thinner or almost absent at edges of a substrate due to the gas flow streams and this may result in thicker coatings at the edges of a substrate compared to the “flat” exposed part of the substrate [14,20]. The boundary layer thickness can be reduced by (1) elevating the reactant gas temperature at the surface of the substrate, (2) reducing the pressure using a low pressure deposition chamber, (3) increasing the reactant gas flow velocity, (4) reducing the size of the substrate and (5) reducing the substrate-gas inlet gap.

The boundary layer thickness in a vertical wall CVD reaction chamber is the distance across the boundary layer from the substrate to the point where the flow velocity of the gas mixture

is the same as the inlet velocity (“free stream” velocity) of the gas mixture [34]. The thickness of the boundary layer δ_c at the inlet-substrate distance X is related to the Reynolds number (Re) by Equation (4-10). The Reynolds number is a dimensionless parameter that characterises fluid flow dynamics. The gas flow is laminar if $Re < 1000$, otherwise it is turbulent [14] [20]. The Reynolds number depends on the viscosity η , density ρ , flow velocity v of the gas mixture and the diameter of the reactor d . The Reynolds number is estimated from Equation (4-11) [20]:

$$\delta_c \approx \left(\frac{Xd}{Re} \right)^{\frac{1}{2}} \quad (4-10)$$

$$Re = \left(\frac{d\rho v}{\eta} \right) \quad (4-11)$$

4.6 Induction heating process in CVD

Induction heating is commonly used in CVD processes so as to achieve high deposition temperatures in a relatively short time [35,36]. It is a non-contact method in which an electrically conducting material is heated by an alternating magnetic field. This is supported by Faraday’s law of electromagnetic induction. The induction heating system comprises mainly of an alternating-current power supply, an induction coil made from a very good electric conducting material and the material to be heated, called the workpiece or *susceptor*. In this case the latter is a graphite tube which in this study is referred to as the reaction chamber. The alternating current flow through the induction coil creates an alternating magnetic field that passes through the susceptor. This alternating electromagnetic field produces an induced current (eddy current) which is normally resisted by the resistivity of the material. This resistance to the induced current results in the generation of heat in the susceptor [36–38]. Therefore induction heating relies basically on two physical principles: (i) electromagnetic induction and Joule heating [36]. The amount and distribution of the

temperature resulting from the Joule heat depends on the design of the reactor, the input power, the frequency and the coil position and its geometry. Induction heating is in most cases applied in heat treatment and surface heating, since the magnitude of the induced current reduces with distance from the susceptor. However, comparatively uniform heating configurations can be achieved when adequate time is given for heat conduction. To ensure strict control of the heating rates and configurations, great attention must be paid to the radio frequency of the power supply, the rating and the induction coil design [36].

4.6.1 Electromagnetic formulation

The differential forms of Maxwell's Equations (4-12) to (4-15) (in meter-kilogram-second-coulomb units) can be used to predict the behaviour of electromagnetic fields in a material.

$$\nabla \times \vec{B} = \mu \vec{J} + \mu \varepsilon \frac{\partial \vec{E}}{\partial t} \text{ (Ampere's law)} \quad (4-12)$$

$$\nabla \times \vec{E} = -\frac{\partial \vec{B}}{\partial t} \text{ (Faraday's law)} \quad (4-13)$$

$$\nabla \cdot \vec{E} = 0 \text{ (Gauss law)} \quad (4-14)$$

$$\nabla \cdot \vec{B} = 0 \text{ (Gauss law)} \quad (4-15)$$

where E is the eddy electric field induced in the graphite and insulation, B is the magnetic flux density, J is the current density, μ is the magnetic permeability and ε is the permittivity of the media [39].

Assuming the displacement current density is much less than the induced conductive current, then $\frac{\varepsilon \partial \vec{E}}{\partial t} = 0$. This is because the graphite *reaction chamber* used in this study is non-magnetic and the frequency applied is less than 10 MHz (i.e. $f=205$ Hz). Therefore the heat losses due to hysteresis can be neglected [39].

Since $\nabla \cdot \vec{B} = 0$ then \vec{B} can be expressed in terms of the vector potential \vec{A} as $\vec{B} = \nabla \times \vec{A}$. Equations (4-12) and (4-13) can then be expressed by Equations (4-16) and (4-17) respectively, for $\vec{J} = \sigma \vec{E}$.

$$\frac{1}{\mu} \nabla^2 \vec{A} = \sigma \vec{E} \quad (4-16)$$

$$\nabla \times \left(\vec{E} + \frac{\partial \vec{A}}{\partial t} \right) = 0 \quad (4-17)$$

A vector whose curl is zero can be expressed as a gradient of a scalar. Therefore

$$\vec{E} + \frac{\partial \vec{A}}{\partial t} = -\nabla \phi, \text{ where } \phi \text{ is an electric scalar potential satisfying the vector identity}$$

$$\nabla \times (\nabla \phi) = 0.$$

The electric field intensity can then be expressed by Equation (4-18) as:

$$\vec{E} = -\frac{\partial \vec{A}}{\partial t} - \nabla \phi \quad (4-18)$$

Substituting Equation (4-18) in Equation (4-16) results in Equation (4-19);

$$-\frac{1}{\mu} \nabla^2 \vec{A} = \sigma \frac{\partial \vec{A}}{\partial t} + \sigma \nabla \phi \quad (4-19)$$

From Equation (4-19), $\sigma \nabla \phi$ is the conduction current density (current density source in the coil) denoted by \vec{J}_s and $\sigma \frac{\partial \vec{A}}{\partial t}$ is the induced current density (or eddy current) \vec{J}_e [39]:

$$\frac{1}{\mu} \nabla^2 \vec{A} = -(\vec{J}_s + \vec{J}_e) \quad (4-20)$$

This means that the total current density \vec{J} consists of the above two terms. Since there is a single frequency applied, then all electromagnetic quantities are oscillating harmonically with that single particular frequency. Therefore $\vec{J}_s = \vec{J}_0 e^{-i\omega t}$ and $\vec{A} = \vec{A}_0 e^{-i\omega t}$.

$$\Rightarrow \frac{1}{\mu} \nabla^2 \vec{A}_0 = i\omega \sigma \vec{A}_0 - \vec{J}_0 \quad (4-21)$$

\vec{A}_0 is the vector potential amplitude, \vec{J}_0 is the current density amplitude of the external generator and σ is the electrical conductivity. \vec{J}_s differs from zero only in the coil, which implies that the heat q received by the reaction chamber is only from the induced current density $\vec{J}_e = \sigma \vec{E}$ [39–41]:

$$q = \sigma \vec{E} \cdot \vec{E} = \sigma \frac{\partial \vec{A}}{\partial t} \cdot \frac{\partial \vec{A}}{\partial t} = -\omega^2 \sigma A_o^2 e^{-2i\omega t} \quad (4-22)$$

Heat transfer and electromagnetic processes are very complex and therefore the implementation of an exact analytical method is difficult and beyond the scope of this thesis.

The electromagnetic field carries its power from the outer surface of the conductor (in this case the graphite reaction chamber) towards its centre. As the electromagnetic wave penetrates through the conductor, it suffers ohmic losses. Since materials used in induction heating are good conductors, it means the ohmic losses per unit distance are high [40,42]. Therefore the wave decays quickly and dies after short distances from the outer surface as it penetrates the conductor. This is called the skin depth. For this reason, the current normally tends to flow a short distance into the conductor. The variation of electromagnetic wave with time at lower frequencies is slower, thus the wave survives for a longer time as it flows through the conductor [39]. This increases the skin depth. That is why in this study an RF power supply operating at low frequency was chosen. For non-magnetic conductors the skin depth δ is given by $\delta = \sqrt{\frac{2}{\omega\mu\sigma}}$ [41]. This means the skin depth depends on the work piece characteristics and the frequency of the alternating current [43].

If the induction coil is properly designed, its efficiency can even exceed 90%. But the general efficiency of the system (the percentage electrical energy taken from the power line that is basically used in the heating of the work piece) relies on many factors including: (1) coupling

of the coil and the work piece, (2) the conversion efficiency of the power supply, (3) matching of the induction heated load and coil to the induction power supply, and (4) the tuning of the induction heating circuit [36] [43].

4.7 References

- [1] L.I. Maissel, M.H. Francombe, An introduction to thin films, 1st ed., Gordon and Breach Science, New York, 1973.
- [2] A. Wagendristel, Y. Wang, An introduction to physics and technology of thin films, World Scientific, London, 1994.
- [3] A.Z. Moshfegh, Physics and Technology of Thin Films, IWTF 2003, in: A.Z. Moshfegh, H. v Känel, S.C. Kashyap, M. Wuttig (Eds.), PVD Growth Method Phys. Technol., World Scientific, Tehran, 2004: pp. 28–51.
- [4] X.-T. Yan, Y. Xu, Chemical vapour deposition: an integrated engineering design for advanced materials, 1st ed., Springer-verlag, London, 2010.
- [5] M. Ohring, Materials science of thin films, 3rd ed., Academic press, London, 2002.
- [6] C.B. Carter, M.G. Norton, Ceramic Materials Science and Engineering, 2nd ed., Springer-verlag, New York, 2013.
- [7] A.C. Jones, M.L. Hitchman, Chemical Vapour Deposition - Precursors, Processes and Applications, Royal Society of Chemistry, London, 2009.
- [8] K. Oura, V.G. Lifshits, A.A. Saranin, A. V Zotov, M. Katayama Surface science: an introduction, (2003).
- [9] K.A. Jackson, Kinetic Processes: Crystal Growth, Diffusion, and Phase Transformations in Materials, John Wiley & Sons, Weinheim, 2004.
- [10] P. Martin, Introduction to surface engineering and functionally engineered materials, John Wiley & Sons, New Jersey, 2011.
- [11] B. Lee, S. Komarneni, Chemical processing of ceramics, CRC Press, Florida, 2005.
- [12] A. Baskaran, P. Smereka, Mechanisms of Stranski-Krastanov growth, J. Appl. Phys. 44321 (2012) 1–6.
- [13] G. Bracco, B. Holst, Surface science techniques, Springer Science & Business Media,

- New York, 2013.
- [14] J. Park, T.S. Sudarshan, Chemical Vapor Deposition, ASM International, Chicago, 2001.
 - [15] K. Seshan, Handbook of Thin-Film Deposition Processes and Techniques: Principles, Methods, Equipments and Applications, 3rd ed., William Andrew, 2012.
 - [16] K.L. Choy, Chemical vapour deposition of coatings, Prog. Mater. Sci. 48 (2003) 57–170.
 - [17] T.T. Kodas, M.J. Hampden-Smith, The chemistry of metal CVD, John Wiley & Sons, Weinheim, 2008.
 - [18] P.M. Martin, Handbook of deposition technologies for films and coatings: science, applications and technology, William Andrew, 2009.
 - [19] J.L. Vossen, W. Kern, Thin film processes II, Academic press, San Diego, 1991.
 - [20] H.O. Pierson, Handbook of chemical vapor deposition: principles, technology and applications, 2nd ed., William Andrew, New York, 1999.
 - [21] J.B. Malherbe, Diffusion of fission products and radiation damage in SiC, J. Phys. D. Appl. Phys. 46 (2013) 27.
 - [22] M.J. Hampden-Smith, T.T. Kodas, Chemical vapor deposition of metals: Part 1. An overview of CVD processes, Chem. Vap. Depos. 1 (1995) 8–23.
 - [23] H.O. Pierson, Handbook of Refractory Carbides & Nitrides: Properties, Characteristics, Processing and Apps., Noyes Publications, New Jersey, 1996.
 - [24] C. Liu, B. Liu, Y.L. Shao, Z.Q. Li, C.H. Tang, Vapor pressure and thermochemical properties of ZrCl₄ for ZrC coating of coated fuel particles, Trans. Nonferrous Met. Soc. China (English Ed. 18 (2008) 728–732.
 - [25] P. Patnaik, Handbook of inorganic chemicals, McGraw-Hill New York, 2003.
 - [26] Y.M. Jung, M.K. Gyeong, L. Moonyong, Measurement of Bubble Point Pressures of Zirconium and Hafnium Tetrachloride Mixture for Zirconium Tetrachloride Purification Process, Int. J. Chem. Eng. Appl. 3 (2012) 427–429.
 - [27] L. Chao, L. Bing, Y.-L. Shao, Z.-Q. Li, C.-H. Tang, Vapor pressure and thermochemical properties of ZrCl₄ for ZrC coating of coated fuel particles, Trans. Nonferrous Met. Soc. China. 18 (2008) 728–732.

- [28] D. Kim, M.J. Ko, J.Y. Park, M.S. Cho, W.-J. Kim, Influence of free carbon on the characteristics of ZrC and deposition of near-stoichiometric ZrC in TRISO coated particle fuel, *J. Nucl. Mater.* 451 (2014) 97–103.
- [29] Q. Liu, L. Zhang, L. Cheng, Y. Wang, Morphologies and growth mechanisms of zirconium carbide films by chemical vapor deposition, *J. Coatings Technol. Res.* 6 (2009) 269–273.
- [30] Y. Wang, Q. Liu, J. Liu, L. Zhang, L. Cheng, Deposition mechanism for chemical vapor deposition of zirconium carbide coatings, *J. Am. Ceram. Soc.* 91 (2008) 1249–1252.
- [31] J.G. Kim, D.J. Choi, D.K. Kim, Y.-W. Lee, J.Y. Park, Microstructure and mechanical properties of chemical vapor deposited ZrC film on SiC/graphite substrate, *J. Ceram. Process. Res.* 10 (2009) 21–24.
- [32] C.M. Hollabaugh, R.D. Reiswig, P. Wagner, L. a. Wahman, R.W. White, A new method for coating microspheres with zirconium carbide and zirconium carbide-carbon graded coats, *J. Nucl. Mater.* 57 (1975) 325–332.
- [33] M. Ohring, *Engineering materials science*, Academic press, San Diego, 1995.
- [34] H. Schlichting, K. Gersten, E. Krause, H. Oertel, *Boundary-layer theory*, 4th ed., McGraw-Hill, New York, 1960.
- [35] R. Wang, R. Ma, An integrated model for halide chemical vapor deposition of silicon carbide epitaxial films, *J. Cryst. Growth.* 310 (2008) 4248–4255.
- [36] S. Zinn, S.L. Semiatin, *Elements of induction heating: design, control, and applications*, 2nd ed., ASM International, New York, 1988.
- [37] J.S. Park, S. Taniguchi, Y.J. Park, Maximum Joule heat by tubular susceptor with critical thickness on induction heating, *J. Phys. D. Appl. Phys.* 42 (2009) 1–6.
- [38] P.G. Simpson, *Induction heating: coil and system design*, McGraw-Hill, New York, 1960.
- [39] N. Di Luo, M. Fontana, B. Arcondi, Modelling of induction heating of carbon steel tubes: Mathematical analysis, numerical simulation and validation, *J. Alloys Compd.* 536S (2012) S564–S568.
- [40] F. Bay, V. Labbé, Y. Favennec, J.-L. Chenot, A numerical model for induction heating processes coupling electromagnetism and thermomechanics, *Int. J. Numer. Methods*

Eng. 58 (2003) 839–867.

- [41] Y. Favennec, V. Labbé, F. Bay, Induction heating processes optimization a general optimal control approach, *J. Comput. Phys.* 187 (2003) 68–94.
- [42] [https://www.researchgate.net/post/Why does an AC current tend to flow in the outer area of a conductor and why does this skin effect increases as the frequency increases](https://www.researchgate.net/post/Why_does_an_AC_current_tend_to_flow_in_the_outer_area_of_a_conductor_and_why_does_this_skin_effect_increases_as_the_frequency_increases) (accessed August 20, 2017).
- [43] J. Callebaut, Application Notes-Induction Heating, (2011). www.leonardo-energy.org (accessed February 6, 2017).

CHAPTER 5

ANALYTICAL AND CHARACTERISATION TECHNIQUES

After the deposition process, the as-deposited ZrC layers were analysed and characterised by several techniques. The main techniques used in this study were scanning electron microscopy (SEM), energy dispersive X-rays spectroscopy (EDS), X-ray diffraction (XRD), and Raman spectroscopy. This chapter discusses the key aspects of these techniques in relation to this work.

5.1 X-Ray Diffraction Technique

5.1.1 Background

X-ray diffraction (XRD) is a non-destructive technique that is very significant in materials characterisation, including films and coatings. It is used to study the crystallographic structure and chemical composition of materials. Information about films and other material properties such as crystallite size, residual stress, dislocation density, lattice strain, preferred orientation, film thickness and lattice parameter can be obtained from XRD measurements [1].

X-rays were discovered in 1895 by Willhelm Roentgen. They are electromagnetic radiation with energy range from 0.1 keV to 10 MeV, and wavelengths of the order of 1 Å. In diffraction analysis only hard X-rays (short wavelengths down to 0.1 Å) are used. X-rays are produced by bombarding a metal target with a beam of high energetic electrons [2]. The intensity of X-rays and the direction of the scattered beam are usually measured by the detector, which is crucial for diffraction analysis. X-ray detection is rooted in the fact that X-rays have the ability to interact with matter, produce signals and other effects that can be

registered. This means that every photon entering the X-ray detector originates from a particular event, or even a series of events, which may be registered. From these event(s) the intensity (total photon count) is determined [3]. The X-ray wavelength is of the same order of magnitude as the interatomic distance in the crystal lattice. Therefore XRD is the best technique for probing the structure of a crystalline material [1].

5.1.2 Phase and composition identification

When a single monochromatic beam of X-rays of a particular frequency is directed towards a sample, it will interact with a sample. After interaction, the originally single X-ray beam is diffracted by the crystallites in the sample at various angles. The intensities of the diffracted beams and the corresponding angles of diffraction are then recorded by the detector. This information is normally represented graphically by the use of suitable software as a plot of intensities (which correspond to the diffraction beam strength) against angles (corresponding to the beam position) resulting in a diffraction pattern. From the angles and the intensities of the diffraction pattern, phase identification and quantification can be made. This is due to the fact that the angles of diffraction depend on the geometry of the crystal lattice. Therefore the crystal structure of the sample and the size of the unit cell can be determined as explained in Section 5.1.3. The intensity of a diffraction line depends on the type of atoms, its arrangement in the crystal lattice and the crystallographic orientation [4]. Usually an XRD system is installed with a search/match software data base which is used to identify the phases and compounds present in the XRD pattern. The angle/position of the XRD pattern being measured is matched with reference data in the data base. If all the angular positions correspond with each other, then the compound or phase in the sample is identified to be the same as that in the data base.

XRD measurements are more sensitive to structural differences than to chemical differences and therefore additional techniques such as EDS are typically used in conjunction.

5.1.3 Crystal lattice structure and Bragg diffraction

A crystal structure can be studied through the diffraction of neutrons, electrons and photons. The level of diffraction is determined by the wavelength of the incident radiation and the crystal structure of the material being studied. If the incident radiation has a wavelength which is close to or smaller than that of the lattice constant, then the diffracted beam may take a different direction compared to that of the incident beam [5]. The diffraction of an X-ray beam in crystalline materials was explained by Bragg. It was argued that the diffraction of an X-ray beam from crystalline materials may be described and conceptualised with the help of mirror reflection notations [3] as depicted in Figure 5-1.

For Bragg's condition, radiation of wavelength λ incident on atoms of a crystalline lattice is scattered and undergoes constructive interference. Therefore, the two waves are in phase. For constructive interference to occur the path difference of the two waves should be equal to an integral multiple of the wavelength. From Figure 5-1 the path difference is $BC+CD$ and $BC=CD$. Thus, $2BC = n\lambda$. Therefore, the Bragg condition may be written as:

$$2d \sin\theta = n\lambda \quad (5-1)$$

where n , d and θ are the order of reflection, the interplanar spacing and Bragg's angle for the (hkl) plane, respectively [3,5].

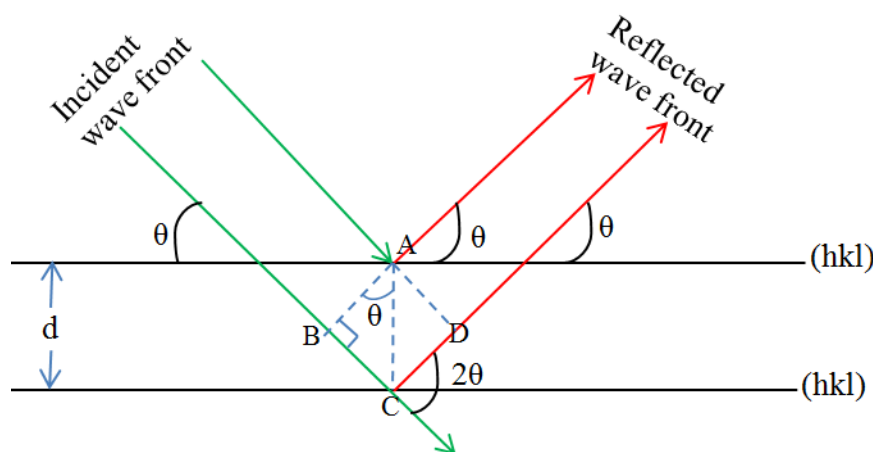


Figure 5-1: Bragg's law [3].

Using Bragg's equation (5-1), the values of d can be determined. For cubic crystalline materials such as ZrC, the lattice parameter (a) is described by Equation (5-2):

$$a^2 = d_{hkl}^2 / (h^2 + k^2 + l^2) \quad (5-2)$$

Since hkl are the Miller indices for the (hkl) plane, then $(h^2 + k^2 + l^2)$ is a constant denoted by m . Therefore, by combining Equations (5-1) and (5-2), the value of a can be determined from Equation (5-3):

$$a^2 = \frac{m\lambda^2}{4\sin^2 \theta_{hkl}} \quad (5-3)$$

The peaks of the diffraction pattern must first of all be indexed, in order to obtain the correct value of m , so that a is analytically obtained [1] from Equation 5-3. The crystal structure of a material can also be identified from the family of Miller indices [6].

5.1.4 Peak broadening of XRD patterns

In general, peak broadening of an XRD peak is caused by three factors: (1) crystallite size, (2) instrumental broadening and (3) the presence of strain in the material. If the instrumental broadening is corrected, peak broadening can be used to determine crystallite size and the strain in the material. This is because peak broadening decreases with increase in the crystallite sizes and increases with an increase in strain [7]. Let the measured peak broadening of the standard and that of the sample at full maximum at half maxima (FWHM) intensity of the peaks be B_s and B_m , respectively. The correct broadening B in relation to the sample's diffraction peaks can then be determined from Equation (5-4) [8]:

$$B = (B_m^2 - B_s^2)^{\frac{1}{2}} \quad (5-4)$$

From Figure 5-2 we assume that the intensity is zero at $2\theta_1$ and $2\theta_2$ so that B can be estimated as half the difference between the two angles, given by Equation (5-5):

$$B = \frac{1}{2}(2\theta_1 - 2\theta_2) = \theta_1 - \theta_2 \quad (5-5)$$

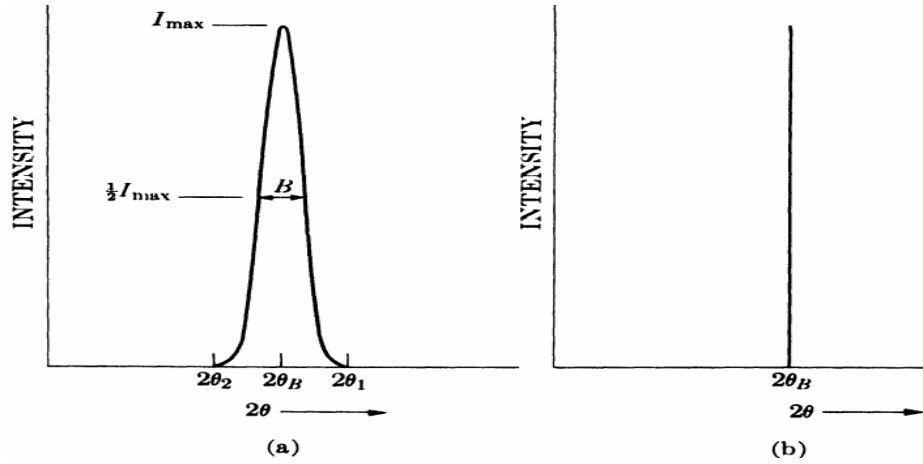


Figure 5-2: Schematic illustration of XRD peak broadening in crystalline materials. Taken from [8].

Applying Bragg's law, the path differences for the two angles are given by Equation (5-6):

$$\begin{aligned} (n+1)\lambda &= 2D \sin \theta_1 \\ (n-1)\lambda &= 2D \sin \theta_2 \end{aligned} \quad (5-6)$$

This gives:

$$\lambda = D(\sin \theta_1 - \sin \theta_2) = 2D \cos\left(\frac{\theta_1 + \theta_2}{2}\right) \sin\left(\frac{\theta_1 - \theta_2}{2}\right) \quad (5-7)$$

But $\theta_1 + \theta_2 = 2\theta_B$ and $\sin\left(\frac{\theta_1 - \theta_2}{2}\right) = \left(\frac{\theta_1 - \theta_2}{2}\right)$, therefore Equation (5-7) becomes:

$$2D \left(\frac{\theta_1 - \theta_2}{2}\right) \cos \theta_B = \lambda \quad (5-8)$$

The crystallite size D is then given by Equation (5-9):

$$D = \frac{K\lambda}{B \cos \theta_B} \quad (5-9)$$

Equation (5-9) is referred to as Scherrer's formula. To compensate for the peak shape, a constant K called the shape factor was introduced, which is usually about 0.94 as derived by Scherrer for cubic structures [9]. The sizes of crystallites in polycrystalline materials have

significant effects on its properties. For instance, decreasing the crystallite size increases the hardness and strength of the material [8]. Therefore, it is important to determine the crystallite sizes of the materials prepared.

From the calculated values of crystallite sizes, the dislocation density δ can be estimated. The dislocation density has been defined as the total length of all the dislocation lines per unit volume of a crystalline material [10]. Taking the crystallite size as the cube root of the crystallite volume and assuming all the crystallites have the same size and shape, Smallman, 1956 [11] expressed the relationship between δ and D to Equation (5-10):

$$\delta = \frac{nD}{D^3} = \frac{n}{D^2} \quad (5-10)$$

where n is number of dislocation lines in a unit volume of the crystallite.

5.1.5 Microstrain and residual stress in films

During the deposition of films strain may be introduced in the lattice planes. This causes the value of the interplanar spacing to change. This difference between the interplanar spacing values before and after the stress was introduced is comparable to the amount of stress. If the d -values, after the stress has been introduced, are constant in a particular plane for any set of (hkl) planes then uniform microstrain is produced. However, if the d -values for any particular set of (hkl) planes keep changing from plane to plane, it means the strain present is non-uniform. Uniform microstrain causes the diffraction peaks to shift from their original position before stress was introduced, whereas non uniform microstrain causes peak broadening of the respective diffraction peaks as illustrated in Figure 5-3. From the peak shift and peak broadening of the diffraction peaks, the amount of strain in the material can be estimated [8]. The level of strain in a material relates to the degree of distortion and crystal imperfection in that material. The microstrain ε is calculated from peak broadening B and diffraction angle θ [12] as indicated by Equation (5-11):

$$\varepsilon = \frac{B}{4 \tan \theta} \quad (5-11)$$

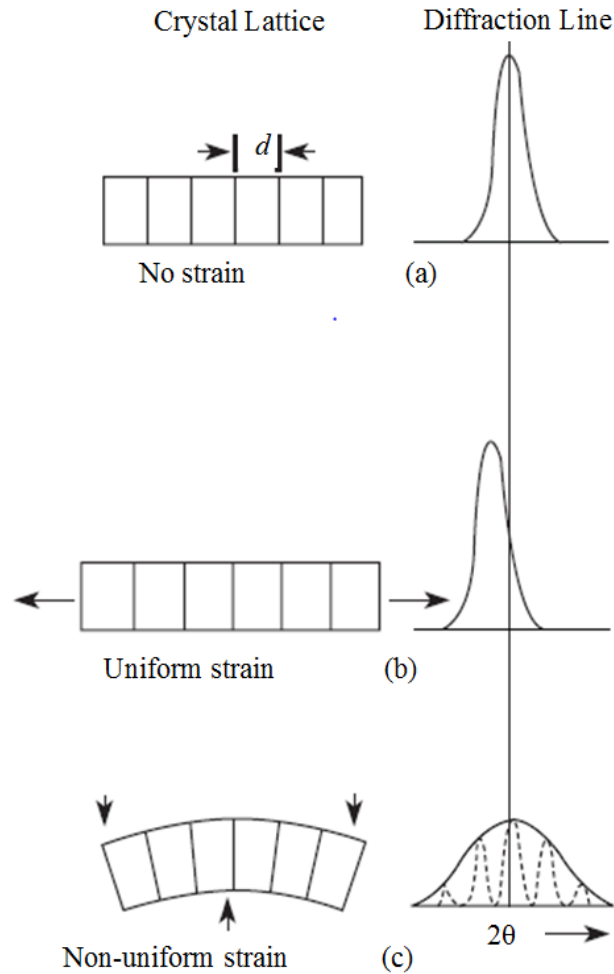


Figure 5-3: Effect of microstrain on peak position and broadening. Taken from [8].

The contributions of strain and crystallite size to peak broadening (i.e. B_ε and B_D respectively) do not depend on one another. It has been reported that crystallite sizes are best approximated by the Cauchy distribution, whereas microstrain (lattice distortions) is best approximated by a Gaussian distribution. Therefore, peak broadening may be given by either $B = B_D + B_\varepsilon$ (Cauchy) or $B = B_D^2 + B_\varepsilon^2$ (Gauss) [13][14]. Studies using transmission electron microscopy have reported that the best fit was obtained for the Cauchy distribution. This could be because the contribution to peak broadening due to crystallite size is much greater

than that from microstrain [13]. The overall peak broadening is then given by combining Equations (5-9) and (5-11) [12]:

$$B = 4\varepsilon \tan \theta + \frac{K\lambda}{D \cos \theta} \quad (5-12)$$

Rewriting Equation (5-12), we get the Williamson-Hall equation (5-13):

$$B \cos \theta = 4\varepsilon \sin \theta + \frac{K\lambda}{D} \quad (5-13)$$

If Equation (5-13) is plotted with $B \cos \theta$ on the vertical axis and $4 \sin \theta$ on the horizontal axis, the strain can be determined from the slope of the graph and the crystallite size from the vertical intercept [12,15].

The strain existing in a film can also be determined directly from the change in lattice parameter, obtained from XRD measurements [16]:

$$\varepsilon = \frac{a - a_o}{a_o} \times 100\% \quad (5-14)$$

where a_o is the bulk lattice constant.

The stress is usually caused by the presence of an external force on the material. However, in some cases, even when the external force has been removed, the material remains stressed. This kind of stress is called residual stress. Residual stress may be caused by chemical and/or thermal processes during the deposition process. Residual stress arises from the heating and cooling processes due to the differences in the coefficients of thermal expansion between the substrate and the deposited material and also during solid state transformations. Other processes influencing residual stress include the chemical composition of the film and growth induced stresses (e.g. due to misfit between the substrate and the film) of the reaction products formed on the substrate [17]. Increasing the film thickness reduces the effect of the substrate on the film and improves layer uniformity, which in turn reduces stress in the film.

The residual stress σ can be determined from XRD results (from the lattice strain). Using Hooke's law, stress is proportional to strain [1]; hence, stress in terms of strain and Young's modulus E is given by Equation (5-15):

$$\sigma = \varepsilon E \quad (5-15)$$

Therefore Equation (5-13) becomes:

$$B \cos \theta = 4 \frac{\sigma}{E} \sin \theta + \frac{K\lambda}{D} \quad (5-16)$$

If the value of Young's modulus is known, the values of the stress in the material can be determined.

5.1.6 Texture analysis and preferred orientation

Preferred orientation is a situation whereby the distribution of crystal orientations is non-random [8]. In the deposition of films it is very important to ascertain whether crystals with the required orientation have been grown. The properties of crystalline materials usually depend on how the crystal planes are oriented, since they are in most cases anisotropic. The preferred orientation is obtained by texture analysis. There are mainly two ways of determining preferred orientation; either in terms of pole figures and or texture coefficients [1,8]. Pole figure measurements by XRD is performed in such a way that the scattering angle remains constant while the tilt angle α and rotational angle β keep changing as the diffraction intensity is being measured [18] (see Figure 5-4). Stereographic representations, sometimes called equal area projections, are the most commonly used pole figure [1]. The values of the diffraction intensity when plotted as a function of angles α and β give the pole figure [18]. The intensity of a particular (hkl) reflection is proportional to the number of (hkl) planes in the reflecting condition. Therefore the pole figure determines the probability of getting a particular plane normal as a function of the sample orientation. If the values of the intensity obtained are uniform, it implies that the grains in the sample are randomly oriented [1].

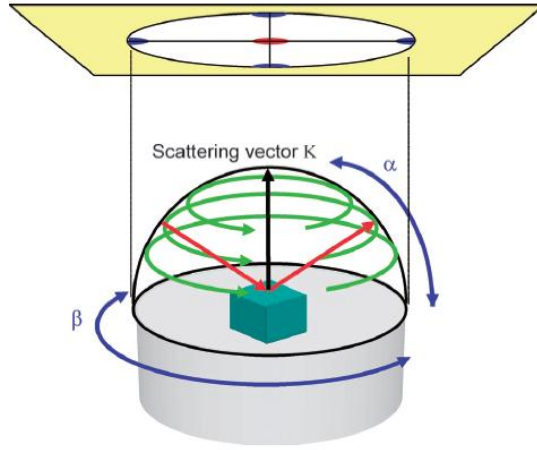


Figure 5-4: Stereographic projections and fixed scattering angle. Taken from [18].

Preferred orientation can also be determined analytically by means of texture coefficients.

The texture coefficient $T(hkl)$ is usually determined from Equation (5-17) [19]:

$$T(hkl) = \frac{I(hkl)/I_0(hkl)}{(1/N)\sum_N I(hkl)/I_0(hkl)} \quad (5-17)$$

In the Equation (5-17), $I(hkl)$ is the relative intensity of the (hkl) plane as measured from the diffraction pattern of the sample and N is the number of diffraction peaks considered. The quantity $I_0(hkl)$ is the relative integrated intensity of the reference randomly oriented grains (i.e. a powder sample) [8,19]. The value of $I_0(hkl)$ for the corresponding plane can be obtained from the ICDD data file. In this study ICDD data file number ZrC: 03-065-8833 and C: 00-008-0415 was used. If the values of $T(hkl)$ are less than or equal to one, it means the crystallites in that plane are randomly oriented and when the value of $T(hkl)$ is greater than one, it implies preferred orientation of the crystallites in a given $[hkl]$ direction [10,19].

$I_0(hkl)$ can also be calculated by considering the six factors which mainly influence relative intensity. The six main factors are the structure factor, multiplicity factor, Lorentz factor, polarization factor, temperature factor and absorption factor. However, other than the

structure factor F , multiplicity factor p and Lorentz factor $\frac{1 + \cos^2 \theta}{\sin^2 \theta}$, the other factors are

constant for all the diffraction peaks for a particular diffraction pattern. Therefore they are always left out in the expression for calculating the relative integrated intensity [8]. Hence the relative integrated intensity can be calculated from Equation (5-18) [2,8]:

$$I_o = |F|^2 P \left(\frac{1 + \cos^2 \theta}{\sin^2 \cos \theta} \right) \quad (5-18)$$

The degree of preferred orientation of the whole sample α is obtained by determining the standard deviation of all the values of $T(hkl)$ estimated from the sample as per Equation (5-17). This is given by Equation (5-19) [19]:

$$\alpha = \sqrt{\frac{\sum_N [T(hkl) - T_o(hkl)]^2}{N}} \quad (5-19)$$

The value of $T_o(hkl)$ is always equal to 1 since it represents the texture coefficient of a powder sample [19–21]. A sample with α -values greater than zero implies a preferred orientation, whereas one with an α -value equal to zero implies that the sample is completely randomly oriented. Since α is an indication of the degree of preferred orientation of the sample it is used in comparing samples for randomness and preferred orientation [19–21].

In this study XRD investigation of the crystal structure, the composition and the preferred orientations of the ZrC layers was carried out using a Bruker D8 Advance diffractometer, equipped with a theta-theta goniometer. Measurements conducted covered almost the whole geometry of the top surface of the as-deposited ZrC samples. The measurements were taken using a copper tube (Cu K α radiation source with $\lambda=1.54056 \text{ \AA}$). The working potential and the corresponding current used during spectrum acquisition were 1 kV and 40 mA, respectively. The incident angle of the X-rays to the sample was set at 7.5° for all the measurements. At the incident angle of 7.5° , the penetration of an X-ray wavelength into the ZrC layer was $1.8 \text{ }\mu\text{m}$. Since the thickness of all the deposited layers was greater than $1.8 \text{ }\mu\text{m}$,

then all the phases present in the XRD patterns were assumed to be from the deposited sample.

Diffraction data were collected using a LynxEye position sensitive detector. The composition of the ZrC layers was analysed by the Rietveld refinement method using the TOPAS V4.2 [22] software package. The general guidelines for structure refinement using the Rietveld (whole-profile) method formulated by the International Union of Crystallography Commission on Powder Diffraction were applied, both in XRD pattern collection and phase refinement [22]. The agreement indices were used to evaluate the refinement. For all the spectra, the weighted R profile and goodness of fit ranged from 2.6% to 5.8% and from 24.6 to 48.8 respectively.

5.2 Energy dispersive X-Ray spectroscopy

5.2.1 Principle of analysis

Energy dispersive X-Ray Spectroscopy (EDS or sometimes EDX) is a non-destructive quantitative and qualitative chemical microanalysis technique. EDS is normally attached to a transmission electron microscope (TEM) or a scanning electron microscope (SEM). In principal, EDS has the capability of analysing the elemental composition of materials whose atomic number is greater than three [23]. However, not all EDS instruments are equipped to detect light elements with atomic number less than ten ($3 < Z < 10$). Information on the material composition can be achieved both as a map or a point layout. Normally a beam of electrons from the electron microscope is directed into the sample [17]. Figure 5-5 illustrates the formation of X-rays when the incident electron beam interacts with the atoms in a sample.

The beam of incident electrons (typical energy 5 keV to 20 keV) bombarding the sample loses energy. One of the ways in which energy is lost is by emission of X-rays. This happens when the incident electrons bombard the atoms of the sample causing electrons to be ejected from inner electronic shells, thus creating electron vacancies [23,24].

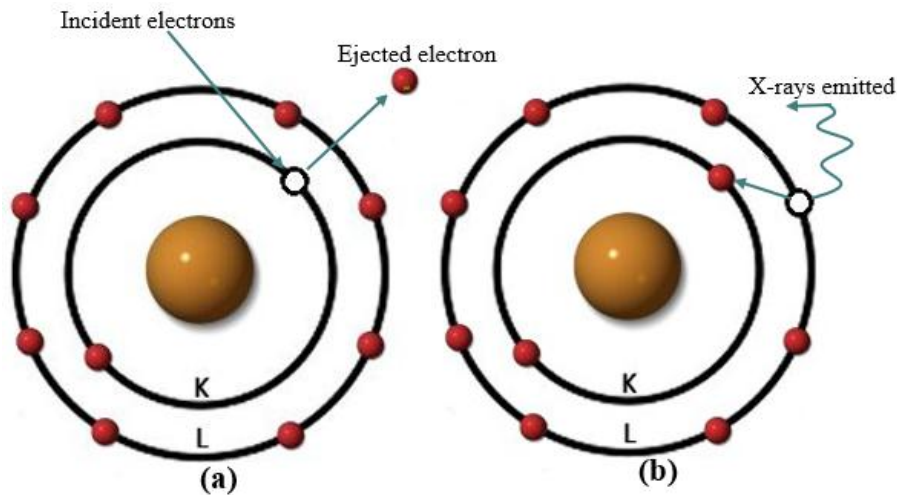


Figure 5-5: Schematic diagram illustrating incident electron bombardment of an atom in the sample and X-ray emission: (a) a vacancy is created in the K shell and (b) the vacancy is filled from the L shell.

The electron vacancies will make the atom unstable. Electron rearrangement in the shells will therefore occur so as to minimise the energy. Usually the electrons from higher energy levels fall to an inner shell to fill the vacancies. The electrons from the higher energy level have more energy than the ones being replaced. The energy difference will then be given out in the form of X-ray photons. Every element in a sample emits a unique and characteristic spectrum of X-rays. The energies of these X-ray photons are characteristic of the elements of the sample from which they are emitted [24][25]. The characteristic X-ray lines are identified based on the shell from which the electron is removed and the shell where the filling electron is dropped. For example, in Figure 5-5, the characteristic X-ray line is $K\alpha$.

The X-rays emitted from a sample are gathered by the EDS detector to determine the elemental chemical composition of the material. The EDS detector filters the characteristic X-rays of different elements in sample into energy bands or a spectrum. The elemental composition of the sample is determined by evaluating the spectrum obtained [23]. A typical EDS spectrum is given in Figure 5-6.

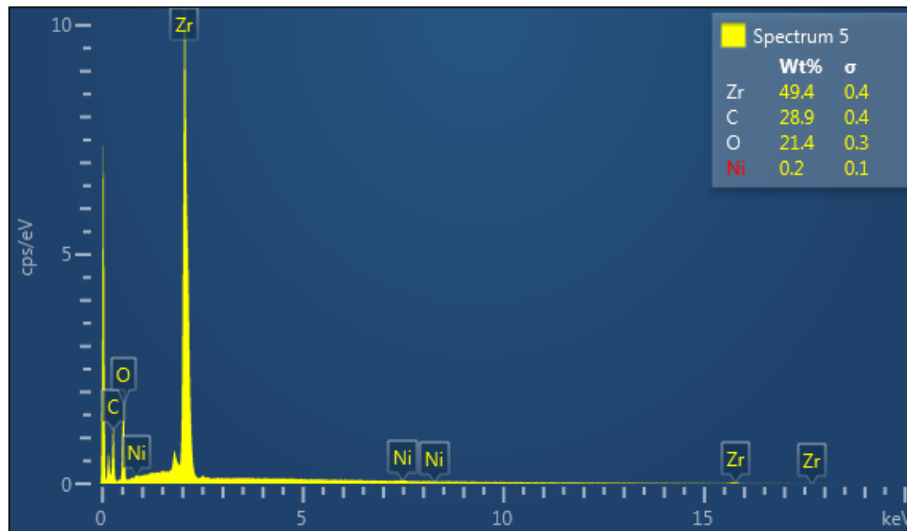


Figure 5-6: Example of EDS spectrum with characteristic peaks and elemental weight percentage of a sample.

5.3 What happens inside the EDS detector

When an incident X-ray strikes the detector, the detector converts the energy of each individual X-ray into a voltage signal proportional to the X-ray energy [23][26]. Normally there are three sequential processes through which it is accomplished. (1) The atoms are ionised in the semiconductor crystal (either lithium or silicon), which converts the X-rays into charge pulses. (2) Each charge pulse is converted into a voltage signal by a charge-sensitive preamplifier. This generated voltage signal is still proportional to X-ray energy. (3) The voltage signal is then transmitted to a multichannel analyser for processing. The voltage that is turned out from the multichannel analyser is in the form of a ‘ramp’. Each voltage step on the ramp corresponds to a particular X-ray energy. This energy for each incident X-ray as determined from the voltage measurement is then sent to a computer for display and further data evaluation [23].

In this study, the EDS instrument used for the characterisation of the elemental composition of the ZrC layers was manufactured by Oxford Instruments. It was mounted on a Zeiss Ultra Plus FE-SEM. The accelerating voltage while collecting the EDS spectra was set at of 15

keV. For this voltage, the interaction volume (depth of penetration) of electrons in ZrC layer was determined using Monte Carlo simulation for electrons software called MC-set. The penetration depth was found to be 1.3 μm , which is less than the thickness of all the layers that were deposited. This means that the carbon detected by EDS did not originate from the graphite substrate. Also compared to the entire interaction volume, the contribution of carbon from the surface contamination (if any) to the measured data is very negligible. It is important to note that, hand gloves together with tweezers were used during sample handling and the samples were stored in airtight clean containers. To cater for inhomogeneity in the sample, five measurements from five different regions on the surface of each sample were taken and the average of this was taken as the ‘true’ elemental composition of the sample. For this study, the instrument generated the elemental composition values as a weight percentage. The weight percentage of each element (i.e. W_i of i^{th} element) was therefore converted into atomic percentage (*at%*) by considering the atomic weight of each element (i.e. A_i of i^{th} element) in the sample composed of n elements. This was calculated from Equation (5-20)

$$At\% = \frac{W_i/A_i}{\sum_{i=1}^n W_i/A_i} \times 100\% \quad (5-20)$$

5.4 Raman Spectroscopy

5.4.1 Introduction to Raman

Raman spectroscopy is a non-destructive technique for structural and chemical composition characterisation of materials by employing the Raman scattering effect [27]. The Raman scattering effect was discovered in India in 1928 by Chandrasekhara Venkata Raman [28] and this later gave birth to the Raman spectroscopy technique. Raman spectroscopy is based on inelastic scattering of intense monochromatic light from a laser. For inelastic scattering to occur, it implies that the photon frequency of monochromatic laser light changes after

interaction with a sample [27,29]. Photons of the laser light are absorbed by the sample and then re-emitted. The frequency of the reemitted photons is shifted up or down in comparison to the original monochromatic frequency, which is called the Raman effect [27,29,30]. This shift provides information about vibrational, rotational and other low frequency transitions in the molecules. Raman spectroscopy can be used to study solid, liquid and gaseous samples [29]. Therefore Raman scattering can be used to reveal the structure and composition of crystals and molecules [19].

There are generally four major fundamental components of a Raman system. These are (1) the sample illumination system and light collection optics, (2) the excitation source (laser), (3) a detector and (4) a wavelength selector (filter or spectrophotometer) (see Figure 5-7). The sample to be measured is usually irradiated with a laser beam. The laser beam used in Raman analysis is normally in the near ultraviolet, visible or near infrared region. The radiation after interaction with the sample is collected with the help of a lens. The lens then directs this scattered radiation through an interference filter or a spectrophotometer to obtain a Raman spectrum of the sample.

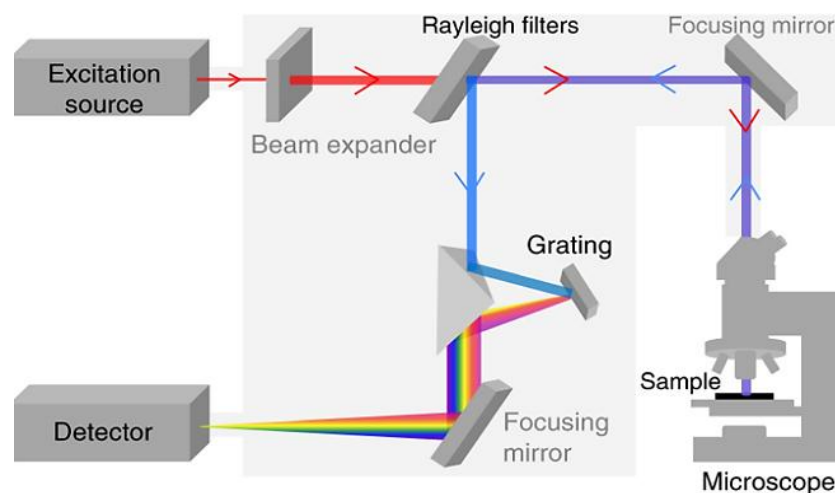


Figure 5-7: Schematic diagram of a basic Raman spectroscopy instrument and the radiation beam flow path. Taken from [31].

5.4.2 Raman spectroscopy and Raman spectra

In Raman spectroscopy the sample is irradiated by an intense laser beam with frequency ν_o . The incident beam after interacting with the sample molecules is scattered in all directions [32]. Figure 5-8 illustrates the different radiations produced when an incident beam is scattered by a sample. The scattered light is usually observed in the direction perpendicular to the incident beam. A big fraction of the scattered radiation has a frequency similar to that of the incident beam ν_o . This type of scattering is elastic and is called Rayleigh scattering. The remaining small fraction about 10^{-5} of the incident beam has frequencies $(\nu_o \pm \nu_m)$, where ν_m is the vibrational frequency of a molecule. This type of scattering is inelastic and it represents Raman scattering. When the frequency of the scattered radiation is lower than the incident radiation (i.e. the frequency is $(\nu_o - \nu_m)$), we get the Stokes lines in a Raman spectrum. If the frequency of scattered radiation is higher than the incident radiation (i.e. its frequency is $(\nu_o + \nu_m)$), anti-Stokes lines appear in the Raman spectrum [33]. Thus, in Raman spectroscopy we measure the vibrational frequency (ν_m) as a shift from incident beam frequency (ν_o). Figure 5-9 shows the Rayleigh and Raman scattering, including Stokes and anti-Stokes lines [32].

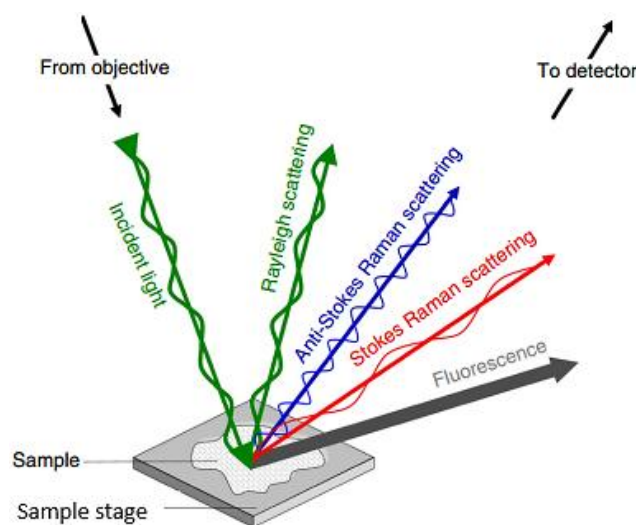


Figure 5-8: Schematic illustration of different radiations produced after an incident beam is scattered by a sample. Taken from [31].

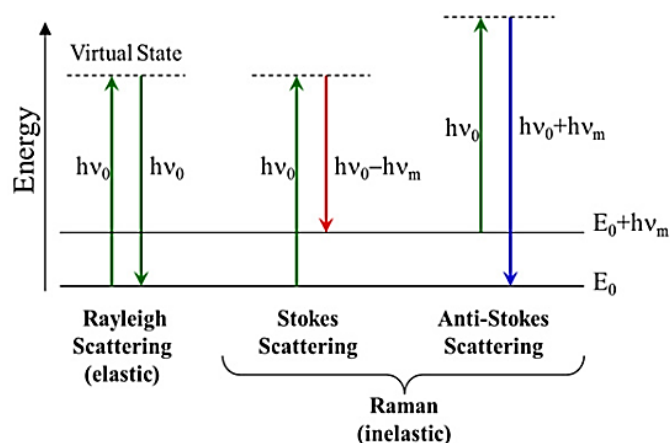


Figure 5-9: Diagrammatic illustration of Rayleigh and Raman scattering. Stokes and anti-Stokes lines are indicated. Taken from [34].

Stokes lines are more intense than anti-Stokes lines. In Stokes scattering the photons are scattered to lower energy, implying that the wavelength tends towards the red end of the spectrum. This is because at room temperature molecules are normally in their ground vibrational states. For this reason the Stokes transition outweighs the anti-Stokes transition lines and can easily be detected using a basic Raman equipment [30,35]. Usually a small number of molecules is vibrationally excited prior to irradiation of the sample by the laser beam. The scattered photons from these molecules have higher energy than the photons scattered from the rest of the molecules in the sample. This energy gain implies a shift in wavelength towards the blue end of the spectrum for anti-Stokes Raman lines. The gain or loss in energy a photon experiences as it interacts with a molecule is a characteristic of the vibrational modes of a particular bond in a molecule. This is because the photon energy shift differs from bond to bond (i.e. C-O is not the same as C-C and not the same as Zr-C, etc). Therefore, when the whole spectrum is recorded, spectral features can be used to identify and characterise the molecules. This is because spectral features are associated with the various different bonds and vibrations [30].

5.4.3 Raman scattering

According to classical electromagnetic theory, Raman scattering can be explained as follows; The electric field strength E of an incident electromagnetic wave (laser beam) fluctuates with time t as shown in Equation (5-21):

$$E = E_0 \cos(2\pi\nu_0 t) \quad (5-21)$$

where E_0 is the vibrational amplitude of the laser [28,36]. The scattering of a photon is caused by molecular polarisation. Polarisation allows the electric field intensity E to induce an electric dipole moment in atom or molecule [28,30]. The induced electric dipole moment P may be given by Equation (5-22):

$$P = \alpha E = \alpha E_0 \cos(2\pi\nu_0 t) \quad (5-22)$$

Here α is the polarizability [23]. Since the molecule is vibrating with frequency ν_m and with a particular vibrational amplitude, say q_0 , then the displacement q of the molecule about its origin can be represented by Equation (5-23):

$$q = q_0 \cos(2\pi\nu_m t), \quad (5-23)$$

For small amplitudes of vibration, α is a linear function of q and it can be represented by Equation (5-24):

$$\alpha = \alpha_0 + \left(\frac{\partial\alpha}{\partial q}\right)_0 q + \dots \quad (5-24)$$

Here, α_0 is the polarizability at the equilibrium position and $\left(\frac{\partial\alpha}{\partial q}\right)_0$ is the rate of change of α with respect to a change in q evaluated at the equilibrium position. Therefore, by combining Equations (5-23) and (5-24), the induced dipole moment is given by Equation (5-25):

$$P = \alpha_0 E_0 \cos(2\pi\nu_0 t) + \left(\frac{\partial\alpha}{\partial q}\right)_0 q E_0 \cos(2\pi\nu_0 t) \quad (5-25)$$

$$\Rightarrow P = \alpha_0 E_0 \cos(2\pi\nu_0 t) + \left(\frac{\partial\alpha}{\partial q}\right)_0 q_0 E_0 \cos(2\pi\nu_0 t) \cos(2\pi\nu_m t) \quad (5-26)$$

$$\therefore P = \alpha_0 E_0 \cos(2\pi\nu_0 t) + \frac{1}{2} q_0 E_0 \left(\frac{\partial\alpha}{\partial q}\right)_0 [\cos 2\pi(\nu_0 + \nu_m)t + \cos 2\pi(\nu_0 - \nu_m)t] \quad (5-27)$$

According to the classical theory, the first term of Equation (5-27) represents an oscillating dipole that radiates at the light frequency ν_0 (Rayleigh scattering), while the second term of the same equation corresponds to the Raman scattering at frequencies $\nu_0 + \nu_m$ (anti-Stokes) and $\nu_0 - \nu_m$ (Stokes). If $\left(\frac{\partial\alpha}{\partial q}\right)_0 = 0$, then the vibration is not Raman active. So for the vibration to

be Raman active the rate of change of polarizability with vibration must not equal to zero [28,36]. In normal Raman spectroscopy, the excited line is chosen so that its energy is far below the first electronic excited state. Under normal conditions the Stokes lines are stronger than anti-Stokes lines. Since both give the same information it is customary to measure only the Stokes side of the spectrum [37,38].

In this study the Raman spectroscopy analysis was performed using a Horiba Jobin-Yvon T64000 spectrometer with an argon-krypton laser of an excitation wavelength of 514 nm and a laser power of 148 mW. The spectra were acquired from Raman shifts ranging from 200 cm^{-1} to 1800 cm^{-1} at the aperture of the 50 times objective lens. The analysis of the Raman spectra was performed by Labspec 5 software, which enabled the measurement of peak height, position and width.

5.5 Scanning electron microscopy

5.5.1 Description of the technique

Scanning electron microscopy (SEM) is a non-destructive evaluation technique for high-resolution imaging of sample surfaces [39]. It provides information about the surface morphology, crystal structure, chemical composition and electrical behaviour of the sample

[40]. Compared to optical microscopy, which uses visible light for imaging, the scanning electron microscope (SEM) uses electrons [39]. One of the main advantages of SEM over optical microscopy is that SEM has a higher resolution and therefore has a higher magnification (over 150,000×). This allows for the visualization of fine structures on the sample that optical microscopy cannot reveal [41]. SEM has a large depth of field. The depth of field is the distance between the nearest and furthest point which are in focus. Thus, information on three-dimensional topography of the sample [42][43] is provided. SEM is one of the most popular and very versatile instruments. It is capable of obtaining images of sample surfaces of a wide variety of materials. The images obtained by SEM have a wide range of applications [23].

The basic components of a SEM (see Figure 5-10) may be grouped into four categories: (1) the electron column, (2) the specimen (or sample) chamber, (3) the vacuum pumping system and (4) the electron control and imaging system [44]. The SEM generates a beam of incident electrons in an electron column above the sample chamber. The electrons are produced by a thermal emission source, such as a heated tungsten filament, or by a field emission cathode. The energy of the incident electrons can be as low as 100 eV or as high as 30 keV depending on the evaluation objectives [39]. These electrons are emitted by the electron gun in the SEM column and are focused into a small beam through a series of electromagnetic lenses onto the sample surface, which is usually mounted on a mobile sample holder (see Figure 5-10). The electron beam upon impinging on the sample surface is scanned in a raster pattern over the sample surface for imaging [45]. Scanning coils near the end of the column direct and position the focused beam onto the sample surface [39]. The beam can also be focused at a single point or scanned along a line for X-ray analysis. The beam can be focused to a final probe diameter as small as about 10 Å [39][46]. The emitted electrons are detected for each position in the scanned area by an electron detector. The intensity of the emitted electron

signal is displayed as brightness on a cathode ray tube or the monitor. By synchronizing the monitor scan to that of the scan of the incident electron beam, the monitor display represents the morphology of the sample surface area scanned by the beam [45].

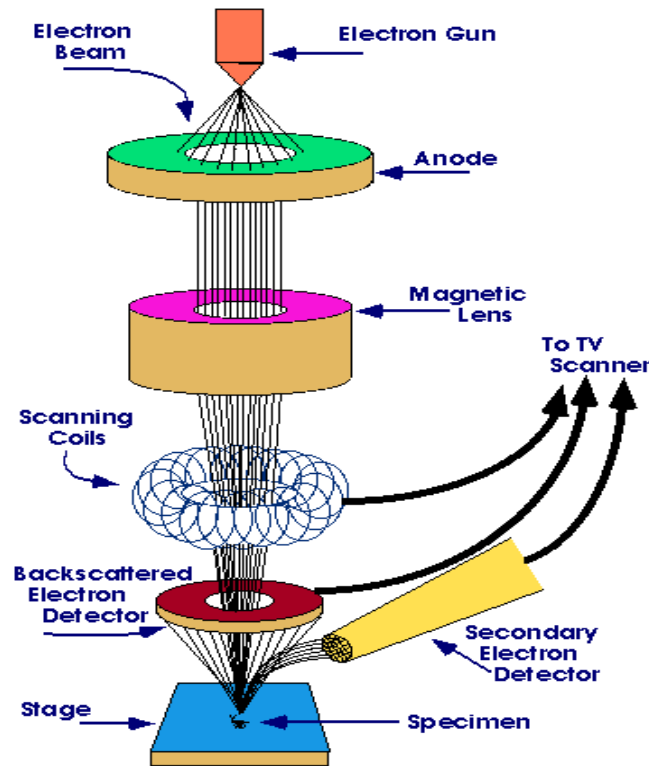


Figure 5-10: Schematic diagram of the electron paths in a conventional scanning electron microscope. Taken from [47].

5.5.2 Electron beam sample interaction and detection

When the incident electron beam interacts with the sample, some electrons are scattered, others are absorbed and transmitted, hence giving out a number of signals [47,48]. The signals given out by the sample include secondary electrons, backscattered electrons, Auger electrons, X-rays and cathodoluminescence (light) [40] as shown in Figure 5-11. As much as all these signals are generated at the same time, they are collected and analysed by various detectors independently. The SEM utilizes these signals to observe and analyse the sample surface (or just beneath the surface) [39].

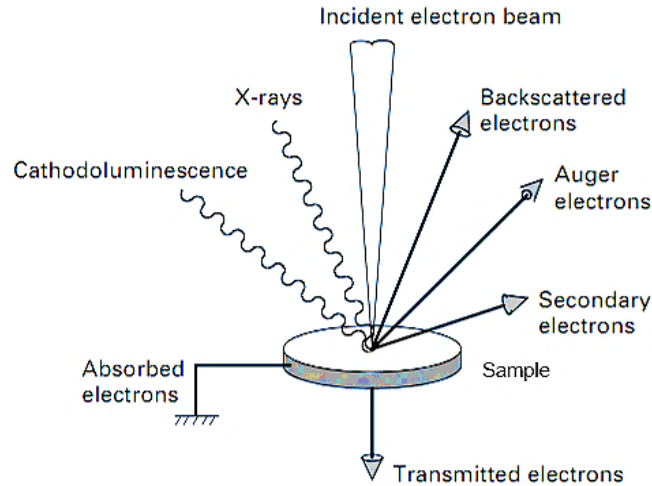


Figure 5-11: Incident electron beam interaction with the sample and radiations emitted. Taken from [49].

The incident electrons cause electrons to be emitted from the sample due to elastic and inelastic scattering events within the near-surface region of the material. Figure 5-12 is a schematic diagram that illustrates how various signals are emitted from the sample. High-energy electrons that are ejected by an elastic collision of an incident electron, typically with a sample atom's nucleus, are referred to as backscattered electrons. The energy of backscattered electrons is comparable to that of the incident electrons [39] [50]. The detected signals of the backscattered electrons are used for differentiating between areas on the sample surface with different chemical compositions. This is made use of by looking at the atomic number contrast and topographical contrast. For instance, in a ZrC micrograph formed by the signals from the backscattered electrons, the areas with zirconium will appear brighter than those with C. This is because Zr has a higher atomic number. Backscattered electrons are also used to form electron backscatter diffraction (EBSD) from which crystallographic structure of the sample can be determined [42] [43].

The emitted lower-energy electrons resulting from inelastic scattering are called secondary electrons. Secondary electrons can be formed from inelastic scattering of the loosely bound

valence electrons (in the K-shell) from the sample [39] [50]. The energy of secondary electrons is ≤ 50 eV [23]. Their signal is used to study the surface topography and morphology of the sample. These electrons are generated along the incident electrons' trajectory but only those generated within few nano-meters underneath the sample surface are detected— the others are absorbed in the sample owing to their low energy.

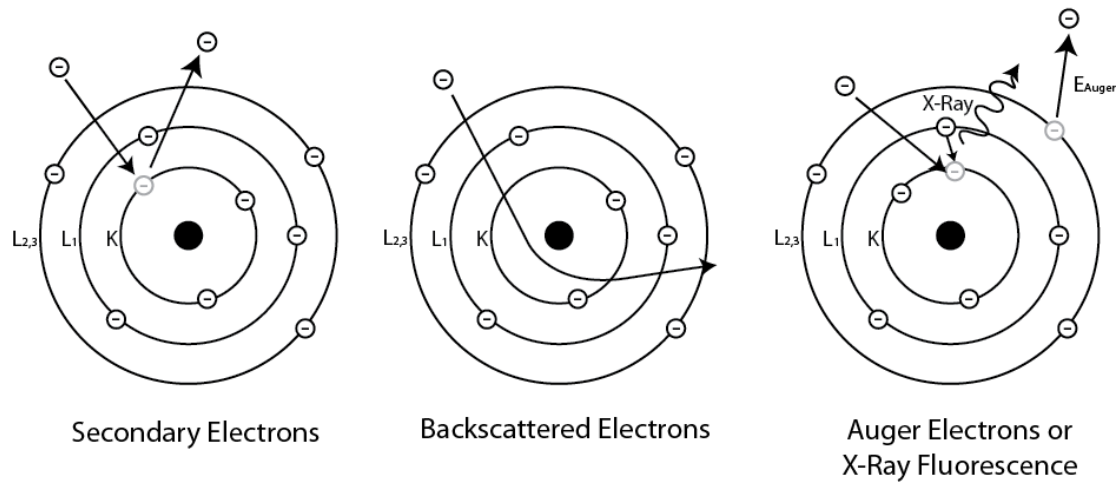


Figure 5-12: Emission of various signals from the sample. Taken from [50].

Auger electrons result from higher energy level electrons filling the vacancies in a lower energy level, as already explained in Section 5.2. The difference in the two energies is carried away through the emission of Auger electrons (low energy electrons) or the production of X-rays. The signals that result from these Auger electrons can be used for chemical analysis of the sample surface. The X-ray signals are used in chemical characterization of the samples by EDS [23].

The volume with in the sample in which the incident electrons interacts with the sample is referred to as the “interaction volume” (see Figure 5-13). The elemental atomic numbers of the sample, sample density and incident electron beam energy determines the magnitude of electron scattering inside the sample. An increase in electron beam energy increases the

scattering range. However, materials of large atomic numbers and densities produce small electron scattering ranges [49].

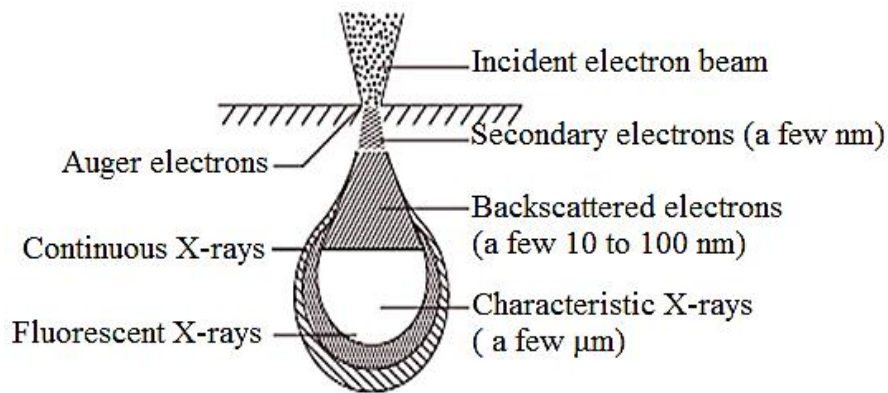


Figure 5-13: Schematic of the volume of generation of various radiations emitted by the incident electron beam interacting with the sample. Taken from [51].

5.5.3 Sample requirements

The SEM column and sample chamber are operated under vacuum in the range of 10^{-3} to 10^{-4} Pa. This is done to allow the electrons to travel freely from the electron beam source to the sample and then to the detectors. The good vacuum in the chamber also enhances high-resolution imaging [39][51]. Because SEM is operated under high vacuum, the nature of samples to be studied must meet this requirement. This implies that samples of materials such as liquids and volatile samples require special treatment before they are studied with SEM. The powder samples must be specially prepared to avoid contamination of the sample chamber. The samples must also be firmly fixed on the SEM sample holder. If the sample is non-conductive, it has to be coated with materials like graphite, gold or platinum to improve its conductivity. The coating must be done in such a way that the surface morphology of the material being coated is not affected significantly [39] [52]. Samples to be analysed in secondary electron mode must all be electrically conductive. In backscattered electron imaging mode both conductive and nonconductive samples can be analysed [39][51]. In an attempt to solve some of these sample limitation issues, some special SEM instruments have

been manufactured. These include variable-pressure SEM (VPSEM), which operates at higher specimen chamber pressures, thus allowing for non-conductive materials, and environmental SEM (ESEM) that allows the analysis of samples of wet materials. The samples to be studied should also be of the dimensions a given SEM sample chamber and sample holder can accommodate. Typically SEM equipment can accommodate with ease samples of dimensions up to 200 mm diameter and 50 mm height [39].

In this study the surface morphology of as-deposited ZrC layers were analysed using ultrahigh resolution field-emission scanning electron microscopy (FE-SEM, Zeiss Ultra Plus). This SEM instrument is equipped with detectors for secondary electron, backscattered electron and an in-lens secondary electron. The EDS detector is also attached to this SEM, the use of EDS has already been discussed in Section 5.2. The in-lens detector system was used to study the topography and morphology of the ZrC layers. The purpose of the in-lens detector system is to acquire images of high resolution by shortening the gap between the objective lens and sample, and enhancing the lens performance. The gap between the sample and the lens is made short by placing the sample in the magnetic field of the lens. The secondary electrons from the sample move upward in the strong magnetic field of the lens and are collected by the in-lens detector positioned above the objective lens. The image contrast when the in-lens detector is used is different from that of the conventional objective lens. Furthermore, since the use of in-lens detectors is a modern development, such SEM systems also have better electron optics allowing low acceleration voltages. Low accelerating voltages allow for more surface features of the sample to be revealed (i.e. it is more surface sensitive) and minimisation of charging effects [49]. This is good for studying the uniformity of the surface structure of the samples. The in-lens system allows the detection of surface defects—a very important parameter in the growth process of ZrC, as defects can create an easy diffusion path for the fission products. Surface defects are a disadvantage for the

purpose of using ZrC as a diffusion barrier layer. The electron beam of the Zeiss Ultra Plus FE-SEM at the University of Pretoria can be varied from 200 eV to 20 keV with good focussing capabilities. This enables the detection of the top surface as well as features deeper inside the layer. For the analysis of the ZrC layers the accelerating voltage was set at 1 kV and the working distance ranged from 2.0 to 3.0 mm. The surface morphology of the as-deposited ZrC layers was found to vary depending on the deposition parameters. The discussion of micrographs of ZrC layers deposited at different conditions and parameters is given in Chapter 7.

5.6 References

- [1] R. Sharma, D.P. Bisen, U. Shukla, B.G. Sharma, X-ray diffraction: a powerful method of characterizing nanomaterials, *Recent Res. Sci. Technol.* 4 (2012) 77–79.
- [2] Y. Waseda, E. Matsubara, K. Shinoda, X-ray diffraction crystallography: introduction, examples and solved problems, Springer Science & Business Media, New York, 2011.
- [3] V.K. Pecharsky, P.Y. Zavalij, Fundamentals of powder diffraction and structural characterization of materials, 2nd ed., Springer, New York, 2008.
- [4] C.T. Kniess, J.C. De Lima, P.B. Prates, The Quantification of Crystalline Phases in Materials : Applications of Rietveld Method, in: S. Volodymyr (Ed.), *Sinter. - Methods Prod.*, Open Access Publisher, Rijeka, Colombia, 2012: pp. 293–316.
- [5] C. Kittel, P. McEuen, P. McEuen, Introduction to solid state physics, Wiley New York, 1976.
- [6] C. Suryanarayana, M.G. Norton, X-ray diffraction: a practical approach, Springer Science & Business Media, New York, 1998.
- [7] K. Venkateswarlu, A.C. Bose, N. Rameshbabu, X-ray peak broadening studies of nanocrystalline hydroxyapatite by Williamson-Hall analysis, *Phys. B Condens. Matter.* 405 (2010) 4256–4261.
- [8] B.D. Cullity, S.R. Stock, Elements of X-ray Diffraction, 1st ed., Addison-Wesley Publishing company Inc, Massachusetts, 1956.
- [9] M. Ermrich, D. Opper, XRD for the analyst: Getting acquainted with the principles,

PANalytical, Eindhoven, 2013.

- [10] S. Aksoy, Y.Y.Y. Caglar, S. Ilican, M. Caglar, Effect of deposition temperature on the crystalline structure and surface morphology of ZnO films deposited on p-Si, *Adv. Control. Chem. Eng. Civ. Eng. Mech. Eng.* (2010) 227–231.
- [11] G.K. Williamson, R.E. Smallman, III. Dislocation densities in some annealed and cold-worked metals from measurements on the X-ray debye-scherrer spectrum, *Philos. Mag.* 1 (1956) 34–46.
- [12] V.D. Mote, Y. Purushotham, B.N. Dole, Williamson-Hall analysis in estimation of lattice strain in nanometer-sized ZnO particles, *J. Theor. Appl. Phys.* 6 (2012) 1–8.
- [13] T. Ekstrom, C. Chatfield, W. Wruss, M. Maly-Schreiber, The use of X-rays diffraction peak-broadening analysis to characterise ground Al₂O₃ powders, *J. Materials Sci.* 20 (1985) 1266–1274.
- [14] L. Hosseinzadeh, J. Baedi, A.K. Zak, X-ray peak broadening analysis of Fe₅₀Ni₅₀ nanocrystalline alloys prepared under different milling times and BPR using size strain plot (SSP) method., *Bull. Mater. Sci.* 37 (2014) 1147–1152.
- [15] V.S. Vinila, R. Jacob, A. Mony, H.G. Nair, S. Issac, S. Rajan, A.S. Nair, J. Isac, XRD Studies on Nano Crystalline Ceramic Superconductor PbSrCaCuO at Different Treating Temperatures, *Cryst. Struct. Theory Appl.* 3 (2014) 1–9.
- [16] N. Revathi, P. Prathap, Y.P. V Subbaiah, K.T. Ramakrishna Reddy, Substrate temperature dependent physical properties of In₂S₃ films, *J. Phys. D. Appl. Phys.* 41 (2008) 155404.
- [17] T. Ericsson, Residual stresses caused by thermal and thermochemical surface treatments, in: A. Niku-Lari (Ed.), *Adv. Surfaces Treat. Technol.*, 1st ed., Pergmon press, New York, 1987: pp. 87–113.
- [18] K. Nagao, E. Kagami, X-Ray Thin-Film Measurement Techniques VII. Pole Figure Measurement, *Rigaku J.* 27 (2011) 6–14.
- [19] J.P. Enríquez, X. Mathew, Influence of the thickness on structural, optical and electrical properties of chemical bath deposited CdS thin films, *Sol. Energy Mater. Sol. Cells.* 76 (2003) 313–322.
- [20] K.H. Kim, J.S. Chun, X-ray studies of SnO₂ prepared by chemical vapour deposition, *Thin Solid Films.* 141 (1986) 287–295.

- [21] H.R. Moutinho, F.S. Hasoon, F. Abulfotuh, L.L. Kazmerski, Investigation of polycrystalline CdTe thin films deposited by physical vapor deposition, close-spaced sublimation, and sputtering, *J. Vac. Sci. Technol. A.* 13 (1995) 2877–2883.
- [22] A.X.S. Bruker, TOPAS, Version 4.2, Bruker AXS, Karlsruhe, Ger. (2009).
- [23] J. Goldstein, D.E. Newbury, P. Echlin, D. Joy, D.R.J. Alton, C. Lyman, F. Charles, E. Lifshin, *Scanning electron microscopy and x-ray microanalysis: A Text for Biologists, Materials Scientists, and Geologists*, 2nd ed., Plenum, New York, 1984.
- [24] J. Kuo, *Electron microscopy: Methods and protocols*, 2nd ed., Humana Press, New Jersey, 2007.
- [25] D. Vaughan, *Energy-dispersive X-ray microanalysis: An introduction*, Kevex Instruments, Middleton, 1999. <http://www.noran.com>.
- [26] B. Hafner, *Energy Dispersive Spectroscopy on the SEM: A Primer*, Charact. Facil. Univ. Minnesota. (2006) 7–10.
- [27] P.M. Martin, *Handbook of deposition technologies for films and coatings: science, applications and technology*, William Andrew, 2009.
- [28] R.L. McCreery, *Raman spectroscopy for chemical analysis*, John Wiley & Sons, New York, 2005.
- [29] Raman spectroscopy basics, Princet. Instruments. (2012) 1–5. www.piacton.com (accessed January 30, 2016).
- [30] J.R. Ferraro, K. Nakamoto, C.W. Brown, *Introductory Raman Spectroscopy*, Academic press, San Diego, 2012.
- [31] H.J. Butler, L. Ashton, B. Bird, G. Cinque, K. Curtis, J. Dorney, K. Esmonde-white, N.J. Fullwood, B. Gardner, P.L. Martin-hirsch, M.J. Walsh, M.R. Mcainsh, N. Stone, F.L. Martin, Using Raman spectroscopy to characterize biological materials Using Raman spectroscopy to characterize biological materials, *Nat. Protoc.* 11 (2016) 664–687.
- [32] G.S. Bumrah, R.M. Sharma, Raman spectroscopy – Basic principle, instrumentation and selected applications for the characterization of drugs of abuse, *Egypt. J. Forensic Sci.* 6 (2016) 209–215.
- [33] D.L. Andrews, A.A. Demidov, *An introduction to laser spectroscopy*, 2nd ed., Springer Science & Business Media, New York, 2002.

- [34] Theory of Raman Scattering - B&W Tek. <http://bwtek.com/raman-theory-of-raman-scattering/> (accessed August 1, 2017).
- [35] E. Smith, G. Dent, *Modern Raman Spectroscopy - A Practical Approach*, 2005.
- [36] M.J. Pelletier, *Analytical applications of Raman spectroscopy*, Wiley-Blackwell, 1999.
- [37] J.R. Ferraro, *Introductory raman spectroscopy*, Academic press, 2003.
- [38] I.R. Lewis, H. Edwards, *Handbook of Raman spectroscopy: from the research laboratory to the process line*, CRC Press, 2001.
- [39] L.D. Hanke, *Handbook of analytical methods for materials*, Materials evaluation and engineering Inc, Plymouth, 2001. <http://www.mee-inc.com>.
- [40] K.D.D. Vernon-Parry, *Scanning electron microscopy: an introduction*, III-Vs Rev. 13 (2000) 40–44.
- [41] S.J.B. Reed, *Electron microprobe analysis and scanning electron microscopy in geology*, 2nd ed., Cambridge University Press Cambridge, New York, 2005.
- [42] C. Suryanarayana, *Experimental Techniques in Materials and Mechanics*, CRC Press, New York, 2011.
- [43] E.N. Kaufmann, *Characterisation of materials*, 2nd ed., John Wiley & Sons, New York, 2012.
- [44] I. Hampshire Material Laboratory, *Scanning Electron Microscopes (SEM)*, (1998).
- [45] M.A. Sutton, N. Li, D.C. Joy, A.P. Reynolds, X. Li, *Scanning electron microscopy for quantitative small and large deformation measurements part I: SEM imaging at magnifications from 200 to 10,000*, *Exp. Mech.* 47 (2007) 775–787.
- [46] C.E. Lyman, D.E. Newbury, J. Goldstein, D.B. Williams, D.R.J. Alton, J. Armstrong, P. Echlin, C. Fiori, D.C. Joy, E. Lifshin, K.R. Peters, *Scanning electron microscopy, X-ray microanalysis, and analytical electron microscopy: a laboratory workbook*, Plenum Press, New York, 1990.
- [47] M. Joshi, A. Bhattacharyya, S.W. Ali, *Characterization techniques for nanotechnology applications in textiles*, *Indian J. Fibre Text. Res.* 33 (2008) 304–317.
- [48] V.S. Ramachandran, J.J. Beaudoin, *Handbook of analytical techniques in concrete science and technology: principles, techniques and applications*, Elsevier Science, New York, 2001.

- [49] JEOL USA Inc., Scanning Electron Microscope A to Z: Basic knowledge for using the SEM., JEOL USA Electron Opt. Doc. (2009). www.jeolusa.com (accessed February 15, 2015).
- [50] CCWJ Teaching, <https://sites.ualberta.ca/~ccwj/teaching/microscopy/> (accessed August 1, 2017).
- [51] M.T. Postek, The scanning electron microscope, in: J. Orloff (Ed.), *Handb. Charg. Part. Opt.*, CRC Press, New York, 1997: pp. 363–399.
- [52] I.M. Watt, *The principles and practice of electron microscopy*, 2nd ed., Cambridge University Press, New York, 1997.

CHAPTER 6

EQUIPMENT FABRICATION AND CONSTRUCTION

Prior to the design of the CVD system for the deposition of ZrC layers, a thermodynamic analysis was carried out. This was done in order to establish the feasibility of the chemical reactions of the reactants at room temperature and at elevated temperatures. The results of this analysis were used as guidelines for the selection of the appropriate materials for the construction of the reactor system. The precursor compounds for ZrC were $ZrCl_4$ and CH_4 , as zirconium and carbon sources, respectively. The feasibility of the chemical reaction is predicted by the change in the Gibbs free energy. When the Gibbs free energy of the reaction is negative, the reaction is feasible under the given conditions [1]. The Gibbs free energy of the reaction and the corresponding equilibrium thermodynamic constant were calculated. The results are discussed in Chapter 7 of this thesis. HSC Chemistry software (a thermochemical software package) [2] was also used to show the speciation of the reactants with temperature. Based on the results of the thermodynamic analysis, deposition temperatures ranging from 1200 °C to 1600 °C were selected.

6.1 Design and fabrication of the CVD system

In this study a vertical-wall thermal CVD system, as indicated in Figure 6-1, was developed in-house at Necsa. The detailed Standard Operating Procedures (SOP) for this equipment were developed and are given in Appendix I. The process parameters and reactor geometry were engineered so as to control the growth and quality of ZrC layers. The main components required for the fabrication and construction of the CVD system were strategically designed, selected and assembled with careful planning and adherence to engineering principles. The CVD system was constructed with components that can accommodate the high substrate

temperatures for ZrC growth, even beyond 1700 °C, and the very reactive and hazardous deposition gases (ZrCl₄, methane and hydrogen).

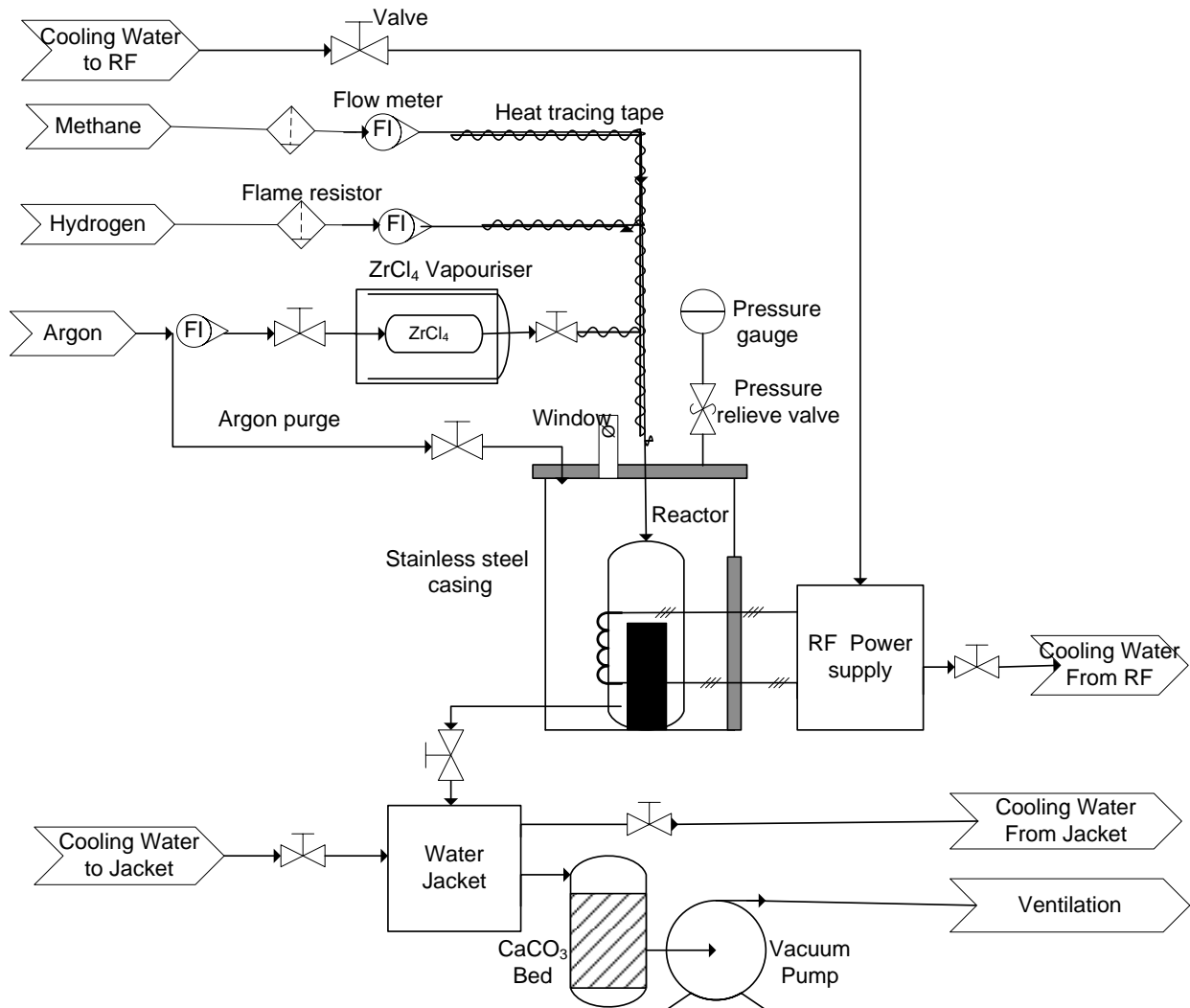


Figure 6-1: Piping and instrumentation diagram of the CVD reactor assembly.

This in-house-built CVD system consisted of four basic components. These were:

- (i) The gas supply and delivery system (including ZrCl₄ vaporiser system)
- (ii) An RF Power supply system and the induction coil
- (iii) The reactor system (including the graphite reaction chamber), and
- (iv) The exhaust/scrubber system

6.1.1 Power supply system

An RF induction heating source with maximum power output of 10 kW was used. This RF power supply model EASYHEAT LV AT 8310 was manufactured by Ambrell, Ameritherm Inc, USA. It was connected to a copper tubing induction heating coil. The copper coil was water cooled to prevent it from melting and reduce internal heat losses. The gap between the four-turn helical copper coils and the graphite reaction chamber was kept to a minimum to ensure good RF coupling with the coil. This distance was sufficient to accommodate the thermal insulation (using ceramic material) to reduce heat transfer from the heated graphite reaction chamber to the coil. The ceramic material also secured the graphite reaction chamber at the centre of the coil in a fixed position. When the material to be heated is placed close to the coil, there is increased current flow, which raises the amount of heat induced in that material. To achieve uniform heating it is required that the coupling distance C_d should be equal but not more than twice the coil pitch [3], since heating effects also depends on the pitch of coil windings. The coupling distance was estimated using Equation (6-1);

$$C_d = \frac{D_{in} - d_g}{2} \quad (6-1)$$

where D_{in} is the inner diameter of the coil and d_g is the diameter of the graphite reaction chamber (acting as the work piece). Table 6-1 gives a summary of the specifications of the coil used. To ensure maximum uniform heating, the effective heating length of the coil on the graphite reaction chamber was estimated using Equation (6-2) [4] and was found to be 6.34 cm:

$$h_g = N(d_c + C_p) \quad (6-2)$$

Here h_g is the portion of the length of the cylindrical graphite tube with maximum heating, C_p is the pitch of the coil winding, d_c is the diameter of conductor (copper tubing) and N is number of coil turns able to produce maximum uniform heating on about 6.34 cm of the

length of the graphite reaction chamber. The inductance of this coil was calculated using Wheeler's formula [5] given in Equation (6-3) and was found to be 0.832 μH .

$$L = \frac{D^2 N^2}{9D + 10l} \quad (6-3)$$

Here L is the coil inductance, N is the number of turns, D and l is the diameter and length of the coil in inches, respectively.

Table 6-1: Coil design specifications.

Specification	Design value
Material	Copper
Coil type	Helical (round)
Number of turns	4
Inner diameter (cm)	5.1
Outer diameter (cm)	6.38
Diameter of the coil tubing (cm)	0.64
Coil length (cm)	3.60
Coil pitch (cm)	0.945
Coupling distance (cm)	0.80
Gap between the windings	0.305
Coil inductance (μH)	0.832

6.1.2 Power supply calibration

As already mentioned, the required temperatures for the growth of ZrC layers from ZrCl_4 and methane were predetermined by a thermodynamic analysis (see Chapter 7). The results indicated that the growth of ZrC is realised at temperatures above 1000 $^\circ\text{C}$. Therefore, a suitable power supply with the capability of generating these temperatures was secured. The power-temperature calibration was carried out before the actual ZrC deposition experiments were conducted. During power-temperature calibration, the substrates were loaded in the reaction chamber and only argon was used to maintain a similar environment as that during deposition. The substrate temperatures were measured by an infra-red optical pyrometer through a quartz viewing window at the top of the flange (see Figure 6-1). The pyrometer readings were recorded while the graphite reaction chamber top-lid was open, in order to

measure the actual temperature of the substrates. The power calibration experiments were carried out five times and the average temperature values were considered to avoid errors which may arise from the pyrometer readings. This is because the pyrometer readings also depended on how well it was focused on the hottest part of the heated material through the window of the reactor. The pyrometer readings with respect to the power supplied and the current are given in Table 6-2.

Table 6-2: RF Power Supply settings and the temperature generated

Power output (W)	Current (A)	Substrate Temperature (°C)
1463	42	1090
1650	44	1151
1843	46	1256
2031	48	1311
2241	50	1369
2472	52	1409
2633	54	1468
2848	56	1537
3056	58	1599
3276	60	1637
3530	62	1689
3734	64	1720

These average values were used to plot a graph of power supplied and resulting temperature, as shown in Figure 6-2. The plot in Figure 6-2 was used to set the approximate ‘final’ substrate temperature for the deposition of ZrC layers. During the deposition of ZrC, the top-lid of the graphite reaction chamber was closed, to avoid contamination of the ZrC layer and to ensure all the inlet gases reach the substrate. Therefore, the power output of the RF power supply was set at a value corresponding to the desired substrate temperature in line with the power-temperature calibration data given in Figure 6-2.

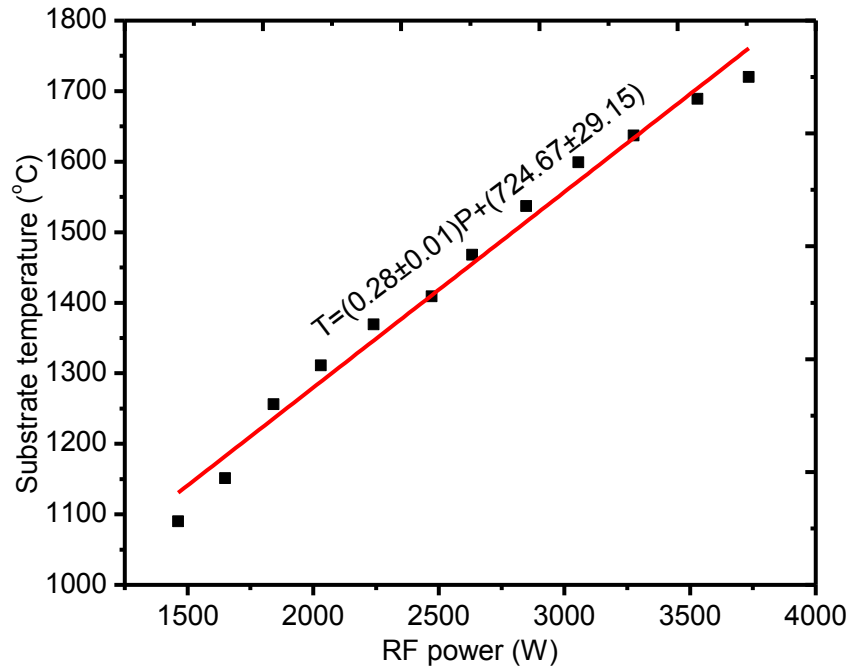


Figure 6-2: The RF power supply calibration curve.

6.1.3 The CVD reactor system

The CVD reactor system shown in Figure 6-1 was fabricated and constructed at Necsas as already mentioned. The elbow stainless steel outer casing and the graphite reaction chamber are among the many components.

The stainless steel reactor casing was made 420 mm high with an internal diameter of 237 mm. The thickness of its walls was 27 mm. Figure 6- gives the physical layout of the reactor system, indicating the dimensions of the components. The schematic of the CVD reaction chamber system showing its parts is given in Figure 6-4 (cross section) and Figure 6-5 (physical layout). One of the roles of the stainless steel outer casing was to confine the corrosive exit gases and enable safe extraction.

6.1.3.1 The stainless steel reactor casing

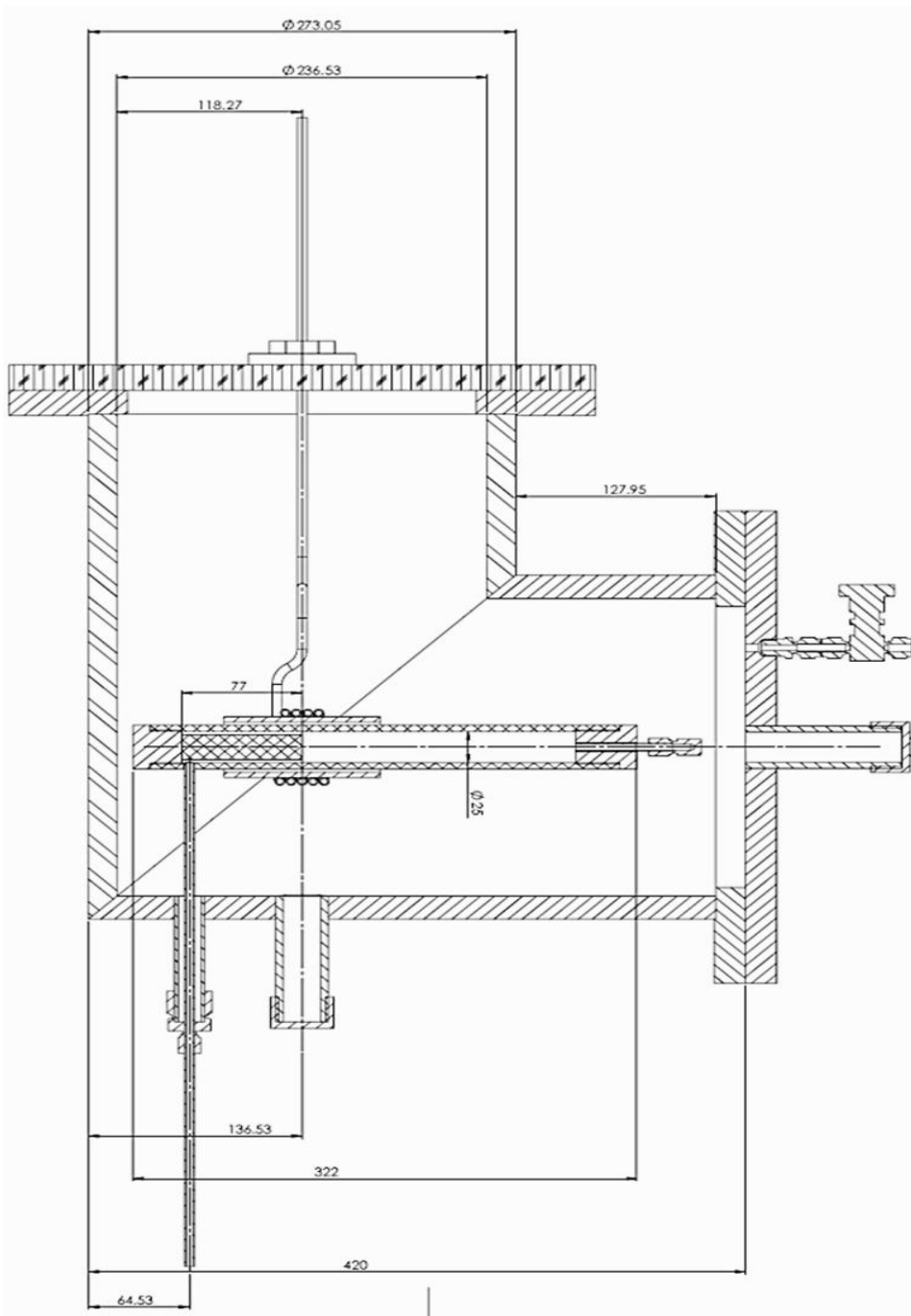


Figure 6-3: Dimensional schematic layout of the reactor system. All dimensions are in millimetres

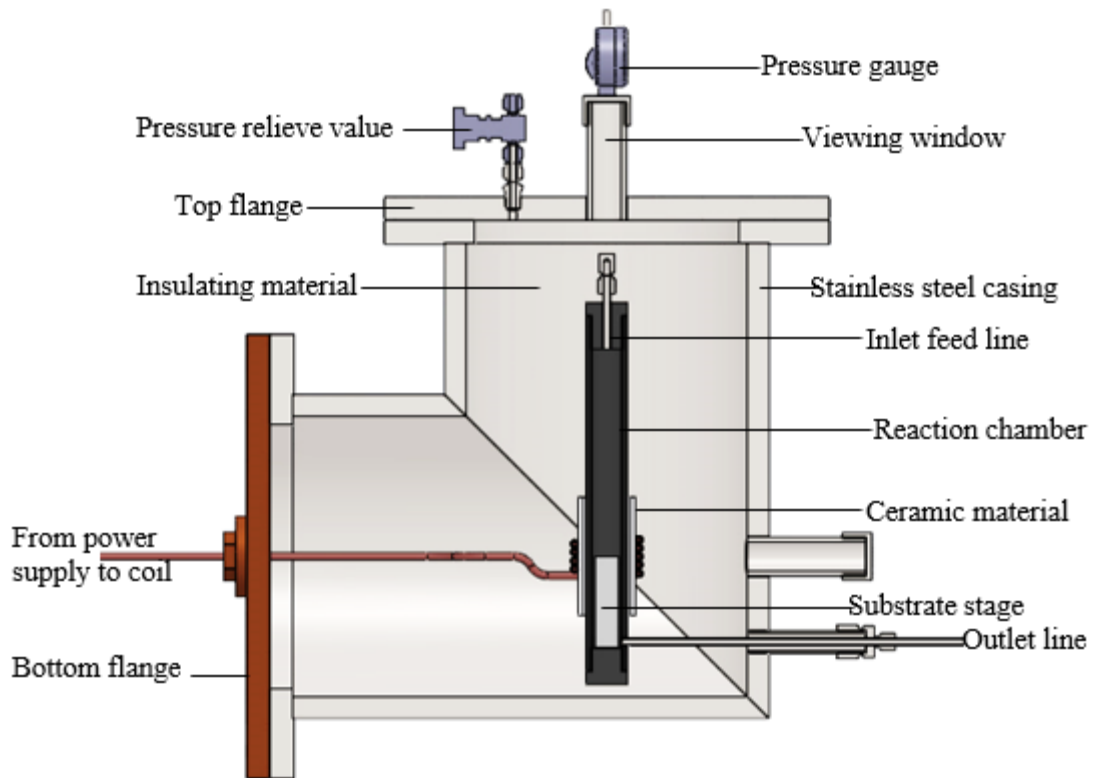


Figure 6-4: The cross section of the reactor system.

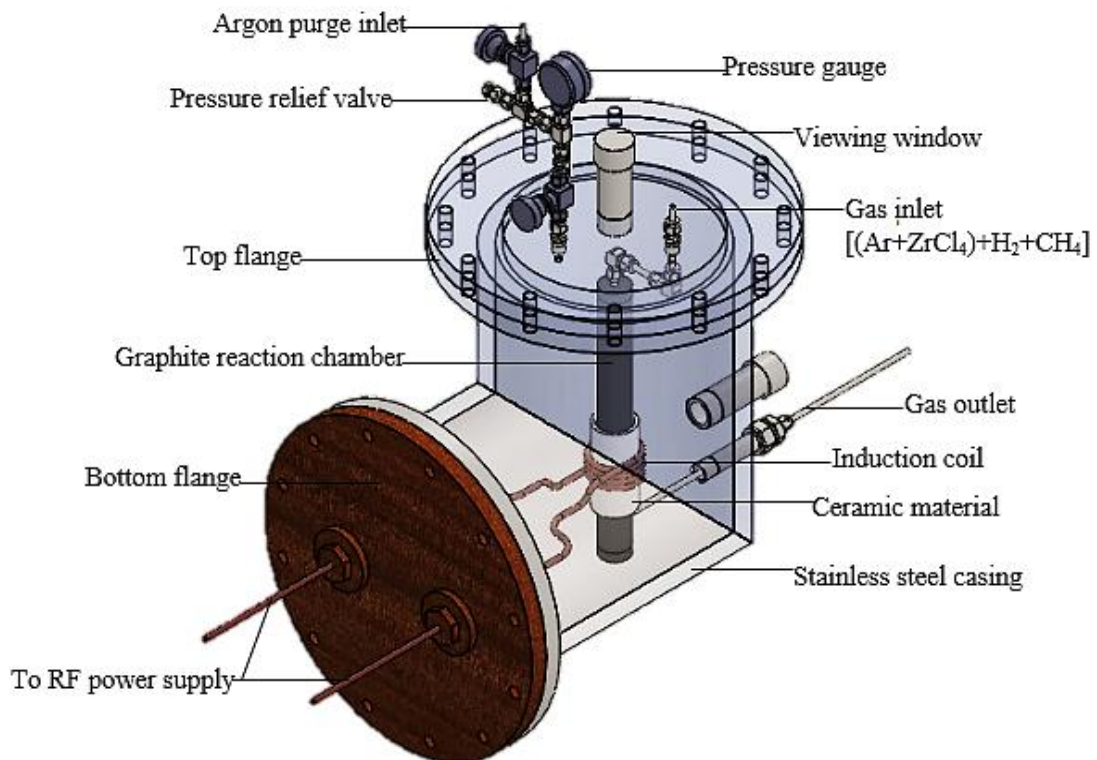


Figure 6-5: Schematic of the physical layout of the CVD reactor system.

6.1.3.2 The graphite tube reaction chamber

The cylindrical high density grade graphite tube manufactured by Le Carbone-Lorraine had an inner diameter of 2.5 cm and a length of 30 cm. This type of graphite is denoted “anode carbon” or “carbon 20/20”. The cylindrical graphite tube (reaction chamber) together with a substrate stage made of the same material attached at its bottom end were fixed inside the steel casing, as shown in Figure 6-4 and Figure 6-5. The 74.1 g solid cylindrical graphite substrate stage had a length of 13.5 cm and diameter of 2.2 cm. The graphite tube was at the same time used as the work piece for induction heating to attain the required temperature for the substrates (1200 °C up to 1700 °C for this experiment). Table 6-3 gives a summary of the material specifications and properties of the graphite tube that was used in this study.

Table 6-3: Reaction chamber material specification.

Specification	Design value
Material	Graphite
Purity	100.00%
Thermal conductivity ($\text{Wm}^{-1}\text{°C}^{-1}$)	8.5
Coefficient of thermal expansion (°C^{-1})	4.3×10^{-6}
Inner diameter (cm)	2.5
Outer diameter (cm)	3.5
Length (cm)	30
Density (gcm^{-3})	1.77
Grain size (μm)	15
Porosity	9%

The graphite tube was equipped with leads on both ends, i.e. the gas inlet at the top and outlet at the bottom. The gas inlet and outlet permitted the flow of the gases past the heated substrates mounted on the substrate stage. The distance from the inlet to the substrate stage varied between 70 mm and 170 mm. Zirconia wool was used as an insulator for both heat and electricity and was placed between the steel casing and the graphite reaction chamber.

6.1.4 The gas delivery system

The gas delivery system comprised of three separate pressurised cylinders (methane, argon and hydrogen cylinders) fitted with pressure gauges and flow meters. The precursors used in deposition of ZrC were anhydrous zirconium tetrachloride powder (purity > 99.5%; Hf < 50 mg kg⁻¹ manufactured by Sigma-Aldrich (Pty) Ltd) and methane (CH₄, 99.99% pure). ZrCl₄ was carried from the vaporisation chamber to the reaction chamber by argon (Ar, 99.999% pure). Hydrogen gas (H₂, 99.999% pure) was used to provide a reducing and diluting environment for the ZrCl₄ vapour and the HCl effluent. Argon was also used to flush the reactor by continuously (4 times before each deposition) pressurising and depressurising it in order to remove air (oxygen) and atmospheric moisture. Methane, hydrogen and argon volumetric flow rates were manually controlled by pre-calibrated flow meters and directed into the reaction chamber as shown in Figure 6-1. The deposition was carried out at atmospheric pressure (which was about 87 kPa absolute at location).

The flow meters were calibrated at room temperature and atmospheric pressure using the Gilian Gilibrator-2 NIOSH Primary Standard Air Flow Calibrator. The purity of the gases was tested using a tripple quadrupole gas chromatography mass-spectrometry (GC-MS) system. Argon was passed through the vaporiser loaded with ZrCl₄ powder so that it could carry ZrCl₄ vapour to the reaction chamber at the required flow and proportion. The feed pipes made of stainless steel carrying hydrogen, methane and ZrCl₄ (under argon) were joined together and then fed into the reaction chamber. To avoid ZrCl₄ agglomerating and clogging the inlet pipe, the feed pipes were heated to 300 °C (ZrCl₄ vaporiser temperature) by an electric heat tracing tape. The pipes were also covered with heat insulating material (zirconium wool) so as to avoid heat losses to the surroundings. Argon was also used as a purge gas and to stabilise the total reactor pressure.

6.1.5 The $ZrCl_4$ vaporisation system

The control and transport of $ZrCl_4$ vapour into the reaction chamber are crucial for the production of ZrC with the desired stoichiometry and morphology. $ZrCl_4$ was first vaporised in the vaporisation system and the vapour was continuously swept to the reaction chamber using argon carrier gas. $ZrCl_4$ was vaporised to the required vapour pressure in order to optimise the growth characteristics of the ZrC layers. Several studies have been conducted on the CVD growth of ZrC from zirconium halides. It has been noted that $ZrCl_4$, as opposed to other halides such as $ZrBr_4$ and ZrI_4 , produces ZrC with relatively good stoichiometry, and is less toxic and relatively more volatile [6]. That is the reason it was selected as a precursor for this study. The physical properties of $ZrCl_4$ are listed in Table 4-2 (Chapter 4).

The $ZrCl_4$ vaporisation system consisted of an oven heated to 300 °C (just below its phase transition temperature at 331 °C) and a cylindrical steel vessel, 24.6 cm long with inner diameter of 4.3 cm. The loaded cylindrical steel vessel was connected to the inlet pipes, and argon was allowed to sweep through freely. Figure 6- shows the physical layout of the $ZrCl_4$ vaporiser system.

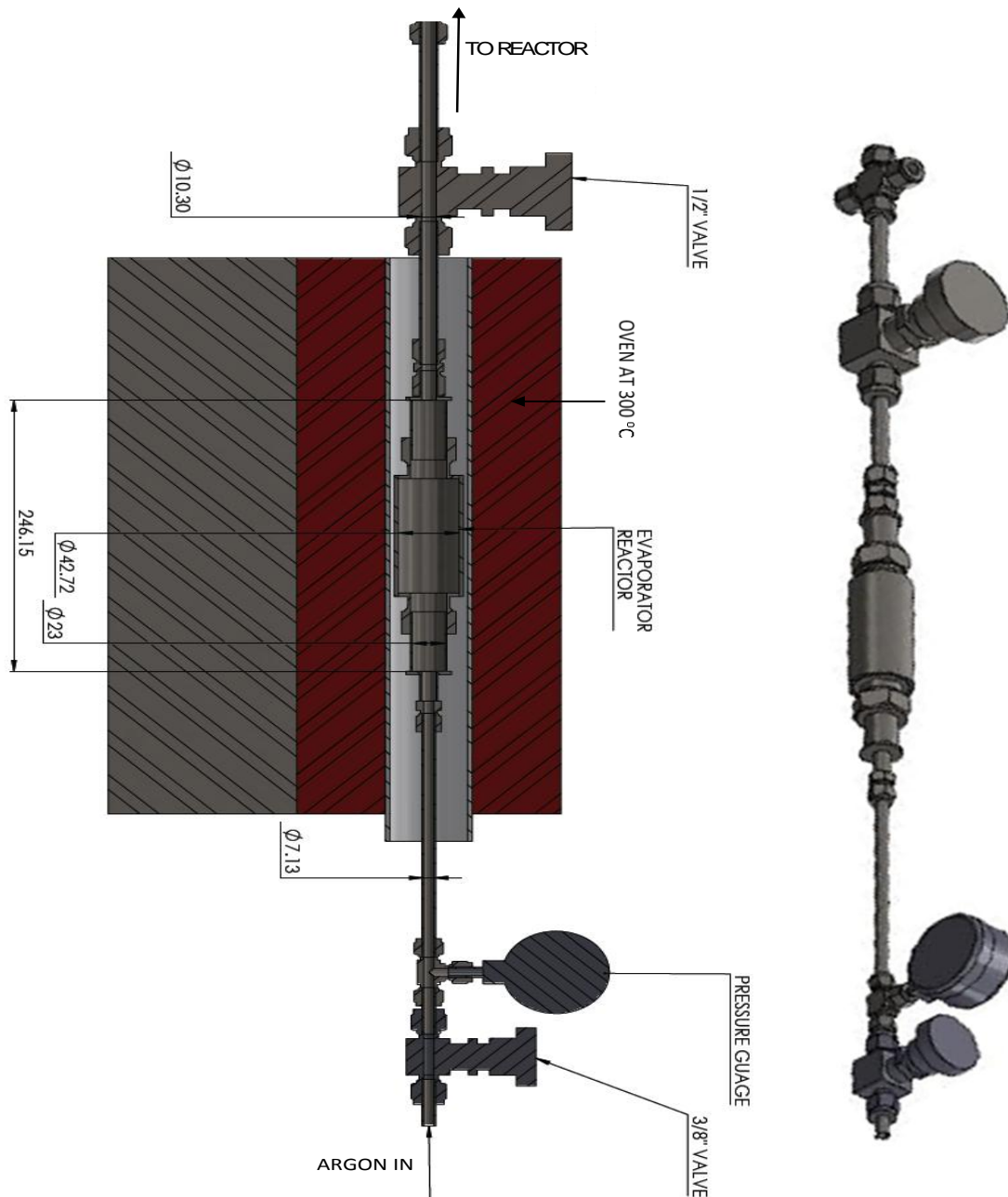


Figure 6-6: Physical layout of the $ZrCl_4$ vaporiser system.

Since $ZrCl_4$ powder is very hygroscopic; precautions were taken to avoid its exposure to atmospheric moisture as far as possible. To determine and optimise the vapour pressure of $ZrCl_4$ for the deposition of ZrC layers, $ZrCl_4$ was heated under vacuum and under argon for 3 minutes at each temperature. Table 6-4 gives the values of the temperature and the corresponding $ZrCl_4$ vapour pressures. Figure 6- shows a plot of the gauge pressure as a function of temperature, measured under vacuum and at argon gauge pressure of 11 kPa.

Table 6-4: Temperature and ZrCl₄ pressure.

T (°C)	Pressure under vacuum (kPa)	Pressure under argon (kPa)
20	0	11
50	1	11
100	5	15
150	9	25
200	20	35
250	36	53
300	54	75
320	95	114
340	110	127
360	116	135
380	118	144
400	121	148

For ZrCl₄ under argon, the total pressure measured was the sum of the ZrCl₄ (vapour) and argon partial pressures. It was observed that the presence of argon in the ZrCl₄ does not change the pressure-temperature trend of ZrCl₄, as shown in Figure 6-. From room temperature up to 150 °C the increase in pressure of ZrCl₄ is small. There is a rapid increase from around 190 °C to about 330 °C. A quick raise in vapour pressure is due to an increase in ZrCl₄ vapour molecules as the temperature is increased [7]. After 330 °C the trend of the curve changed, indicating full sublimation of the ZrCl₄. To avoid full sublimation and have a manageable vapour pressure, a temperature of 300 °C was chosen throughout this study.

The ZrCl₄ vaporisation process was investigated by thermodynamic analysis. It was found that the vaporisation process of ZrCl₄ does not generate other lower halides such as ZrCl₃, ZrCl₂ or ZrCl, as illustrated by Figure 6-. This is because the Gibbs free energies of formation of ZrCl₃, ZrCl₂ and ZrCl are all greater than zero within the experimental conditions.

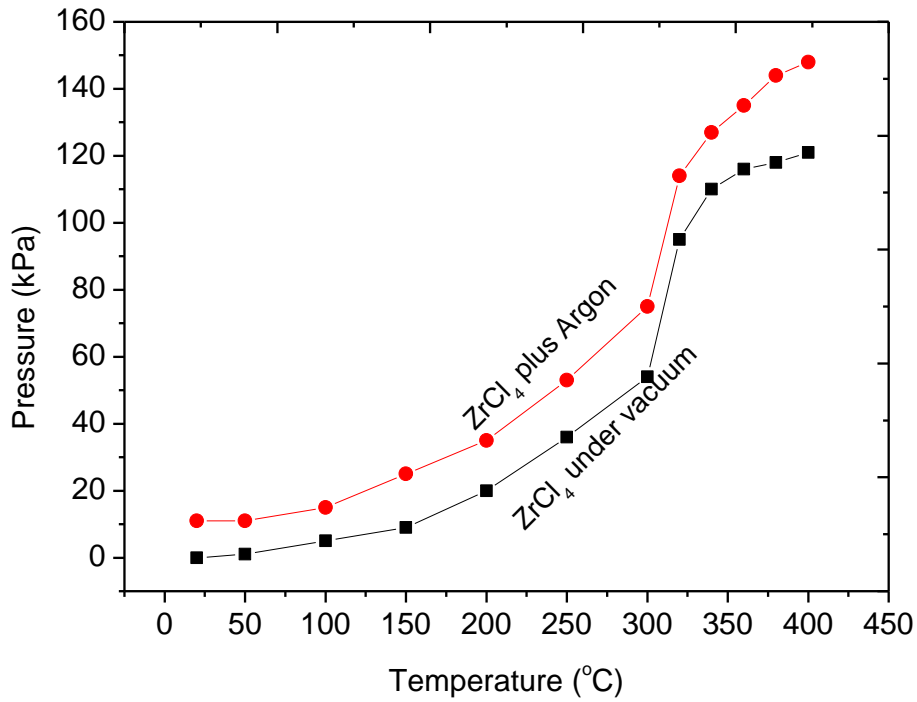


Figure 6-7: variation of $ZrCl_4$ vapour pressure with temperature.

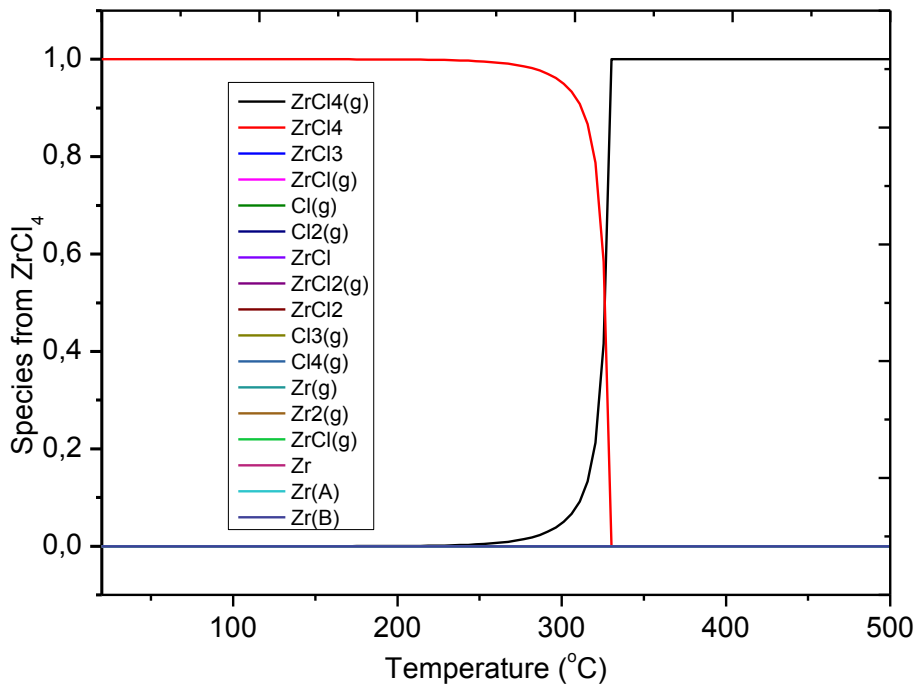


Figure 6-8: Decomposition of $ZrCl_4$.

6.1.6 $ZrCl_4$ mass transfer rate calibration

As mentioned, the $ZrCl_4$ vapour was delivered into the reaction chamber by an argon flow, subsequently mixed with the methane and the hydrogen feed. The vapour pressure and the

mass transfer rate of ZrCl₄ mainly depend on the temperature at which ZrCl₄ is vaporised and the argon flow rate. The mass flow rate of ZrCl₄ was controlled by varying the argon flow rate and keeping the vaporiser temperature at 300 °C. The ZrCl₄ mass transfer rate as a function of argon flow rate is shown in Table 6-5 and Figure 6-. The calibration curve was obtained by flowing argon through the ZrCl₄ powder at different argon flow rates for 20 minutes, and determining the mass difference after each run. The mass transfer rate of ZrCl₄ for each run was determined from Equation (6-4), derived experimentally:

$$\text{ZrCl}_4 \text{ mass transfer rate} = \frac{M_b - M_a}{t} \quad (6-4)$$

where M_b is the mass of the loaded ZrCl₄ vaporiser before vaporisation and argon flow and M_a is the mass of the loaded ZrCl₄ vaporiser after vaporisation and argon flow for time t .

Table 6-5: ZrCl₄ mass flow in argon at 300 °C.

Ar flow rate (sccm)	Mass of ZrCl ₄ loaded in vaporiser (g)		M=(M _b -M _a) (g)	M(g/h)
	before (M _b)	after (M _a)		
100	981.95	981.71	0.24	0.48
200	983.7	983.41	0.29	0.58
300	984.81	984.49	0.32	0.63
400	981.91	981.54	0.37	0.75
500	981.22	980.75	0.47	0.94
600	981.51	981	0.51	1.01
700	982.41	981.84	0.57	1.14
800	981.87	981.23	0.64	1.27

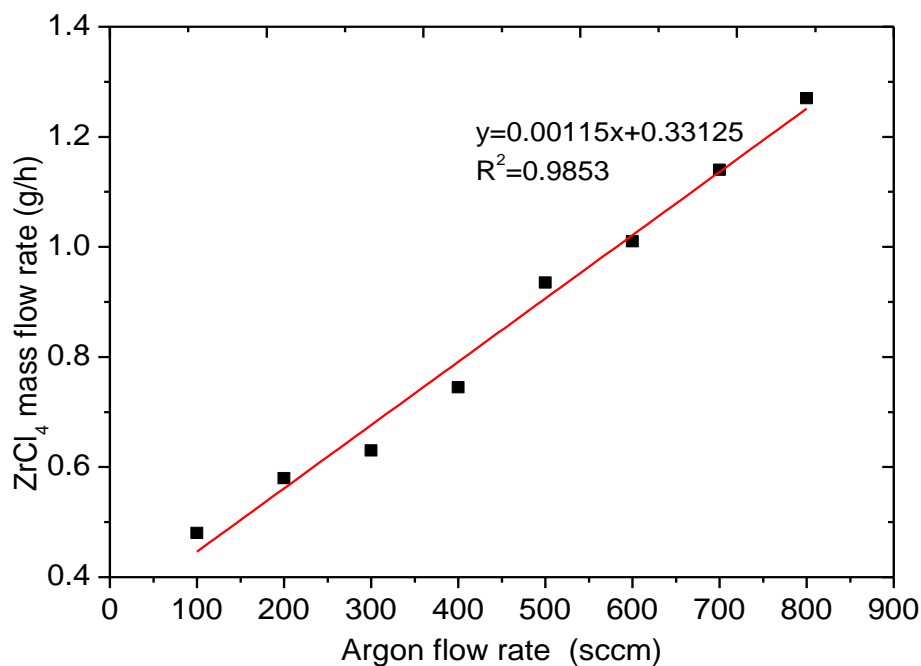


Figure 6-9 Calibration curve of ZrCl₄ mass flow rate in argon.

6.1.7 The exhaust system

The exhaust system was another essential part of the system. It consisted of a vacuum pump, cooling water jacket, scrubber containing calcium carbonate chips (CaCO₃) and extraction ventilation. First of all, the hot exit gases from the reaction chamber were passed through a coiled steel pipe equipped with a cooling water jacket, before entering the scrubber containing calcium carbonate. The reason for passing the exit gases through the calcium carbonate scrubber was to remove hydrogen chloride gas and any unreacted ZrCl₄ before it was released through the extraction system. Within the scrubber, a dust trap was installed to filter the exhaust gases before release into the environment. To regulate the reactor total pressure and to avoid accumulation of the exit gases in the reactor, which may otherwise cause contamination of the deposit, the reactor system was connected to a rotary vane vacuum pump.

6.1.8 Low Flammable limits of Hydrogen and Methane

Hydrogen and methane are explosive and flammable gases, whose flammability are enhanced by high temperature, pressure and the presence of oxygen. Since the experimental environment was operated under all these conditions, caution was taken to curb the associated dangers. For safety and environmental considerations the maximum flow rates of hydrogen and methane that should not be exceeded, were determined. This was based on the minimum concentrations of hydrogen and methane that are necessary to support combustion, referred to as the lower flammable or explosive limit (LFL or LEL). The standard LFL of hydrogen and methane at room temperatures are 4% and 5% by volume, respectively. This implies that below these limits the gases are too “lean” to burn. However, Necsa demands that the hydrogen and methane concentration should be below 20% of their LFL. The ventilation effective volumetric flow rate of air Q , was calculated using Equation (6-5):

$$Q = AV \left(\frac{T_0}{T_v} \right) \left(\frac{P_v}{P_0} \right) \quad (6-5)$$

Here A is the cross sectional area of the extraction ventilation, whose diameter was measured as 10.3 cm, V is the ventilation extraction rate measured as 310 cm/s, $T_v=292$ K and $T_o=273$ K are the temperature of the extraction ventilation and absolute temperature, and $P_v=87$ kPa and $P_o =101$ kPa are the pressure of the extraction ventilation and standard atmospheric pressure, respectively. The effective volumetric flow rate of air Q , was found to be 20660 cm³/s. The maximum methane or hydrogen flow rates (Q_x) that were used for these experiments were 42 cm³/min (~ 0.7 cm³/s) and 870 cm³/min (~14.5 cm³/s). These values were assumed to be the maximum leak rate. Therefore, the percentage methane or hydrogen concentration (C_x) in the extraction was determined from Equation (6-6):

$$C_x = \frac{Q_x}{(Q + Q_x)} 100\% \quad (6-6)$$

The 0.070% and 0.0034% hydrogen and methane concentrations obtained were below the LFL of 4% and 5% for hydrogen and methane, respectively. Therefore the Necsa restriction of the hydrogen and methane concentrations being below 20% of its LFL was also satisfied.

6.1.9 Leak detection

A strong effort was made to reach the required level of vacuum in the reactor system. Another difficult part was to maintain that level of vacuum by minimising leakages. The source of leakages that were monitored included those along the gas supply lines, the reactor system and the exhaust lines. Three methods were used for leak detection. This was done by: (1) pressuring the reactor with argon and leaving it for over two hours, while monitoring the pressure drop, (2) checking the joints with soap bubbles and (3) using a hydrogen leak detector. The leak detection tests were carried out before and during every experiment. When the required minimum leak rate was achieved, the CVD system was considered fit for deposition. In fact, whenever there was a leak, ZrC layers hardly grew on the substrate and when any deposit did occur, the layer uniformity was compromised.

6.2 Substrate Preparation

The substrates of average diameter 10 mm and thickness 2.5 mm were cut from bulk high density (1.71g cm^{-3}) graphite discs. These substrates had the same physical properties as those of the graphite reaction chamber listed in Table 6-3. These graphite substrates were hand polished on a polishing wheel, using 1000 grit silicon carbide paper. They were then sequentially cleaned by ultrasonic agitation in acetone, ethanol and then demineralised water for 20 minutes each. The clean substrates were dried in an oven at 200 °C for 2 hours. The cleaning and polishing was done to remove any oils, oxides and other contaminants. In order to enhance adhesion and reduce the number of impurities in the layer being deposited, the substrates were polished and cleaned. After the cleaning and drying process all the substrates

were weighed to determine the mass of each substrate before deposition. These substrates were then kept in airtight desiccators ready for deposition. Prior to deposition, the substrates were mounted on the clean graphite substrate stage inside the graphite reaction chamber. The substrate stage was cleaned in a similar way to the substrates, to avoid contamination. The substrate stage was positioned such that its top, where the substrates sit, was within the area circumscribed by the induction coil. This was done to maximise and control the temperature.

6.3 References

- [1] X.-T. Yan, Y. Xu, Chemical vapour deposition: an integrated engineering design for advanced materials, 1st ed., Springer-verlag, London, 2010.
- [2] Outotec, HSC Chemistry 7 (Thermo-chemical software), (2007).
- [3] P.G. Simpson, Induction heating: coil and system design, McGraw-Hill, New York, 1960.
- [4] H.P. Wai, S.S. Aung Jr, T. Win, Work Coil Design used in Induction Hardening Machine, Work Acad. Sci. Eng. Technol. 44 (2008) 352–356.
- [5] H. Wheeler, others, Inductance formulas for circular and square coils, Proc. IEEE. 70 (1982) 1449–1450.
- [6] J.H. Park, C.H. Jung, D.J. Kim, J.Y. Park, Temperature dependency of the LPCVD growth of ZrC with the ZrCl₄-CH₄-H₂ system, Surf. Coatings Technol. 203 (2008) 324–328.
- [7] C. Liu, B. Liu, Y.L. Shao, Z.Q. Li, C.H. Tang, Vapor pressure and thermochemical properties of ZrCl₄ for ZrC coating of coated fuel particles, Trans. Nonferrous Met. Soc. China (English Ed. 18 (2008) 728–732.

CHAPTER 7

INVESTIGATING THE GROWTH OF ZrC LAYERS BY CHEMICAL VAPOUR DEPOSITION

The deposition of the ZrC layers was conducted at atmospheric pressure. At the start of every experimental run, a 10 minute interval was taken before taking each reading to allow the temperatures of the substrates and the reaction chamber to reach thermal equilibrium. Several deposition parameters were varied to study their effects on the properties of the ZrC deposited layers. These included (i) substrate temperatures, (ii) CH₄/ZrCl₄ molar ratios, (iii) inlet-substrate gaps, (iv) precursor partial pressures and (v) deposition time.

7.1 Optimisation of the synthesis of ZrC layers in an RF induction-heating CVD system using response surface methodology

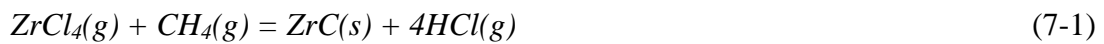
7.1.1 Introduction

This section details the development of a deposition process for the preparation and optimisation of ZrC layers from ZrCl₄-Ar-CH₄-H₂ precursors using induction thermal CVD at atmospheric pressure. The objectives were to: (1) assess the fabricated CVD system, (2) investigate the microstructure and composition of ZrC layers deposited as a function of the input variables and (3) maximise the growth rate and minimise the amount of free carbon in the deposited ZrC layers. To achieve these objectives, a statistical optimisation method to grow ZrC layers in a CVD system using response surface methodology was introduced. This method allows one to determine the deposition parameters for obtaining specific layer properties, e.g. ZrC layers with a specific composition. This has not yet been reported for ZrC layer growth. The ZrC layers were produced by CVD at temperatures ranging from 1200 °C to 1600 °C and CH₄/ZrCl₄ molar ratios from 6.04 to 24.44. The temperature and the CH₄/ZrCl₄ ratio were chosen as the most important variables influencing the properties of

ZrC layers. In order to achieve optimum conditions for growing ZrC layers, a statistical experimental design methodology (central composite design) was applied to explore the effects of these variables [1]. Other deposition conditions such as total reactor pressure, deposition time, reactor geometry, hydrogen flow and carrier gas and its flow were maintained constant throughout the experimental process.

7.1.2 Thermodynamic feasibility of ZrC growth

The overall chemical reaction, considering only reagents and the two main products, is:



The Gibbs free energy of formation and the corresponding equilibrium thermodynamic constant was also calculated from equations (7-2) and (7-3) respectively:

$$\Delta_r G_T^\ominus = \sum (\Delta_f G_T^\ominus)_{\text{product}} - \sum (\Delta_f G_T^\ominus)_{\text{reactant}} \quad (7-2)$$

$$K_T = \exp\left(-\frac{\Delta_r G_T^\ominus}{RT}\right) \quad (7-3)$$

The temperature-dependent values of the Gibbs free energy of formation of methane, zirconium carbide, hydrogen chloride gas and zirconium tetrachloride at atmospheric pressure were obtained from JANAF thermodynamic tables [2,3]. Table 7-1 gives the details of the calculated values of the Gibbs free energy change for the reaction and thermodynamic equilibrium constant for temperatures from 298.15 K to 2000 K at atmospheric pressure.

The Gibbs free energy change for the reaction as a function of temperature, and the corresponding equilibrium constant [4], are shown in Figure 7-1. The Gibbs free energy change at 298.15 K was found to be +311.3 J mol⁻¹ and only becomes zero at 1600.8 K (1327.6 °C). This indicates that the reaction for the production of ZrC is only feasible starting from the temperature of 1600.8 K, since at that temperature $\Delta_r G_T^\ominus < 0$ and $K_T > 1$.

Table 7-1: Gibbs free energy of formation of ZrC and equilibrium thermodynamic constant resulting from the reaction of CH₄ and ZrCl₄ at atmospheric pressure.

T/K	Gibbs free energy (J/mol)				$\Delta_r G^\theta$ (J/mol)	K_T
	CH ₄	ZrCl ₄	ZrC	HCl		
298.15	-50.768	-835.003	-193.282	-95.300	311.289	0.881986
300	-50.618	-834.786	-193.262	-95.318	310.870	0.882817
400	-42.054	-823.139	-192.208	-96.280	287.865	0.917080
500	-32.741	-811.635	-191.299	-97.166	264.413	0.938374
600	-22.887	-800.24	-190.508	-97.985	240.679	0.952898
700	-12.643	-788.929	-189.806	-98.747	216.778	0.963437
800	-2.115	-777.679	-189.168	-99.465	192.766	0.971434
900	8.616	-766.470	-188.570	-100.146	168.700	0.977707
1000	19.492	-755.286	-187.995	-100.799	144.603	0.982758
1100	30.472	-744.113	-187.428	-101.430	120.493	0.986911
1200	41.524	-732.717	-186.635	-102.044	96.382	0.990386
1300	52.626	-721.224	-185.744	-102.644	72.278	0.993335
1400	63.761	-709.755	-184.875	-103.234	48.183	0.995869
1500	74.918	-698.303	-184.023	-103.815	24.102	0.998069
1600	86.088	-686.863	-183.182	-104.388	0.0410	0.999997
1700	97.265	-675.430	-182.349	-104.956	-24.008	1.001700
1800	108.445	-663.996	-181.519	-105.519	-48.044	1.003216
1900	119.624	-652.558	-180.687	-106.077	-72.061	1.004572
2000	130.802	-641.108	-179.849	-106.631	-96.067	1.005794

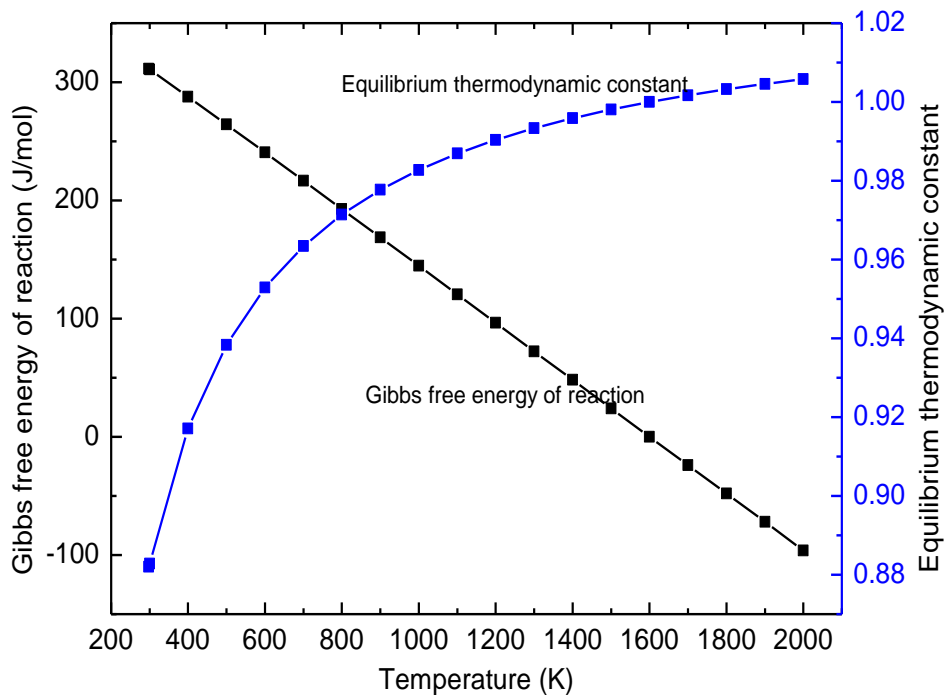


Figure 7-1: Gibbs free energy of formation and equilibrium thermodynamic constant of ZrC.

A more sophisticated thermodynamic approach, taking into account all possible product species, is via the minimisation of the system Gibbs free energy [5]. Figure 7-2 shows speciation results obtained using this method. The software HSC Chemistry [6] was used for this purpose. It is clear from Figure 7-2 that the growth of ZrC is possible at temperatures as low as 900 °C, but higher yields are expected at higher temperatures. The temperature of 1600.8 K (1327.6 °C) in Table 7-1 and Figure 7-1, therefore indicates the equilibrium point of the reactants and the products. The temperature range predicted from the plots in Figure 7-1 and Figure 7-2 is similar to those reported in the literature [7–9].

It should be noted that methane is unstable at temperatures higher than 400 °C (see Figure 7-2), yielding carbon and hydrogen upon decomposition. On the other hand, hydrogen does not reduce ZrCl₄, in the absence of other substances, within this experimental range. The formation of ZrC is thus controlled by the presence of methane, with its decomposition making carbon available for the reaction process. Independent deposition of carbon alone on the substrate is thus possible. The reaction rate of methane with zirconium tetrachloride is strongly influenced by the temperature of the substrate surface. As the temperature increases the chemical reaction is pushed to the region of high yields of ZrC and concomitantly higher degrees of dissociation of ZrCl₄.

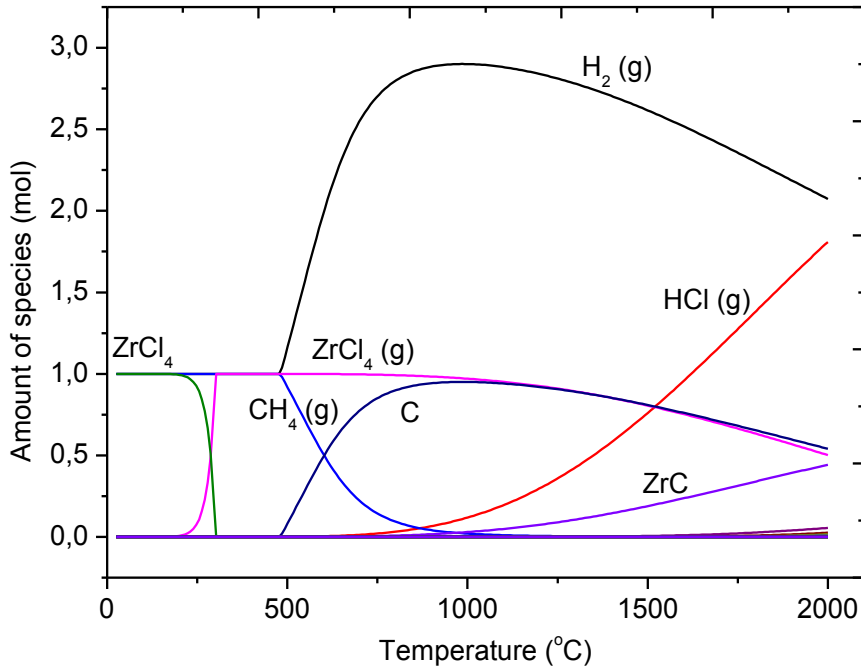


Figure 7-2: Temperature dependence of reactant speciation.

7.1.3 Design of experiments and response surface methodology

Design of experiments (DOE) is a systematic statistical technique for establishing the relationship between factors influencing a process and their output. DOE may be applied when: (1) developing a new process and product, (2) improving and optimising the already existing process and product quality, (3) examining the important process factors, and (4) minimising cost and testing of robustness of both the process and product [10]. For this study, a collection of mathematical and statistical procedures, called response surface methodology (RSM), was applied [1,11]. The effect of the independent variables on the response(s) in question is analysed and modelled [1]. A model of response Y related to two or more independent variables (X_1, X_2, \dots, X_n) is obtained by regression analysis applied to the raw experimental data. A regression equation represents the response Y parametrically in terms of the independent variables, i.e. $Y = f(X_1, X_2, \dots, X_n) \pm \varepsilon$. Equation (7-4) and (7-5) below represent the general expression for linear and quadratic models, respectively:

$$Y = C_0 + C_1X_1 + C_2X_2, \dots, C_nX_n \pm \varepsilon \quad (7-4)$$

$$Y = C_0 + \sum_{i=1}^n C_i X_i + \sum_{i=1}^n C_{ii} X_i^2 + \sum_{j < i} \sum_{i=1}^n C_{ij} X_i X_j + \varepsilon \quad (7-5)$$

Here n is the number of an independent variable, ε is the error or noise, C_0 is a constant, C_{ij} the interaction coefficient, C_i the linear coefficient and C_{ii} the quadratic coefficient. The value and the sign of the coefficients of X in these equations represent the magnitude and trend of the influence of that term on the response. A positive sign of the coefficient in the equation implies an increase in the response and a negative sign a decreasing effect [12]. When the response Y is plotted, a surface (response surface) is generated [13].

The ZrC deposition process was investigated using a central composite design (CCD). Two independent variables (substrate temperature, $X_1=T$) and molar ratio $\text{CH}_4/\text{ZrCl}_4$ ($X_2=M$) were chosen. The experimental design was studied using DESIGN-EXPERT[®] 7.0 [14], a statistical software package. Substrate temperature and molar ratio $\text{CH}_4/\text{ZrCl}_4$ were all studied, each at five levels coded as $-\alpha$, -1 0 1 and α . Figure 7-3 shows the CCD for the two variables. Thirteen experimental points were generated. These included four axial points, four factorial points, and five replicated centre points, as shown in Table 7-2. Coding of levels allows the analysis of input variables having orders of magnitude (or range) difference between them, i.e. this prevents the ones with large values to dominate the lower value ones in the statistical analysis. It involves transforming the actual values of each input variable into dimensionless coordinates (values). Equation 7-6 was applied to transform actual values (X_i) into coded values (x_i) based on the experimental design [15,16]:

$$x_i = \left(\frac{X_i - X_i^o}{\Delta X_i} \right) \alpha \quad (7-6)$$

If in the actual scale the upper value is X_h and the lower value is X_l , then the centre point $X_i^0 = (X_h + X_l)/2$ and the distance between the upper or lower and centre point

$\Delta X_i = (X_h - X_l)/2$. α is the major coded limit value of the experimental matrix. For two input variables $\alpha = \sqrt{2} = 1.41421$ [15].

Table 7-2: Experimental design matrix for the parameters of the CVD experiments.

Exp. Number	Point type	Temperature (°C)	CH ₄ /ZrCl ₄	CH ₄ flow rate (sccm)	H ₂ flow rate (sccm)	Ar flow rate (sccs)	ZrCl ₄ flow (gh ⁻¹)
1	Axial	1400	24.44	43.3	853	562	1.0
2	Axial	1400	6.04	10.7	853	562	1.0
3	Factorial	1541	8.73	15.5	853	562	1.0
4	Factorial	1259	21.75	38.5	853	562	1.0
5	Centre	1400	15.24	27.0	853	562	1.0
6	Axial	1600	15.24	27.0	853	562	1.0
7	Centre	1400	15.24	27.0	853	562	1.0
8	Centre	1400	15.24	27.0	853	562	1.0
9	Centre	1400	15.24	27.0	853	562	1.0
10	Factorial	1259	8.73	15.5	853	562	1.0
11	Factorial	1541	21.75	38.5	853	562	1.0
12	Centre	1400	15.24	27.0	853	562	1.0
13	Axial	1200	15.24	27.0	853	562	1.0

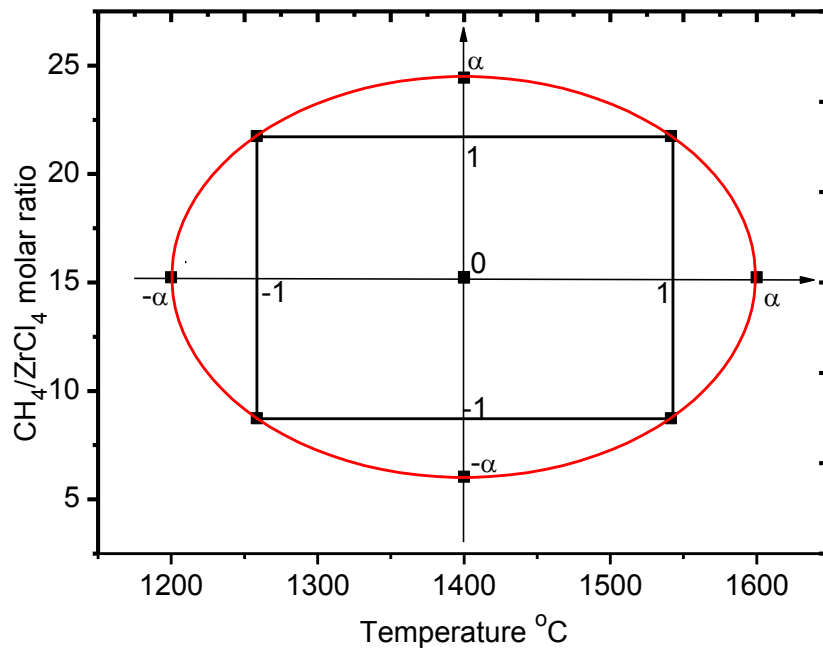


Figure 7-3: The CCD of temperature and CH₄/ZrCl₄ in actual and coded terms.

Growth rate (Y_1), atomic ratio of C/Zr (Y_2) and average crystallite size (Y_3) were selected as dependent variables (responses). For the purpose of analysing the raw data and testing the goodness of fit of the model, an analysis of variance (ANOVA) was implemented. The testing of model adequacy involved testing for significance of the regression model, testing for significance on model coefficients and testing for lack of fit [13]. The p -value, F -value, R -squared, predicted R -squared, and adjusted R -squared values of the statistical tests were used as quality indicators. The model with a p -value (Probability $> F$) less than 0.05 is considered to be statistically significant [1]. R -squared, known as the coefficient of determination, is a measure of variability in the observed response values that can be explained by the experimental independent variables and their interactions. The R -squared value range between 0 and 1 (0% and 100%). The model is regarded very strong and with better prediction of the response when R -squared is close to or equal to 1 [17]. The adjusted R -squared corrects the R -squared value for the sample size and for the number of terms in the model. The closer their values to one another, the better the model is [18]. Another component in assessing the model suitability is the concept “adequate precision”, which compares the range of predicted values at design points to average design error, and measures the signal-to-noise ratio. A value of greater than 4 is acceptable [18].

7.1.4 Growth rate of zirconium carbide

The growth rate Y_1 (change in layer thickness per unit time) was estimated using the mass increase of the substrate. The layer thickness was obtained using Equation (7-7):

$$Y_1 = \frac{M}{tS\rho_{ZrC}} \quad (7-7)$$

Here M is the mass of the layer, S is the surface area of the substrate, ρ_{ZrC} is the density of zirconium carbide (6.59 kg m^{-3}) and t is the deposition time. The use of a constant zirconium carbide density value obviously introduces an error into the calculation of the

growth rate. The values of the growth rate at different substrate temperatures and CH₄/ZrCl₄ molar ratio are presented in Table 7-3.

Table 7-3: Experimental results. The growth rate was determined from Eq. (7-7). The average crystallite size was calculated from the Scherrer formula given in Eq. (5-9). C/Zr is the ratio of the elemental atomic composition determined by EDS.

Run	Factor 1 A:Temperature (°C)	Factor 2 B:CH ₄ /ZrCl ₄ (mol/mol)	Response 1 Growth rate (µm/h)	Response 2 C/Zr (mol/mol)	Response 3 Grain size (nm)
1	1400.0	24.4	9	2.57	21.8
2	1400.0	6.0	5.4	1.05	23.9
3	1541.4	8.7	5	1.06	29.1
4	1258.6	21.7	5.3	1.09	28.4
5	1400.0	15.2	7.6	1.53	31.9
6	1600.0	15.2	8.3	1.88	34.1
7	1400.0	15.2	7.9	1.23	32
8	1400.0	15.2	7.4	1.15	34.2
9	1400.0	15.2	7.2	1.13	33.4
10	1258.6	8.7	4.2	1.03	25.8
11	1541.4	21.7	9.3	1.68	27.8
12	1400.0	15.2	7.9	1.26	32.6
13	1200.0	15.2	3.7	1.08	26.3

From the analysis of the effect of temperature and CH₄/ZrCl₄ on the growth rate by RSM, the best fitted-model was found to be quadratic. The relationship between the growth rate (response Y_1) and the independent variables (temperature and CH₄/ZrCl₄) was represented in actual and coded factors by the regression Equations (7-8a) and (7-8b) respectively.

Table 7-4 presents the ANOVA results for the growth rate of ZrC coatings. This model was also statistically significant with a p -value less than 0.05 (95% confidence). As required the lack-of-fit was non-significant with an F -value and p -value of 4.28 and 0.0969 respectively. The coefficient of determination R -squared and adjusted R -squared values were 96% and 93%, indicating that the regression model gives a good description of the relationship between the temperature and CH₄/ZrCl₄ (independent variables), and the growth rate (response). Therefore this model can be used to navigate the design space reliably.

$$Y_1 = -87.22 + 0.13T - 0.75M + 8.7 \times 10^{-4}TM - 4.81 \times 10^{-5}T^2 - 8.57 \times 10^{-3}M^2 \quad (7-8a)$$

$$Y_1 = 7.60 + 1.41A + 1.31B + 0.80AB - 0.96A^2 - 0.36B^2 \quad (7-8b)$$

Table 7-4: ANOVA quadratic model results for growth rate (response Y1).

Source	Sum of squares	Degrees of freedom	Mean of square	Standard Error	F-value	p-value Prob > F	
Model	39.14	5	7.83	0.12	34.23	< 0.0001	significant
A-Temperature	15.98	1	15.98	0.17	69.88	< 0.0001	
B-CH ₄ /ZrCl ₄	13.76	1	13.76	0.17	60.17	0.0001	
AB	2.56	1	2.56	0.24	11.2	0.0123	
A ²	6.44	1	6.44	0.18	28.19	0.0011	
B ²	0.91	1	0.91	0.18	4	0.0857	
Residual	1.6	7	0.23				
Lack of fit	1.22	3	0.41		4.28	0.0969	not significant
Pure error	0.38	4	0.095				
Corrected total	40.74	12					
Standard deviation = 0.48						R ² =0.9607	
Mean = 6.78						Adjusted R ² =0.9327	
%Coefficient of variation= 7.05						Predicted R ² =0.7724	
Predicted residual error of sums (PRESS)=9.27						Adequate precision=18.85	

Figure 7-4 and Figure 7-5 shows the response surface contour and three dimensional plots illustrating the effects of substrate temperature and CH₄/ZrCl₄ molar ratio on the growth rate. The dots represent the experimental values (given in Table 7-2). The numbers in rectangles denote the values of the response along the given contour given by Equation 7-8. The numerical symbol “5” represents the five replicated centre points. Generally, increasing temperature and CH₄/ZrCl₄ ratio increase the coating growth rate. The effect of temperature on the ZrC growth rate is expected both thermodynamically and from a kinetic viewpoint, since increasing temperature increases the species diffusivities, rates of chemical reaction and promotes adsorption of the active species onto the substrate [4,19]. A high CH₄/ZrCl₄ molar ratio increases the availability of carbon in the reaction zone, which arguably will increase both the nucleation and growth rate.

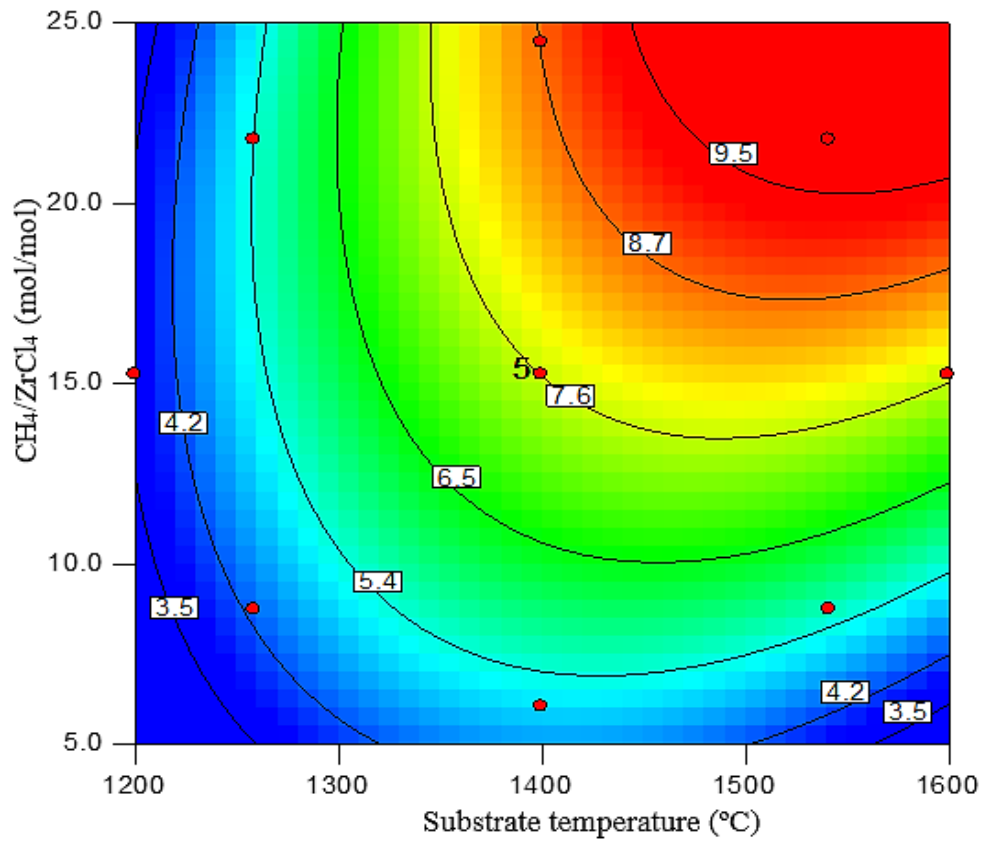


Figure 7-4: The contour plot indicating the effect of substrate temperature and $\text{CH}_4/\text{ZrCl}_4$ ratio on the growth rate of ZrC. The dots and numerical values are explained in the text.

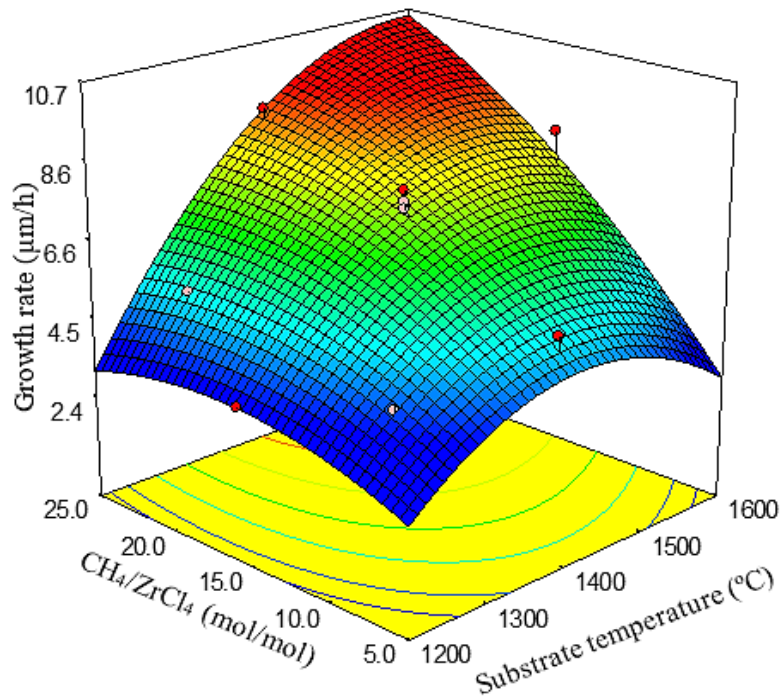


Figure 7-5: The three dimensional plot indicating the effect of substrate temperature and $\text{CH}_4/\text{ZrCl}_4$ ratio on growth rate of ZrC. The dots and numerical values are explained in the text.

7.1.5 Crystallographic structure and phase composition

Figure 7-6 shows typical XRD patterns of ZrC layers deposited at a substrate temperature of 1259 °C for CH₄/ZrCl₄ molar ratio of 8.73 and 21.7 denoted by (a) and (b), respectively. Those deposited at 1541 °C for CH₄/ZrCl₄ of 8.73 and 21.7 are denoted by (c) and (d), respectively. Ten reflections ((111), (200), (220), (311), (222), (400), (331), (420), (422) and (511)) of ZrC layers were observed. These reflections indicate that polycrystalline face-centred cubic structure of the ZrC layers have been deposited when matched with the International Centre for Diffraction Data (ICDD) file number 03.065-8833. As the substrate temperature and the CH₄/ZrCl₄ molar ratio were increased, carbon peaks started to emerge whose intensity increased with increasing temperature and CH₄/ZrCl₄ ratio. EDS analysis showed that the atomic percentage ratio of C/Zr varied from 1.03 to 2.57 as the temperature increased from 1200 °C to 1600 °C at various CH₄/ZrCl₄ ratios, as indicated in Table 7-3.

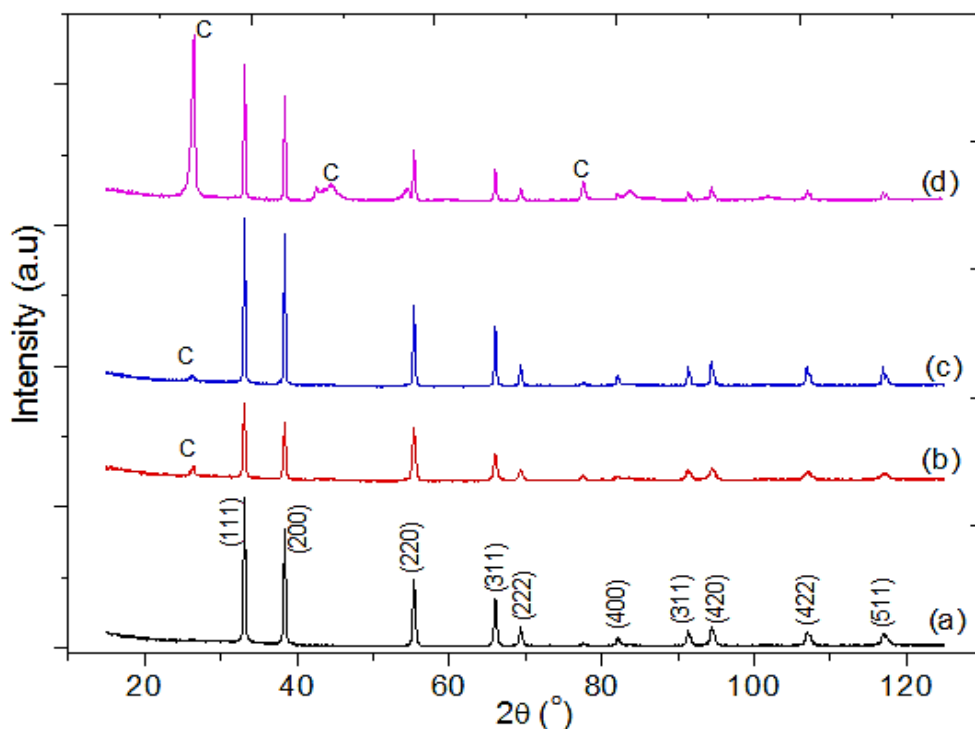


Figure 7-6: Typical XRD pattern for ZrC layers deposited at 1259 °C for a CH₄/ZrCl₄ molar ratio of 8.73 and 21.73 denoted as (a), (b) and those at 1541 °C for CH₄/ZrCl₄ molar ratio of 8.73 and 21.73, denoted as (c) and (d), respectively.

It was observed that at low substrate temperature the increase in CH₄/ZrCl₄ molar ratio did not cause a significant change in C/Zr as compared to higher substrate temperatures (see Figure 7-6).

Table 7-5 gives the ANOVA results for a linear regression model for the atomic ratio of C/Zr. This relationship between the independent variables and the response in terms of actual and coded factors is illustrated by the linear regression Equation (7-9a) and (7-9b) respectively. The model is significant with a *p*-value of less than 0.05 and an F-value of 6.58. The lack-of-fit of the model terms is non-significant, as required. The *R*-squared and adjusted *R*-squared values are 56.83% and 48.20% respectively. The *R*-squared and adjusted *R*-squared values obtained are close to each other, though far from 100%. Since the overall model is significant and lack of fit is non-significant, the *R*-squared value may not affect the interpretation of the relationship between the independent variables (temperature and CH₄/ZrCl₄) and the response (C/Zr).

$$Y_2 = -1.63 + 1.55 \times 10^{-3}T + 0.054M \quad (7-9a)$$

$$Y_2 = 1.36 + 0.22A + 0.35B \quad (7-9b)$$

Table 7-5: ANOVA linear regression model results for C/Zr (response Y₂).

Source	Sum of squares	Degrees of freedom	Mean of square	Standard error	F-value	p-value Prob > F	
Model	1.38	2	0.69	0.090	6.56	0.0150	Significant
A-Temperature	0.38	1	0.38	0.11	3.65	0.0853	
B-CH ₄ /ZrCl ₄	1.0	1	1.00	0.11	9.52	0.0115	
Residual	1.05	10	0.11				
Lack of Fit	0.95	6	0.16		6.15	0.0501	not significant
Pure Error	0.10	4	0.026				
Corrected total	2.44	12					
Standard deviation = 0.32						R ² =0.5683	
Mean = 1.36						Adjusted R ² = 0.4820	
%Coefficient of variation= 23.76						Predicted R ² = 0.1140	
Predicted residual error of sums (PRESS)= 2.16						Adequate precision= 7.352	

The contour plot in Figure 7-7 and the three dimension plot in Figure 7-8 further illustrate the relationship of temperature and $\text{CH}_4/\text{ZrCl}_4$, and the atomic ratio of C/Zr. The same kind of information/notation as in Figure 7-4 was used *mutatis mutandis* in Figure 7-7. There was an increase in C/Zr atomic percentage ratio as both the substrate temperature and $\text{CH}_4/\text{ZrCl}_4$ molar ratio increased. The increase in carbon content may be attributed partly to the differences in the decomposition rates of methane and ZrCl_4 at higher temperatures in the reaction zone. As can be seen from Figure 7-2 methane decomposes into carbon and hydrogen as early as 420 °C. However, Zr-containing species remain in gaseous form throughout the temperature range. This may result in excess carbon in the deposit. The deposition of free carbon leads to an increased C/Zr ratio in the deposited layers and carbon inclusions at high ratios. The presence of free carbon in ZrC layers at elevated deposition temperatures was also reported by Wang et al. [9]. An increase in the $\text{CH}_4/\text{ZrCl}_4$ ratio provides more carbon in the reaction zone, which also leads to increased carbon content in the ZrC layers. Studies have indicated that the properties of ZrC vary with its stoichiometry (C/Zr atomic percentage ratio) [20]. For example, Yang et al. [21] indicated that the C/Zr ratio had a notable effect on the irradiation response of zone-refined ultra-high pure ZrC. They noted that the sub-stoichiometric ZrC samples (C/Zr<1) had an improved irradiation resistant microstructure compared to hyper-stoichiometric ZrC samples (C/Zr>1). Huang et al. [22] reported that ZrC_x material after proton irradiation at 800 °C was highly decorated with dislocation loops. The loop size and density depended both on dose and stoichiometry, with $\text{ZrC}_{1.2}$ showing quite different behaviour compared to the lower C-ratio stoichiometries. Information about the oxidation behaviour for various ZrC stoichiometries is limited. However, in the review by Katoh et al.[20], they speculated that the excess carbon in ZrC can change the oxidation behaviour of ZrC materials. The excess carbon can increase the

production of CO₂, which may increase the chances of inter-crystalline fracture and below normal temperature fracture.

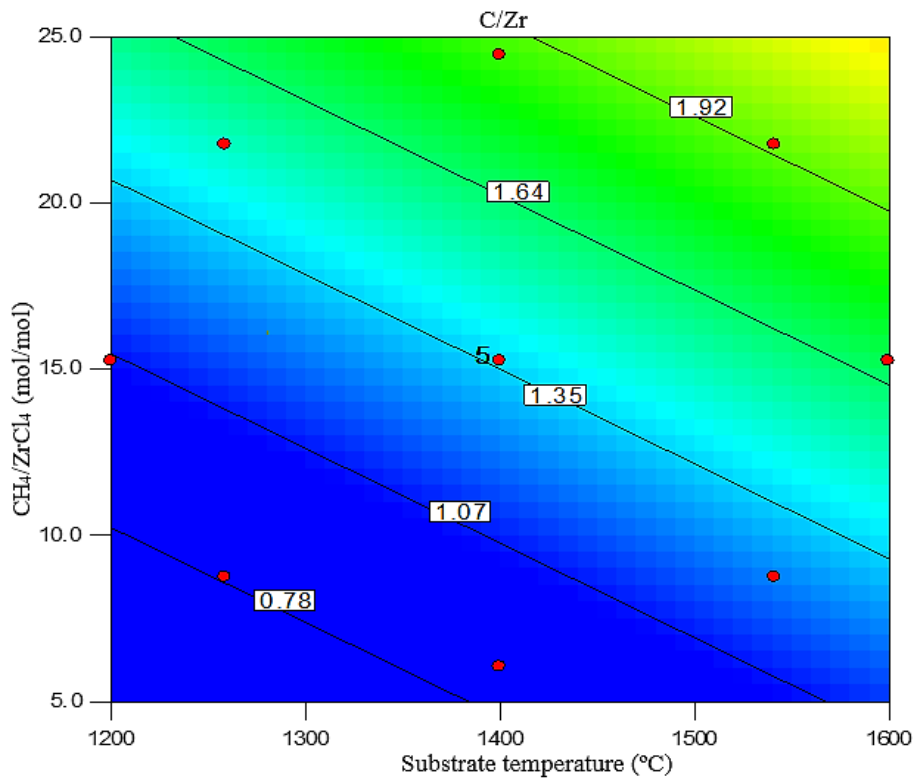


Figure 7-7: The contour plot showing the effect of temperature and CH₄/ZrCl₄ ratio on the C/Zr ratio.

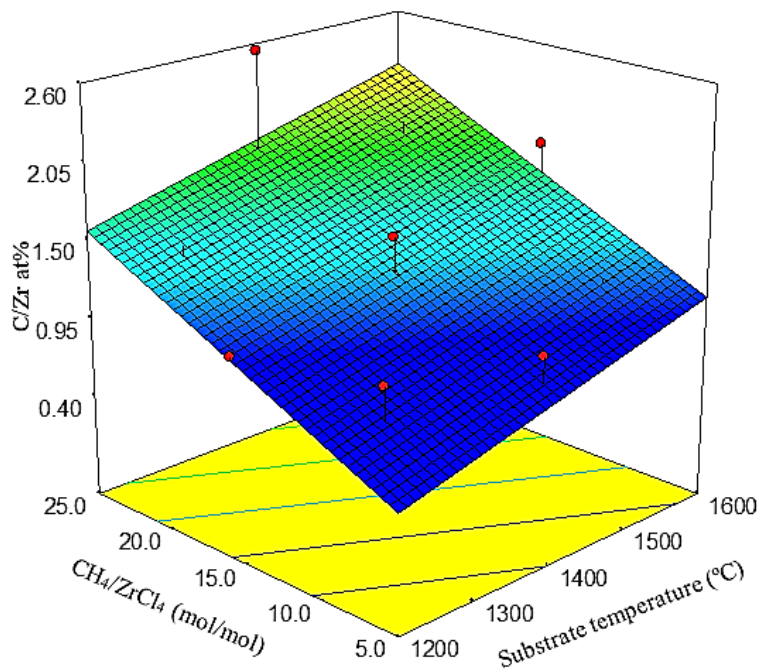


Figure 7-8: The 3-D plot showing the effect of temperature and CH₄/ZrCl₄ ratio on the C/Zr ratio.

7.1.6 Average crystallite size

The average crystallite size, Y_3 was calculated from the Scherrer formula, see Equation (5-9). The crystallite size in polycrystalline materials significantly affects the mechanical properties of the material [23,24]. The average crystallite size varied from 21.8 nm to 34.1 nm as the temperature increased from 1200 °C to 1600 °C at various $\text{CH}_4/\text{ZrCl}_4$ ratios, as indicated in Table 7-2. The execution of RSM produced the regression Equations (7-10a) and (7-10b) that represent the relationship between the average crystallite size and the independent variables in actual and coded factors, respectively. Table 7-6 gives the ANOVA results for the average crystallite size.

$$Y_3 = -129.69 + 0.17T + 4.28M - 1.06 \times 10^{-3}TM - 4.81 \times 10^{-5}T^2 - 8.57 \times 10^{-3}M^2 \quad (7-10a)$$

$$Y_3 = 32.82 + 1.72A - 0.21B - 0.97AB - A^2 - 4.67B^2 \quad (7-10b)$$

Table 7-6: ANOVA quadratic model results for crystallite size (response Y_3).

Source	Sum of squares	Degrees of freedom	Mean of square	Standard error	F-Value	p-value Prob > F	
Model	180.66	5	36.13	0.71	14.14	0.0015	Significant
T-Temperature	23.57	1	23.57	0.57	9.22	0.0189	
M- $\text{CH}_4/\text{ZrCl}_4$	0.35	1	0.35	0.57	0.14	0.7228	
TM	3.8	1	3.8	0.24	1.49	0.262	
T^2	6.92	1	6.92	0.18	2.71	0.1438	
M^2	151.88	1	151.88	0.18	59.44	0.0001	
Residual	17.89	7	2.56				
Lack of fit	14.08	3	4.69		4.93	0.0787	not significant
Pure error	3.81	4	0.95				
Corrected total	198.55	12					
Standard deviation = 1.60						$R^2 = 0.9099$	
Mean = 29.33						Adjusted $R^2 = 0.8456$	
%Coefficient of variation = 5.45						Predicted $R^2 = 0.4658$	
Predicted residual error of sums (PRESS)=106.07						Adequate precision = 9.275	

A quadratic model was found to be statistically significant. The model's corresponding p-value is less than 0.05 (95% confidence). The lack-of-fit is not significant as can be seen from the F-value and p-value of 4.93 and 0.0787, respectively. The R-squared and adjusted R-squared values are 91% and 85%, indicating that the regression model gives a good

description of the relationship between the temperature and $\text{CH}_4/\text{ZrCl}_4$ (independent variables), and the crystallite size (response).

To fully describe the interactions and the quadratic effect of the temperature and $\text{CH}_4/\text{ZrCl}_4$ on crystallite size, the response surface analyses was plotted in a contour and a three dimensional graph given in Figure 7-9 and Figure 7-10, respectively. Again, the same kind of information/notation as in Figure 7-4 was used *mutatis mutandis* in Figure 7-9.

It can be observed that the average crystallite size increases as the temperature and $\text{CH}_4/\text{ZrCl}_4$ ratio increase. This is because increasing temperature increases atomic mobility, which favours crystal growth. There should also be a sufficient $\text{CH}_4/\text{ZrCl}_4$ concentration to facilitate the reaction mechanism. It can also be observed from Figure 7-9 and Figure 7-10 that as the temperature and $\text{CH}_4/\text{ZrCl}_4$ increase further, the crystallite size decreases. The reason for this may be due to an increased amount of free carbon, which acts as an impurity during ZrC crystal growth. This co-deposition of free carbon may retard the growth of ZrC crystallites.

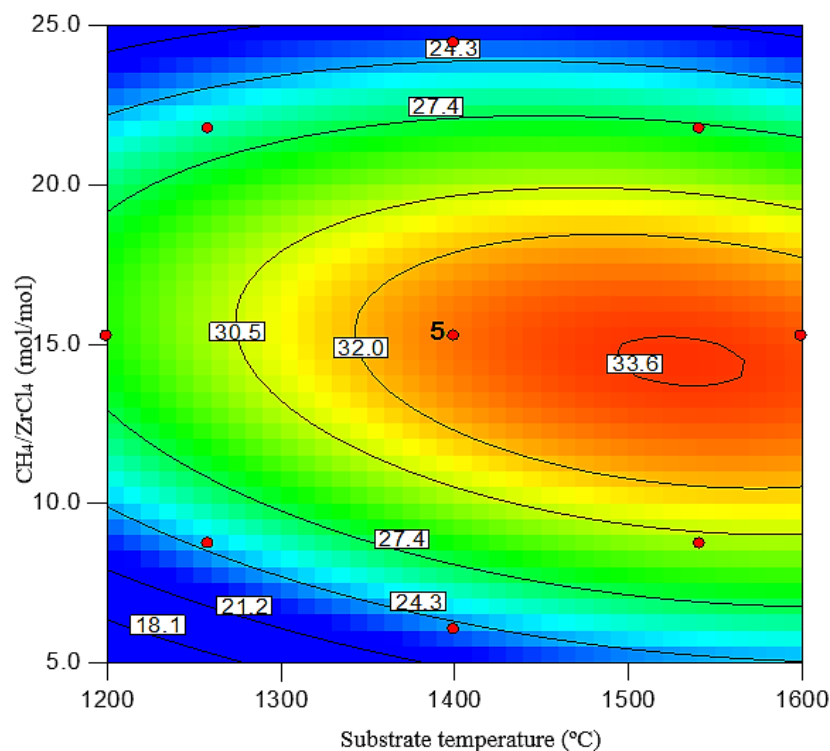


Figure 7-9: A contour plot showing the effect of temperature and $\text{CH}_4/\text{ZrCl}_4$ ratio on the crystallite size.

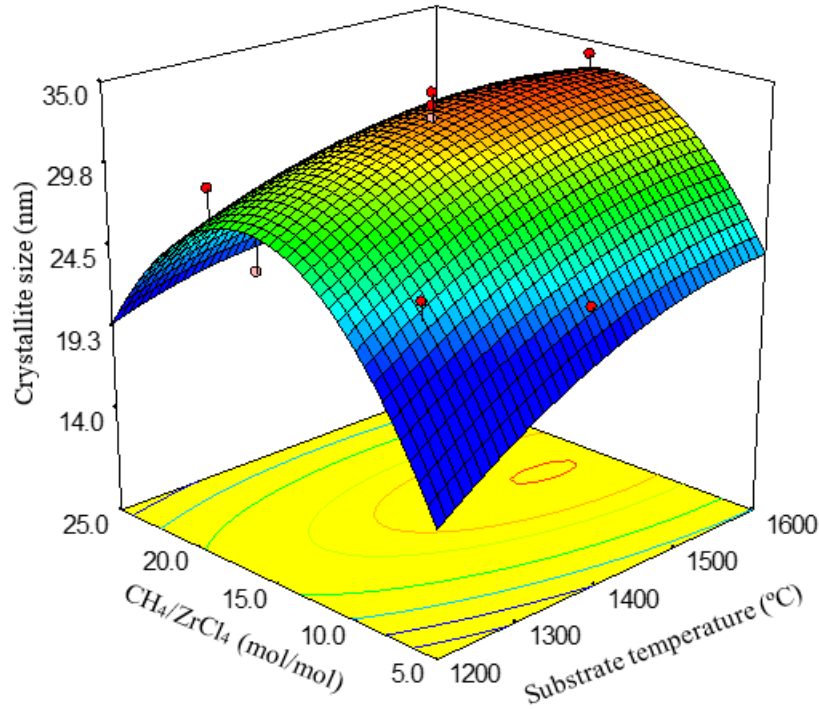


Figure 7-10: The 3-D plot showing the effect of temperature and $\text{CH}_4/\text{ZrCl}_4$ ratio on the crystallite size.

7.1.7 Optimisation of the experimental and model results

Following the examination of the regression equations and the contour plots representing the independent variables and responses, an additional optimisation process was carried out using Design Expert software. The target was to maximise the growth rate and minimise the amount of free carbon in the deposited layers. These two responses (factors) have a direct influence on the other response (crystallite size) generated. It can be observed from Section 7.1.4, that the value of C/Zr ratio is increased by increasing the substrate temperature or $\text{CH}_4/\text{ZrCl}_4$ molar ratio, or both. Therefore these two independent variables must be minimized as indicated in Table 7-7. The optimal substrate temperature and $\text{CH}_4/\text{ZrCl}_4$ molar ratio were determined to be 1347 °C and 10.6 respectively. For these parameter conditions, the predicted growth rate (Y_1), C/Zr atomic percentage ratio (Y_2) and average crystallite size (Y_3) were 6.05 $\mu\text{m}/\text{h}$, 1.03 and 29.56 nm, respectively. The combined statistical desirability for these optimised values was found to be 0.67. Alternatively, one can solve Equations 7-8, 7-9 and 7-10 to obtain the targeted conditions for the desired responses.

Table 7-7: Optimum conditions and constraints for stoichiometric ZrC coating growth

Constraints						
Name	Goal	Lower Limit	Upper Limit	Lower Weight	Upper Weight	Importance
Temperature	Minimize	1200	1600	1	1	3
CH ₄ /ZrCl ₄	Minimize	6.04	24.4	1	1	3
C/Zr	Minimize	1.03	2.57	1	1	3
Grain size	is in range	21.8	34.2	1	1	3
Growth rate	Maximize	3.7	9.3	1	1	3

Solutions						
Number	Temperature (°C)	CH ₄ /ZrCl ₄ (mol/mol)	C/Zr At%	Grain size (nm)	Growth rate (µm/h)	Desirability
1	1346.9	10.6	1.03	29.56	6.05	0.67 Selected

7.1.8 Surface morphology

The variation of the surface morphology of the ZrC layers deposited at varying substrate temperatures and CH₄/ZrCl₄ molar ratios is highlighted in Figure 7-11. Samples prepared at 1259 °C with CH₄/ZrCl₄ molar ratios of 8.73 and 21.75 are denoted by (a) and (b), whereas samples deposited at a substrate temperature of 1541 °C with CH₄/ZrCl₄ ratios of 8.73 and 21.73 are denoted by (c) and (d), respectively. Sample (a) shows small grains surrounded by lots of cavities. When the CH₄/ZrCl₄ was increased to 21.75 the grain size increased and the amount and size of cavities reduced (see Figure 7-11 (b)). The grains also tend to cluster together, forming a cauliflower-like structure. This might be an indication of small grains agglomerating to form much bigger grains during deposition. Increasing the CH₄/ZrCl₄ molar ratio increases the amount of carbon-containing species that would readily combine with Zr-containing species to form ZrC. This implies that the layer growth was increasingly less limited by carbon availability.

The grains became much denser and bigger as the deposition temperature increased to 1541 °C for a CH₄/ZrCl₄ ratio of 8.73 (see Figure 7-11 (c)). This may be attributed to an increase in the mobility of the deposited molecules on the substrate surfaces as the temperature was

increased. This might have resulted in increased lateral diffusion and clustering of the atoms at the surface of the substrate. Particles tend to cluster in order to reduce the high surface energy they possess at high temperatures. Keeping the temperature at 1541 °C and increasing the CH₄/ZrCl₄ molar ratio to 21.75, the surface of the layers became much smoother with almost no islands (see Figure 7-11 (d)). No cavities were visible between the particles. This observation may be explained with reference to Section 7.1.5. An increase in temperature and CH₄/ZrCl₄ ratio increased the growth rate and the carbon content in the layers. The excess carbon may act as additional nucleation sites, thus increasing the size of particles and levelling the islands. From these results, it is quite clear that both the substrate temperature and the CH₄/ZrCl₄ molar ratio had a significant impact on the surface morphology of the deposited layers

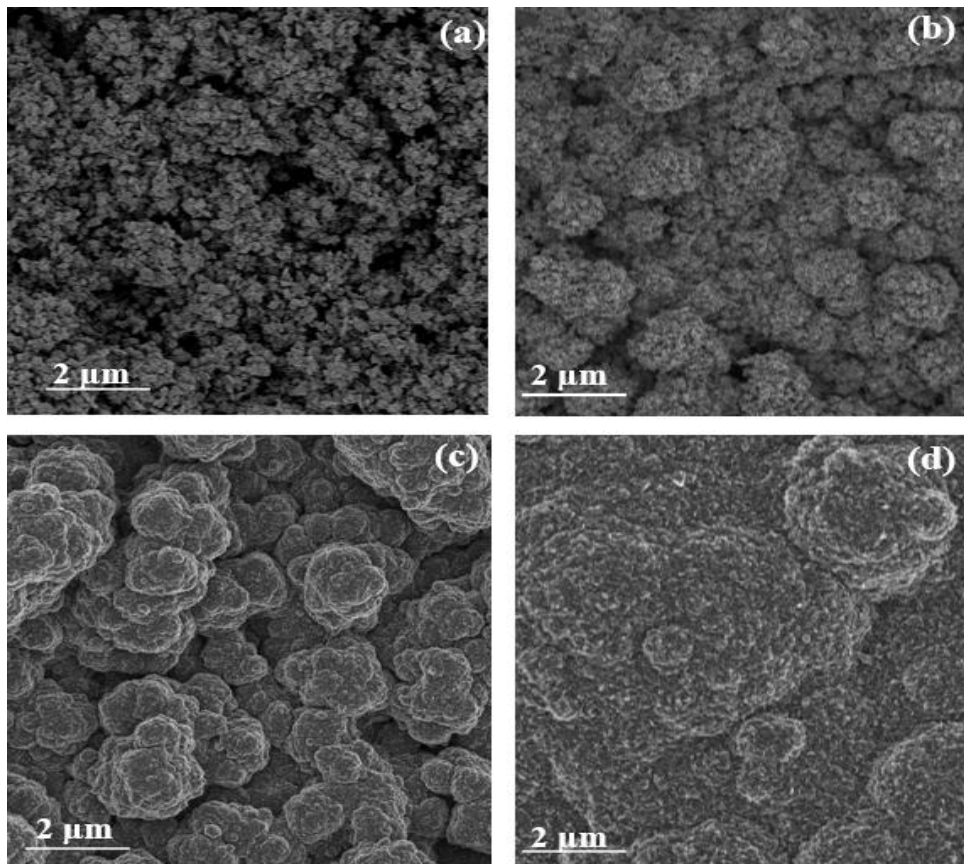


Figure 7-11: FE-SEM images of the surface morphology of ZrC layers deposited at 1259 °C ((a) and (c)) and 1541 °C (i.e. (b) and (d)) for CH₄/ZrCl₄ molar ratio of 8.73 ((a) and (b)) and 21.73 ((c) and (d)).

7.2 Influence of the substrate gas-inlet gap on the growth rate, morphology and microstructure of ZrC layers

7.2.1 Introduction

During the course of the experimental work, it became evident that the position of the reactive gas inlet above the substrate had a distinct and unexpected effect on the growth parameters of ZrC. This possibility has been mentioned before in a computational study by Vanka et al. [25]. They noted that the gap between the substrate and the inlet is a sensitive parameter since it determines the natural convection parameters and therefore affects the growth dynamics of the layers [25]. To our knowledge, no experimental work has been reported on the growth and properties of ZrC layers in an induction heated CVD reactor at different substrate-gas inlet gaps. This part of the study reports on the influence of the substrate-gas inlet gap on the growth rate, surface morphology and microstructure of ZrC films deposited on graphite substrates. Lui et al. [8] noted that the deposition of ZrC layers at substrate temperatures below 1250 °C and above 1250 °C is controlled by two different growth processes. For this reason substrate temperatures of 1200 °C and 1400 °C were selected for this work.

The substrate-gas inlet gap (ZY) (Figure 7-12) was varied from 70 mm to 90 mm, 120 mm, 145 mm and 170 mm. This was done by changing the inlet (Y) feed line lengths and maintaining the substrates at the same position on the top of the substrate stage (Z). Changing the substrate position would result in changes to the temperature of the substrate and its immediate vicinity, since the temperature at any point inside the reactor is dependent on its position relative to the induction heating coil. As discussed in Section 7.1, temperature plays a major role in the composition and morphology of the deposited layers. Therefore, changing the substrate position would negate an investigation of the effect of the substrate-gas inlet

gap. The deposition was conducted at atmospheric pressure at two substrate temperatures viz. 1200 °C and 1400 °C for 2 hours. The deposition parameters are indicated in Table 7-8.

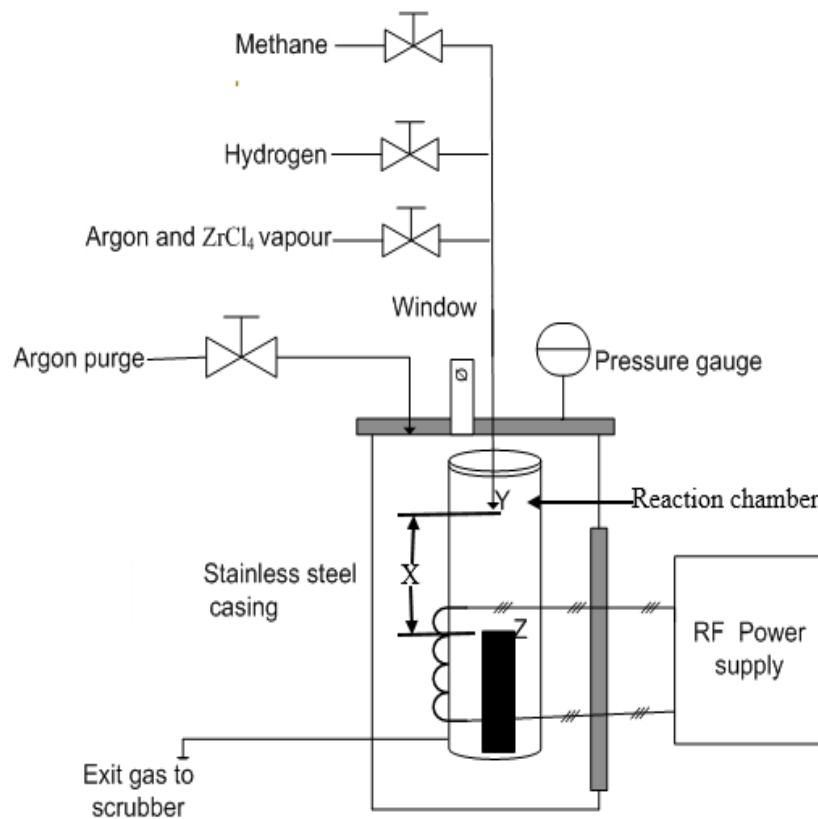


Figure 7-12: Schematic diagram of the CVD reactor system.

7.2.2 Gas flow parameters in the reaction chamber

It was assumed that the total reactant gas pressure was uniform throughout the reactor space for the entire deposition time and the reactants did not react chemically in the vapour phase to form ZrC. Some of the gas properties are indicated in Table 7-8.

The velocity V of the mixture of gases entering the reaction chamber was calculated using Equation (7-11).

$$V = \frac{\sum_i \rho_i V_i}{\sum_i \rho_i} \quad (7-11)$$

where ρ_i and V_i are the density and velocity of the i^{th} component respectively with $V_i = Q_i / (60\pi r^2)$ and r (0.32 cm) being the radius of the inlet steel pipes. The velocity V of the gas mixture was found to be 0.183 m/s.

The values of density, velocity and viscosity of $ZrCl_4$ vapour were not included in the calculations since $ZrCl_4$ vapour constituted the smallest (and negligible) fraction of the total gas mixture. The density of the gas mixture was estimated from Equation (7-12) and was found to be 0.393 kg/m^3 :

$$\rho = \frac{\sum_i \rho_i Q_i}{\sum_i Q_i} \quad (7-12)$$

The viscosity of the gas mixture was calculated from Equation (7-13).

$$\eta = \frac{\sum_i y_i \eta_i \sqrt{M_i}}{\sum_i y_i \sqrt{M_i}} \quad (7-13)$$

Here, y_i , M_i and η_i are the mole fraction, molar weight and viscosity, respectively of the i^{th} component at the desired temperature. The mole fraction of an individual gas was determined from their volumetric flow rates as $y_i = Q_i / \sum_i Q_i$ [4]. The viscosity of the gas mixture was found to be $2.92 \times 10^{-5} \text{ Pa}\cdot\text{s}$.

The growth of ZrC layers on the substrate is controlled by $ZrCl_4/CH_4$ diffusion to the surface of the substrate. Assuming the concentration of $ZrCl_4/CH_4$ in the vicinity of the substrate surface tends towards zero, then the concentration drop between the bulk and the surface is equal to the inlet concentration N_o . The concentration of individual reactants in the mixture was calculated from Equation (7-14).

$$N_o = \frac{y_i \dot{m}_i}{M_i Q_i} \quad (7-14)$$

where \dot{m}_i is the reactant mass transfer rate and w_i is the molar fraction. In this study, the $ZrCl_4$ concentration in the mixture was found to be 8.12×10^{-8} mol/cm³. The molecular volume of the growing ZrC layer v_k was 15.67 cm³/mol.

From the experimental parameters and gas properties, the Reynolds number (Re) at the inlet inside the reaction chamber was found to be 61.7, indicating that the flow of the reactants in the reaction chamber was mainly laminar. The Reynolds number was determined from Equation (7-15):

$$Re = \frac{V\rho d}{\eta} \quad (7-15)$$

Here $d=2.5$ cm is the diameter of the reaction chamber.

Table 7-8: Experimental growth parameters for ZrC layers when changing the substrate-gas inlet gap.

Time (h)	Pressure (atm)	Substrate temperature (°C)	Substrate-gas inlet gap (mm)	Vaporiser temperature (°C)
2	1.0	1200 and 1400	70-170	300

Gases	Flow rate Q_i (sccm)	Velocity V_i (m/s)	Density ρ_i (kg/m ³)	Viscosity $\times 10^{-5} \eta_i$ (Pa.s)
CH ₄	26	0.442	0.6669 at 20 °C	1.1 at 20°C
H ₂	853	0.0135	0.0838 at 20 °C	0.88 at 20 °C
Ar	562	0.291	0.8494 at 300 °C	3.67 at 300 °C

Due to natural convection and the friction between the reactant flow and the substrate surface (viscosity of the reactants), the velocity of the reactants in the vicinity of the substrate surface reaches a minimum. The difference in the gas flow velocities at the substrate surface and the bulk gives rise to a stagnant boundary layer. The boundary layer thickness δ is related to the Reynolds number by Equation (7-16) [19]:

$$\delta = \sqrt{X} \sqrt{\frac{d}{Re}} \quad (7-16)$$

The boundary layer thickness was estimated to be 5.3 mm, 6.0 mm, 7.0 mm, 7.8 mm and 8.3 mm for a substrate-inlet gap X equal to 70 mm, 90 mm, 120 mm, 145 mm and 170 mm, respectively.

7.2.3 Growth rate

The change in layer thickness per unit deposition time (i.e. the growth rate, k) was determined from Equation (7-7).

The effect of substrate-inlet gap and substrate temperature on the growth rate of ZrC layers is shown by Figure 7-13. From these plots, it is quite clear that the growth rate decreases almost linearly with increase in substrate–inlet gap at both temperatures. The results also show an increased growth rate when the temperature is increased from 1200 °C to 1400 °C. The effect of the gas inlet position may be due to an increased diffusion rate of reactant species across the boundary layer [26] and the temperature effect may be due to increased surface reaction kinetics at higher temperatures [27]. The transport of the reactants in the reaction chamber is controlled by complex fluid dynamics [19,28]. A detailed examination of fluid dynamics in the vertical wall CVD is not presented in this work. We shall limit our discussion to diffusion of the reactants through the boundary layer. The boundary layer gives rise to changes in the reactant flow velocity, which results in a concentration gradient of reactant gases in the vicinity of the substrate surface [19,23]. The reactant gas concentration in the vicinity of the substrate surface is usually higher when the gas inlet is closer to the substrate. The higher gas concentration results in an increased mass transfer rate and this increases the arrival rates of reacting species to the substrate surface. The flux J of the reactant through the boundary layer in the vicinity of the substrate surface inside the reaction chamber is given by Equation (7-17):

$$J = \frac{-DN_0}{\delta} \quad (7-17)$$

Here D is the diffusion constant (a proportionality constant between the molar flux due to molecular diffusion and the gradient in concentration of the reactant species) and N_o is the concentration difference over the boundary layer thickness δ [29]. Therefore, increasing the boundary layer thickness reduces the diffusion flux of the reactants. The growth rate k , in terms of diffusion flux, boundary layer thickness and substrate–inlet gap is expressed by Equation (7-18):

$$k = -v_k J = \left(v_k D N_o \sqrt{\frac{\text{Re}}{d}} \right) \frac{1}{\sqrt{X}} \quad (7-18)$$

Here v_k is the molecular volume of the crystal [33]. This expression shows that the growth rate is determined by the reciprocal of the square root of the substrate-inlet gap. This is in agreement with our experimental results obtained in Figure 7-13, where the growth rate is observed to have a linear relationship to the reciprocal of the square root of the substrate-inlet gap.

It was also observed (by visual inspection) that when the substrate–inlet gap was large (short inlet feed line), the amount of ZrCl_4 gas diffusing out of the reaction chamber increased and deposited on the top lid of the stainless-steel casing. This might have decreased the concentration of ZrCl_4 reaching the substrate and consequently contributed to the decrease in ZrC layer growth rate as the substrate-inlet gap increased.

From the slope of the curves in the insert in Figure 7-13 ($1.111 \times 10^{-6} \text{ cm}^{-3/2}$ for 1200 °C and $1.393 \times 10^{-6} \text{ cm}^{-3/2}$ for 1400 °C) and the parameters of the multicomponent reactant gaseous mixture indicated in Section 7.2.2, the diffusion coefficients of the reactants for the ZrC layer growth process were determined from Equation (7-19):

$$D = \left(\sqrt{\frac{d}{\text{Re}}} \right) \frac{\text{slope}}{v_k N_o} \quad (7-19)$$

The reactant diffusivity was found to be $0.176 \text{ cm}^2/\text{s}$ and $0.200 \text{ cm}^2/\text{s}$ for $1200 \text{ }^\circ\text{C}$ and 1400°C , respectively. These values show that the derived diffusion coefficients increase marginally as the substrate temperature is increased. The values of diffusion coefficients above are likely to be low, since they are determined from the actual growth rate of the layers, and yet not all the diffusing reactants are effectively used to form the ZrC layer. The reactant loss may arise from parasitic reactions inside the reaction chamber and the reactants diffusing out of the chamber unreacted.

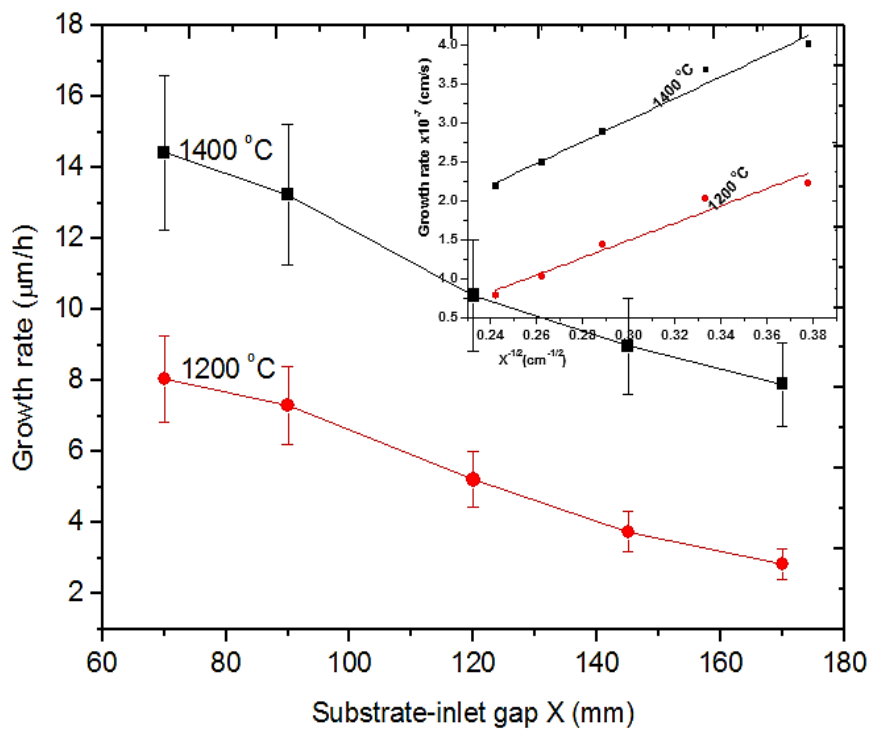


Figure 7-13: Dependence of growth rate of ZrC layers on substrate-inlet gap

To explain the deposition mechanism, we use a concentration boundary layer model given in Figure 7-14. A number of steps are involved in the growth process: (1) The inlet gases (ZrCl_4 in Ar, CH_4 and H_2) are transported to the heated substrate surface or boundary layer, (2) gas phase reactions take place and the intermediate species (i.e. $\text{CH}_4 = \text{C} + 2\text{H}_2$) which form are transported (diffuse) through the boundary layer to the substrate, (3) the reactants and their intermediate species diffuse and are absorbed onto the heated substrate surface. This

produces the ZrC deposit and by-products, (4) the ZrC deposit then diffuse along the heated substrate surface forming crystallisation centres, leading to the growth of the ZrC layer according to the Burton-Cabrera-Frank step-flow mechanism [34]. In parallel with this, (5) the by-products and unreacted reactants are removed from the deposited film surface first by diffusion through the boundary layer and then by convection, (6) some reactants and their intermediate product are lost within and from the reaction chamber, and (7) the by-products and unreacted reactants are transported away from the reaction chamber. The slowest process determines the actual layer growth rate. For the deposition conditions and parameters used in this work, mass transport (diffusion) across the boundary layer becomes the rate controlling step.

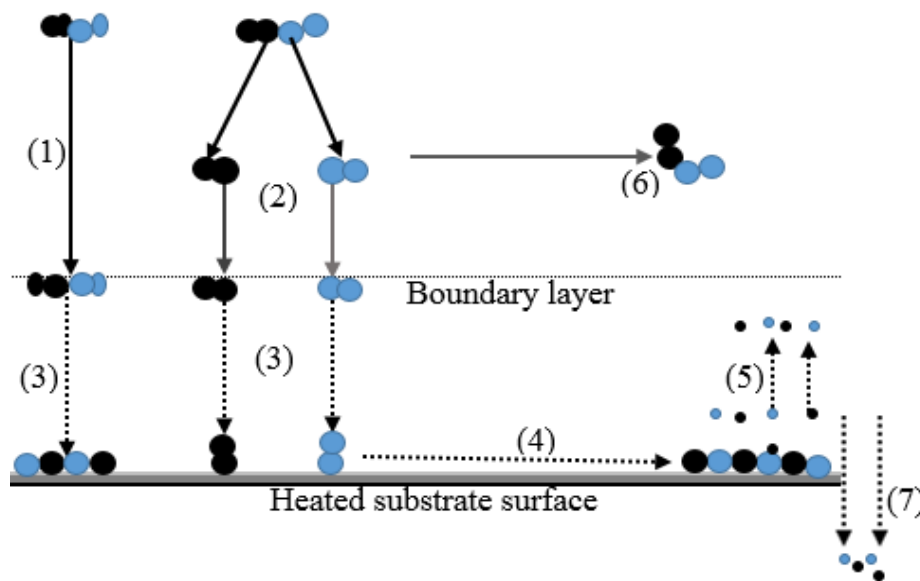


Figure 7-14: Concentration boundary layer model for CVD process of ZrC layers in the vertical reaction chamber.

7.2.4 Crystallographic structure and phase composition

The crystal structure and phase composition of all the deposited ZrC layers were investigated by XRD analysis. Figure 7-15 and Figure 7-16 show the XRD patterns of ZrC layers deposited at 1200 °C and 1400 °C, respectively. The peaks and their corresponding Miller indices are also indicated in the figures. The diffraction peaks present were indexed within a

cubic rock salt (NaCl) structure and confirmed using the International Centre for Diffraction Data (ICDD) file number ZrC: 03-065-8833. Carbon peaks (matched with ICDD file number C: 00-056-0159) are evident in the XRD patterns. The carbon peak intensities were observed to increase with both substrate-inlet gap increase (from 70 mm to 170 mm) and temperature increase (from 1200 °C to 1400 °C). Phase quantification was performed by Rietveld refinement [35]. The results revealed that the samples consisted mainly of the ZrC phase and some amounts of free carbon. The C/ZrC ratios at the two temperatures for each substrate-inlet gap was determined and plotted as shown in Figure 7-17. At 1200 °C the C/ZrC ratio is lower than at 1400 °C for all the substrate-inlet gaps. The figure also shows a general increase of C/ZrC ratio with an increase in substrate-inlet gap. The increase in free carbon may be attributed to the fact that the rate at which methane decomposes to form carbon and hydrogen increases with increasing temperature; higher growth rates imply higher fluxes of reactants to the deposition surface, and a higher probability for methane to decompose rather than to take part in a concerted reaction to form the carbide. Generally the diffusion rate of heavy gas molecules is lower compare to the light gas molecules and this corresponds to their participation in the growth process. When the substrate-inlet gap is narrowed, ZrCl₄ is brought closer to the substrate and its participation in the growth process is improved, hence C/ZrC decreases.

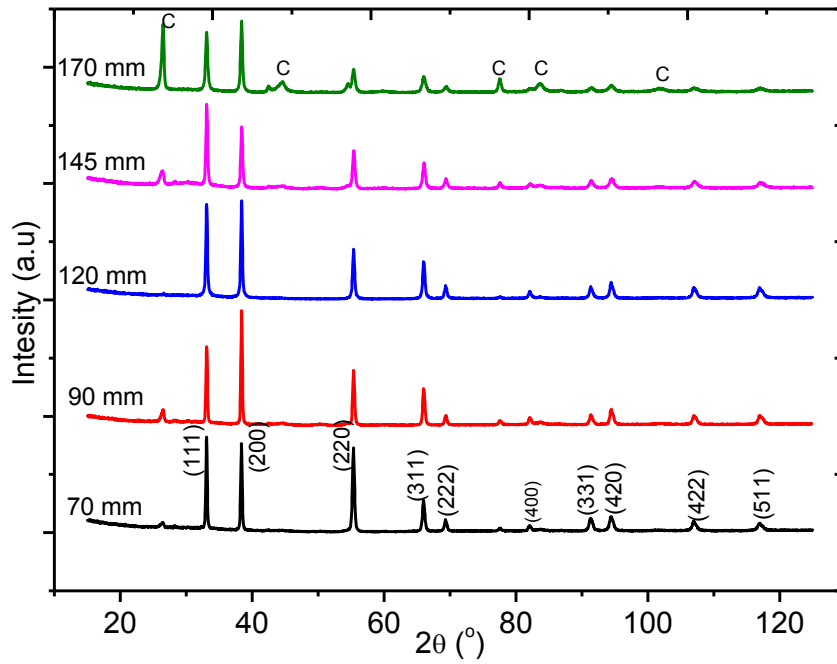


Figure 7-15: XRD pattern of ZrC layers deposited at 1200 °C for different substrate-inlet gaps.

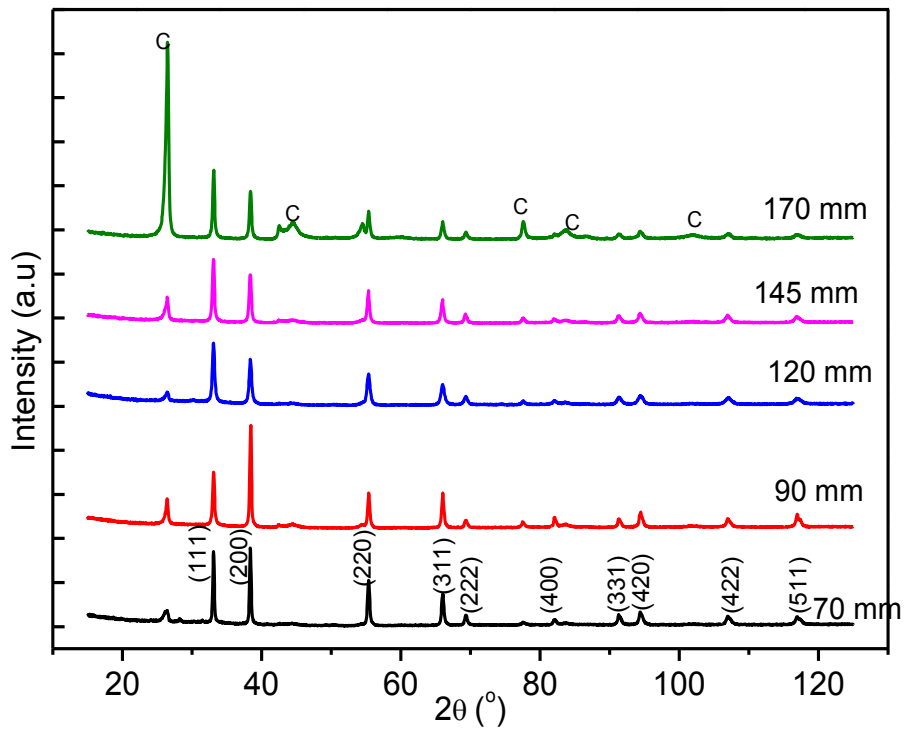


Figure 7-16: XRD patterns of ZrC layers deposited at 1400 °C for different substrate-inlet gaps.

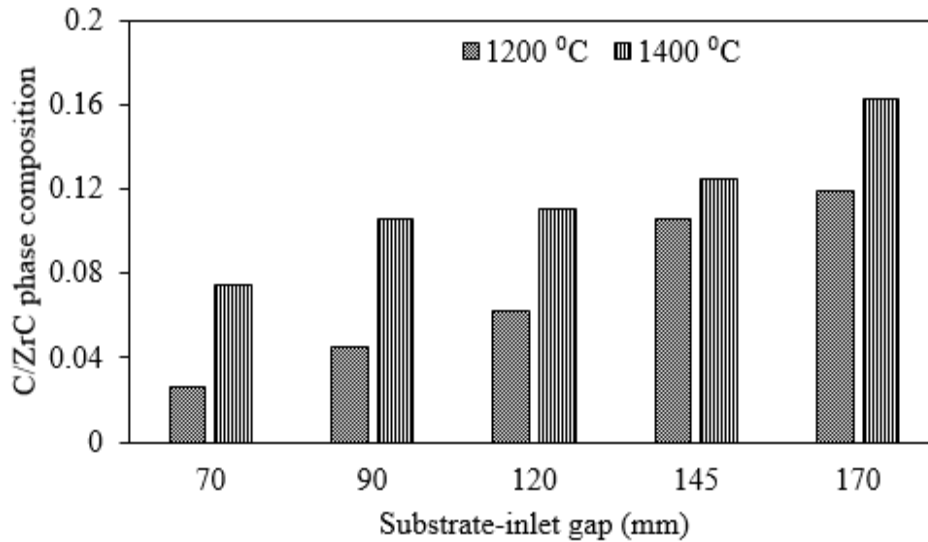


Figure 7-17: C/ZrC phase composition as a function of substrate-inlet gap.

7.2.5 Crystallite size

The crystallite size of polycrystalline materials affects their mechanical properties [23]. The average crystallite size was calculated from the Scherrer formula using Equation (5-9).

Figure 7-18 illustrates the dependence of average crystallite size of ZrC layers on substrate-inlet gap at 1200 °C and 1400 °C. The average crystallite size decreased from 33.3 ± 0.8 nm to 22.8 ± 1.0 nm for ZrC layers deposited at 1200 °C and from 30.8 ± 0.2 nm to 21.2 ± 0.6 nm for layers deposited at 1400 °C as the substrate-inlet gap increased from 70 mm–170 mm.

This reduction in average crystallite size might be due to two reasons. The reduced reactant concentrations at the substrate surface at wider substrate-inlet gaps may retard crystallite growth. Furthermore, as indicated in Figure 7-17, an increase in substrate-inlet gap results in an increase in the amount of free carbon. This free carbon, which is deposited as a secondary phase, acts as impurities in the deposited layer. The presence of impurities in the ZrC layers may also cause retardation in the crystallite growth.

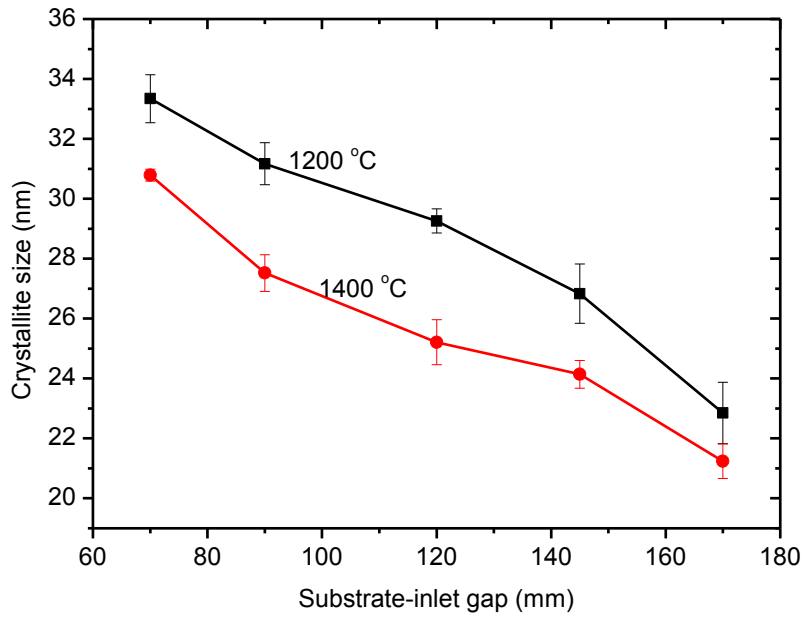


Figure 7-18: Dependence of average crystallite size of ZrC layers on the substrate-inlet gap.

7.2.6 Peak broadening and lattice strain

Figure 7-19 shows a plot of the FWHM for the (200) diffraction peak as a function of substrate-inlet gap. From this figure, it is quite clear that the FWHM increases with substrate-inlet gap indicating peak broadening. Broadening of XRD peaks indicates a possible decrease in crystallite size (grain refinement) and/or the presence of lattice strain in the material [36].

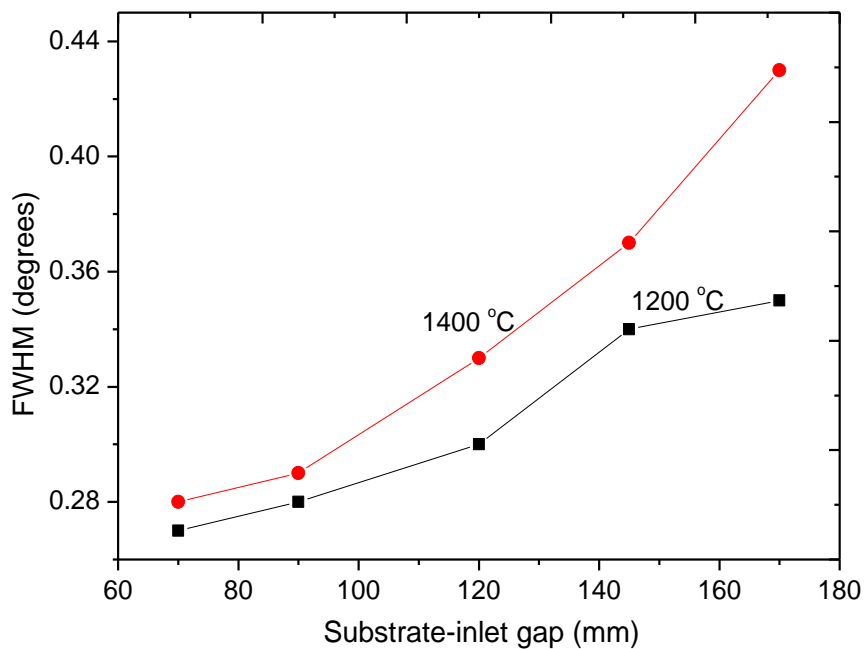


Figure 7-19: FWHM as a function of substrate-inlet gap at 1200 °C and 1400 °C.

Strain is a measure of distortions and crystal imperfections in the material. The strain was calculated from the FWHM using Equation (5-11) [37].

The results in Figure 7-20 shows that as the substrate-inlet gap increases, the strain in the ZrC layers increased. The strain in the layers is likely to have been introduced in the lattice planes during deposition by chemical and thermal processes. Polycrystalline layers deposited on a substrate are usually in a strained state [38]. The increase in strain in the layer as the substrate-inlet gap increased may be due to reduced layer thickness, decreased reactant concentrations, the effects of crystallite size, and also the increase in secondary phases (free carbon). Strain causes the interplanar spacing to change from the stress free values to values comparable to the amount of stress introduced [23,39]. A very thin layer is likely to be discontinuous [40], introducing stress in the material.

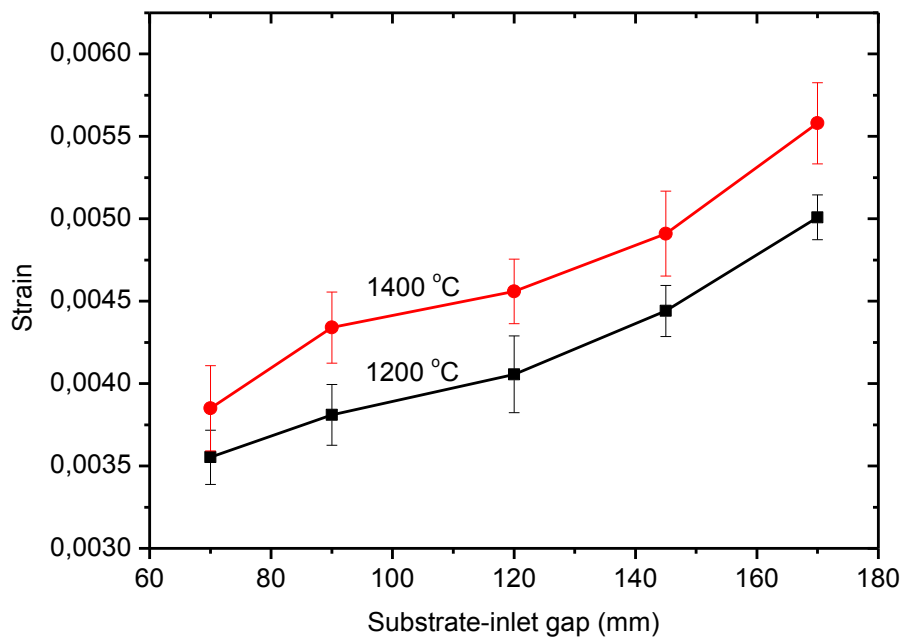


Figure 7-20: Effect of substrate -inlet gap on lattice strain at 1200 °C and 1400 °C.

7.2.7 Preferred orientation

To ascertain whether the crystals displayed preferred orientation, texture coefficients were determined. Texture coefficients $T(hkl)$ of the samples were calculated using Equation (5-17) from the first five ZrC diffraction peaks for each sample.

Preferred orientation influences the properties of crystalline materials. Values of the texture coefficient, $T(hkl)$, less than or equal to one means that the crystallites are randomly oriented, while a value of $T(hkl)$ greater than one implies preferred orientation of the crystallites in a given [hkl] direction [41–43]. Figure 7-21 and Figure 7-22 show the variation of texture coefficients with substrate-inlet gap at a substrate temperature of 1200 °C and 1400 °C, respectively.

At 1200 °C, the texture coefficients were greater than one for all the layers, implying preferential orientation in all the indicated diffraction planes. The (220) plane was most preferred, with a $T(hkl)$ value of 3.6 at 70 mm. At 90 mm and 120 mm, the (200) plane was slightly more preferred than (220). There was a general decrease in the $T(hkl)$ values for all the diffraction planes at substrate inlet gaps of 145 mm to 170 mm. The (111) diffraction plane was generally the least preferred orientation. This may be due high reactant-substrate interaction energy and reactant concentration when the substrate-inlet gap is narrowed. For ZrC layers deposited at 1400 °C, the (200) plane was more preferred at 70 mm and 90 mm. When the substrate-inlet gap increased, the preferred orientation shifted to (220). Similar to results at 1200 °C, the (111) plane was the least favoured diffraction plane. At increased temperature of 1400 °C the surface energy and atomic mobility are increased; this may be the reason why the (111) plane is less preferred due to non-equilibrium conditions [44]. The accumulation of free carbon (impurities) on the substrate surface has an influence on the substrate energy which may also have an effect on the preferred orientation of the planes.

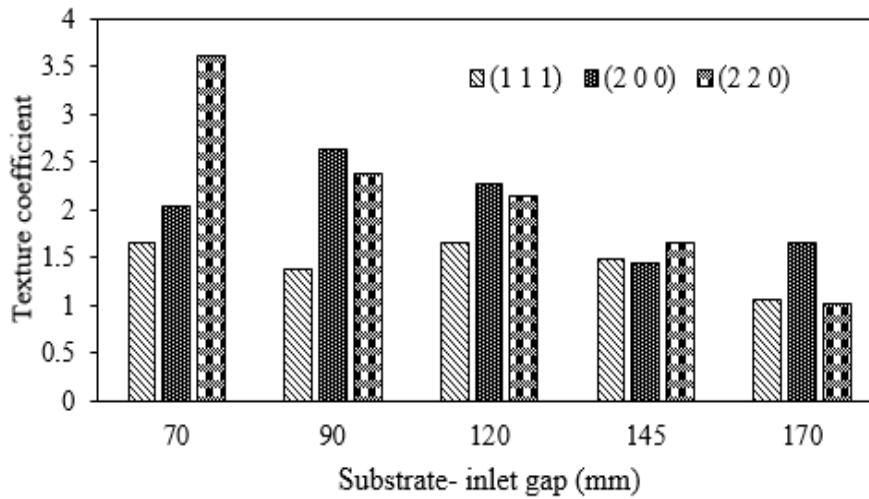


Figure 7-21: Texture coefficients of ZrC layers deposited at 1200 °C as a function of substrate-inlet gap.

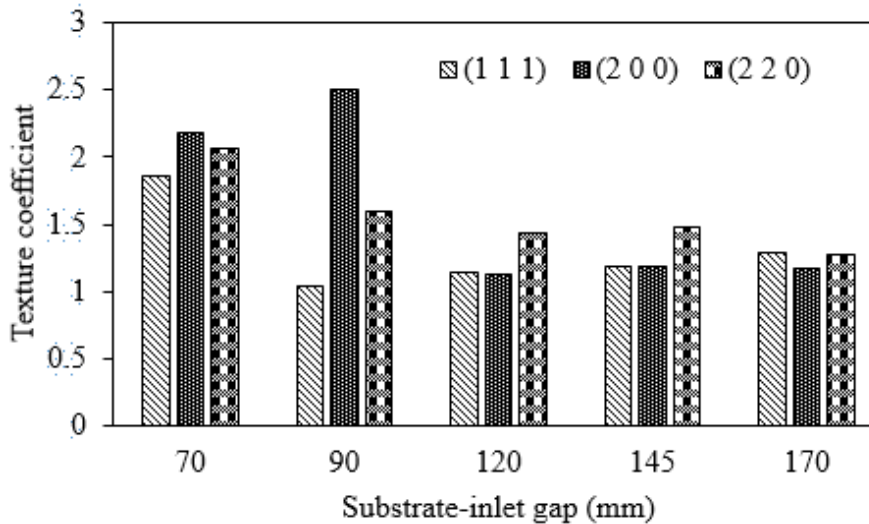


Figure 7-22: Texture coefficients of ZrC layers deposited at 1400 °C as a function of substrate-inlet gap.

The degree of preferred orientation (α) of each sample as a whole was calculated from Equation (5-19). Figure 7-23 shows the variation in the degree of preferred orientation with substrate-inlet gap. All samples have α -values greater than zero, indicating a good degree of preferential orientation at both temperatures. The α -values decrease as the substrate-inlet gap and temperature increases. This indicates that to produce layers with highly preferred orientation a relatively narrow substrate-inlet gap is recommended. As already stated in Section 5.1.6 (Chapter 5) that, some properties of crystalline materials depend on the

orientation of the crystal planes. In polycrystalline materials, an increased degree of preferred orientation would mean different planes are highly oriented preferentially in specified directions. This may create an easy passage of the fission products to diffusion through the layer. The mechanical properties can also be improved, for example the propagation of a crack developed in one plane may be stopped by the adjacent crystal plane. In this case, samples with a low degree of preferred orientation would be more desirable than highly oriented samples.

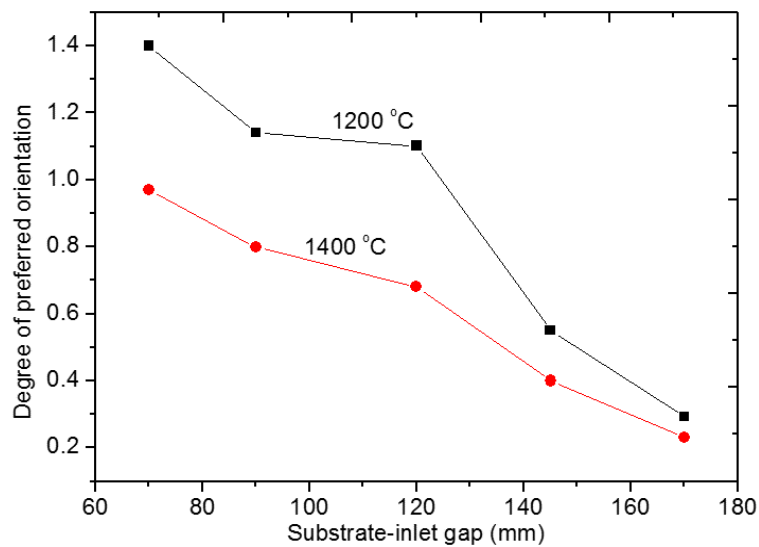


Figure 7-23: Effect of substrate-inlet gap on degree of preferred orientation of ZrC layers.

7.2.8 Surface morphology and microstructure

The FE-SEM was used to examine the surface morphology and microstructure of ZrC layers. The micrographs of ZrC layer surfaces deposited at 1200 °C for different substrate-inlet gaps are depicted in Figure 7-24. At 70 mm (Figure 7-24 (A)), the ZrC layer surface shows a large complex faceted structure surrounded by small particles at the periphery and on top. These small particles have the same shape as the larger ones (see the high magnification insert in Figure 7-24 (A)). The surface morphology at a substrate-inlet gap of 120 mm indicated in Figure 7-24 (B)) shows small granules, almost of the same size, with very few openings on the layer surface. These small granules have the same structure (complex facets) as those at

70 mm (see the insert in Figure 7-24 (B)). At 170 mm (Figure 7-24 (C)), ZrC layer surface shows ball-shaped particles clustered together to form a cauliflower-like shape. The cauliflower-like clusters of varying sizes are surrounded by numerous large openings, compared to that of the image for a 120 mm gap.

Figure 7-25 shows the surface morphology of ZrC layers deposited at 1400 °C for a substrate-inlet gap of 70 mm (Figure 7-25 (A)), 120 mm (Figure 7-25 (B)) and 170 mm (Figure 7-25 (C)). For 70 mm gap, the surface morphology consists of agglomerates of ball-like particles surrounded by openings. When the gap was increased to 120 mm, the agglomerates (cauliflower-like) become bigger and the size of the openings surrounding them reduces significantly. Further substrate-inlet gap increase to 170 mm, the surface morphology became more uniform, dense and smoother with almost no openings around the clusters. The cauliflower-like clusters tend to pebble-like structure.

The average particle sizes for the different gap conditions increased for the 1400 °C grown layers. This can be attributed to the increase in the surface energy and mobility of the ZrC molecules on the surfaces of the deposited (poly-crystalline) ZrC crystals at the higher temperature. Another reason for the increase in particle size (agglomeration) as substrate-inlet gap increased may be due to the increase in carbon content in the layers, which acts as additional nucleation sites. Judging from these results, it is quite clear that the substrate-inlet gap and substrate temperature control the morphology and growth uniformity of ZrC layers.

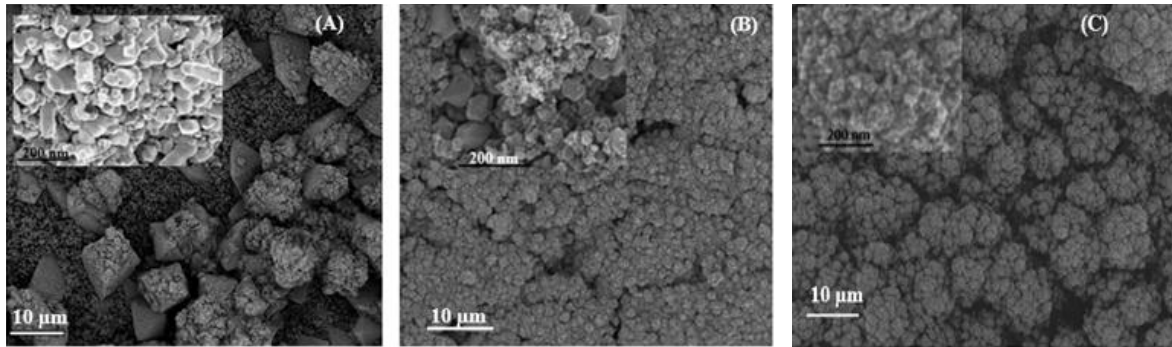


Figure 7-24: SEM images of ZrC layers deposited at 1200 °C for a substrate-inlet gap of (A) 70 mm, (B) 120 mm and (C) 170 mm.

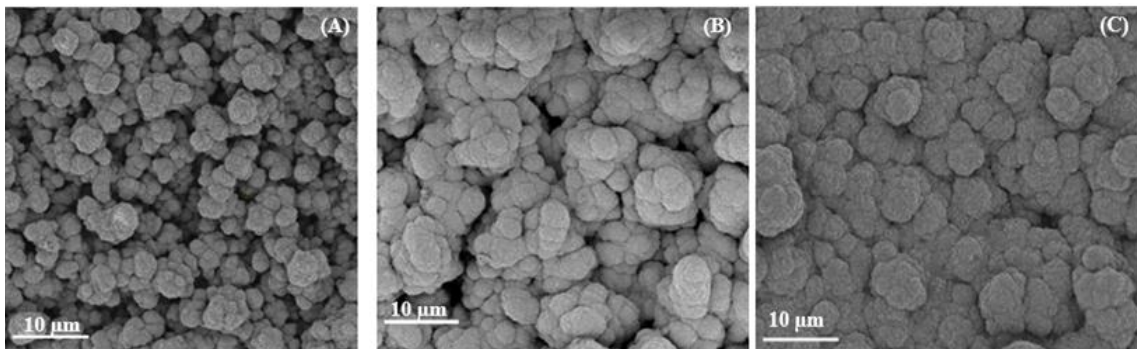


Figure 7-25: SEM images of ZrC layers deposited at 1400 °C for a substrate-inlet gap of (A) 70 mm, (B) 120 mm and (C) 170 mm.

7.3 The role of ZrCl₄ on the growth characteristics of ZrC layers

7.3.1 Introduction

The inlet gas concentration is primarily regulated by the partial pressure of the precursors. The partial pressure of a gas determines the thermodynamic activity of its molecules. It has been noted that gases will diffuse, react or dissolve according to their partial pressures, and not necessarily according to their concentrations in a gas mixture [45]. In a CVD reactor, the partial pressure depends on gas flow rates, vaporising temperature, and the substrate-gas inlet gap. The influence of substrate-inlet gap on the growth characteristics of ZrC layers has been reported in Section 7.2. Several researchers have studied the effect of carbon source (especially CH₄ and C₃H₆) [9,46,47] and hydrogen flow rates [47,48] on the properties of ZrC layers. The effect of reactor total pressure on the growth and structure of ZrC layers has also

been reported by Zhu et al. [47]. However, no study has been found relating to the effect of $ZrCl_4$ partial pressure on the growth and structure of ZrC layers grown by thermal CVD. Therefore, this part of the study was conducted to investigate the influence of the $ZrCl_4$ partial pressure on the growth rate, microstructure and surface morphology of deposited ZrC layers on graphite substrates.

The vapour pressure of $ZrCl_4$ was determined from the vapour pressure-temperature calibration curve given in Figure 7-26. The partial pressure of $ZrCl_4$ was controlled by controlling the argon flow rate and the temperature of the vaporiser. From Figure 7-26, a temperature of 300 °C corresponds to a $ZrCl_4$ vapour pressure of 43 kPa. The $ZrCl_4$ mass flow rate in argon carrier was determined from the quantity of $ZrCl_4$ swept from the vaporiser during each experimental run. By applying Dalton's law of partial pressure given in Equation (7-20), Amagat's law of partial volume given in Equation (7-21) and the ideal gas equation, we obtain the pressure, volume and the mole amount relation given by equation (7-22) [4,49]:

$$P_T = \sum_{i=1}^n P_i \quad (7-20)$$

$$V_T = \sum_{i=1}^n V_i \quad (7-21)$$

$$\frac{V_i}{V_T} = \frac{P_i}{P_T} = \frac{n_i}{n_T} \quad (7-22)$$

Here V_i is the partial volume of any individual gas component i , P_i is the partial pressure of any individual gas component i , P_T is the total pressure of the gas mixture, n_i is the molar amount of substance of gas i , and n_T is the total amount of substance in the gas mixture.

For steady state conditions (i.e. where the total volume, total the pressure and the deposition temperature are all constant), the partial pressure can be written in terms of the volumetric flow rates of the gases given in Equation (7-23):

$$\frac{P_i}{P_T} = \frac{\Delta V_i / \Delta t}{\Delta V_T / \Delta t} = \frac{\dot{V}_i}{\dot{V}_T} \quad (7-23)$$

Therefore the partial pressure fraction of $ZrCl_4$ (i.e. P_{ZrCl_4}/P_T) was calculated from Equation (7-24) in which the volumetric flow rate \dot{V}_{ZrCl_4} of $ZrCl_4$ was determined from Equation (7-25):

$$\frac{P_{ZrCl_4}}{P_{Total}} = \frac{\dot{V}_{ZrCl_4}}{\dot{V}_{Ar} + \dot{V}_{ZrCl_4} + \dot{V}_{H_2} + \dot{V}_{CH_4}} \quad (7-24)$$

$$\dot{V}_{ZrCl_4} = \frac{\dot{m}RT_V}{MP_V} \quad (7-25)$$

In Equation (7-25), \dot{m} is the mass flow rate of $ZrCl_4$, M is the molar mass of $ZrCl_4$, R is the universal gas constant, T_V is the temperature of the vaporiser and P_V is the vapour pressure of $ZrCl_4$ in the stream of inlet gases. Table 7-9 gives the deposition conditions.

Table 7-9: Deposition parameters and gas properties.

Experiment number	1	2	3	4	5
Gas flow rates					
CH ₄ (sccm)	15	15	15	15	15
H ₂ (sccm)	853	853	853	853	853
Ar (sccm)	264	415	562	704	849
ZrCl ₄ (g/h)	0.64	0.81	0.98	1.14	1.34
ZrCl ₄ (sccm)	5.07	6.42	7.77	9.04	10.38
ZrCl ₄ partial pressure fraction ($\times 10^{-3}$)	4.45	4.98	5.40	5.72	6.01
Gas at 300 °C					
Viscosity $\times 10^{-5}$ (Ns/m ²)	1.883	1.353		3.67	
Density (kg/m ³)	0.337	0.042		0.8494	

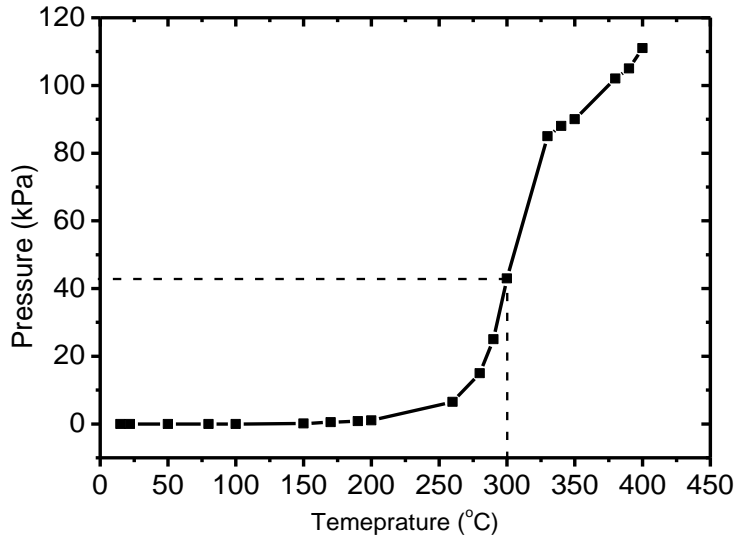


Figure 7-26: Variation of $ZrCl_4$ vapour pressure with vapouriser temperature. The experimental procedure of how this was arrived at is described in Chapter 6.

7.3.2 Gas flow behaviour and analytical description model of the gas flow process

The flow behaviour of the gases in the reaction chamber was established by calculating the magnitudes of the following dimensionless quantities. They were the Reynolds number, Re , and Grashof number, Gr . The values of these quantities, given in Table 7-10, were calculated using Equations (7-16) and (7-26) [4,19,50]:

$$Gr = \frac{g\rho^2 d^3 \Delta T}{T_o \eta^2} \quad (7-26)$$

Here ΔT is the temperature difference between the reactor wall and the substrate and T_o is the temperature of the gases as it enters the reactor. The gas flow was found to be laminar (i.e. $Re < 1000$ [19]) and forced convection dominated (i.e. $Gr/Re^2 < 10$ [19]). The boundary layer thickness δ was also calculated from Equation (7-17), with the diameter of the reaction chamber $d = 25$ mm and the substrate-gas inlet gap $X = 90$ mm.

The velocity v , density ρ and viscosity η of the mixture of gases entering the reaction chamber were calculated using equations (7-11), (7-12) and (7-13) [4], respectively.

Table 7-10: Gas flow parameters and dimensionless quantities.

Experiment #	1	2	3	4	5
Partial pressure fraction $\times 10^3$	4.45	4.98	5.4	5.72	6.01
v (cm/s)	11.2	16.6	21.9	27.0	32.2
ρ (kg/m ³)	0.234	0.307	0.363	0.407	0.444
$\eta \times 10^{-5}$ (Ns/m ²)	2.618	2.921	3.065	3.160	3.231
Re	24.5	43.6	64.7	86.7	110.5
$\delta \times 10^{-3}$ (m)	9.6	7.2	5.9	5.1	4.5
$Gr \times 10^3$	2.1	3.0	3.7	4.4	5.1
Gr/Re^2	3.4	1.6	0.9	0.6	0.4

In an attempt to increase the $ZrCl_4$ partial pressures, the argon flows were increased, which improved the overall mean flow velocity of the reactants. Therefore this increased argon flow (and hence increase in the overall mean flows) decreased the boundary layer thickness (see Figure 7-27), consequently increasing the arrival rate (the flux) of the reactants. The boundary layer thickness was found to decrease from 9.11 mm to 4.82 mm as the $ZrCl_4$ partial pressure fraction increase from 4.45×10^{-3} to 6.01×10^{-3}

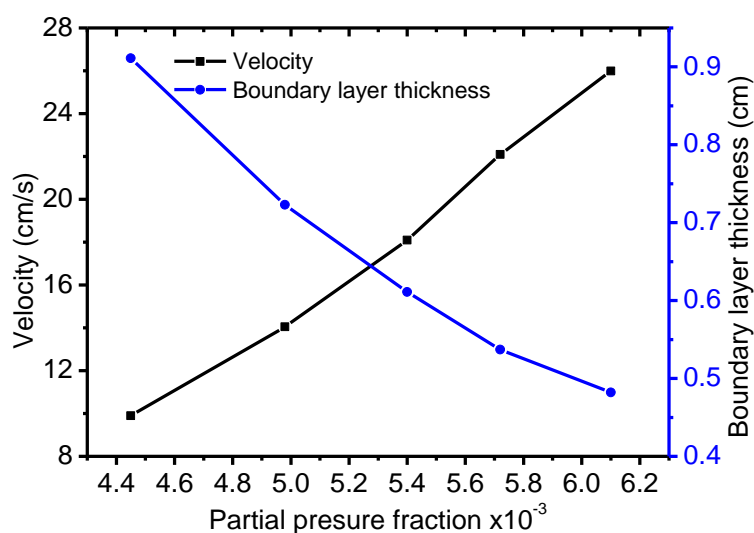


Figure 7-27: Variation of boundary layer thickness and mean gas velocity with $ZrCl_4$ partial pressure fraction.

The inlet gas stream was considered to be an ideal gas that was being transported through a boundary layer to the deposition surface. Then by applying Fick's law, the diffusion of $ZrCl_4$

vapour from the bulk gas stream towards the substrate may be described by the flux J_1 given

by $J_1 = \frac{-D}{RT} \frac{dp_{ZrCl_4}}{dx}$. In this case, this equation can be approximated by $J_1 = \frac{D}{RT} \frac{p_b - p_s}{\delta}$,

where p_b is the partial pressure fraction of $ZrCl_4$ in the bulk gas stream, p_s is the partial pressure fraction of $ZrCl_4$ at the substrate surface, and T is the deposition temperature [29,51,52]. It is important to note that the $ZrCl_4$ concentration C_{ZrCl_4} is related to its partial

pressure p_{ZrCl_4} by $C_{ZrCl_4} = \frac{p_{ZrCl_4}}{RT}$.

After crossing the boundary layer, the gases arrive at the substrate surface. On arrival, the active gases $ZrCl_4$ and carbon containing species are adsorbed onto the substrate and react to

form a layer. The flux J_2 consumed by the reacting surface may be given by $J_2 = \frac{k_m}{RT} p_s$,

where k_m is the surface reaction rate constant [51]. For the sake of determining p_s , we assumed a steady state condition where the mass flux crossing the boundary layer was equal

to the flux consumed at the substrate surface to form a layer (i.e. $J_1=J_2$), thus $p_s = \frac{\frac{D}{\delta} p_b}{\left(\frac{D}{\delta} + k_m\right)}$.

It has already been established from previous studies that at the current growth conditions,

the deposition of ZrC is mass transport limited [8][53]. In this case $\frac{D}{\delta} \ll k_m$, so that

$p_s \approx \frac{D}{\delta k_m} p_b$ [27,51]. This means that $p_s < p_b$. Therefore the gas transport across the boundary

layer for this deposition process may schematically be presented as shown in Figure 7-28.

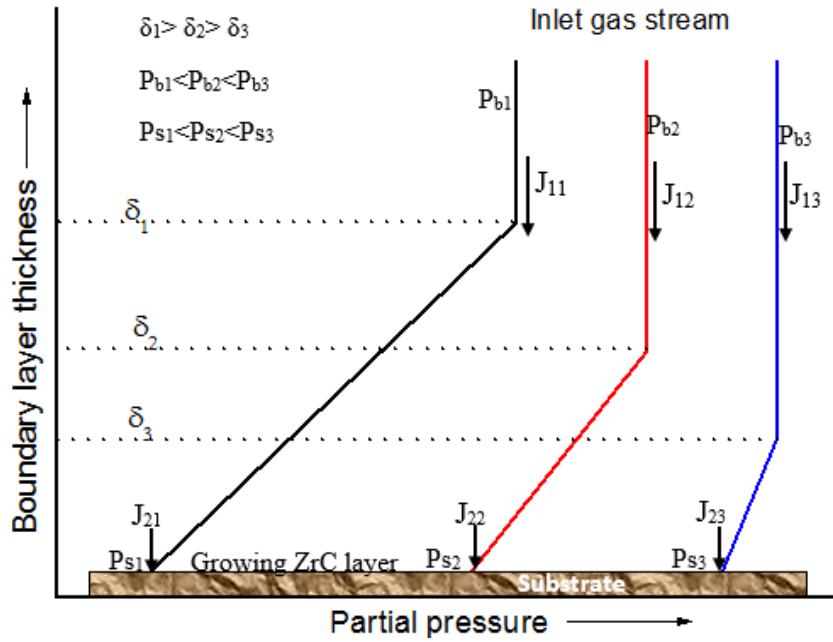


Figure 7-28: Schematic of the CVD reactant transport model across the boundary layer. P_{b1} , P_{b2} , P_{b3} are the partial pressures at the inlet and P_{s1} , P_{s2} , P_{s3} are their corresponding partial pressures at the surface. Also J_{11} , J_{12} , J_{13} are the diffusion fluxes of the gas at the inlet and J_{21} , J_{22} , J_{23} are the corresponding fluxes close to the substrate surface.

7.3.3 Effect of $ZrCl_4$ partial pressure on ZrC growth rate

To establish the dependence of ZrC growth rate on the $ZrCl_4$ partial pressure, the growth rate of ZrC layers deposited at 1400 °C was plotted against the $ZrCl_4$ partial pressure, as indicated in Figure 7-29. This plot shows that, within experimental error, the growth rate of ZrC layers increased linearly with $ZrCl_4$ partial pressure. As indicated in Section 7.3.2, mass transport limits the deposition such that the flux arriving at the substrate is proportional to the rate of chemical reaction of the reacting species at the substrate interface. The flux J_2 , which is proportional to the rate of chemical reaction of the reactants on the growing surface (resulting from partial pressures), and the growth rate k of the layer are related by $k = v_k J_2$, where v_k is the molecular volume of the crystal [51]. This explains the linear growth rate of the layers with partial pressure, and is in agreement with Figure 7-28.

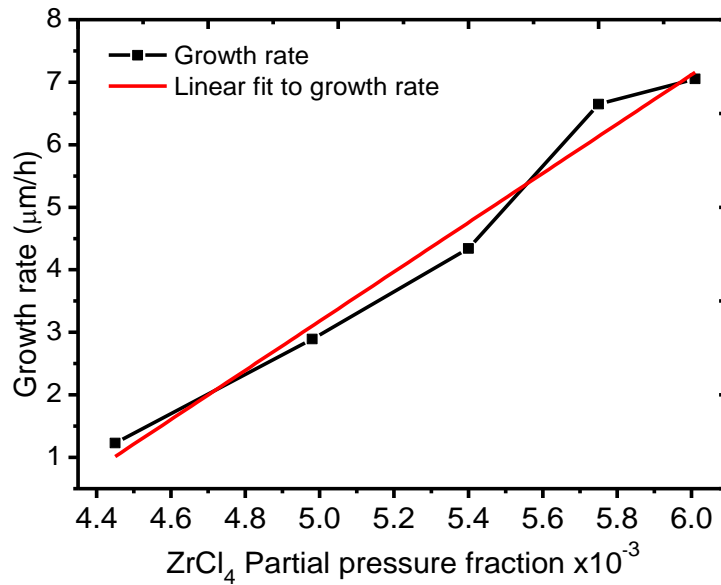


Figure 7-29: Effect of ZrCl₄ inlet partial pressure fraction on growth rate.

Another aspect accounting for the variation of growth rate with partial pressure is the concentration of the reacting species in the gas mixture. At low ZrCl₄ partial pressures, there are more carbon-containing species than zirconium containing species in the reaction chamber, which accounts for the low ZrC growth rate. This is due to the fact that the growth rate of ZrC layers is limited by the availability of Zr-containing species. Therefore any increase in ZrCl₄ partial pressure boosted the ZrC layer growth rate. For further illustration, an HSC chemistry software (a thermodynamic chemical software program) [6] was used to study the behaviour of the reacting species. Figure 7-30 shows the ZrCl₄ concentration dependence speciation curve for the ZrCl₄-CH₄-H₂ system. According to Figure 7-30, at a deposition temperature of 1400 °C, the methane gas was fully decomposed to carbon and hydrogen, while ZrCl₄ remained in its gaseous form. So there was always an excess of carbon and therefore at low ZrCl₄ partial pressures (like those used in this study) the reaction between the active species is zirconium limited.

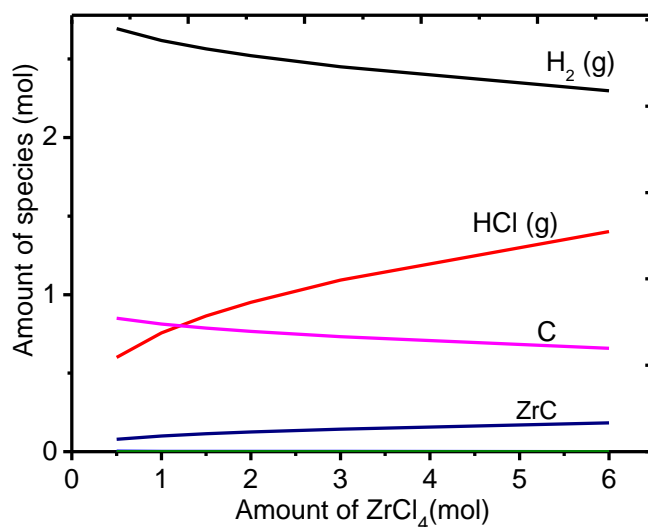


Figure 7-30: $ZrCl_4$ concentration dependence speciation curve for the $ZrCl_4-CH_4-H_2$ feed system at 1400 °C.

7.3.4 Microstructural analysis

Figure 7-31 shows the XRD patterns of ZrC films deposited at 1400 °C for different $ZrCl_4$ partial pressures. For confirmation purposes, the diffraction patterns were matched with the standard ICDD (International Centre for Diffraction Data Release 2007) file numbers ZrC: 03-065-8833 and C: 00-008-0415. Ten reflections (111), (200), (220), (311), (222), (400), (331), (420), (422) and (511) corresponding to $2\theta^\circ$ values of about 32.9, 38.3, 55.2, 65.9, 69.2, 81.9, 91.2, 94.3, 106.8 and 116.8, respectively, are indicated by z in Figure 7-31. The ZrC peaks present were indexed within a cubic rock-salt (NaCl) structure type.

The carbon phase present was found to be hexagonal graphite with its reflections (hkil) of (0002), $(10\bar{1}0)$, $(10\bar{1}1)$, $(10\bar{1}2)$, (0004), $(10\bar{1}3)$, $(11\bar{2}0)$, $(11\bar{2}2)$, (0006), $(20\bar{2}1)$ and $(11\bar{2}4)$ at $2\theta^\circ$ values of about 26.5, 42.4, 44.6, 50.7, 54.9, 60.0, 77.5, 83.5, 87.1, 94.1 and 101.8 respectively. In Figure 7-31 only the most prominent carbon peaks are indicated by c. The intensities of the carbon peaks increased with a decrease in $ZrCl_4$ partial pressure. The decrease in concentration of $ZrCl_4$ vapour as the partial pressure was reduced resulted in excess carbon (from the decomposition of methane), which was deposited as free carbon

alongside ZrC. As illustrated in Figure 7-30, all of the methane gas is decomposed into H₂ and carbon, while the ZrCl₄ remains in gaseous form throughout the experimental run. The amount of carbon from methane is normally higher than ZrCl₄ (see Table 7-9), therefore leading to C being deposited alongside ZrC.

The preferred orientation as determined from the texture coefficient calculated using the Harris method [23,42] was found to vary with ZrCl₄ partial pressure. At the lowest ZrCl₄ partial pressure fraction of 4.45×10^{-3} , the (111) diffraction plane was the preferred orientation. When the ZrCl₄ partial pressure fraction increased to 4.98×10^{-3} and 5.40×10^{-3} , the preferred orientation shifted to (200) and finally at higher partial pressure fractions of 5.72×10^{-3} and 6.01×10^{-3} , the preferred orientation changed to (220). This is due to the growth competition among different crystal planes occurring during deposition, resulting from the differences in surface energies and/or growth anisotropies. At low ZrCl₄ partial pressure, the arrival rate of Zr atoms at the growth surface is low enough for equilibrium crystal growth conditions to be achieved. Therefore, one would expect the planes with the minimum surface energy to grow preferentially compared to those with higher surface energies, thereby minimising the Gibbs free energy of the crystallites, in accordance with Wulff's law [54]. Among all the ZrC planes, the (111) plane has the lowest surface energy, because of the fact that its surface atoms are the most densely packed per unit area. Higher index planes are difficult to form, because they have relatively long Zr-C distances. As the ZrCl₄ partial pressure was increased, the higher arrival rate of ZrCl₄ atoms at the substrate surface resulted in increased atomic collisions and, thus, interacting molecules which allowed for non-equilibrium crystal growth to take place. This implies that the high-index crystallographic planes (200) and (220) also formed.

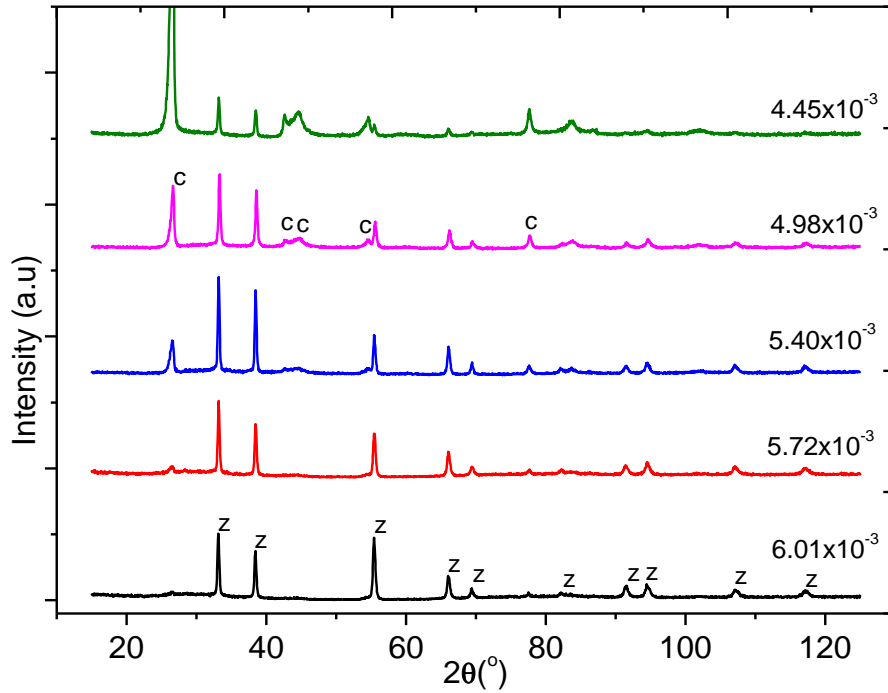


Figure 7-31: XRD patterns of ZrC layers deposited at 1400 °C for different ZrCl₄ partial pressure fractions.

7.3.5 Lattice parameter, lattice strain and residual stress

The lattice parameter (a) of the ZrC layers were determined from the Miller indices (hkl) and interplanar spacings d of the various planes [23] using Equation (5-2).

The lattice parameter values obtained by this method were found to vary from one diffraction plane to another for the same sample. Therefore, Nelson-Riley plots were used to determine the corrected lattice parameter value for each ZrC deposited layer. Nelson-Riley plots are plots of the lattice parameter calculated from Equation (5-2) and the error function $f(\theta)$ calculated from Equation (7-27) [55]:

$$f(\theta) = \frac{1}{2} \left(\frac{\cos^2 \theta}{\sin \theta} + \frac{\cos^2 \theta}{\theta} \right) \quad (7-27)$$

The intercepts of Nelson-Riley plots (i.e. at $\theta=90$) gives the corrected value of the lattice parameter of a particular sample. The Nelson-Riley plots are indicated in Figure 7-32. The

corrected lattice parameter values obtained from the plots decreased from 4.6995 Å to 4.6938 Å with an increase in the ZrCl₄ partial pressure from 4.45×10⁻³ to 6.01×10⁻³ (see Figure 7-33). This observation may be due to the presence of defects in the ZrC layer at low ZrCl₄ partial pressures. At low partial pressure, there are more carbon inclusions in the lattice as illustrated in Figure 7-31. The carbon inclusions in the lattice of the ZrC layers are reduced when the ZrCl₄ partial pressure is increased. The reduction in the carbon inclusions in the ZrC layer might have led to lattice contraction, which then resulted in a reduced lattice parameter value. The presence of carbon inclusions might have increased the distance between the neighbouring atoms in the ZrC lattice structure. This gives rise to relaxation of the lattice causing the lattice parameter to increase.

All the corrected lattice parameter values of the as-deposited ZrC layers were within the range reported for ZrC bulk material (4.6890–4.7017 Å [56–59]). However, it is important to note that layers deposited by CVD always experience some kind of strain [60] and this may be the reason for any variation of the lattice parameter value from the “actual expected value”.

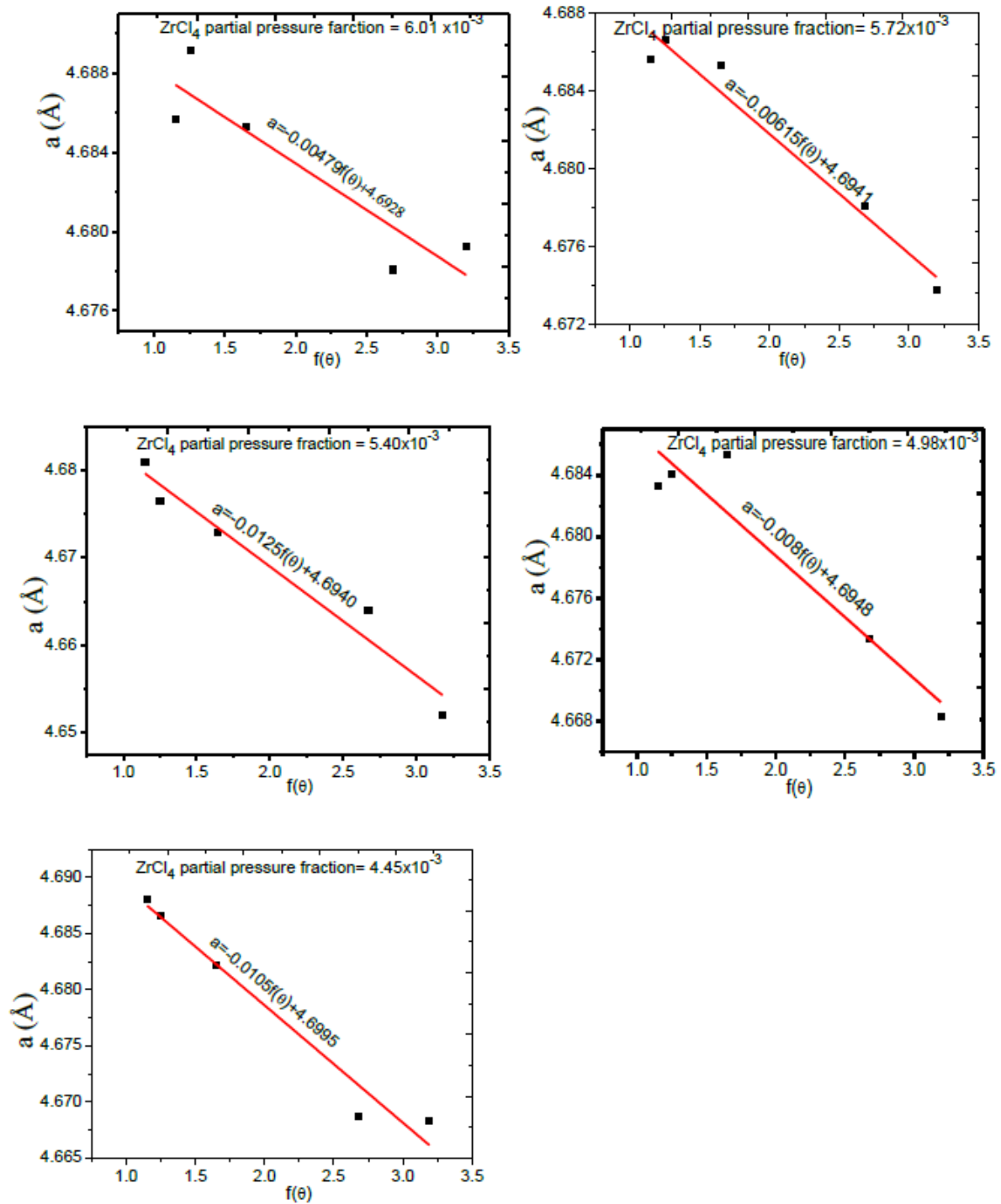


Figure 7-32: Nelson-Riley plots (plots of the lattice parameters as a function of the error function) for different $ZrCl_4$ partial pressure fractions.

Strain measures the level of distortion and crystal imperfection in the material and was calculated from peak broadening at half with full maxima and diffraction angle [37] as indicated by Equation (5-11). There was a decrease in lattice strain from 4.08×10^{-3} to 3.72×10^{-3} as the $ZrCl_4$ partial pressure was increased from 4.45×10^{-3} to 6.01×10^{-3} , as shown in

Figure 7-34. This is because when the $ZrCl_4$ partial pressure was increased the concentration of defects in the as-deposited ZrC layer reduced, which resulted in a reduction in the lattice strain. Also, when the layer thickness increased due to an increase in partial pressure, the influence of the substrate on the layer is reduced. This in turn also reduces the strain in the grown layer.

7.3.6 Average crystallite size and dislocation density

The average crystallite size of ZrC layers deposited at different $ZrCl_4$ partial pressure was determined from Scherrer's formula [23] given by Equation (5-9). The effect of instrumental broadening was subtracted from the XRD profile before calculating the values of crystallite sizes. The values of average crystallite size changed from 21.5 nm to 23.6 nm as the $ZrCl_4$ partial pressure fraction changed from 4.45×10^{-3} to 6.01×10^{-3} , as can be seen from Figure 7-33. As shown in Figure 7-30, methane decomposes into carbon and hydrogen long before the decomposition of $ZrCl_4$. Therefore, at low $ZrCl_4$ partial pressures, carbon is in excess of Zr-containing species and carbon may even deposit on the substrate before ZrC can deposit. The presence of this free carbon will restrict the ZrC crystal growth and crystallisation process. The thermodynamics and kinetics involving ZrC deposition are different from those involving $ZrC+C$, so are their nucleation and growth mechanisms. When the $ZrCl_4$ partial pressure was increased, the Zr-containing species combining with the carbon containing species increased, consequently reducing the amount of free carbon in the layer. A reduction in the amount of free carbon results into increased crystallite size, since carbon inclusions interference with ZrC crystal growth.

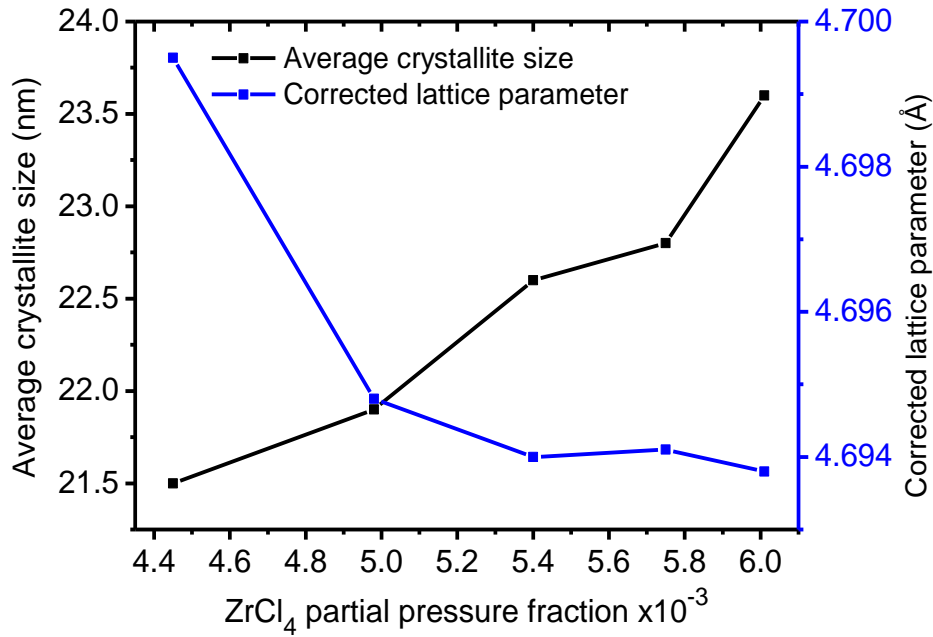


Figure 7-33: Influence of $ZrCl_4$ partial pressure on average crystallite size and lattice parameter.

Assuming a random distribution of dislocations, the number of dislocation lines crossing a unit area in the layer of the deposited ZrC (here referred to as dislocation density L) was calculated from Williamson-Smallman's formula [41] [61] given by Equation (7-28):

$$L = \frac{1}{D^2} \quad (7-28)$$

where D is the average crystallite size. Dislocation density is one of the indications of the number of defects in the layer and it was found to vary from $2.16 \times 10^{15} \text{ m}^{-2}$ to $1.81 \times 10^{15} \text{ m}^{-2}$ as the partial pressure fraction varied from 4.45×10^{-3} to 6.01×10^{-3} (see Figure 7-34).

It is evident from Figure 7-34 that as the partial pressure increased, the lattice strain and the dislocation density decreased. This may be attributed to a reduction in carbon inclusions which can give rise to extended defects such as dislocations. The increase in the average crystallite size results in a decrease in the grain boundaries in ZrC layers.

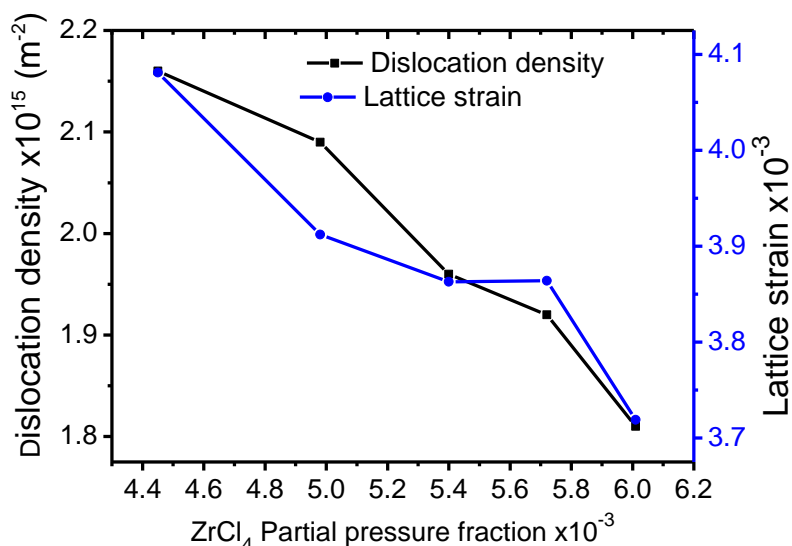


Figure 7-34: Variation of dislocation density and lattice strain with ZrCl₄ partial pressure fraction.

7.3.7 Surface morphology analysis

Figure 7-35 shows the FE-images of ZrC layers deposited at 1400 °C at different ZrCl₄ partial pressures. At the low ZrCl₄ partial pressure fraction of 4.45×10^{-3} (Figure 7-35 (a)), the layer had small crystals tending to cluster together surrounded and by lots of voids. As the ZrCl₄ partial pressure increased, there was increased aggregation of the particles. This resulted in a decrease in both the size and number of voids in the ZrC layer, causing the layer to become increasingly homogeneous. The ZrC layer coverage of the substrate surface was also enhanced. At a ZrCl₄ partial pressure fraction of 6.01×10^{-3} (Figure 7-35 (e)), almost all the clusters joined together, almost completely eliminating the voids. There was no distinctive change in the shape of the crystals as the partial pressure was varied. In line with the average crystallite size as determined by XRD, the particles in the SEM images also increased in size with increasing ZrCl₄ partial pressure. There was an increased tendency of clusters growing on top of each other and whose sizes also increased with an increase in ZrCl₄ partial pressure. It can be deduced that the layer surface grew by both the additions of atoms and the coalescence of primary particles, since crystals tend to pile on top of each other and also merge as they increase in size.

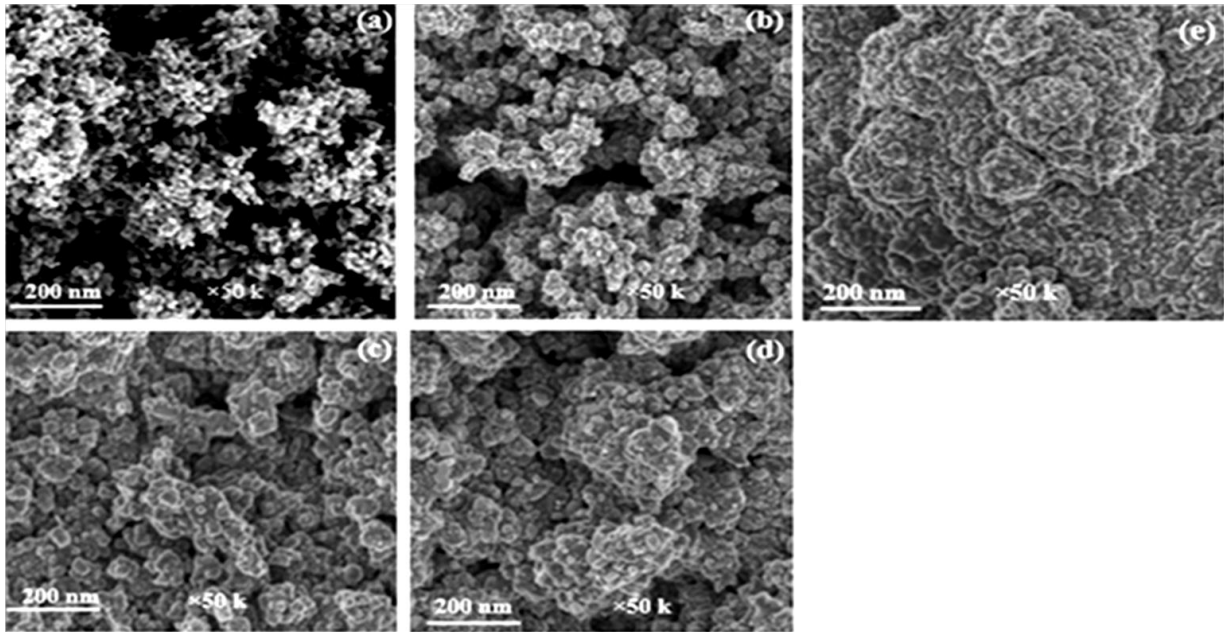


Figure 7-35: FE-SEM images of ZrC layers deposited at 1400 °C at different ZrCl₄ partial pressure fractions: (a) 4.45×10^{-3} ; (b) 4.98×10^{-3} ; (c) 5.40×10^{-3} ; (d) 5.72×10^{-3} ; (e) 6.01×10^{-3} .

7.4 Time dependence of microstructural and morphological evolution of ZrC layers

7.4.1 Introduction

The growth characteristics and properties of ZrC layers grown by CVD are greatly influenced by the deposition conditions. These include the deposition temperature and time, the precursor partial pressures and compositions, the reactor geometry, and the level and state of vacuum in the reaction chamber, among others. Of these conditions, the effect of deposition time on the growth behaviour of ZrC layers has been the least emphasised. And yet certain tendencies in the deposition process and in the microstructural evolution of CVD layers may be evident in the early stages of the growth process. A particular deposition time is required for these growth process steps to reach their fullest, so as to realise quality deposit. This deposition time may depend on the layer being deposited, deposition temperature, nature of the precursors and other deposition parameters.

The deposition ZrC layers were carried out at 1400 °C for different deposition times from 0.5 h to 2.5 h at atmospheric pressure. For each experimental run 6 g of ZrCl₄ powder were

vaporised at 300 °C in a static vaporisation system. The flow rates were maintained at 15 sccm, 862 sccm and 843 sccm for methane, hydrogen and argon respectively.

In this subsection, the flow behaviour of the $ZrCl_4$ precursor in a static vaporiser system at different deposition times was analysed. Furthermore, we have examined the time dependence of microstructural and morphological evolution of the as-deposited ZrC layers. Deposition time is a very important growth parameter that controls the quality of the deposit, the thickness of the layer and its uniformity, among others.

7.4.2 Layer thickness and growth rate

Figure shows the variation in layer thickness and growth rate of as-deposited ZrC layers at various deposition times. There was a general increase in layer thickness as deposition time was increased. The increase in layer thickness was more rapid between 0.5 h and 1.0 h. After 1.0 h, the increase in layer thickness was very small, even when the deposition time was continuously increased, as reflected by the growth rate curve shown in Figure 7-36. The growth rate was more rapid between 0.5 h to 1 h and there after it declined sharply. This observation may be due to loading the same amount of $ZrCl_4$ powder in the vaporiser system for all deposition times. The continuous transportation of $ZrCl_4$ vapour by argon reduces the amount of vapour generated and delivered into the reaction chamber. Even though the feed lines were wrapped with an electrical heat tracing tape, there was still a tendency of $ZrCl_4$ accumulating along the vaporiser feed line to the reaction chamber. This was evidenced by the increase in mass of the vaporiser with deposition time. If the rate at which the amount of $ZrCl_4$ accumulated along the vaporiser feed line was not constant, this might also have affected the amount of $ZrCl_4$ delivered to the reaction chamber, hence affecting the layer growth rate. Figure 7-36 shows the variation of the amount of $ZrCl_4$ consumed from the vaporiser and $ZrCl_4$ mass flow rate to the reaction chamber. It was observed that as the deposition time increased, the amount of $ZrCl_4$ transported into the reaction chamber

increased rapidly between 0.5 h to 1.0 h. Beyond 1 h the increase in the amount of $ZrCl_4$ consumed was not very significant. Therefore, the reduction in the supply of $ZrCl_4$ as the deposition time increased was the reason for the observed trend in both the layer thickness and the growth rate.

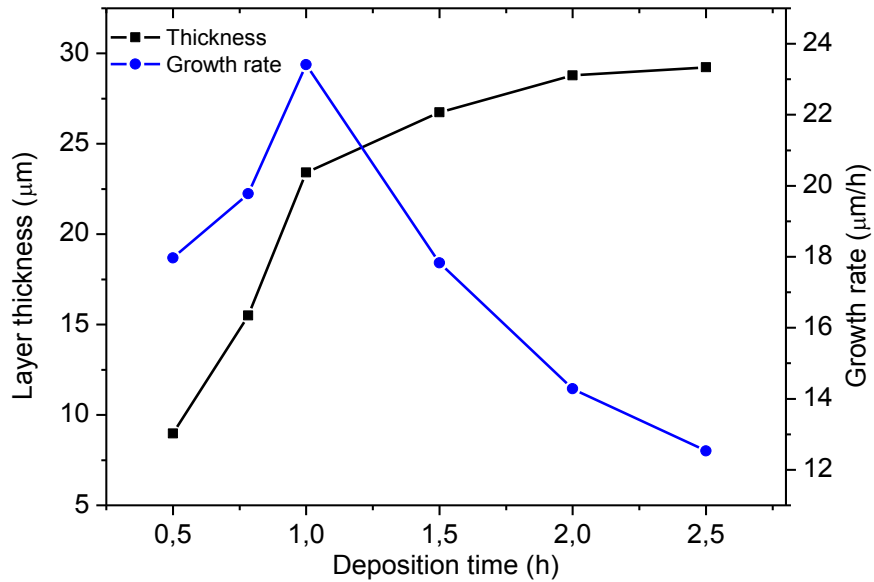


Figure 7-36: Influence of deposition time on layer thickness and growth rate.

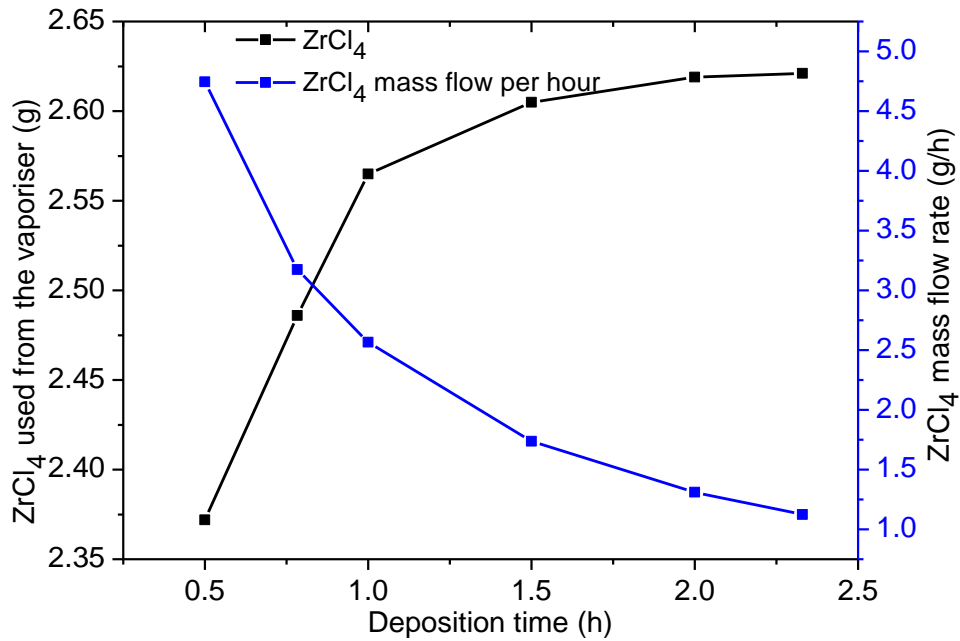


Figure 7-36: Variation of the amount of $ZrCl_4$ used during the ZrC deposition process using the $ZrCl_4$ static vaporiser.

7.4.3 XRD structural and phase analysis

The XRD patterns of ZrC layers deposited for 0.5 h, 1.0 h, 1.5 h, 2.0 h and 2.5 h are shown in Figure 7-38. These patterns belong to a face centred cubic structure. These diffraction patterns revealed only ZrC peaks when matched with the standard data file number ICDD ZrC: 03-065-8833. The diffraction patterns had well-defined sharp Bragg peaks. This indicated that the ZrC layers deposited at all deposition times possessed a good degree of crystallinity. Figure 7-38 also shows that changes in the deposition time had an effect on both the peak intensities and the orientation of the planes, as indicated in Figure 7-39. The preferred orientation as deduced from the texture coefficient determined by the Harris method [23,42] revealed that, the (220) diffraction plane was the preferred orientation for all deposition times. However, its texture coefficient values reduced from 3.32 to 1.02 as the deposition time was increased from 0.5 h to 2.5 h. The (111) and (200) diffraction planes were randomly oriented for all deposition times. The texture coefficient values of (111) and (200) planes increased gradually with deposition time from 0.39 to 0.96.

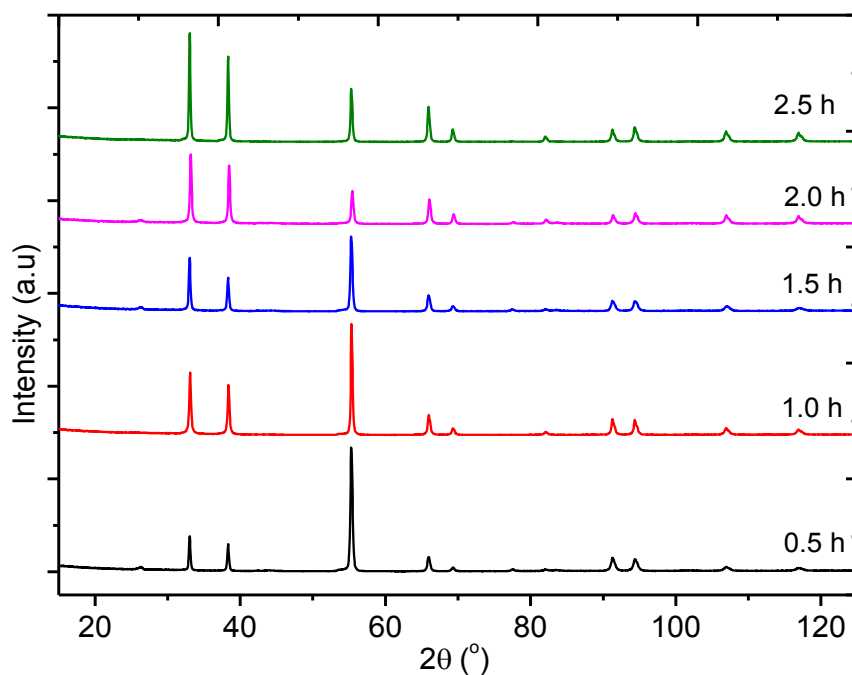


Figure 7-38: XRD pattern of ZrC layers deposited at different deposition times.

At the very early stages of nucleation crystallites are randomly oriented [62]. As the layer thickness is increased crystallites with the fastest growing crystallographic planes normal to the substrate will envelope the other crystallites and determine the final orientation of the deposited layer (evolutionary selection rule) [62] [63]. However, crystallites grow such that they minimize the sum of the surface energy and strain energy in an attempt to attain equilibrium conditions. Since these energies vary from one crystallographic plane to another, the orientation of planes is not always the same. In this case small crystallites were observed for short deposition times (as depicted by the SEM images in Section 7.4.6). The reason for this was the high growth rate of the ZrC layer, which introduced defects. According to the step-flow model of crystal growth [64] these defects act as growth points for new (small) crystallites. As was shown in Figure 7-36, the growth rate decreased with time. This favoured the growth of larger crystals. The growth process was performed at high temperature, i.e. 1400 °C. Consequently, with increasing time the crystallites also grew into larger crystals due to the continued diffusion of the ZrC molecules, acting as source material for the crystallites. Furthermore, small crystallites have high surface energies compared to large crystallites. This favours the growth of high energy crystallographic planes, thereby increasing the areas of the low energy planes in line with Wulf's law [54]. In addition, due to their high surface energies the small crystals gets absorbed into the larger crystals (Ostwald ripening) to minimise the total surface energy. This parasitic growth of the crystals maximises the areas of crystal planes with lower surface energies, also in line with Wulf's law. This explains the reason why the (220) plane was the initial preferred orientation (see Figure 7-39) and why the texture coefficient value gradually decreased with increasing deposition time. Simultaneously, there were gradual increases in the texture coefficient values of the low energy planes (111) and (200).

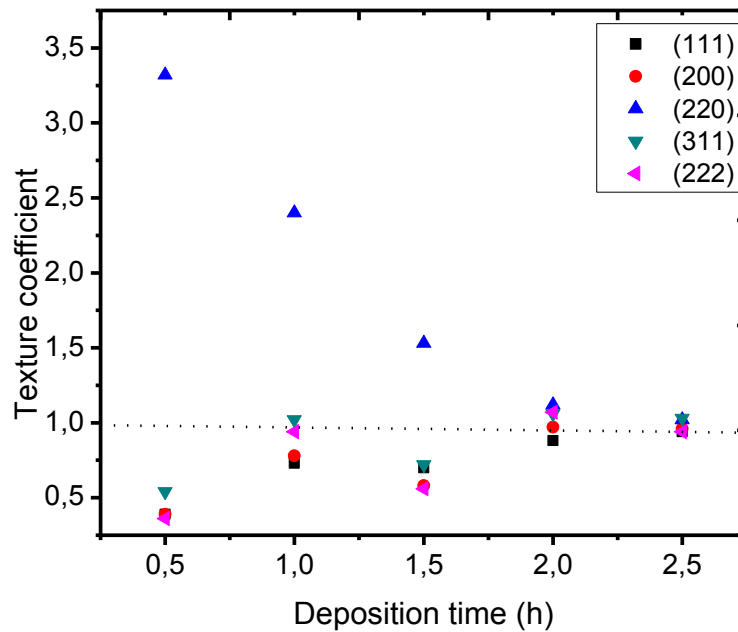


Figure 7-39: Variation of texture coefficient with deposition time.

It is also important to note that the deposition in this study was conducted at high temperatures (1400 °C). It has been reported that at 1400 °C the CVD growth process of ZrC is mass transport controlled [53]. Kajikawa et al. [65] reported that the most densely packed planes (i.e (111)), grow faster than other crystallographic planes in the surface reaction controlled regime, whereas the (220) plane grows faster in the adsorption controlled regime. These results agree with the above findings.

7.4.4 Microstructure evolution

The average crystallite size was calculated from the Scherrer formula given by Equation (5-9). The average crystallite size of the as deposited ZrC layers was found to increase from 27.8 nm to 32.3 nm as the deposition time was increased from 0.5 h to 2.5 h, as indicated in Figure 7-. This is expected, since the continuous supply of the reactants may contribute to further film growth and hence an increase in crystallite size. Other reasons for this crystallite size increase were discussed in the Section 7.4.2. A sharp increase in average crystallite size was observed between 0.5 h to 1.0 h and thereafter the average crystallite size increased gently.

This observation may be due the variation in the supply of $ZrCl_4$ towards the growing surface. At the start, the supply of Zr-containing species per unit time was high and it gradually reduced as deposition time was increased.

The number of crystallites per unit area (N) was determined from Equation (7-29),

$$N = \frac{x}{D^3} \quad (7-29)$$

Here D is the average crystallite size and x is the layer thickness [66,67]. Figure 7-40 also shows that the number of crystallites per unit area increased with an increase in the time of deposition. It can also be observed that the amount of $ZrCl_4$ delivered per unit time in the reaction chamber also affects the number of crystallites per unit area of the layer deposited. One would expect the number of crystallites per unit area to decrease with an increase in crystallite size. However, this is not the case, since increasing the layer thickness increases the area and therefore more crystallites can be accommodated. This is an indication that the layer thickness grows faster than the crystallite size.

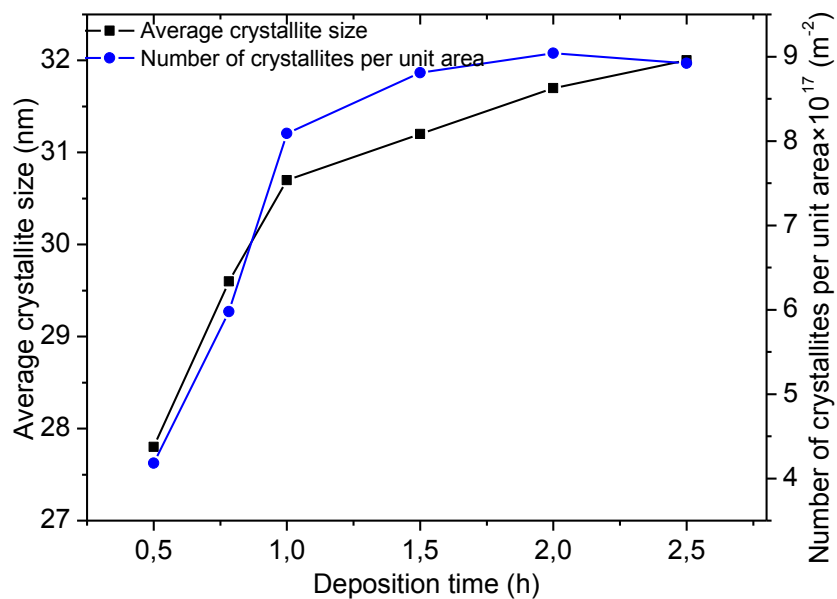


Figure 7-40: Dependence of average crystallite size and number of crystallites per unit area on deposition time.

7.4.5 Raman analysis

Raman spectroscopic analysis was used to establish the purity and composition of the deposited ZrC layers. Raman spectroscopic analysis produce a characteristic spectrum for materials, depending on the vibrational modes of their molecules [68]. Figure 7-41 shows the Raman spectra acquired at room temperature for samples deposited for different deposition times. ZrC possesses a crystal structure like that of NaCl. Stoichiometric compounds with a NaCl structure have all their atoms occupying sites of inversion symmetry and therefore do not allow first-order Raman scattering [69,70]. This means that stoichiometric ZrC is not Raman active and hence no ZrC Raman peak can be detected. However, within the measured spectral range the deposited layers revealed some peaks at Raman shifts of about 210, 290, 522 cm^{-1} , 625 cm^{-1} , 1350 cm^{-1} and 1580 cm^{-1} (see Figure 7-41 and the figure inserted). This means that the deposited ZrC layers are ideally not stoichiometric or contains some level of impurities. It has been reported that the ZrC primitive cell has 2 atoms with 6 vibrational modes, half of which are acoustic and the other half are optical modes [71]. Kim et al. [69] reported that a ZrC Raman spectrum with peaks at around 210 cm^{-1} and 280 cm^{-1} representing acoustic branches and Raman peaks at 540 cm^{-1} and 600 cm^{-1} representing optical branches due to the presence of carbon vacancies in the ZrC structure. The reason for this is that the vacancies in the ZrC structure interrupts the local symmetry, permitting the defect-induced Raman scattering to be detected [69,72]. This means that at low deposition times we have more carbon vacancies in the ZrC structure (i.e. we have a sub-stoichiometric ZrC). As was discussed in Section 7.4.2, for low deposition times the growth rate of the ZrC layer was very high. This high growth rate introduced more defects, including carbon vacancies, into the layer. As the deposition time was increased from 1.0 h to 2.5 h, the peaks at about 210, 290, 522 cm^{-1} and 625 cm^{-1} reduced. Instead, the free carbon peaks originating from carbon inclusions in the ZrC matrix, at around 1350 cm^{-1} and 1580 cm^{-1} became more

prominent. This means that the number of carbon vacancies decreased with a growth in free carbon inclusions. The carbon peaks are evident by the presence of the D and G-peak. The D-band is associated with defects in graphitic materials. The G-peak is associated with in-plane vibrations of C–C bonds and is a measure of graphitization or degree of metallicity of graphitic materials [73,74]. The presence of free carbon was detected by Raman but not by XRD measurements, because Raman is more sensitive to structural changes than XRD. It should be noted that, the carbon observed in the layers is not from the graphite substrate, because of the presence of amorphous carbon.

It was observed that for growth time 0.5 h and 1 h the D and G-peaks are broad. This can be seen from the FWHM variation, illustrated by Figure 7-42. This shows that for short deposition times, there is poor crystallization of the free carbon, which improves as the deposition time is increased, in line with the crystal growth model discussed in Section 7.4.2. For short the growth times (0.5 h and 1.0 h), the free carbon is more of amorphous type than graphitic type, since the 1500 cm^{-1} Raman peak is broad (see Figure 7-41). This is typical for amorphous sp^2 bonded carbon [75].

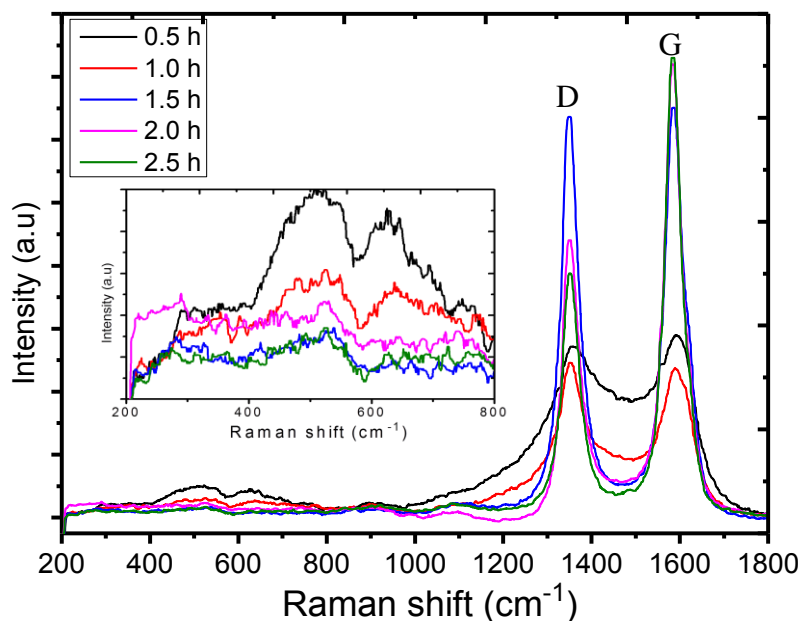


Figure 7-37: Raman spectroscopy analysis of ZrC layers at different deposition times.

Also, as the deposition time increased from 0.5 h to 2.5 h, there was a shift to the left of both the D and G band (from 1359 cm^{-1} to 1348 cm^{-1} and from 1590 cm^{-1} to 1581 cm^{-1} , respectively). There was an overall increase in intensity of the D and G-peaks as the deposition time was increased, as observed from Figure 7-42. This implies that the longer the deposition time the higher the amount of free carbon co-deposited. This was due to the decreased flow of ZrCl_4 and constant supply of methane, the source for the carbon atoms, to the reaction surface, as explained in [76]. However, compared to the intensities of the D-peak (I_D), the intensities of the G-peak (I_G) increased more as the deposition time increased. This was due to the decreasing supply of Zr atoms to the reaction (i.e. growth) surface and the constant supply of C atoms. This relative increase in C atoms led to a higher growth rate of the carbon in the carbon inclusions. In line with this argument, the values of I_D/I_G given in Figure 7-42 decreases with an increase in deposition time.

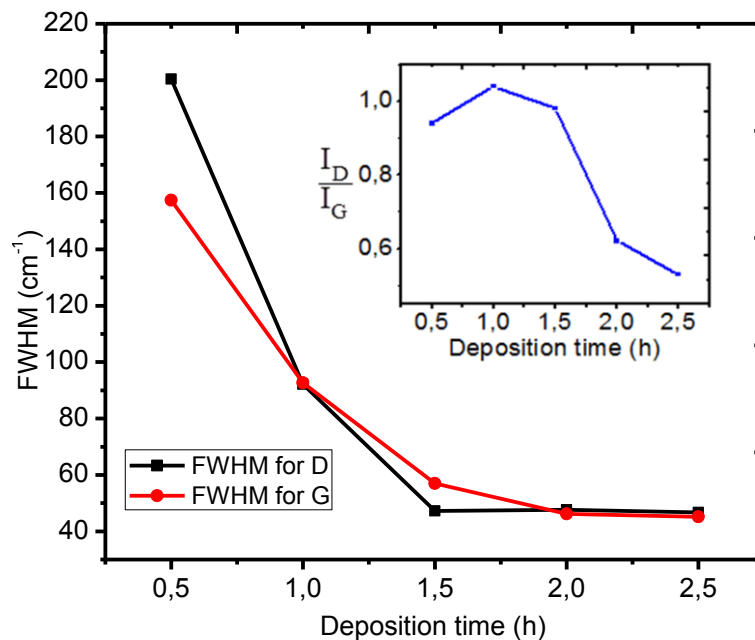


Figure 7-38: Variance of FWHM of D and G carbon peaks with deposition time. The insert indicates the variation of the I_D/I_G with time.

The I_D/I_G ratio is a measure of the presence of defects in the structure of the carbon materials. As already mentioned, the G-peak is a result of in-plane vibrations of sp^2 bonded carbon

atoms whereas, the D-peak is due to out of plane vibrations attributed to the presence of structural defects [73] [77]. This means that I_D/I_G is related to the sp^3/sp^2 ratio. As the deposition time was increased there was a transformation from sp^3 material to sp^2 material, meaning that there was a reduction in the defects in the structure of the carbon material. Thus, the free carbon in the deposited layers became more graphitic. This is supported by the corresponding decrease in the FWHM values of the G-peak.

7.4.6 Morphological evolution

Figure 7-43 shows the surface morphology of ZrC layers deposited at 1400 °C for different deposition times. It was observed that the morphology of the ZrC varied with deposition time.

For a deposition time of 0.5 h, the ZrC layer is consists of small particles. The surface is relatively smooth and flat with uniform particle size. The deposition time of 1 h, the small particles start to form clusters. When the deposition time was further increased almost all the crystals formed clustered and the size of the clusters grew larger. The growth of protrusions on SiC was previously explained by preferential thermophoretic deposition of particles [65].

Even though the average crystallite size calculated from the XRD (using Scherrer's equation) increased with deposition time just as size of crystals observed from the SEM micrographs, they may not easily be compared because of the coalescence of crystals into aggregates.

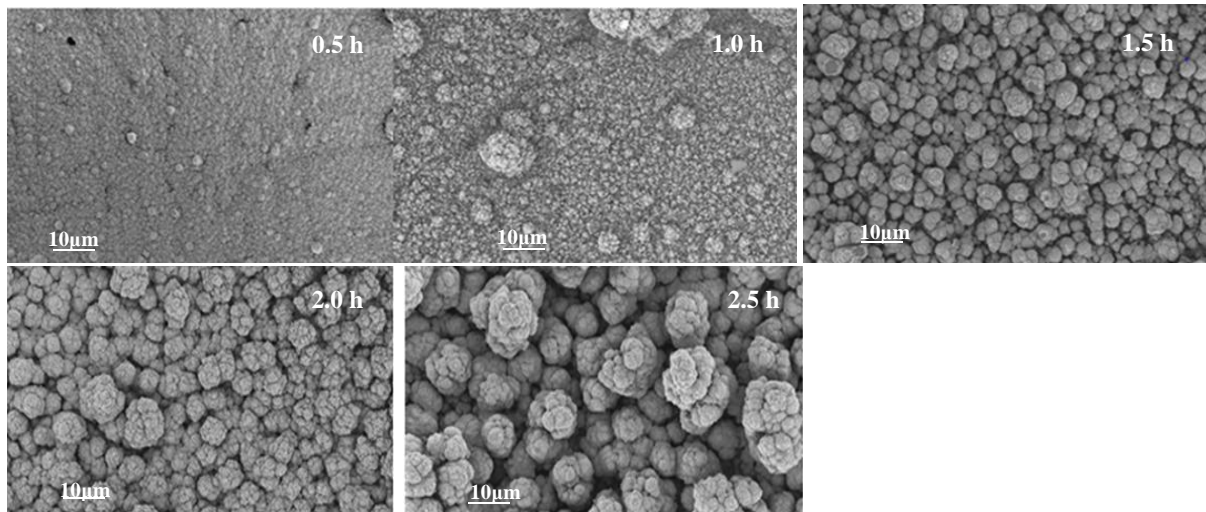


Figure 7-43: The evolution of surface morphology with an increase in deposition time.

7.5 References

- [1] D.C. Montgomery, Design and analysis of experiments, John Wiley & Sons, 2008.
- [2] M.W. Chase Jr, J.L. Curnutt, R.A. McDonald, A.N. Syverud, JANAF thermochemical tables, 1978 supplement, J. Phys. Chem. Ref. Data. 7 (1978) 793–940.
- [3] NIST, NIST-JANAF Thermochemical Tables, NIST-JANAF Thermochem. Tables. (2013). <http://kinetics.nist.gov/janaf/> (accessed July 30, 2015).
- [4] X.-T. Yan, Y. Xu, Chemical vapour deposition: an integrated engineering design for advanced materials, 1st ed., Springer-verlag, London, 2010.
- [5] S. Jarungthammachote, A. Dutta, Equilibrium modeling of gasification: Gibbs free energy minimization approach and its application to spouted bed and spout-fluid bed gasifiers, Energy Convers. Manag. 49 (2008) 1345–1356.
- [6] Outotec, HSC Chemistry 7 (Thermo-chemical software), (2007).
- [7] J. Wagner, C. Mitterer, M. Penoy, C. Michotte, W. Wallgram, M. Kathrein, The effect of deposition temperature on microstructure and properties of thermal CVD TiN coatings, Int. J. Refract. Met. Hard Mater. 26 (2008) 120–126.
- [8] Q. Liu, L. Zhang, L. Cheng, Y. Wang, Morphologies and growth mechanisms of zirconium carbide films by chemical vapor deposition, J. Coatings Technol. Res. 6 (2009) 269–273.
- [9] Y. Wang, Q. Liu, J. Liu, L. Zhang, L. Cheng, Deposition mechanism for chemical vapor deposition of zirconium carbide coatings, J. Am. Ceram. Soc. 91 (2008) 1249–1252.
- [10] L. Eriksson, Design of experiments: principles and applications, MKS Umetrics AB, 2008.
- [11] H.K. Kansal, S. Singh, P. Kumar, Parametric optimization of powder mixed electrical discharge machining by response surface methodology, J. Mater. Process. Technol.

- 169 (2005) 427–436.
- [12] J. Hao, F. Wang, X. Wang, D. Zhang, Y. Bi, Y. Gao, X. Zhao, Q. Zhang, Development and optimization of baicalin-loaded solid lipid nanoparticles prepared by coacervation method using central composite design, *Eur. J. Pharm. Sci.* 47 (2012) 497–505.
- [13] R.H. Myers, D.C. Montgomery, C.M. Anderson-Cook, *Response surface methodology: process and product optimization using designed experiments*, John Wiley & Sons, 2016.
- [14] Stat-Ease, *Design expert version 7.0.0*, Stat-Ease Inc. (2005).
- [15] M.A. Bezerra, R.E. Santelli, E.P. Oliveira, L.S. Villar, L.A. Escaleira, Response surface methodology (RSM) as a tool for optimization in analytical chemistry, *Talanta*. 76 (2008) 965–977.
- [16] D. Bas, I.H. Boyacı, Modeling and optimization I: Usability of response surface methodology, *J. Food Eng.* 78 (2007) 836–845.
- [17] R.L. Mason, R.F. Gunst, J.L. Hess, *Statistical Design and Analysis of Experiments*, 2003.
- [18] A. Vohra, T. Satyanarayana, Statistical optimization of the medium components by response surface methodology to enhance phytase production by *Pichia anomala*, *Process Biochem.* 37 (2002) 999–1004.
- [19] H.O. Pierson, *Handbook of chemical vapor deposition: principles, technology and applications*, 2nd ed., William Andrew, New York, 1999.
- [20] Y. Katoh, G. Vasudevamurthy, T. Nozawa, L.L. Snead, Properties of zirconium carbide for nuclear fuel applications, *J. Nucl. Mater.* 441 (2013) 718–742.
- [21] Y. Yang, W.-Y. Lo, C. Dickerson, T.R. Allen, Stoichiometry effect on the irradiation response in the microstructure of zirconium carbides, *J. Nucl. Mater.* 454 (2014) 130–135.
- [22] Y. Huang, B.R. Maier, T.R. Allen, Irradiation-induced effects of proton irradiation on zirconium carbides with different stoichiometries, *Nucl. Eng. Des.* 277 (2014) 55–63.
- [23] B.D. Cullity, S.R. Stock, *Elements of X-ray Diffraction*, 1st ed., Addison-Wesley Publishing company Inc, Massachusetts, 1956.
- [24] S. Veprek, Recent search for new superhard materials: Go nano!, *J. Vac. Sci. Technol. A.* 31 (2013) 50822.
- [25] S.P. Vanka, G. Luo, N.G. Glumac, Parametric effects on thin film growth and uniformity in an atmospheric pressure impinging jet CVD reactor, *J. Cryst. Growth.* 267 (2004) 22–34.
- [26] E.L. Cussler, *Diffusion: mass transfer in fluid systems*, Cambridge university press, 2009.
- [27] P.M. Martin, *Handbook of deposition technologies for films and coatings: science, applications and technology*, William Andrew, 2009.
- [28] C. Li, L. Huang, G.P. Snigdha, Y. Yu, L. Cao, Role of Boundary Layer Diffusion in Vapor Deposition Growth of Chalcogenide Nanosheets: The Case of GeS, *ACS Nano*.

- 6 (2012) 8868–8877.
- [29] M.S. Kim, J.S. Chun, Effects of the experimental conditions of chemical vapour deposition on a TiC/TiN double-layer coating, *Thin Solid Films*. 107 (1983) 129–139.
- [30] M. Henini, *Handbook of Thin-Film Deposition Processes and Techniques*, Second Edi, William Andrew, New York, 2000.
- [31] D.I. Fotiadis, S. Kieda, K.F. Jensen, Transport phenomena in vertical reactors for metalorganic vapor phase epitaxy: I. Effects of heat transfer characteristics, reactor geometry, and operating conditions, *J. Cryst. Growth*. 102 (1990) 441–470.
- [32] Y. Long, A. Javed, I. Shapiro, Z. Chen, X. Xiong, P. Xiao, The effect of substrate position on the microstructure and mechanical properties of SiC coatings on carbon/carbon composites, *Surf. Coatings Technol.* 206 (2011) 568–574.
- [33] S.K. Ghandhi, R.J. Field, A re-examination of boundary layer theory for a horizontal CVD reactor, *J. Cryst. Growth*. 69 (1984) 619–622.
- [34] W.K. Burton, N. Cabrera, F.C. Frank, The growth of crystals and the equilibrium structure of their surfaces, *Philos. Trans. R. Soc. London A Math. Phys. Eng. Sci.* 243 (1951) 299–358.
- [35] M. Ermrich, D. Opper, *XRD for the analyst: Getting acquainted with the principles*, PANalytical, Eindhoven, 2013.
- [36] K. Venkateswarlu, A.C. Bose, N. Rameshbabu, X-ray peak broadening studies of nanocrystalline hydroxyapatite by Williamson-Hall analysis, *Phys. B Condens. Matter*. 405 (2010) 4256–4261.
- [37] V.D. Mote, Y. Purushotham, B.N. Dole, Williamson-Hall analysis in estimation of lattice strain in nanometer-sized ZnO particles, *J. Theor. Appl. Phys.* 6 (2012) 1–8.
- [38] G. Janssen, Stress and strain in polycrystalline thin films, *Thin Solid Films*. 515 (2007) 6654–6664.
- [39] R. Sharma, D.P. Bisen, U. Shukla, B.G. Sharma, X-ray diffraction: a powerful method of characterizing nanomaterials, *Recent Res. Sci. Technol.* 4 (2012) 77–79.
- [40] S. Franssila, *Introduction to microfabrication*, John Wiley & Sons, 2010.
- [41] S. Aksoy, Y.Y.Y. Caglar, S. Ilıcan, M. Caglar, Effect of deposition temperature on the crystalline structure and surface morphology of ZnO films deposited on p-Si, *Adv. Control. Chem. Eng. Civ. Eng. Mech. Eng.* (2010) 227–231.
- [42] J.P. Enrıquez, X. Mathew, Influence of the thickness on structural, optical and electrical properties of chemical bath deposited CdS thin films, *Sol. Energy Mater. Sol. Cells*. 76 (2003) 313–322.
- [43] H.R. Moutinho, F.S. Hasoon, F. Abulfotuh, L.L. Kazmerski, Investigation of polycrystalline CdTe thin films deposited by physical vapor deposition, close-spaced sublimation, and sputtering, *J. Vac. Sci. Technol. A*. 13 (1995) 2877–2883.
- [44] U.C. Oh, J.H. Je, Effects of strain energy on the preferred orientation of TiN thin films, *J. Appl. Phys.* 74 (1993) 1692–1696.
- [45] G.T. Farmer, J. Cook, *Climate Change Science: A Modern Synthesis: Volume 1-The*

Physical Climate, Springer Science & Business Media, 2013.

- [46] D. Kim, M.J. Ko, J.Y. Park, M.S. Cho, W.-J. Kim, Influence of free carbon on the characteristics of ZrC and deposition of near-stoichiometric ZrC in TRISO coated particle fuel, *J. Nucl. Mater.* 451 (2014) 97–103.
- [47] Y. Zhu, L. Cheng, B. Ma, S. Gao, W. Feng, Y. Liu, L. Zhang, Calculation and synthesis of ZrC by CVD from ZrCl₄-C₃H₆-H₂-Ar system with high H₂ percentage, *Appl. Surf. Sci.* 332 (2015) 591–598.
- [48] J.H. Park, C.H. Jung, D.J. Kim, J.Y. Park, Temperature dependency of the LPCVD growth of ZrC with the ZrCl₄-CH₄-H₂ system, *Surf. Coatings Technol.* 203 (2008) 324–328.
- [49] K.W. Woo, S.I. Yeo, Dalton's Law vs, Amagat's Law for the Mixture of Real Gases, (1995).
- [50] R. Kossowsky, *Surface Modeling Engineering*, CRC Press, Florida, 1989.
- [51] J. Park, T.S. Sudarshan, *Chemical Vapor Deposition*, ASM International, Chicago, 2001.
- [52] M. Ohring, *Materials science of thin films*, 3rd ed., Academic press, London, 2002.
- [53] S. Biira, B.A.B. Alawad, H. Bissett, J.T. Nel, T.P. Ntsoane, T.T. Hlatshwayo, P.L. Crouse, J.B. Malherbe, Influence of the substrate gas-inlet gap on the growth rate, morphology and microstructure of zirconium carbide films grown by chemical vapour deposition, *Ceram. Int.* 43 (2017) 1354–1361.
- [54] C.-C. Liu, J.-H. Huang, C.-S. Ku, S.-J. Chiu, J. Ghatak, S. Brahma, C.-W. Liu, C.-P. Liu, K.-Y. Lo, Crystal Orientation Dynamics of Collective Zn dots before Preferential Nucleation, *Sci. Rep.* 5 (2015) 12533.
- [55] J.B. Nelson, D.P. Riley, An experimental investigation of extrapolation methods in the derivation of accurate unit-cell dimensions of crystals, *Proc. Phys. Society.* 57 (1945) 160–177.
- [56] P. Schwarzkopf, R. Kieffer, F. Benesousky, *Refractory hard metals: borides, carbides, nitrides and silicides*, Macmillan, New York, 1953.
- [57] H.O. Pierson, *Handbook of Refractory Carbides & Nitrides: Properties, Characteristics, Processing and Apps.*, Noyes Publications, New Jersey, 1996.
- [58] E.K. Storms, *The refractory carbides*, Academic Press, New York, 1967.
- [59] L. Toth, *Transition metal carbides and nitrides*, Academic press, New York, 1971.
- [60] G.S. Schajer, *Practical residual stress measurement methods*, John Wiley & Sons, 2013.
- [61] G.K. Williamson, R.E. Smallman, III. Dislocation densities in some annealed and cold-worked metals from measurements on the X-ray debye-scherrer spectrum, *Philos. Mag.* 1 (1956) 34–46.
- [62] Y. Kajikawa, N. Sugura, K. Hirosha, Mechanisms Controlling Preferred Orientation of Chemical Vapor Deposited Polycrystalline Films, *Solid State Phenom.* 93 (2003) 411–418.

- [63] Y. Kajikawa, Texture development of non-epitaxial polycrystalline ZnO films, *J. Cryst. Growth*. 289 (2006) 387–394.
- [64] W.-K. Burton, N. Cabrera, F.C. Frank, The growth of crystals and the equilibrium structure of their surfaces, *Philos. Trans. R. Soc. London A Math. Phys. Eng. Sci.* 243 (1951) 299–358.
- [65] Y. Kajikawa, N. Suguru, K. Hiroshi, Preferred orientation of chemical vapor deposited polycrystalline silicon carbide films, *Chem. Vap. Depos.* 8 (2002) 99–104.
- [66] S. Prabakar, M.Ā. Dhanam, CdS thin films from two different chemical baths—structural and optical analysis, *J. Cryst. Growth*. 285 (2005) 41–48.
- [67] S.A. Jassim, A.A. Rashid, A. Zumaila, G. Abdella, A. Al, Influence of substrate temperature on the structural, optical and electrical properties of CdS thin films deposited by thermal evaporation, *Results Phys.* 3 (2013) 173–178.
- [68] K.S. Munir, M. Qian, Y. Li, D.T. Oldfield, P. Kingshott, D.M. Zhu, C. Wen, Quantitative Analyses of MWCNT-Ti Powder Mixtures using Raman Spectroscopy: The Influence of Milling Parameters on Nanostructural Evolution, *Adv. Eng. Mater.* 17 (2015) 1660–1669.
- [69] D. Kim, Y.B. Chun, M.J. Ko, H. Lee, M. Cho, J.Y. Park, W. Kim, Microstructure evolution of a ZrC coating layer in TRISO particles during high-temperature annealing, *J. Nucl. Mater.* 479 (2016) 93–99.
- [70] S. Pellegrino, L. Thomé, A. Debelle, S. Miro, P. Trocellier, Radiation effects in carbides: TiC and ZrC versus SiC, *Nucl. Inst. Methods Phys. Res. B.* 327 (2014) 103–107.
- [71] L. Hui, L. Zhang, Q. Zeng, H. Ren, K. Guan, Q. Liu, L. Cheng, First-principles study of the structural, vibrational, phonon and thermodynamic properties of transition metal carbides TMC (TM=Ti, Zr and Hf), *Solid State Commun.* 151 (2011) 61–66.
- [72] H. Wipf, M. V Klein, W.S. Williams, Vacancy-Induced and Two-Phonon Raman Scattering in ZrCx, NbCx, HfCx, and TaCx, *Phys. Status Solidi.* 108 (1981) 489–500.
- [73] A.C. Ferrari, J. Robertson, Interpretation of Raman spectra of disordered and amorphous carbon, *Phys. Rev. B.* 61 (2000) 95–107.
- [74] E. Petrova, S. Tinchev, P. Nikolova, Interference effects on the ID/IG ratio of the Raman spectra of diamond-like carbon thin films, (2011). <http://arxiv.org/abs/1112.0897> <http://www.arxiv.org/pdf/1112.0897.pdf>.
- [75] M. Patel, C.L.A. Ricardo, P. Scardi, P.B. Aswath, Morphology, structure and chemistry of extracted diesel soot—Part I: Transmission electron microscopy, Raman spectroscopy, X-ray photoelectron spectroscopy and synchrotron X-ray diffraction study, *Tribol. Int.* 52 (2012) 29–39.
- [76] S. Biira, P.L. Crouse, H. Bissett, T.T. Hlatshwayo, E.G. Njoroge, J.T. Nel, T.P. Ntsoane, J.B. Malherbe, The role of ZrCl₄ partial pressure on the growth characteristics of chemical vapour deposited ZrC layers, *Ceram. Int.* 43 (2017) 15133–15140.
- [77] A.C. Ferrari, J. Robertson, Resonant Raman spectroscopy of disordered, amorphous, and diamondlike carbon, *Phys. Rev. B.* 64 (2001) 75414.

CHAPTER 8

CONCLUSIONS AND FUTURE WORK

8.1 Conclusion

This study focused on detailing the development of a deposition process for the preparation and optimisation of ZrC layers from $\text{ZrCl}_4\text{-Ar-CH}_4\text{-H}_2$ precursors, using induction thermal CVD at atmospheric pressure. A vertical wall thermal CVD reactor was designed, fabricated and used for the deposition of ZrC layers. This CVD reactor has the capability of depositing a variety of films and coatings for various research and industrial applications. The process parameters and the CVD reactor geometry were engineered so as to control the growth and quality of ZrC layers. $\text{ZrCl}_4\text{-CH}_4\text{-H}_2\text{-Ar}$ mixtures were used for the deposition of ZrC layers. ZrCl_4 vapour flow control was achieved by careful designing of the CVD vaporiser system and controlling the argon carrier gas flow plus the vaporisation temperature. The amount of ZrCl_4 loaded and its surface area exposed to the carrier gas was also carefully managed. The ZrC layers were deposited on graphite substrates under a variety of conditions. The deposited ZrC layers were then studied according to their deposition condition, namely substrate temperature, precursor flow ratios and partial pressures, reactor geometry and deposition time.

The substrate temperature (1200 °C-1600 °C) and $\text{CH}_4/\text{ZrCl}_4$ ratio (6.0 to 24.4) were examined both thermodynamically and experimentally and were found to have a major influence on ZrC growth kinetics. Response surface methodology (RSM) was used to give a correlation between the responses (average crystallite size, growth rate and composition) and the independent variables (substrate temperature and $\text{CH}_4/\text{ZrCl}_4$ ratio). The growth rate and average crystallite size followed a quadratic trend, whereas the composition (C/Zr) followed a linear trend. The optimum conditions for producing relatively thick near-stoichiometric ZrC

layers (i.e. C/Zr of 1.03 and a growth rate of 6.05 $\mu\text{m/h}$) with crystallite size of 29.8 nm were determined as 1353.3 $^{\circ}\text{C}$ for the substrate temperature and 10.14 for the $\text{CH}_4/\text{ZrCl}_4$ molar ratio.

The influence of the gap between the gas inlet and the substrate (70 mm–170 mm) on ZrC layer growth characteristics was investigated at 1200 $^{\circ}\text{C}$ and 1400 $^{\circ}\text{C}$. The growth rate decreased with increasing substrate-inlet gap at both temperatures. When the gap between the substrate and the inlet was reduced the boundary layer thickness decreased. The decreased boundary layer thickness resulted into higher fluxes of reactants and hence increased growth rates. The diffusion coefficient of the gas mixture at 1200 $^{\circ}\text{C}$ was lower than at 1400 $^{\circ}\text{C}$. Correspondingly, the layer growth rate at 1200 $^{\circ}\text{C}$ was lower than at 1400 $^{\circ}\text{C}$. The C/ZrC ratio increased with an increase in substrate-inlet gap at both temperatures, with 1400 $^{\circ}\text{C}$ yielding the highest ratio. Increasing the substrate-inlet gap both at 1200 $^{\circ}\text{C}$ and 1400 $^{\circ}\text{C}$ resulted in a decreased in the average crystallite size and increased the lattice strain. The increase in lattice strain was probably due to an increase in lattice imperfection, resulting from the increased concentration of free carbon in the deposited layer. The (111) diffraction plane was the least favoured orientation, whereas (200) and (220) were more favoured planes. The degree of preferred orientation decreased with substrate-inlet gap at the two temperatures. The samples deposited at 1200 $^{\circ}\text{C}$ had a higher degree of preferred orientation than those deposited at 1400 $^{\circ}\text{C}$. For the 1200 $^{\circ}\text{C}$ substrate temperature, at 70 mm substrate-inlet gap, the crystals had better developed facets with high crystallinity, which deteriorated with an increase in substrate-inlet gap. The morphology of the deposited layers changed as the substrate-inlet gap and substrate temperature were varied.

Furthermore, the role of ZrCl_4 partial pressure on the microstructure and surface morphology was investigated. The boundary layer thickness decreased with an increase in the ZrCl_4 partial pressure resulting in higher fluxes and growth rates. The gas flows were laminar and

forced convectional. The growth rate of the ZrC layers increased almost linearly with increasing ZrCl₄ partial pressure. The ZrC layer microstructure and morphology were found to vary with ZrCl₄ partial pressure. At low ZrCl₄ partial pressure ZrC and carbon were co-deposited. The amount carbon in the layers decreased with an increase in ZrCl₄ partial pressure values. The (111) diffraction plane was a more favoured orientation at lower ZrCl₄ partial pressure, whereas the (200) and (220) were the more favoured planes at higher ZrCl₄ partial pressure. There was a general increase in average crystallite size with increasing ZrCl₄ partial pressure. The lattice parameter, lattice strain and dislocation density decreased with increasing ZrCl₄ partial pressure. At low ZrCl₄ partial pressures, the ZrC layer had small particles tending to cluster together and surrounded by lots of voids. When the ZrCl₄ partial pressure was further increased the crystals increased in size and became more dense and coarse. The clustering and aggregation of particles into large agglomerates were also enhanced as the ZrCl₄ partial pressure increased.

The dependence of growth rate, microstructure and morphological evolution of ZrC layers on deposition times was also studied. The ZrC layers were deposited at 1400 °C for different deposition time ranging from 0.5 h to 2.5 h. The results indicated that the stagnant ZrCl₄ vaporiser and deposition time had an effect on the quantity of ZrCl₄ delivered to the reaction chamber. The amount of ZrCl₄ delivered to the reaction chamber declined as the deposition time increased. Meanwhile, the mass of the ZrCl₄ vaporiser increased as the deposition time increased implying, that more and more ZrCl₄ got clogged in the vaporiser. The ZrC layer thickness increased rapidly from 0.5 h to 1.5 h and thereafter the increase was not significant. There was an increase in growth rate of the ZrC layers up to the deposition time of 1 h and thereafter the growth rate started declining. For all deposition times, the structure of the layers deposited was polycrystalline and face centred. The preferred orientation of the diffraction planes varied with the deposition time with the (220) and (200) planes more

preferred for short and long deposition times, respectively. The crystallite size increased from 27.8 nm to 32.3 nm as the deposition time increased from 0.5 h to 2.5 h. The number of crystallites also increased with the deposition time. The Raman spectra showed the presence of free carbon, which increased with an increase in deposition time. At the early stages of deposition the free carbon was amorphous but its level of crystallisation increased with deposition time. The deposition time had an influence on the surface morphology as well. For short deposition times, the surfaces of the ZrC layers were relatively flat and smooth. As the time increased, islands emerged which increased in size with time.

In summary:

- The deposition of ZrC layers can be achieved with a careful design of the CVD system and by controlling the deposition conditions. The controlled delivery of ZrCl_4 into the reaction chamber is very important for obtaining layers of the desired properties. To achieve this, the vaporization temperature, ZrCl_4 surface area exposed, carrier gas flow rate and time have to be maintained constant.
- ZrC layers of different stoichiometry can be produced by controlling (a) the precursor flow rates (either by varying the ZrCl_4 flow rate and keeping the methane flow rate at constant, or varying the methane flow rate and keeping the ZrCl_4 flow rate constant), (b) the gap between the substrate and the gas inlet and (c) the deposition temperature. However, for all the deposition conditions studied, hardly sub-stoichiometric ZrC layers were produced even at a reduced methane flow rate. Very low methane flow rates yielded very thin layers (or no layer), making it difficult to characterize.
- The growth rates of the ZrC layers have a strong dependence on the boundary layer thickness and the precursor fluxes. Increasing deposition temperature, deposition time and precursor flow rates, all have a positive effect on the ZrC layer growth rate.

- ZrC layers deposited by varying the substrate temperature, precursor flow rates (compositions and partial pressures), deposition time and substrate-gas inlet gap exhibit distinct microstructural and morphological differences.
- Other studies have indicated that sub-stoichiometric ZrC samples ($C/Zr < 1$) had an improved irradiation resistant microstructure compared to hyper-stoichiometric ZrC samples ($C/Zr > 1$).

Based on the results of this study, the conclusion can be drawn that stoichiometric or near stoichiometric ZrC layers can be produced and that they appear promising for application as fission product barrier in the nuclear TRISO fuel particle.

8.2 Future work

For further improvement and optimization of the CVD process, as well as improving the fundamental understanding of the whole process so as to obtain high quality ZrC layers, the following studies are recommended:

- Computer simulations of the relevant physical and chemical phenomena that are difficult to measure.
- Investigation of the temperature distribution inside the CVD reactor and how it is influenced by changes in induction coil frequency, power input to the coil and graphite reactor chamber thickness.
- A comparison of ZrC layer characteristics deposited in a hot-wall and a cold-wall reaction chamber, and a vertical-wall and a horizontal-wall reaction chamber to ascertain which reactor type can produce quality ZrC layers.
- Irradiation by fast, heavy, highly-charged particles of the ZrC layers produced.

CHAPTER 9

PUBLICATIONS AND CONFERENCES

9.1 Publications

This study has resulted into a number of peer review articles which have been published in international journal. These articles are:

- (1) **S. Biira**, P.L. Crouse, H. Bissett, B.A.B. Alawad, T.T. Hlatshwayo, J.T. Nel, J.B. Malherbe, “*Optimisation of the synthesis of ZrC coatings in an RF induction-heating CVD system using surface response methodology*”, Thin Solid Films. Vol 624 (2017) pp. 61-69.
- (2) **S. Biira**, B.A.B. Alawad, H. Bissett, J.T. Nel, T.P. Ntsoane, T.T. Hlatshwayo, P.L. Crouse, J.B. Malherbe, “*Influence of the substrate gas-inlet gap on the growth rate, morphology and microstructure of zirconium carbide films grown by chemical vapour deposition*”, Ceramics International Vol 43 (2017) pp. 1354-1361.
- (3) **S. Biira**, P.L. Crouse, H. Bissett, T.T. Hlatshwayo, E.G. Njoroge, J.T. Nel, T.P. Ntsoane, J.B. Malherbe, “*The role of ZrCl₄ partial pressure on the growth characteristics of chemical vapour deposited ZrC layers*”, Ceramics international. Vol 43 (2017) pp. 15133-15140.
- (4) **S. Biira**, P.L. Crouse, H. Bissett, T.T. Hlatshwayo, J.H. van Laar, J.B. Malherbe, “*Design and fabrication of a chemical vapour deposition system with special reference to ZrC layer growth characteristics*”, The Journal of the Southern African Institute of Mining and Metallurgy. Vol. 117 (2017) pp. 931-938.
- (5) **S. Biira**, P.L. Crouse, H. Bissett, T.T. Hlatshwayo, J.B. Malherbe, “*Effect of deposition time on structural and morphological evolution of chemical vapour deposited ZrC*

layers”, To be published.

- (6) B.A.B Alawad, **S. Biira**, H. Bissett, J.T. Nel, T.T. Hlatshwayo, P.L. Crouse, and J.B. Malherbe, “*CVD Growth of ZrC Layers at Different Temperatures.*” *Physics and Materials Chemistry*, vol 4 (2016) pp. 6-9.
- (7) **S. Biira**, B.A.B. Alawad, H. Bissett, J.T. Nel, T.T. Hlatshwayo, J.B. Malherbe, *Deposition of ZrC layers in a vertical wall CVD system*, (SAIP 2016).

9.2 Conferences

The outcomes of this study have been presented to both regional and international conferences. The conferences are:

- (1) Advanced Metals (AMI), Nuclear materials conference 2015, Port Elizabeth, South Africa October 28- 30, 2015. (Poster presentation).
- (2) South African institute of Physics (SAIP), 2016, University of Cape town, South Africa 4-8 July 2016. (Oral talk).
- (3) Advanced Metals (AMI), Ferrous metals conference 2016, Durban, South Africa October 17- 20 2016. (Invited delegate).
- (4) Nuclear Materials Conference 2016, Montpellier, France Novemver 7-10, 2016. (Poster presentation).
- (5) Surface Modifications of Materials by ion Beam (SMMIB) conference 2017, Lisbon Portugal July 10-14, 2017. (Poster Presentation).
- (6) Advanced Metals (AMI), Precious metals conference 2017, Limpopo, South Africa October 17- 20 2017. (Oral talk).

Appendix A: Standard operating procedure (SOP) for the CVD of ZrC (Doc no. AC-AMI-SOP-15001)

1. Purpose and scope

The purpose and scope of this document is to describe the processes applicable to the start-up, running and shut-down of the chemical vapour deposition setup. This includes the 10 kW induction power supply, reactor system, gas supply system and exhaust/scrubber. Possible emergency situations are addressed as well as risks associated with the procedure. Using these procedures hydrogen and methane concentration should never exceed 20% of its lower flammability limit. For a more detailed project description and scope, see the project plan (Doc no. AC-AMI-DES-15004). The document Doc no. AC-AMI-DES-15004 has been integrated in the thesis and therefore not given in the appendix.

2. Background information

The setup is used to inductively heat the reactor (graphite tube), which is inserted in the centre of the induction water cooled copper coil. The graphite tube acts as the work piece and generates the temperatures required to initiate the chemical vapour deposition of ZrC layers on the graphite substrates. The precursors are introduced in the reaction chamber when the required temperatures have been attained and the gases are left to flow for the desired time. For more detailed background information, see the process description (Doc no. AC-AMI-DES-15004).

Applications of this technology described here include the synthesis of zirconium carbide layers using $ZrCl_4$ and methane as precursors. The equipment can potentially be adjusted to allow for direct deposition of other materials such as SiC, TiN, TaC, TiC, ZrN onto a substrate of various dimensions and orientations.

3. SOP for the RF induction heating CVD setup

The relevant documentation for the RF induction power supply is provided within the lab safety file, located at the entrance to the lab. Also, **the operator should familiarize him/herself with the material safety data sheets (MSDS) files of the various materials before commencing any experiments.**

The process and instrumentation diagram (P&ID) of the process is located on page 198 in Appendix A. The start-up, running and shutdown procedures are based on this diagram and equipment numbering system.

3.1 Pre-experimental preparations

Ensure all the person protective equipment (PPE) are available and in good conditions. PPE must be dressed before the start of any operations relating to the experiment. For this experimental process the most important PPEs are the Lab coat, face mask, rubber gloves, heat resistant gloves, latex gloves safety shoes, Respirators. The ventilation system, water system and electrical system have to be checked to ascertain their conditions

3.1.1 Storage and loading of $ZrCl_4$

$ZrCl_4$ powder is stored in an enclosed cupboard in Lab 142. It will be scooped from its container with a specular into a small sample bottle placed inside a glove box. The small sample bottle containing $ZrCl_4$ will be transferred to Lab 329 and kept in the desiccator. A desired amount will be loaded in the vaporiser as quick as possible to avoid contact with moisture and personal exposure. A vapour/dust respirator should be used during this process.

3.1.2 Installation of graphite tube

For every experimental run the graphite tube is installed at the start and uninstalled at end of the experiment when it has sufficiently cooled. In order to avoid contamination of the deposit, it is important that the tube cleaned properly for every experimental run. It should also be well position so that the inlet gases are properly directed right to its inside and the exit gas pipe well fixed to its port. The effectiveness of the centring is dependent on window located at the top of the flange.

3.2 Start-up procedure

1. Mount the substrates on a clean substrate stage and fix the substrate stage in the graphite tube (reaction chamber)
2. Fix the loaded graphite tube at the centre of the induction coil inside the steel casing.
3. Fasten the exit gas pipe on the graphite reaction chamber
4. Ensure that the insulating material has been used to prevent heating of the steel casing
5. Ensure that the reactor system is tightly closed and the inlet pipe is properly directed into the reaction chamber.

6. Ensure that cooling water (CW) is flowing through the induction RF power supply and also the cooling water jacket in the exhaust system. Open valves V-1 & V-9, then V-6 & V-7
7. Ensure that all valves are closed except those of the CW.
8. Flow argon in the reactor for some time and open the vacuum pump so that all the oxygen and moisture is extracted away from the reactor. Open valve V-3
9. Ensure that the required amount of $ZrCl_4$ powder is loaded in vaporiser and the temperature of the vaporisation system is set to the desired level.
10. Switch on the heating tape and set it at required temperature to heat the pipes of other gases.
11. Switch on the RF power supply and allow time of about 10 minutes to preheat.
12. Open FI-101 and set the flow rate of the methane (CH_4) stream to desired value
13. Open FI-102 and set the flow rate of the hydrogen gas to the desired value.
14. Open FI-103 and set the flow rate of the argon gas to the desired value.
15. Open V-2 and V-4 and release $ZrCl_4$ to the reactor.
16. Keep valves V-3 and V-7 open for the desired deposition time and maintain the vacuum pump valve on.
17. Pressure indicator (P-101) should indicate the required pressure inside the reactor. It is always a good idea to close V-7 and check whether required pressure is maintained within the reactor.
18. Check that total reactor pressure remains at about atmospheric pressure.

3.3 During operation

During operation, the gas flow rates can be altered, however the user must be vigilant of the operating pressure inside the reactor, as higher flow rates will increase the pressure.

The total power is also adjustable during operation, although if power is reduced too much the required deposition temperatures of ZrC may not be achieved and hence no deposit.

The operator can at any time shutdown the RF power supply, without adjusting the flow rates, by pressing the large red button on the user interface controller connected to the power supply, or by pressing “Stop” on the touch screen of the controller.

Experimental runs should be closely monitored and must under no circumstances be left unattended. At least two people (who are both familiar with the operation of the system) must be present during experimental runs.

3.4 Shut-down procedure

1. First switch off the RF power supply by pressing the large red button connected on the user interface controller or by pressing “Stop” on the touch screen of the controller. Press “Stop” again to initiate the cool down phase.
2. Close V-5 to prevent the flow of hydrogen, methane and $ZrCl_4$.
3. Close valve V-2 and V-4, and the gas cylinder valves for methane and hydrogen
4. Keep valve V-3 open for some time for argon to stabilise the temperatures and to flush the pipes of any residual $ZrCl_4$. Be aware that the reactor or graphite tube will still remain hot for a while.
5. Close V-3 to stop the flow of argon.
6. Shutdown the vacuum pump.
7. Close valves V-7.
8. Ensure all the gas bottles are tightly closed
9. Clean the collection sample containers in order to keep the material deposit (ZrC).
10. When the user interface controller indicates that the cooling phase has finished, switch off the power supply.
11. Close valves V-1 and V-9, V-6 and V-7 and (in that order) and shut off the flow of CW.
12. After the graphite reactor has cooled sufficiently uninstall it from the system
13. First clean the outside of the graphite to avoid contamination of the ZrC coatings
14. Open it to remove the substrate stage and then remove the substrates. It is expected that ZrC layer will be coated on the substrates. And keep the ZrC coated substrates in a clean airtight containment

3.5 Emergency procedures

In case of any emergency, immediately shut off the system by pressing the large red button on the user interface controller. Afterwards, stop the flow of gas, specifically that of hydrogen, methane and $ZrCl_4$, by closing the valves of all gas cylinders. Switch off the power from the heating tape. Also switch off the power connected to the vaporiser system. Shut down the vacuum pump/scrubber.

3.6 Safety risk scenarios

The focus of these procedures is partly to maintain a hydrogen and methane concentration that never exceeds 20% of its lower flammability limit. For hydrogen this amounts to no more than

0.8% (v/v) and methane it is not more than 1% v/v. The following are a few scenarios that might occur during the course of the experiments, as well as the procedures to be followed should such a scenario occur. Also, one should familiarize oneself with the MSDS of all chemicals involved, in the case of accidental contact, inhalation or ingestion.

3.6.1 ZrCl₄ spill

In the case of ZrCl₄ spill, absorb with DRY earth, sand or other non-combustible material. DO NOT bring into contact with water. DO NOT touch spilled ZrCl₄. Prevent entry into sewers, basements or confined areas. Dispose-off properly.

3.6.2 ZrCl₄ reaction

WARNING: Hydrogen chloride gas is produced during reaction. Other toxic products such as halogenated compounds and metallic oxides may also be produced. DO NOT USE WATER. Use DRY chemical powder or sand. Wear gas mask and hand gloves.

3.6.3 Gas leaks

The entire system will, in all cases, run slightly higher than atmospheric pressure, which will prevent oxygen gas from leaking into the reactor. However, gas leaks are to be checked for throughout the system on a regular basis (at least once a week) and before each experimental run. This can be done by flushing the system with an inert gas and placing soap water over all the valves, fittings and connections. Hydrogen and methane leak tests are also to be performed using a portable hydrogen and methane leak detectors, which can be found in the lab. If the leak detector is not in the lab, speak to the person responsible.

The lab ventilation system must be checked regularly (at least once daily), and should be running on a continuous basis, in order to ensure the prevention of any gas build-up within the labs. Ventilation outlets are located within the fume cupboards as well as at various points throughout the ceiling. The hydrogen and methane gas cylinders are to be equipped with flame resistors. The hydrogen and methane lines are to be connected to the reactor via continuous steel piping (i.e. no in-between connections).

In the event that an operator becomes aware of a leak during operation (which might be indicated by an increase in pressure or the presence of an unknown odour), immediately press the large red button on the user interface controller and close all cylinder valves (specifically hydrogen,

methane and $ZrCl_4$). Switch off vacuum pump/scrubber. Wait for gas to exit through the ventilation system, and check for leaks throughout entire process. The doors of the lab must be kept clear open during experimental operation.

3.6.4 Current leakage

The reactor system casing is earthed to avoid possibility of electrical shock from the body of the steel casing. The graphite reaction chamber is isolated from the rest of other connections and from the steel casing. The insulating material (zirconia wool) has been placed between the graphite reaction chamber and the steel casing to avoid any leakage. Also the connecting pipes to the graphite reaction chamber are made of ceramic materials so that there is no electrical conduction what so ever. However the user has to ensure safety by wearing the appropriate gloves. In case of serious power problems switch of the circuit breaker

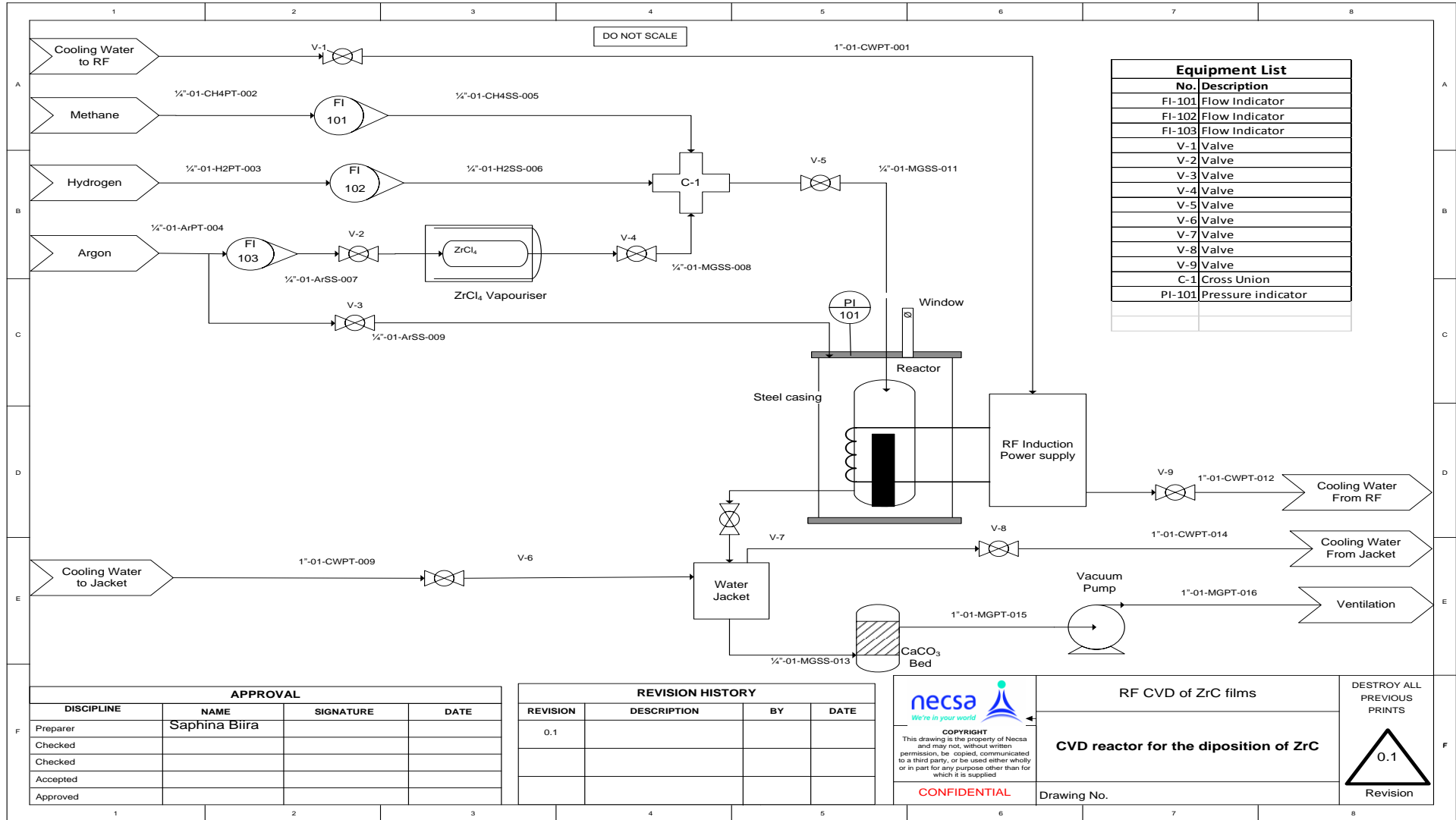
3.6.5 Overheating of the system

The maximum temperature of operation for this experiment is 1600 °C. The RF induction system is water cooled. One has to ensure cooling water is switched on and all the inlet and outlet water valves are open before the RF power supply is started. This water has to remain open for appropriate time after the experiment has stopped until the system cools down. The exit pipe is equipped with water jacket to cool the exit gases before entering the scrubber. The zirconia wool in between the graphite reaction chamber and the steel casing is also a good insulator of heat.

3.6.6 Duration of experimental runs

These procedures are written for experimental runs of not long than three hours approximately performed at temperatures from 1100 °C to 1600 °C. Experimental runs should be closely monitored and shall under no circumstances be left unattended. At least two people (who are both familiar with the operation of the system) must be present during experimental runs. It is again noted that the hydrogen and methane concentration that never exceeds 20% of its lower flammability limit. The start-up and shut-down procedures apply for each experimental run, and should therefore be followed accordingly. This includes closing of cylinder valves between runs. The figure below represents the PI&D diagram for this process.

This document is the property of NECSA and shall not be used, reproduced, transmitted or disclosed without prior written permission



Equipment List	
No.	Description
FI-101	Flow Indicator
FI-102	Flow Indicator
FI-103	Flow Indicator
V-1	Valve
V-2	Valve
V-3	Valve
V-4	Valve
V-5	Valve
V-6	Valve
V-7	Valve
V-8	Valve
V-9	Valve
C-1	Cross Union
PI-101	Pressure indicator

APPROVAL			
DISCIPLINE	NAME	SIGNATURE	DATE
Preparer	Saphina Biira		
Checked			
Checked			
Accepted			
Approved			

REVISION HISTORY				
REVISION	DESCRIPTION	BY	DATE	
0.1				

necsa
We're in your world

COPYRIGHT
This drawing is the property of Necsa and may not, without written permission, be copied, communicated to a third party, or be used either wholly or in part for any purpose other than for which it is supplied

CONFIDENTIAL

RF CVD of ZrC films

CVD reactor for the diposition of ZrC

Drawing No.

DESTROY ALL PREVIOUS PRINTS

0.1

Revision

Appendix B: Safety risk evaluation for the project (DOC NO: AC-AMI-HRA-15002)

1. Scenario

Chemical vapour deposition of zirconium carbide coatings using induction heating system

2. Motivation

ZrC coatings are to be synthesised and deposited onto surfaces

3. Safety Risk Evaluation Outcome

B: Moderate

4. Chemical scenarios to be used

4.1 Zirconium (IV) chloride (CAS #:10026-11-6)

Use description: Chemical is to be evaporated and injected into the reactor

Motivation: $ZrCl_4$ is used as precursor for the synthesis of ZrC

Quantity description: Less than 25 g

Operation description: Enclosed/Sealed process (eg Glove box, hot cell or closed reactor system) or possible exposure < 10% of its occupational exposure limit (OEL)

Resulting risk level: A: Negligible/Low

4.2 Argon (CAS #:7440-37-1)

Use description:

Argon gas will flow through the reactor

Motivation:

Argon is inert and will feed the $ZrCl_4$ into the reactor and will be used to prevent oxygen from entering the reactor

Quantity description: Less than 10 kg

Operation description: Manual semi-enclosed process (e.g. inside a fume cupboard) or possible exposure 50-100% of OEL

Resulting risk level: A: Negligible/Low

4.3 Hydrogen gas (CAS #:1333-74-0)

Use description: Hydrogen will flow through the reactor

Motivation: Hydrogen helps create a reducing environment to help the $ZrCl_4$ to form ZrC in the presence of a carbon source

Quantity description: Less than 1 kg

Operation description: Manual semi-enclosed process (e.g. inside a fume cupboard) or possible exposure 50-100% of OEL

Resulting risk level: A: Negligible/Low

4.4 Zirconium carbide (CAS #:12070-14-3)

Use description: Product from the reaction between $ZrCl_4$, H_2 and methane

Motivation: Desired product

Quantity description: Less than 100 g

Operation description: Manual semi-enclosed process (e.g. inside a fume cupboard) or possible exposure 50-100% of OEL

Resulting risk level: A: Negligible/Low

4.5 Hydrogen chloride (CAS #:7647-01-0)

Use description: Waste product from the reaction

Motivation: HCl forms as by-product and will be neutralised by a scrubber

Quantity description: Less than 25 g

Operation description: Manual semi-enclosed process (e.g. inside a fume cupboard) or possible exposure 50-100% of OEL

Resulting risk level: A: Negligible/Low

4.6 Methane (CAS #:74-82-8)

Use description: Methane will be used as carbon source in the production of ZrC coatings during the reaction with $ZrCl_4$

Motivation: Methane will be used as carbon source

Quantity description: Less than 100 g

Operation description: Manual semi-enclosed process (e.g. inside a fume cupboard) or possible exposure 50-100% of OEL

Resulting risk level: A: Negligible/Low

5. Other safety risk elements

Heading	Question	Answer	Motivation	Risk Level
Experimental setup	What is the total volume of the experimental setup?	Laboratory setup inside fume hood where $V < 5L$		A: Negligible/Low
Experimental setup	Are you going to work in glass and what will the value of pressure (in kPa) x volume (in L) be?	Not working in glass		A: Negligible/Low
Experimental setup	Are you going to work in plastic and what will the value of pressure (in kPa) x volume (in L) be?	Not working in plastic		A: Negligible/Low
Experimental setup	Are you going to work in metal and what will the value of pressure (in kPa) x volume (in L) be?	pV is less than 500 and $p < 1000 \text{ kPa(g)}$ or p is less than half the design pressure of the vessel		A: Negligible/Low
Experimental setup	Will you be working with flammable liquids?	Flash point $> 38^\circ\text{C}$ and Volume $< 25L$ or flash point $< 38^\circ\text{C}$ and Volume $< 2.5L$ and working in fume hood		A: Negligible/Low
Experimental setup	Will you be working with flammable gas?	Total inventory in mol x 0.0373% \geq Lower flammable/explosion limit AND working in ventilated enclosure (eg. fume cupboard, vented box, etc.)		B: Moderate

Experimental setup	Will you be working with flammable solids?	No flammable solids		A: Negligible/Low
Experimental setup	Will it be necessary to move any expensive equipment?	No		A: Negligible/Low
Experimental setup	How much effluent do you expect to generate?	V < 50L		A: Negligible/Low
Ionizing Radiation	What will the size of your inventory of radioactive material be?	Uncontrolled. No radioactive material.		A: Negligible/Low
Ionizing Radiation	What is the possibility of radioactive contamination?	Uncontrolled. No contamination possible.		A: Negligible/Low
Ionizing Radiation	What is the possibility of radiation exposure?	Uncontrolled. No exposure possible.		A: Negligible/Low
Ionizing Radiation	Will you have to transfer radioactive material?	No transfer required.		A: Negligible/Low
Facility	Will all the criteria as specified in the facility specific basic operational rules be adhered to?	Yes		A: Negligible/Low
Facility	How will you	Work within the current		A: Negligible/Low

	influence the current ventilation system?	ventilation system. No modification to the system.		
Facility	How will you influence the current electrical system?	Use existing electrical infrastructure as is		A: Negligible/Low
Facility	How will you influence the current utility supplies?	Use existing outlets		A: Negligible/Low
Facility	How will you influence the current effluent system?	Use existing outlets		A: Negligible/Low
Facility	How will you influence the current building structure?	Use existing structure		A: Negligible/Low
Physical and Environmental Factors	What will the level of noise be that an operator will be exposed to?	<85dB(A)		A: Negligible/Low
Physical and Environmental Factors	What will the wet bulb globe temperature (WBGT) index be in your work area?	WBGT index < 25		A: Negligible/Low
Physical and Environmental Factors	What will the dry bulb temperature (DBT) be in your work area?	DBT > 5°C		A: Negligible/Low
Physical and Environmental Factors	Will your work area be exposed to glare or your	Mild degree of glare (e.g. Computer screen, indoor lights, etc.)		A: Negligible/Low

	experiment involve strong light emmissions?			
Physical and Environmental Factors	Will you be exposed to segmental vibration?	No vibration		A: Negligible/Low
Physical and Environmental Factors	Will you be exposed to whole body vibration?	No vibration		A: Negligible/Low
Physical and Environmental Factors	Will you use a laser and what classification will it be?	No laser will be used		A: Negligible/Low
Physical and Environmental Factors	To what degree will ergonomic stress be encountered?	Low demand (Low repetition, normal body position and low weight)		A: Negligible/Low

Appendix C: Hazard and operability study (HAZOP) report on the CVD of ZrC (Doc no. AC-AMI-HRA-15001)

1. Introduction

The purpose of this phase of the project is to deposit zirconium carbide onto graphite substrates under varying operating parameters. Zirconium tetrachloride and methane are used as precursor, and are injected into an induction heated reactor at pressure close to atmosphere.

The long term goal envisions the encapsulation of nuclear waste and fission products, with zirconium carbide serving as a replacement or an added layer on silicon carbide in the nuclear fuel particle for the prevention of radionuclide release.

2. Purpose

The purpose of this report is to present the results of the HAZOP performed on the system and to outline the recommendations that have emerged from this study.

3. Scope

The study was performed on the CVD process given in Appendix A

4. References

- a) AC-AMI-SOP-15001: Standard operating procedure for chemical vapour deposition equipment
- b) AC-AMI-DES-15004: Process description for chemical vapour deposition of zirconium carbide
- c) AC-AMI-HRA-15002: Safety risk evaluation for the Project

5. Methodology

Each of the deviations in the list on the study proforma was applied to the path, questioning whether it could occur. If the deviation was not likely to occur or create a problem or hazard, NA (Not Applicable) was added to the column and it was given no further consideration.

If it was decided that the event could occur and its consequences would be unacceptable, then a cross was made in the 'Yes' column and a number (1,2,3...) entered in the 'Ref'

column. The hazardous event was then referred to in the study record proforma and analysed with respect to the following:

- Causes (e.g. failures);
- Likelihood (frequency);
- Consequences (e.g. problems or hazards);
- Preventative measures which will eliminate the causes;
- Protective or emergency measures to reduce the consequences;
- Risk rating (likelihood x consequence);
- Recommendations to either prevent the event or protect against its consequences not already provided for in the preliminary design; and
- Assigning a person responsible for carrying out the actions to implement the recommendations.

The consequence matrix was used to determine the risk rating for each hazard. The hazards with the highest risk rating will be of highest priority. The consequence matrix is shown below:

Risk rating

		4	8	12	16
Frequency	4	4	8	12	16
	3	3	6	9	12
	2	2	4	6	8
	1	1	2	3	4
		1	2	3	4
		Consequence / Severity			

Where:

Likelihood/ Frequency	Rating
Cause will occur frequently - weekly or monthly	4
Cause is expected to occur every year	3
Cause is expected to occur once every few/10 years	2
Cause could occur rarely - maybe once during plant life	1

Consequences/ Severity	Rating
Fatality/permanent injury, facility destruction, off-site environmental consequences, facility closed for financial reasons.	4
Severe injury, major damage to facility, on-site environmental consequences, serious financial setback.	3
Injury, minor damage to facility, localized environmental consequences, financial setback.	2
No injury or property damage but could lead to unscheduled maintenance and loss of production with minor financial implications.	1

The person to take action is Saphina Biira (SB) supervised by Hertzog Bissett (HB)

5. Summary of identified recommended actions

Recommended actions (reference to study results in parentheses)	Resp.
Check regulator, Install a pressure relief valve on the best position (1,3,22)	SB,HB
Install HCl dry scrubber (Calcium carbonate bed) before vacuum pump (2,26)	SB,HB
Check reactor temperature during runs; Put off system (power supply) if the temperature reaches 1700C (14)	SB,HB
Operator reactor above atmospheric pressure, Check vacuum integrity of system, Update operating procedure (ensure system leak tight), If leak then pressurise and snoop to detect	SB,HB
Connect pressure relief outlet to extraction or vent, Stop experiment (24)	SB,HB
Flame arrestor valves (10)	SB,HB
Do not perform or stop experiment if ventilation is off (30)	SB,HB
Check vacuum of system before each run (use snoop) (33)	SB,HB
Use portable hydrogen and methane detector, lower flammability limit calculations were done, First runs will be under supervision (35)	SB,HB
Check scrubber regularly, calculations were done of the maximum amount of HCl which can form (39)	SB,HB
Do not perform or stop experiment if ventilation is off, Put of power supply on circuit breaker in passage (SAP) (42)	SB,HB
Check argon supply before run (43)	SB,HB
Handle as chemical waste according to specifications (48)	SB,HB
Make sure no leaks, Use PPE, MSDS available (51)	SB,HB
Fire brigade assessment (Additional assessment)	SB,HB

6. Study results

6.1 HAZOP 3 Record

No	Description	Scenario	Probability	Severity	Risk	Preventive action or established control	Resp.
1	Pressure High	Human error, pressure regulators	Highly unlikely	Minor injury and/or significant cost	Low	Check regulator, Install pressure relief valve on the best position	HB, SB
2	Pressure Surge	Vacuum pump	Highly unlikely	No impact	Very Low	Check vacuum pump and blockage of CaCO ₃ bed	
3	Pressure High Inlet	Similar to No1	Highly unlikely	Minor injury and/or significant cost	Low	Check regulator, Install pressure relief valve on the best position	HB, SB
4	Pressure Low Inlet		Never	No impact	Very Low		
5	Pressure Low Discharge		Never	No impact	Very Low		
6	Pressure Vacuum	Vacuum pump default	Highly unlikely	No impact			
7	Flow High	Regulator and flow meters, Cooling	Highly unlikely	Minor cost and/or loss of time	Very Low		
8	Flow Low	Similar to No7	Highly unlikely	Minor cost and/or loss of time			
9	Flow No	Similar to No7	Highly unlikely	Minor cost and/or loss of time	Very Low		
10	Flow Reverse	Methane and Hydrogen lines	Highly unlikely	Minor cost and/or loss of time	Very Low	Flame arrestor valves	HB, SB
11	Flow Two Phase		Never	No impact	Very Low		
12	Flow to / from other direction		Never	No impact	Very Low		
13	Velocity High	Similar to No7					
14	Temperature High	Faulty power supply	Possible	Minor cost and/or loss of time	Medium	Check reactor temperature during runs; Put off system (power supply) if the temperature reaches 1700C	
15	Temperature Low		Never	No impact	Very Low		
16	Temperature Freezing		Never	No impact			
17	Level High		Never	No impact	Very Low		
18	Level Low		Never	No impact	Very Low		
19	Level No		Never	No impact	Very Low		
20	Composition	Faulty flow meters or regulators, Presence of oxygen (explosion)	Unlikely but possible	Disabling injury and/or severe cost	Medium	Operator reactor above atmospheric pressure, Check vacuum integrity of system, Update operating procedure (ensure system leak tight), If leak then pressurise and snoop to detect area of leak	SB
21	Property Change		Never	No impact	Very Low		

22	Contamination	water leak in reactor (type defective)	Highly unlikely	Disabling injury and/or severe cost	Medium	Check water lines before runs for leaks, Pressure relief valve	HB, SB
23	Material / Product addition		Never	No impact	Very Low		
24	Relief Pressure	Pressure relief valve opens	Highly unlikely	Minor cost and/or loss of time	Very Low	Pressure relief outlet connected to extraction or vent, Stop experiment	HB, SB
25	Relief Thermal		Never	No impact	Very Low		
26	Compatibility Material / Pressure / Equipment	HCl gas will form	Likely	No impact	Very Low	CaCO ₃ bed used as scrubber to capture the HCl gas	
27	Corrosion / Erosion	Presence of HCl	Possible	Minor cost and/or loss of time	Medium	System made of stainless steel	
28	Vibration		Never	No impact	Very Low		
29	Water Hammer	Water cooling system	Highly unlikely	No impact	Very Low		
30	Vents / Drains	Building ventilation off	Highly unlikely	No impact	Very Low	Do not perform or stop experiment if ventilation is off	
31	Sample Points		Never	No impact	Very Low		
32	Dead Legs		Never	No impact	Very Low		
33	Critical pipelines and valves	All types (cooling and gas), pipe and valves leaking	Highly unlikely	Minor injury and/or significant cost	Low	Check vacuum of system before each run (use snoop)	
34	Static electricity		Never	No impact	Very Low		
35	Fire protection	Run away temperature (No 14), Hydrogen leak	Unlikely but possible	Disabling injury and/or severe cost	Medium	Portable hydrogen detector, lower flammability limit calculations were done, First run will be under supervision	
36	Civil considerations		Never	No impact	Very Low		
37	Utilities	Electricity failure	Highly unlikely	Minor cost and/or loss of time	Very Low		
38	Lines and bends	See No33	Highly unlikely	Minor cost and/or loss of time	Very Low		
39	Pollution Air / Noise / Environment	Scrubber fails	Highly unlikely	Minor cost and/or loss of time	Very Low	Check scrubber regularly, calculations were done of the maximum amount of HCl which can form	
40	Electrical control systems	Power supply failure	Highly unlikely	Minor cost and/or loss of time	Very Low		
41	Actuated valves		Never	No impact	Very Low		
42	Electrical classification	Building ventilation fails, can cause built-up of hydrogen	Highly unlikely	Minor injury and/or significant cost	Low	Do not perform or stop experiment if ventilation is off, Put of power supply on circuit breaker in passage (SOP)	
43	Purging and inerting	Argon system fail	Highly unlikely	Minor cost and/or loss of time	Very Low	Check argon supply before run	
44	Cathodic protection		Never	No impact	Very Low		
45	Interlock systems	Interlock on power supply fails	Highly unlikely	No impact	Very Low		
46	Ventilation systems	See No30	Highly unlikely	No impact	Very Low		
47	Specification break		Never	No impact	Very Low		

48	Bunding Spillage / waste / effluent	Spend Scrubber waste	Likely	No impact	Very Low	Handle as chemical waste according to specifications	
49	Maintenance Spares / frequency		Never	No impact	Very Low		
50	Operations Procedures / commissioning		Never	No impact	Very Low		
51	Exposure to chemical toxicity	HCl exposure, ZrCl ₄ exposure	Highly unlikely	Minor injury and/or significant cost	Low	Make sure no leaks, Use PPE, MSDS available	

Appendix D: Close out report for Hazop on CVD of ZrC layers (DOC No: AC-AMI-HRA-15003)

1. Aim/Background

The aim of this report is to identify possible problems and comply with recommended actions in order to satisfy the HAZOP (Doc. AC-AMI-HRA-15001) and project safety committee recommendations (Doc. AC-AMI-HRA-15001).

2. Description/Results

The recommended actions were listed in the above mentioned documents. The action has been taken as indicated in Table 1 and Table 2 below.

Table 1. Hazop recommended actions and completed actions

Recommended actions (reference to study results in parentheses)	Complete	Date
Check regulator, Install a pressure relief valve on the best position (1,3,22,24)	yes	20/07/2015
Install HCl dry scrubber (Calcium carbonate bed) before vacuum pump (2,26)	yes	10/07/2015
Check reactor temperature during runs; Put off system (power supply) if the temperature reaches 1700C (14)	yes	
Operator reactor above atmospheric pressure, Check vacuum integrity of system, Update operating procedure (ensure system leak tight), If leak then pressurise and snoop to detect area of leak (20)	yes	
Flame arrestor valves (10)	yes	01/07/2015
Do not perform or stop experiment if ventilation is off (30)	yes	
Check vacuum of system before each run (use snoop) (33)	yes	
Use portable hydrogen and methane detector, lower flammability limit calculations were done, First runs will be under supervision (35)	yes	
Check scrubber regularly, calculations were done of the maximum amount of HCl which can form (39)	yes	
Do not perform or stop experiment if ventilation is off, Put of power supply on circuit breaker in passage (SAP) (42)	yes	
Check argon supply before run (43)	yes	
Handle as chemical waste according to specifications (48)	yes	
Make sure no leaks, Use PPE, MSDS available (51)	Yes	
Fire brigade assessment (Additional assessment)	Yes	09/07/2015

Table 11: Project safety committee recommendations and completed actions

Action No.	Recommended actions	Completed	Date
1	Transport zirconium tetrachloride in airtight plastic container	Yes	
2	Engineer must check and approve explosive limits and dilution calculations	Yes	23/07/2015
3	Experimental check list before start of experiment	Yes	22/07/2015
4	Indicate quantities of waste generated and the disposal route in SOP	Yes	22/07/2015
5	Indicate the quantities used per experimental run and flow rates	Yes	22/07/2015
6	Submit close-out Hazop report	Yes	23/07/2015

3. Conclusion



All of the recommended actions were completed, dated and signed in this closeout report.

Appendix E: Fire and explosion risk evaluation of the experimental CVD of ZrC layers

	<h3>SAFETY AND LICENSING DEPARTMENT</h3> <p><i>This document is the property of Necsa and shall not be used, reproduced, transmitted or disclosed without prior written permission</i></p>	
---	--	---

DOCUMENT NO.	SLD-FP2015-REP-0028
REVISION NO.	1.0
TITLE	FIRE AND EXPLOSION RISK EVALUATION OF THE EXPERIMENTAL CHEMICAL VAPOUR DEPOSITION OF ZIRCONIUM CARBIDE

	NAME	SIGNATURE	DATE
PREPARED	L H Pienaar (Emergency Services: Fire Prevention Officer)		09-07-2015
APPROVED	G S Venter (Emergency Services: Manager)		09/07/2015
DISTRIBUTION	SLD RECORDS JH VAN LAAR		

	<h2>SAFETY AND LICENSING DEPARTMENT</h2>						
<p><i>This document is the property of Necsa and shall not be used, reproduced, transmitted or disclosed without prior written permission</i></p>							
DOC NO.	SLD-FP2015-REP-0028	REV.	1.0	PAGE	2	OF	2
TITLE	<p>FIRE AND EXPLOSION RISK EVALUATION OF THE EXPERIMENTAL CHEMICAL VAPOUR DEPOSITION OF ZIRCONIUM CARBIDE</p>						

1 PURPOSE

To report on a fire and explosion risk evaluation of the small scale experimental chemical vapour deposition of zirconium carbide in lab 329 in building V-H2. Up to two approximately one hour experimental runs can be done per day for a period of approximately three months.

2 FIRE AND EXPLOSION RISK CLASSIFICATION

Based on the safety measures as documented in document AC-AMI-SOP-15001, hazardous mixtures of the flammable gases such as hydrogen and methane, is unlikely to occur, even under abnormal conditions. The experimental setup is therefore considered to be safe in terms of SANS 10108.

3 PORTABLE FIRE FIGHTING EQUIPMENT

The number and positions of fire extinguishers were evaluated and considered to be adequate for the fire risk.

4 GENERAL

- 4.1 The gas cylinders must be chained separately. See SHEQ-INS-2160 in this regard.
- 4.2 Any change in the area that might have an influence on the fire safety, must be brought under the attention of the Manager: Emergency Services for re-evaluation.